Modeling the thermoelectric convection in a rectangular cavity

Elhadj Boubacar Barry

Normandie Université

THÈSE

Pour obtenir le diplôme de doctorat

Spécialité PHYSIQUE

Préparée au sein de l'Université Le Havre Normandie

Modélisation de la convection thermoélectrique dans une cavité rectangulaire

Présentée et soutenue par
ELHADJ BOUBACAR BARRY

Thèse soutenue le 29/06/2022 devant le jury composé de		
M. CHRISTOPH EGBERS	PROFESSOR, BRADENBURG UNIV OF TECHNO COTTBUS (DE)	Rapporteur du jury
M. HARUNORI YOSHIKAWA	MAÎTRE DE CONFERENCES (HDR), UNIVERSITE CÔTE D'AZUR	Rapporteur du jury
M. CHANGWOO KANG	ASSOCIATE PROFESSOR, JEONBUK NATIONAL UNIVERSITY (KR)	Membre du jury
M. OLEG KIRILLOV	SENIOR LECTURER, UNIVERSITY OF NORTHUMBRIA (UK)	Membre du jury
MME MARIE-CHARLOTTE RENOULT	MAÎTRE DE CONFERENCES, INSTITUT NATIONAL DES SCIENCES APPLIQUEES ROUEN NORMANDIE	Membre du jury
M. PATRICE LE GAL	DIRECTEUR DE RECHERCHE, AIX-MARSEILLE UNIVERSITE	Président du jury
M. INNOCENT MUTABAZI	PROFESSEUR DES UNIVERSITES, Université Le Havre Normandie	Directeur de thèse

Thèse dirigée par INNOCENT MUTABAZI (Laboratoire Ondes et Milieux Complexes)

UNIVERSITÉ LE HAVRE NORMANDIE

ED 591 PSIME

LABORATOIRE ONDES et MILIEUX COMPLEXES

Normandie Université

THESE

Pour obtenir le diplôme de doctorat

Spécialité PHYSIQUE

Préparée au sein de L'Université Le Havre Normandie

Modélisation de la convection thermoélectrique dans une cavité rectangulaire

Présentée et soutenue par
Elhadj Boubacar BARRY

Thèse soutenue publiquement le 29/06/2022 devant le jury composé de		
Mr Christoph EGBERS	Professeur / Université de Technologie de Brandenburg, Cottbus, Germany	Rapporteur du jury
Mr Harunori YOSHIKAWA	Maître de Conférence HDR / Université côte d'Azur, Nice	Rapporteur du jury
Mr Patrice LE GAL	Directeur de Recherche CNRS / IRPHE, Aix Marseille Université	Membre du jury
Mme Marie-Charlotte RENOULT	Maître de Conférence / CORIA, Normandie Univ, INSA ROUEN, UNIROUEN	Membre du jury
Mr Changwoo KANG	Assistant Professor / Jeonbuk National University, Republic of Korea	Membre du jury
Mr Oleg KIRILLOV	Professor / University of Northumbria, United Kingdom	Membre du jury
Mr Christophe DELAROCHE	Ingénieur CNES / Toulouse	Membre invité
Mr Innocent MUTABAZI	Professeur / Université Le Havre Normandie	Directeur de thèse

Thèse dirigée par Innocent MUTABAZI, Laboratoire Ondes et Milieux Complexes (LOMC)

UNIVERSITÉ LE HAVRE NORMANDIE

591 ED PSIME

LABORATOIRE ONDES et MILIEUX COMPLEXES

Acknowledgment

My thesis was funded by the CNES and Région de Normandie. Besides the scientific aspects covered during this thesis, these years of work have been an opportunity for me to live such a good experience. Therefore, my first thanks go to Pr. Innocent Mutabazi, my thesis advisor, who found in me the energy and skills necessary to carry out this work. The patience, the rigor, the rich and varied experiences, without forgetting the criticisms and the outspokenness, of my thesis advisor have been a guiding vector of my learning and production processes over the past four years.

First of all, I would like to thank Dr. Harunori Yoshikawa who introduced me to coding and linear analysis of thermal and thermoelectric instabilities produced in a dielectric liquid during my visit to Nice as an internship student. His pedagogy and his availability for scientific discussions aroused my curiosity during the whole Ph.D. I also would like to thank Dr. Changwoo Kang for supervising this thesis. He introduced me to Computational Fluid Dynamics (CFD) and always reminded me to work hard for the obtention of valuable and good results. I thank Dr. Olivier Crumeyrolle for the discussions and reservations during our missions in Bordeaux.

In collaboration with the German team of Pr. Christoph Egbers, I had the opportunity to be invited to Cottbus for the preparation of the experiment designed for the Parabolic Flight Campaigns (PFC). This allowed me to carry out experiments in the laboratory and in microgravity. Thus, I experienced the exceptional sensation of weightlessness. Here, I then thank Pr. Egbers, Dr. Martin Meier, Dr. Peter Szabo, and the whole team. Especially I address my thanks to Dr. Antoine Meyer for his availability, discussions, all directions, the correction of the first draft of my manuscript, and the hosting of my defense online. I am grateful to all the personnel from LOMC Le Havre, from the laboratory in Cottbus, and from Novespace.

I would like to express my thanks to my referees (Pr Egbers and Dr Yoshikawa) for the time they spent reading and for the suggestions they made to improve the manuscript. I am very grateful to all jury members (Patrice Le Gal, Marie-Charlotte Renoult, Oleg Kirillov) for the examination of my manuscript and their engagement during my thesis defense.

My thanks go to everyone who participated, directly or indirectly, in the realization of this work (Sadou-Mbooka, Diaby-Thug, Abdoul-Ovale, Abdoulaye-Pakpak, Amadou-bonaa). I Would like to thank particularly my friends and colleagues: Dr. Abdillah (Quantic man), Belaïd (Papache),

Emerance (Le Cercle), Oussama (Edge state man), Ziad (Ghost rider), Ahmad (Akhi), Hassane (Yaa Akhi), Marc (Hype), Paul, Nihad, Tess, Ichrak, Sanaa (Dr. JBL), Dr. Cheikh (Kiriya), Anupam (Pizza triangle), Olivier (Gwadada), Walid (Technicien), Hrishi… as well as all the others.

Finally, I sincerely thank my parents for the good education they conferred to me and for their continuous support. I wish good luck to my sister Mariama Baïlo Barry who wants to be Dr. in Medicine. Obtaining this thesis is a promise I made to myself to pay tribute to my late big brother Mamadou Yaya Barry. He was a mentor and a second father to me. I also pay tribute to my grand-mother and my uncle (Yaya Barry) who I lost during my last year of the thesis.

Contents

Chapter 1: General Introduction

Since the early 1980s, new techniques have been developed for manufacturing millimeter and submillimeter instruments and devices [1]. If this miniaturization has made it possible to group on a small surface maximum of electrical and electronic components for optimal functionality, it is faced with an increase in temperature due to the impossibility of installing fans or ordinary cooling systems based on pumps. In recent years, several techniques (active and passive) have been used to improve heat transfer in miniaturized systems. These methods are also implemented in heat exchangers in some industrial fields such as power plants, aeronautics, and aerospace to enhance heat transfer [2–4]. Passive methods involve changing the geometry of considered systems or using additives to fluids, while active methods use an external force such as acoustic vibration of the considered system, the application of electric, or magnetic fields [5,6].

In this work, we are interested in the use of the electric field for the generation of thermo-convective motions in dielectric fluids. When a fluid layer is subject to an alternating electric field and a thermal gradient, the thermoelectric coupling creates a body force called *dielectrophoretic force*. The intensity of this force is controlled through the applied electric potential. The dielectrophoretic force consists of two terms: a conservative force that can be combined with the pressure gradient, and a non-conservative force which can be considered as a thermal buoyancy force with an associated effective gravity called *electric gravity*. This buoyancy force is responsible for the convective motion in the fluid under certain conditions to be determined. Therefore, the control of the heat transfer by the regulation of the applied electric potential to a dielectric fluid should permit an energetic optimization of the cooling systems for microfluidic systems which can be incorporated in aerospace or aeronautic equipments [7–9].

Besides technical applications, the dielectrophoretic force can also be used for the simulation of some natural phenomena. For example, large-scale geophysical convective flows are, generally, generated by the coupling between the gravity fields, temperature gradients, and magnetic fields. In this manner, the thermo-convective flow of a fluid layer confined in spherical shells with a high-frequency electric voltage has been investigated to simulate thermal convection in the Earth mantle or stars [10–15]. In that case, the artificial gravity considered by the authors is centripetal as the

Earth's gravity. The application of an electric field to a fluid layer with temperature gradients, in the presence of Earth gravity and under microgravity conditions, has shown a variety of flow dynamics [16,17]. In addition, other investigations on thermal convection generated by the electric gravity in cylindrical geometries have been performed [8,18–21]. All authors demonstrated that thermal convection can be induced by the artificial electric gravity in different geometry systems with dielectric fluids and modifies the resulting heat transfer. To have only a purely central gravity field, experiments have been carried out under a microgravity environment in parabolic flight on Zero-G airbus [22–24], and on the International Space Station (GEOFLOW experiment, Cottbus, Germany) [16,25]. These experiments showed the similarity between electric and Archimedean buoyancies in the convective flow generation as well as the variety of bifurcation phenomena.

The flow of a dielectric fluid confined between two parallel plane plates subject to both a temperature gradient and an alternating electric field has been investigated for some decades [26–32]. These authors have shown that the dielectrophoretic force can destabilize the base state and the global heat transfer is consequently modified. This configuration then represents a good model for the improvement of plate heat exchangers' efficiency in some industrial domains. However, none of these investigators have realized the characterization of the dynamic flow regimes generated by electric buoyancy. For these reasons, flow regimes induced by the Archimedean and electric buoyancies in rectangular horizontal or vertical cavities have been studied to complete the existing literature.

1.1. Previous works

1.1.1. Thermal convection in horizontal and vertical rectangular cavities

When a fluid layer is confined between two horizontal parallel plates kept at different temperatures, with the hotter lower plate, it experiences convective motions when the temperature difference reaches a critical value. This result is due to the competition between the stabilizing forces (viscous and thermal) and the destabilizing Archimedean buoyancy caused by the gravity and the fluid density variation with temperature. This natural convection is known as Rayleigh-Bénard convection [33]. Numerous theoretical, numerical, and experimental studies have shown that beyond the onset of thermal convection, a rich variety of flow patterns that can be stationary, time-dependent, chaotic, or turbulent, occur depending on the physical properties of the fluid and the container geometry. The fluid dynamics in this system can be described using two control parameters: the Rayleigh number $Ra = \alpha \Delta T g d^3/\nu\kappa$, and the Prandtl number $Pr = \nu/\kappa$ (where α is the thermal expansion coefficient, ΔT the temperature difference, d the thickness of the fluid layer, ν the viscosity, κ the thermal diffusivity and g the Earth gravity). Thermal convective motions set in when Ra reaches the critical value $Ra_c = 1708$ independently on Pr. The Rayleigh-Bénard convection is a good model for the understanding of many large-scale flows occurring in nature as the dynamics of the atmosphere, dynamics of oceans, and meteorological and astrophysical phenomena [34,35].

In the case of a fluid layer between two infinite vertical parallel plates kept at different temperatures, the torque of the Archimedean buoyancy generates a basic state which is characterized by an ascending flow near the hot plate and descending flow near the cold one. This yields a large circulation cell stability of which depends on the Grashof number (Gr). In this case, the Earth's gravity is perpendicular to the imposed temperature gradient. This problem of thermal convection is well known in the literature [3,36–40]. These investigations revealed the existence of many flow regimes that occur depending on the aspect ratio $\Gamma = h/d$ (where h is the height), the Rayleigh number Ra and the Prandtl number Pr. In particular, for extended systems i.e. $\Gamma \rightarrow \infty$, it has been shown numerically that when the Rayleigh number reaches the critical value, the mechanism of the basic flow destabilization depends on the Prandtl number Pr [41–43]. For $Pr < 12.45$, the critical mode is a hydrodynamic mode composed of a transverse stationary vortices;

while for $Pr > 12.45$, the critical mode is thermal mode composed of transverse oscillatory mode. The heat transfer enhancement in the vertical slot has also been highlighted by computing the Nusselt number [42]. Furthermore, one can find more details about the literature review on thermal convection in vertical cavities in the thesis of Tadie Fogaing [42] or in the book by Gershuni and Zhukhovitskii [39], and in some published articles [40,41,44–51].

1.1.2. Thermoelectric convection in a horizontal fluid layer

A dielectric fluid layer, differentially heated and subject to a high-frequency electric field, undergoes electric buoyancy analogous to the Archimedean buoyancy. The fluid layer is stressed by an alternating electric voltage between two electrodes with a high enough frequency to avoid the accumulation of electrons and ions in the bulk. As in the Rayleigh-Bénard problem, this force can generate thermal convection in the presence of Earth gravity and under a microgravity environment. Since the beginning of the 1960s, many theoretical, experimental, and numerical studies have been performed on horizontal fluid layers to understand the mechanism generating thermoelectric convection and the resulting heat transfer efficiency [26–32,52–56]. The two configurations studied by the authors are presented in Figure 1.1. According to their results, the quiescent base state bifurcates to a steady convective flow when the electric field E exceeds the critical value E_c for a given temperature difference; thus heat transfer increased.

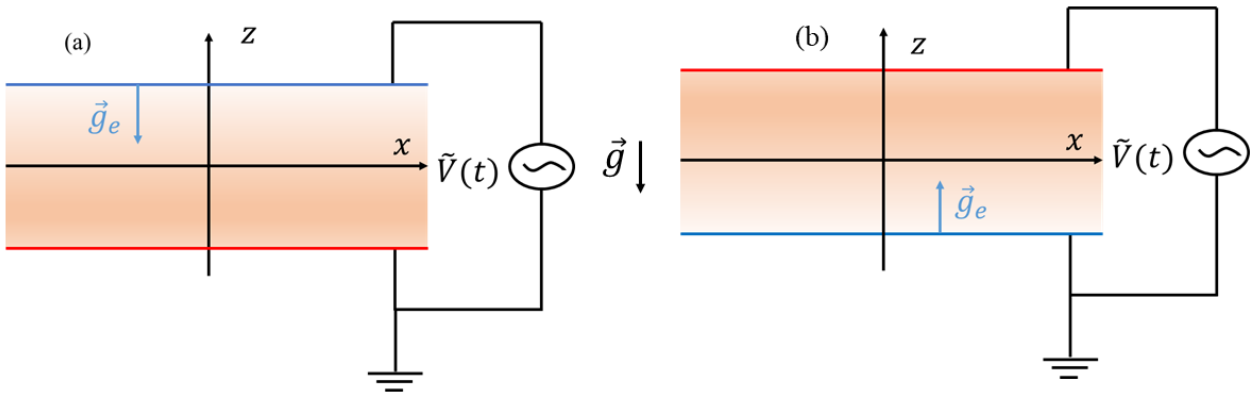

Figure 1.1: Configuration of horizontal parallel electrodes: (a) thermally unstable stratification & (b) thermally stable stratification of the dielectric fluid layer in the absence of the dielectrophoretic force. Configuration of Turnbull [30] and Stiles [27].

Gross and Porter [53] carried out in 1966 one of the first experiments concerning the effects of the electric field on the stability of a horizontal dielectric fluid layer. The liquid used for their experiments is transformer oil which has thermal dependence of dielectric constant about $10^{-4}/°C$. The investigators found the formation of patterns similar to those of Bénard instability for constant electric tension; while no effects were observed for the applied alternating electric field. They explained these results as the effects of the electric field on the free charges due to the strong temperature dependence of the conductivity of the experiment oil. In 1968, Gelmont and Ioffe performed a linear stability analysis of this problem with the upper plate warmer [52]. Their results showed that the electric field has destabilizing effects on the conductive base state of a horizontal fluid layer under microgravity conditions and in the case of stable stratification of the density due to the action of the dielectrophoretic force. They determined a critical value beyond which the influence of the electric field E becomes important; its estimated value for a given system ($\kappa = \nu = 3.10^{-3} cm^2/s$, $\alpha \sim 10^{-3} K^{-1}$, the thickness of the layer $h = 0.1cm$ and the wavenumber $k_z = \pi/h$) is about $E_c \sim 2 \times 10^5 V/m$. This result was confirmed by Roberts and Turnbull in 1969 who, separately, performed a two-dimensional linear stability analysis of the thermoelectric Rayleigh-Bénard problem [26,30]. The authors also characterized the flow patterns' behavior with different boundary conditions. Since the dielectrophoretic buoyancy can be analogous to the Archimedean buoyancy regarding the convective flow generation, Roberts [26] introduced the electric Rayleigh number L ($L = \alpha \, \Delta T g_e d^3/\nu\kappa$ with g_e the electric gravity), which is similar to the Rayleigh number Ra. This control parameter compares the electric effects to the diffusive forces (viscous dissipation and thermal diffusion) in the fluid. When the effects of the dielectrophoretic buoyancy predominate, the base state is destabilized and the quiescent state bifurcates to a thermo-convective flow regime at a critical electric Rayleigh number L_c. Under microgravity conditions, where the electric buoyancy is the sole source of instability, the critical value of the electric Rayleigh number is $L_c \approx 2129$ and the critical wave number is $k_c = 3.226$. On Earth values of the threshold L_c depends on the intensity and the direction of the heating i.e. the Rayleigh number Ra. Turnbull and Melcher performed both linear stability analysis and an experiment on a inhomogeneous fluid layer [31]. Authors considered a system heated from the top and subject to a high-frequency alternating electric field. They found a good agreement between the linear stability analysis and the experiments for viscous fluids (phenylmethyl silicone fluid and dimethyl silicone fluid). The

occurrence of thermoelectric convection is characterized by stationary convective rolls for all cases of fluid stratification [26,30,31].

Stiles [27] performed a linear analysis of a horizontal fluid layer with a stable thermal stratification, by assuming stationary critical modes, for high values of the Rayleigh number Ra. This corresponds to an extension of Roberts's results and the author gave a more precise explanation of Turnbull and Melcher's experimental results. The critical wave number and the critical electric Rayleigh number at the onset of convection increase when $|Ra|$ increases as shown in Figure 1.2. For Rayleigh number in the range of $10^3 - 10^4$, the critical electric Rayleigh number is given by the following linear relationship $L_c = 2129 - 1.246Ra$; while the slope of L_c is unity for large values of $|Ra|$. His results also showed that, when the Rayleigh number $|Ra| > 10^9$, convective patterns set in when the critical electric Rayleigh number L_c exceeds moderately the $|Ra|$ value. That explains the linear growth of L_c for large values of $|Ra|$. Since $L_{0c} \approx 2129$ is the value of L_c under microgravity conditions and $Ra_{0c} = 1708$ is the critical value of the classical Rayleigh-Bénard problem, the ratio $L_{0c}/Ra_{0c} \approx 1.246$ corresponds to the slope of $L_c = f(Ra)$.

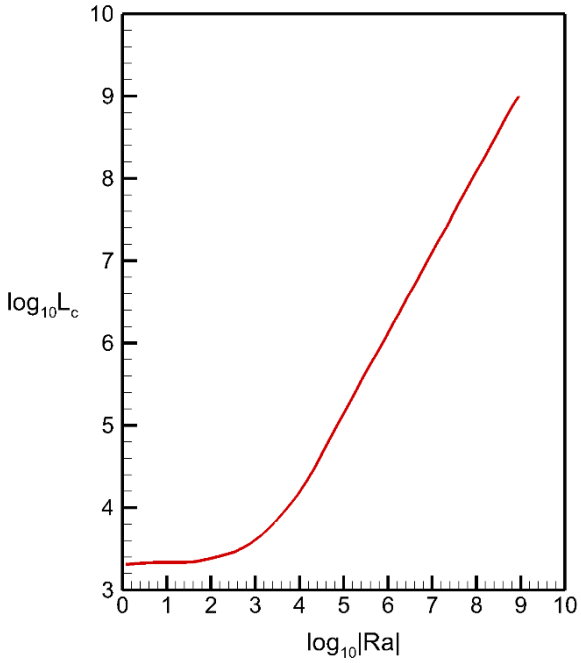

Figure 1.2: Critical electrical Rayleigh number L_c as a function of the gravitational Rayleigh number |Ra| for a dielectric fluid layer bounded by two electrodes and heated from the top [45].

All previous studies showed that the mechanism of the onset of the stationary dielectrophoretic convection depends considerably on Ra; the values of the critical electric Rayleigh number L_c are independent of the diffusive nature of the fluid i.e. Prandtl number Pr. However, no explanation has been given for the difference between the critical electric Rayleigh number $L_c \approx 2129$ and the classical critical Rayleigh number $Ra_c = 1708$.

Yoshikawa *et al.* [32] performed a two-dimensional linear stability analysis of a horizontal dielectric fluid layer of infinite length, with a temperature difference applied across the fluid gap, under microgravity conditions. They showed that the electric gravity of the perturbed flow can be decomposed into two terms: the basic electric gravity and the perturbed electric gravity. The latter represents the thermoelectric feedback due to the electric field perturbations generated by temperature disturbances when the thermoelectric coupling parameter $\gamma_e = e\Delta T$ becomes significant i.e. $\gamma_e \geq 0.2$ [32]. It was shown that the perturbed electric gravity performs a negative power i.e. it dissipates energy and this explained the difference between the threshold of the classic Rayleigh-Bénard convection ($Ra_c = 1708$) and the thermoelectric Rayleigh-Bénard convection ($L_c = 2128.7$).

To extend the analysis of thermoelectric convection, weakly nonlinear analysis of the thermoelectric convection has been performed by Stiles *et al.* and Yoshikawa *et al.* [28,32] who confirmed that the occurrence of thermoelectric structures (when $L > L_c$) leads to the increase of the heat transport between the two parallel plates, even under a microgravity environment. The Nusselt number Nu, which represents the ratio of the total heat flux (conduction + convection) to that by conduction, can be determined in terms of parameters such as Ra, Pr, and $\delta = L/L_c - 1$. Turnbull and Melcher [31] measured the Nusselt number Nu by means of the Schmidt-Milverton technique for phenyl-methyl-silicone fluid and dimethyl-silicone fluid. The results showed that the value of the Nu increases when a thermoelectric instability occurs for both liquids.

Under microgravity conditions ($Ra = 0$), Yoshikawa *et al.* [32] have performed a weakly nonlinear analysis of the thermoelectric convection in dielectric fluid layers of aspect ratio $\Gamma = 114$ for $\gamma_e = 0.03$. They showed that the thermoelectric convection in microgravity occurs via a stationary supercritical bifurcation, hence it can be described by the stationary Ginzburg-Landau equation.

Figure 1.3 (a) shows the Nusselt dependence on Ra for a system heated from above obtained by Stiles *et al.* [28]. The behavior of the Nusselt number Nu as function of the criticality near the threshold obtained by Yoshikawa *et al.* [32] is presented in Figure 1.3 (b). The authors confirmed the correlation of $Nu\ (\delta)$ near the threshold obtained by Stiles *et al.* [28] for $Pr \geq 1$; they also provided an explanation of the difference in the slopes of $Nu(\delta)$ near the threshold of the thermoelectric convection and of the Rayleigh-Bénard convection.

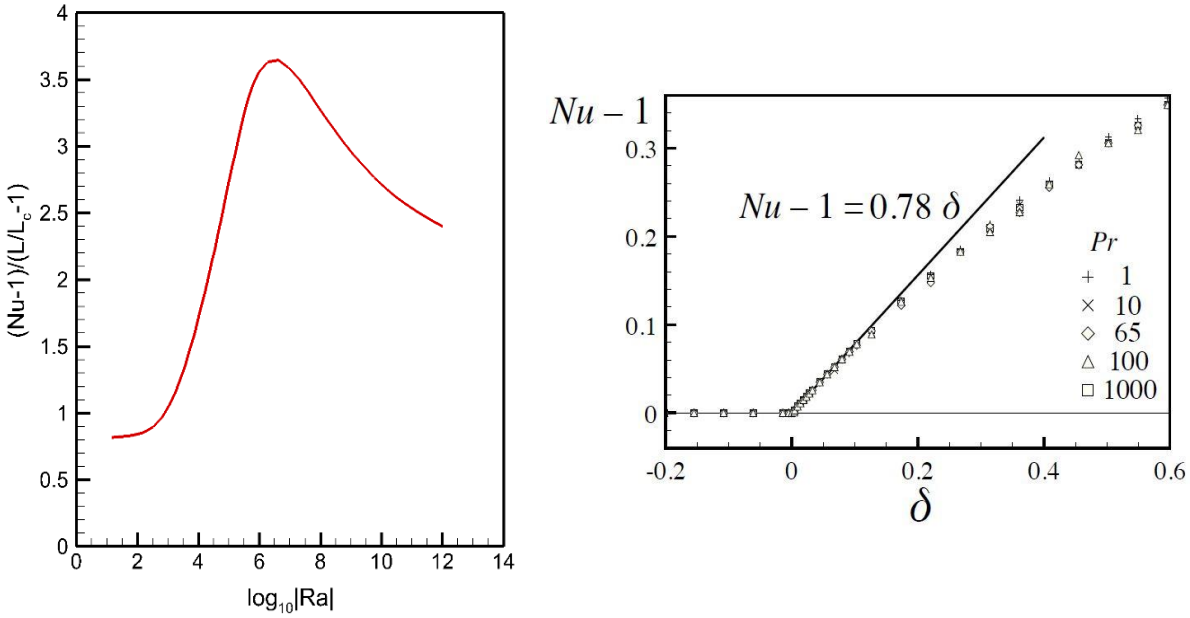

(a) (b)

Figure 1.3: Scaled Nusselt number behavior as a function of Ra for a system heated from above with $Pr = 10$ (a) [28]; variation of the Nusselt number with the supercriticality parameter δ for thermoelectric convection, under microgravity conditions (b) [32].

However, the characterization of thermoelectric convective regimes and associated heat transfer has not yet been investigated for large values of the electric potential away far from the threshold. This point represents one of the objectives of this thesis.

1.1.3. Thermoelectric convection in a vertical fluid layer

When a dielectric liquid is confined in an infinitely-long vertical rectangular cavity subject to a horizontal temperature difference, the latter induces a stationary unidirectional vertical flow which consists of an ascending flow near the hot plate and a descending flow near the cold one.

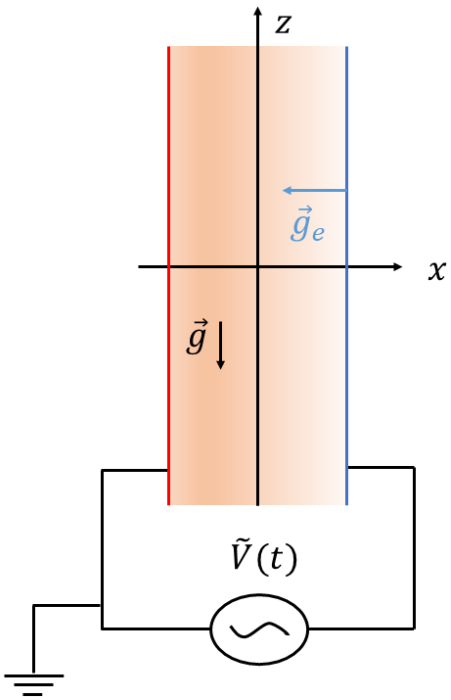

Figure 1.4: A dielectric fluid confined between two vertical plane electrodes with a horizontal temperature gradient and a high-frequency voltage.

Adding a horizontal high-frequency electric voltage to this vertical cavity (Figure 1.4) generates a third mode called electric mode which appears when the electric voltage exceeds a certain critical value [42,54,57,58]. The electric gravity generated by the thermoelectric coupling effect is oriented from the cold plate toward the hot plate and it is then perpendicular to the Earth gravity (Figure 1.4). We will still focus on the stability of a vertical fluid layer subject to both a horizontal temperature gradient and an alternating electric field. Takashima and Hamabata [58] performed a linear stability analysis to investigate the effect of electric buoyancy on the stability of the convective cell of dielectric fluid in a vertical cavity. The authors assumed two-dimensional perturbations in the framework of Squire's theorem. For small values of the electric Rayleigh

number L, they recovered stationary hydrodynamic modes for $Pr < 12.45$ and oscillatory thermal modes for $Pr > 12.45$. However, for $L_c = 2128.7$, the convective cell becomes unstable to a stationary electric mode for low values of the $Pr < 0.1$, independently of Grashof number Gr ($= Ra/Pr$). This critical value L_c is the same as that obtained in the case of thermoelectric convection in a horizontal fluid layer under microgravity conditions. Nevertheless, for dielectric fluids with $Pr > 0.1$, the critical value of the electric Rayleigh number depends on the Grashof number Gr and Prandtl number Pr. Smorodin and Velarde [54] considered the parametric excitation of the vertical fluid layer by averaging in time the electrohydrodynamic force for the linear stability analysis. Their results showed that thermoelectric instability can be investigated considering the time-averaged dielectrophoretic force when the quantity $\omega\tau_v \geq 100$ where ω and τ are the dimensionless modulated frequency and the viscous dissipation time respectively.

Recently, Tadie Fogaing [42] revisited the work of Takashima and Hamabata [58] and performed linear stability analysis in a vertical slot subject to dielectrophoretic force in order to elucidate the effect of the electric buoyancy on hydrodynamic and thermal modes. She took into account the feedback of the thermoelectric effects on the flow through the parameter γ_e. She established a state diagram in the plane (L, Ra_c) for different values of Pr and for a fixed value of $\gamma_e = 0.022$ (Figure 1.5). When $Ra = 0$, the critical electric Rayleigh number is $L_c \approx 2129$ independently of Pr. The stability state diagram shows that the thresholds of hydrodynamic and thermal modes are not affected by the electric field for weak values of L and weakly decrease when L approaches L_c from below. Both the stability diagrams of Takashima & Hamabata and Tadie Fogaing show that for all values of Pr, there are three unstable modes: either hydrodynamic mode and electric mode or thermal mode and electric mode. They also found the occurrence of bistability for $Pr > 0.1$ when L overcomes $L_c = 2129$. The dependence of the critical wavenumbers and the critical frequency exhibited similar complex behaviors. The origin of this bistability was questionable as no physical interpretation was convincingly provided by the authors.

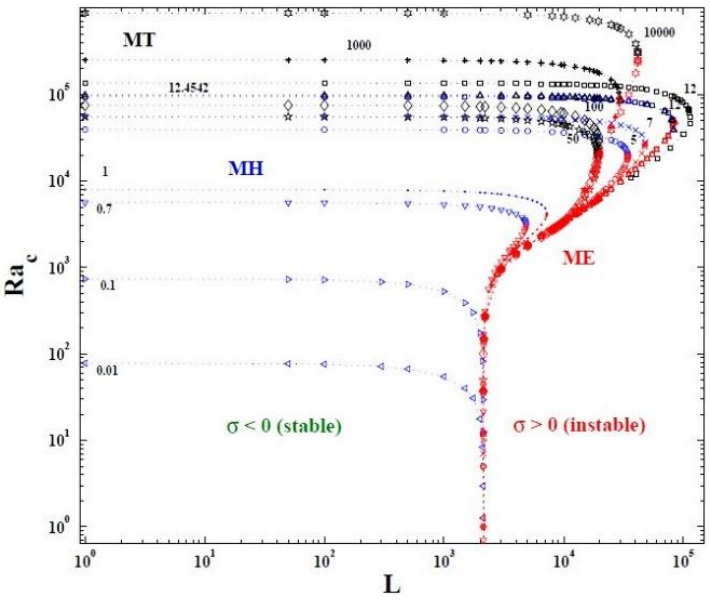

Figure 1.5: Diagram of the Ra_c variation with the electric Rayleigh number L for $Pr \in [0.01,10000]$ and $\gamma_e = 0.022$ [42].

Recently, Meyer [59] investigated, during his thesis work, the thermoelectric convection in a vertical cylindrical annulus in the presence of Earth gravity and under a microgravity environment. Under microgravity conditions, the electric buoyancy induces thermoelectric convection which manifests by stationary helical modes independently of Prandtl number Pr. More details can be found in the thesis report of A. Meyer [59]. They also found critical modes in form of vertical columnar rolls in the vertically cylindrical capacitors subject to both dielectrophoretic force and Archimedean buoyancy. These columnar modes have also been observed in the laboratory and under microgravity conditions [20,23,60,61]. A numerical study of the columnar modes induced by the dielectrophoretic force in cylindrical annulus has been performed for large values of the electric potential [21]. All these studies suggest that the use of 2D models for the analysis of the thermoelectric convection in the vertical rectangular cavity may not be appropriate. Thus, flow perturbations in the vertical cavity subject to a dielectrophoretic buoyancy should be three-dimensional. Therefore, the present study aims to extend the works by Takashima & Hamabata [58] and Tadie Fogaing [42] by investigating the stability of the flow against three-dimensional perturbations. This is one of the objectives of the thesis.

1.2. Thesis organization

This thesis aims to investigate the thermal convection induced by the dielectrophoretic force generated by the coupling of the temperature gradient and the high-frequency voltage applied to rectangular cavities. For each given temperature difference, the applied electric potential is increased to elucidate the effect of the electric buoyancy on the dielectric fluid. In the horizontal cavity, the present study aims to extend the work by Yoshikawa *et al*. [32] and to compute the heat transfer in the thermoelectric Rayleigh-Bénard convection in the thermal unstable ($0 < Ra < Ra_c$) and thermally stable configurations ($Ra < 0$) for all acceptable values of L.

The general formulation of the thermoelectric convection problem is presented in Chapter 2 where we introduced the electric buoyancy from the dielectrophoretic force and the general governing flow equations. Then this thesis is split into two parts: the first part concerns the effect of the electric buoyancy in the horizontal cavity i.e. the study of thermoelectric Rayleigh-Bénard convection (RBC) and the second part treats the effects of the dielectrophoretic force on the flow in a vertical rectangular cavity. Chapter 3 addresses the linear stability analysis of the thermoelectric RBC for three cases: microgravity conditions ($Ra = 0$), unstable stratification when $Ra > 0$ and stable stratification ($Ra < 0$). The variation of the critical electric Rayleigh number L_c and the critical wavenumbers k_c against Ra will be presented. An energetic study at the threshold elucidates the contribution of each intervening force to the destabilization of the base state. The nature of the bifurcation from the base state to thermo-convective state is analyzed for all cases in Chapter 4. The evolution of the flow patterns beyond the threshold is given for two values of Pr: $Pr = 1$ and $Pr = 65$. We then computed the heat transfer coefficient to estimate the thermal efficiency of thermoelectric convective structures. Chapter 5 addresses the linear stability analysis against three-dimensional perturbations in a vertical slot subject to a horizontal temperature gradient and a horizontal electric field. It is complemented with the computation of the kinetic energy balance. The general conclusion and perspectives are given in Chapter 6.

We have added an appendix chapter containing experimental results on the thermoelectric convection in rectangular cavities. The results were obtained during the Parabolic Flight Campaign (PFC VP139) held in Bordeaux in September 2018 performed by the joint team of LOMC (University of Le Havre Normandie) and LAS (Brandenburgische Technische Universität Cottbus-

Senftenberg). The experimental work consists of a preliminary investigation on a dielectric fluid flow in rectangular cavities in microgravity conditions. Additional tables of the critical parameters for both horizontal and vertical cavities, for different values of Pr are also presented in the appendix.

Chapter 2: General formulation of the problem

This chapter deals with the effects of the electrohydrodynamic force induced by the electric field on an inhomogeneous dielectric fluid. We will make some general assumptions to derive the expression of the dielectrophoretic force and the associated electric gravity. After the definition of control parameters, we will present the dimensionless equations governing the thermoelectric convection.

2.1. Electrohydrodynamic force

When an electric field is applied to a dielectric fluid of density ρ and permittivity ϵ, in addition to the motion of the free charges, it modifies the polarization depending on the chemical bonds in the fluid. This mechanism then induces a net force, called *electrohydrodynamic (EHD) force* the density of which is given by [62]:

$$\vec{f}_{EHD} = \rho_e \vec{E} + (\vec{P} \cdot \vec{\nabla})\vec{E}, \tag{2.1}$$

where ρ_e is the density of electric charges in the fluid volume and $\vec{P}$ is the polarization vector which depends on the fluid permittivity ϵ and the electric field $\vec{E}$. The first term in (2.1) called electrophoretic force represents the density of coulomb force. It arises from the action of the electric field on the free charges in the fluid layer. If the electric field is generated by a direct potential, the electrophoretic force is the dominant term of the EHD force. The second term of the equation (2.1) can be split into two terms: the electrostriction (ES) force and the dielectrophoretic (DEP) force as follows [63]:

$$(\vec{P} \cdot \vec{\nabla})\vec{E} = \vec{\nabla}\left[\frac{\rho}{2}\left(\frac{\partial \epsilon}{\partial \rho}\right)_T \vec{E}^2\right] - \frac{\vec{E}^2}{2}\vec{\nabla}\epsilon, \tag{2.2}$$

where ρ is the density of the dielectric fluid. The ES force is conservative and it can be lumped with the pressure term of the momentum equation; so that it does not affect the fluid motion for incompressible flows in a rigid enclosure [64].

The DEP force arises from the inhomogeneity of the fluid permittivity and acts on neutral fluid particles. This inhomogeneity can be created by a temperature difference ΔT or a concentration gradient. In this study, the permittivity variation is due to the applied temperature difference and to the geometry. Indeed, in a cylindrical annulus or in a spherical shell, the electric force is directed towards the inner surface, where the field lines are more concentrated. The physical mechanism of the EHD force, when the system is subject to an alternating electric potential, is sketched in Figure 2.1.

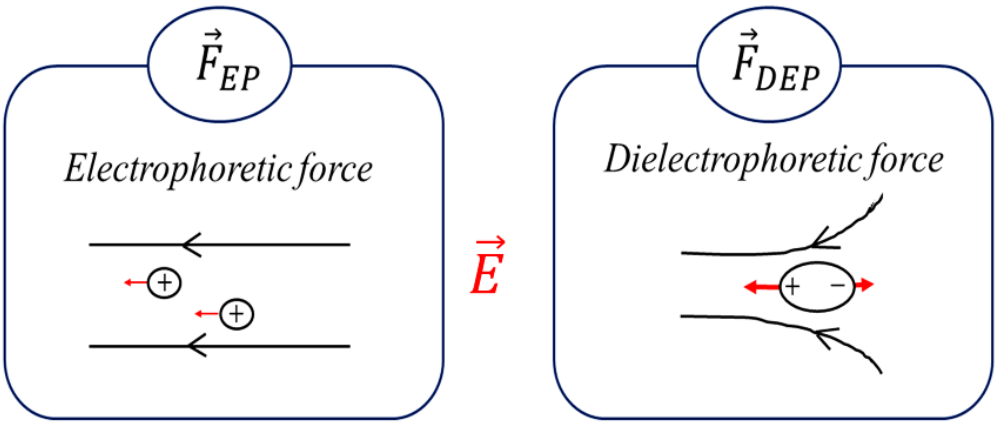

Figure 2.1: Schematic representation of the different components of the electrohydrodynamic force [65].

2.1.1. Dielectrophoretic force

For a fluid in a container with a characteristic length d, we can introduce the characteristic timescales using the kinematic viscosity ν, the thermal diffusivity κ, the permittivity ϵ, and the electric conductivity σ_E as follows:

- the viscous dissipation timescale : $\tau_\nu = d^2/\nu$,
- the thermal diffusion timescale : $\tau_\kappa = d^2/\kappa$
- the charge relaxation time that characterizes the free charges injection : $\tau_e = \epsilon/\sigma_E$,
- the characteristic timescale for ions migration with mobility μ under a field E: $\tau_m = d/\mu E$.

If the frequency f of the applied electric field is much larger than all frequencies corresponding to the characteristic timescales

$$f \gg \left(\frac{1}{\tau_v}, \frac{1}{\tau_\kappa}, \frac{1}{\tau_e}, \frac{1}{\tau_m}\right), \tag{2.3}$$

the fluid cannot follow to the rapid variation of the electric field $\vec{E}$. Indeed, when we apply a high-frequency voltage $V(t) = \sqrt{2}V_0 sin(2\pi f t)$, the quasi-static approximation suggests that the fluid motion is affected only by the constant part $\langle E \rangle^2 = \frac{E_0^2}{2}$ of the time-averaged component of the DEP force. Hence, during a period of the oscillation of the electric field, the contribution to the dielectrophoretic force comes from the constant part of the electric field. In addition, if the gap size d is larger than the thickness of the Debye layer near charge surfaces, the free charges accumulation can then be avoided. Thus, the dielectrophoretic force predominates over the electrophoretic force in equation(2.1) [31,64].

In addition to the physical phenomena described above, the displacement due to the polarization may produce internal heating in the fluid when the frequency of the applied electric field is too large [66]. In the present study, we will assume that the dielectric heating arising from the dielectric loss is negligible, and we will focus on the effect of the dielectrophoretic force to generate thermoelectric convection in the fluid. Moreover, we will assume for small temperature difference ΔT, so that the density ρ and the permittivity ϵ of most of the dielectric fluids are approximated by linear functions of temperature

$$\rho(\theta) = \rho_{ref}[1 - \alpha\theta] \;; \qquad \varepsilon(T) = \varepsilon_{ref}[1 - e\theta]; \tag{2.4}$$

where $\rho_{ref} = \rho(T_{ref})$ is the density taken at the reference temperature T_{ref}, α is the thermal expansion coefficient, $\epsilon_{ref} = \epsilon(T_{ref})$ is the dielectric permittivity at T_{ref}, e is the coefficient of thermal permittivity, and $\theta = T - T_{ref}$ is the temperature deviation from the reference temperature T_{ref}. For most of dielectric fluids, $\alpha \sim 10^{-3} K^{-1}$ and e $\in [10^{-3}\text{-}10^{-1}]\text{K}^{-1}$ [18,27].

For a fluid domain bounded by two walls kept at different constant temperatures T_1 and $T_2 = T_1 - \Delta T$, the reference temperature can be chosen as the mean value of those two temperatures:

$$T_{ref} = \frac{T_1+T_2}{2}. \tag{2.5}$$

Under these assumptions, the DEP force reads

$$\vec{F}_{DEP} = \vec{\nabla}\left[\frac{e\varepsilon_{ref}\vec{E}^2}{2}\right] - \frac{e\varepsilon_{ref}\vec{E}^2}{2}\vec{\nabla}T. \tag{2.6}$$

2.1.2. Electric buoyancy and electric gravity

The expression of the DEP force (2.6) can be written as follows:

$$\vec{F}_{DEP} = \vec{\nabla}\left(\frac{e\varepsilon_{ref}\theta\vec{E}^2}{2}\right) - \alpha\rho_{ref}\,\theta\vec{g}_e, \tag{2.7}$$

The first term is conservative and it can be included in the pressure term of the Navier-Stokes equation; the second term is the non-conservative part and it represents the dielectrophoretic buoyancy with an effective electric gravity $\vec{g}_e$ [10,32,66]. This effective electric gravity can be written[♣]:

$$\vec{g}_e = -\vec{\nabla}\Psi \tag{2.8}$$

where the quantity $-\alpha\rho_{ref}\Psi = \frac{e\varepsilon_{ref}\vec{E}^2}{2}$ is the electric energy contained in the capacitor [68]. The thermoelectric buoyancy is the analogue of the Archimedean buoyancy force ($\alpha\rho_{ref}\theta g$), and the electric gravity $\vec{g}_e$ plays a similar role as the Earth's gravity g in the generation of thermal convection [10,21,31,32]. Thus, the dielectrophoretic buoyancy represents the source of vorticity can be a source of thermoelectric convective motions in dielectric fluids. In particular, it can be used to trigger the heat transfer particularly in small-size systems where the electric field can reach large values even for small values of the electric tension difference.

[♣] In Planetary Physics, the quantity Ψ is called geopotential [67].

2.2. General governing equations

2.2.1. Flow equations in the electrohydrodynamic Boussinesq approximation

For a small temperature difference ($\gamma_a = \alpha\Delta T \ll 1$) in buoyancy-driven flows, the electrohydrodynamic Boussinesq approximation can be adopted for the mathematical description of the problem [26,69]. This approximation consists in considering the density and the permittivity of the dielectric fluid constant with respect to the temperature, everywhere in the governing equations, except in the buoyancy term and in the electro coupling term.

The incompressible flow of a Newtonian dielectric fluid can be described by the equation of mass conservation, the momentum equation, the energy equation, and the Gauss equation:

- Continuity equation: $\vec{\nabla} \cdot \vec{u} = 0,$ (2.9)
- Momentum equation: $\frac{\partial \vec{u}}{\partial t} + (\vec{u} \cdot \vec{\nabla})\vec{u} = -\vec{\nabla}\pi + \nu\Delta\vec{u} - \alpha\theta(\vec{g} + \vec{g}_e),$ (2.10)
- Energy equation: $\frac{\partial \theta}{\partial t} + (\vec{u} \cdot \vec{\nabla})\theta = \kappa\Delta\theta,$ (2.11)
- Gauss equation: $\vec{\nabla} \cdot [\epsilon(\theta)\vec{E}] = 0$, where $\vec{E} = -\vec{\nabla}\phi,$ (2.12)

where $\vec{u}(x, y, z) = u\vec{e}_x + v\vec{e}_y + w\vec{e}_z$ is the velocity field in the Cartesian coordinates, and ϕ is the electric potential. The quantity π is the Bernoulli function that represents the total pressure acting on the fluid divided by the density. The total pressure involves the hydrostatic pressure, the non-conservative part of the DEP force, and the electrostriction pressure. The quantity represents the generalized hydraulic charge:

$$\pi = \frac{p}{\rho_{ref}} + gz + \frac{e\varepsilon_{ref}\theta\vec{E}^2}{2} - \frac{1}{2}\left(\frac{\partial\epsilon}{\partial\rho}\right)_T \vec{E}^2. \quad (2.13)$$

The last term on the r.h.s of the momentum equation (2.10) represents the source of the thermos-convective instabilities in the fluid. It includes Archimedean buoyancy and thermoelectric buoyancy. The Gauss equation describes the coupling between the temperature and the electric field $\vec{E}$ through the variation of the permittivity with the temperature.

The set of governing equations is completed by the boundary conditions at the surfaces (S_1 and S_2) bounding the dielectric fluid layer:

$$u = v = w = 0,\ \theta = \frac{\Delta T}{2},\ \phi = \sqrt{2}V_0 \text{ at } S_1, \tag{2.14}$$

$$u = v = w = 0,\ \theta = -\frac{\Delta T}{2},\ \phi = 0 \text{ at } S_2. \tag{2.15}$$

2.2.2. Vorticity equation

The equation for the vorticity $\vec{\omega} = \vec{\nabla} \times \vec{u}$ is obtained by taking the curl of the momentum equation (2.10) and reads:

$$\frac{\partial \vec{\omega}}{\partial t} + (\vec{u} \cdot \vec{\nabla})\vec{\omega} = (\vec{\omega} \cdot \vec{\nabla})\vec{u} + \nu \Delta \vec{\omega} - \alpha \vec{\nabla}\theta \times \vec{G}. \tag{2.16}$$

with $\vec{G} = \vec{g} + \vec{g}_e$. The term $\alpha \vec{\nabla}\theta \times \vec{G}$ is the baroclinic source of the vorticity. In the Cartesian coordinates, this term reads

$$(\vec{\nabla}\theta) \times \vec{G} = \left[(g + g_{e_z})\frac{\partial \theta}{\partial y} - g_{e_y}\frac{\partial \theta}{\partial z}\right]\vec{e}_x + \left[g_{e_x}\frac{\partial \theta}{\partial z} - (g + g_{e_z})\frac{\partial \theta}{\partial x}\right]\vec{e}_y + \left[g_{e_y}\frac{\partial \theta}{\partial x} - g_{e_x}\frac{\partial \theta}{\partial y}\right]\vec{e}_z.$$

where g_{e_x}, g_{e_y} and g_{e_z} are the components of the electric gravity $\vec{g}_e$. We see that all the components of the electric gravity are coupled with the temperature gradients and thus intervene in all the source terms of vorticity in (2.16). In particular, the coupling between the horizontal gradients with the electric gravity introduce a source for the vertical vorticity in contrast to the Rayleigh-Bénard convection where the vertical component of vorticity obeys a diffusion equation.

2.2.3. The equation for the kinetic energy

The kinetic energy equation is obtained from the momentum equation (2.10) written in the following form:

$$\frac{d\vec{u}}{dt} = -\vec{\nabla}\pi - \nu \vec{\nabla} \times (\vec{\nabla} \times \vec{u}) - \alpha\theta\vec{G}, \tag{2.17}$$

where we have used the equality $\vec{\nabla} \times \left(\vec{\nabla} \times \vec{u}\right) = -\Delta\vec{u}$. The scalar product of the equation (2.17) with $\vec{u}$ gives the equation of the kinetic energy evolution per mass unit :

$$\frac{d}{dt}\left(\frac{1}{2}|\vec{u}|^2\right) = \alpha\theta w g - \alpha\theta(\vec{u} \cdot \vec{g}_e) - \nu\vec{u} \cdot \left(\vec{\nabla} \times \vec{\omega}\right);$$

Integration over the flow volume $\langle X \rangle = \frac{1}{V}\int X\, dV$ yields the equation of kinetic energy balance:

$$\frac{dK}{dt} = P_G + P_{EG} - D_\nu, \tag{2.18}$$

where:

- $K = \langle\frac{1}{2}|\vec{u}|^2\rangle$ is the kinetic energy per mass unit,
- $P_G = \langle\alpha\theta w g\rangle$ represents the power generated by the Archimedean buoyancy,
- $P_{EG} = \langle\alpha\theta(\vec{u} \cdot \vec{g}_e)\rangle$ is the power performed by the electric gravity,
- $\mathrm{D}_\nu = \langle d_\nu\rangle$ is the viscous dissipation,

with

$$d_\nu = 2\nu\left[\left(\frac{\partial u}{\partial x}\right)^2 + \left(\frac{\partial v}{\partial y}\right)^2 + \left(\frac{\partial w}{\partial z}\right)^2\right] + \nu\left[\left(\frac{\partial v}{\partial x} + \frac{\partial u}{\partial y}\right)^2 + \left(\frac{\partial w}{\partial y} + \frac{\partial v}{\partial z}\right)^2 + \left(\frac{\partial u}{\partial z} + \frac{\partial w}{\partial x}\right)^2\right] \text{[70]}. \tag{2.19}$$

2.2.4. Equation of the pressure

Taking the divergence of the momentum equation (2.10) yields:

$$\Delta\pi = \omega^2 - \sigma^2 - \alpha\left[\left(\vec{\nabla}\theta\right) \cdot \vec{G} + \left(\vec{\nabla} \cdot \vec{g}_e\right)\theta\right]; \tag{2.20}$$

where $\sigma^2 = \vec{u} \cdot \left(\vec{\nabla} \times \vec{\omega}\right)$ represents the local dissipation of the kinetic energy by the viscosity and $\omega^2 = \vec{\omega} \cdot \vec{\omega}$ is the enstrophy per unit mass. The equation (2.20) shows that, besides the temperature gradient, the spatial variation of the electric gravity is a source term of pressure.

2.3. Control parameters and dimensionless flow equations

2.3.1. Control parameters

The ratio of the viscous dissipation to the thermal diffusion inside the fluid layer is the Prandtl number:

$$Pr = \frac{\tau_\kappa}{\tau_\nu} = \frac{\nu}{\kappa}. \tag{2.21}$$

Under the action of the Archimedean buoyancy, a hot fluid particle can rise a distance d with a constant acceleration during the characteristic timescale τ_A given by $\tau_A^2 \propto \frac{d}{\alpha g \Delta T}$.

The competition between the stabilizing and the destabilizing forces is characterized by the ratio of timescales of viscous dissipation and thermal diffusion known as the Rayleigh number:

$$Ra = \frac{\tau_\nu \tau_\kappa}{\tau_A^2} = \frac{\alpha \Delta T g d^3}{\nu \kappa} = Gr\, Pr, \tag{2.22}$$

where $Gr = \frac{\alpha \Delta T g d^3}{\nu^2}$ is the Grashof number often used in studies of heat transfer by convection. Under microgravity conditions, the characteristic time for advection of the fluid particle due to the temperature difference is given by $\tau_{DEP}^2 \propto \frac{d}{\alpha g_e \Delta T}$ and the thermoelectric convection can be characterized by the electric Rayleigh number

$$L = \frac{\tau_\nu \tau_\kappa}{\tau_{DEP}^2} = \frac{\alpha \Delta T g_e d^3}{\nu \kappa}, \tag{2.23}$$

where the electric gravity g_e is computed at a given position in the fluid. The electric Rayleigh number L is the measure of the intensity of the dielectrophoretic force relative to the dissipative forces. For any dielectric fluid, there exists an intrinsic electric potential based on the properties of the fluid:

$$V_i = \sqrt{\frac{\rho \nu \kappa}{\epsilon_{ref}}}. \tag{2.24}$$

This quantity can be used to define the dimensionless electric potential as $V_E = V_0/V_i$. Table 2.1 shows the physical properties of some dielectric fluids.

The intensity of the coupling between the temperature difference and the electric field is given by the thermoelectric parameter γ_e:

$$\gamma_e = e\Delta T.$$

The thermal expansion coefficient of the permittivity e has values of order $e \propto 10^{-3}K^{-1}$ for silicone oils, $e \approx 0.2K^{-1}$ for the acetonitrile or the nitrobenzene [42]. We have introduced a new dimensionless number called the modified Archimedes number. The Archimedes number compares gravitational and inertial forces to the viscous effects. To take into account the electric effects on the motion of fluid particles within the fluid volume differentially heated, this modified number Ar' is defined by:

$$Ar' = \frac{\alpha g d^3}{e\nu^2} = \frac{Ra}{Pr\gamma_e} = \frac{\alpha}{e}Ga \;\; ; \;\; Ga = \frac{gd^3}{\nu^2}. \qquad (2.25)$$

Table 2.1: Physical properties of some dielectric liquids at a fixed temperature.

Dielectric Fluids	AK5 (25°C)	AK0.65 (25°C)	Novec 7200 (25°C)	1-Nonanol* (20°C)	Pure water (25°C)
$\rho\ [kg \cdot m^{-3}]$	920	760	1430	820	997
ν $10^{-8}\ [m^2 \cdot s^{-1}]$	5.00	0.65	0.43	14.20	0.89
κ $10^{-8}\ [m^2 \cdot s^{-1}]$	8.49	3.90	7.94	14.60	8.49
ϵ $10^{-11}\ [F \cdot m^{-1}]$	2.39	1.93	6.46	7.61	69.33
ϵ_r	2.70	2.18	7.30	8.60	78.30
Pr	64.60	7.66	11.03	178.84	6.11
V_i [V]	3.86	1.47	0.61	3.48	0.43
Breakdown potential for 2.5 mm (kV)	≥ 35	≥ 35	~40		≥ 160

* The value of the breakdown potential for 1-Nonanol was not found in the literature for this study.

2.3.2. Dimensionless flow equations

In the electrohydrodynamic Boussinesq approximation, the equations (2.9-2.12) can be made dimensionless using the following scales:

- the thickness d of the fluid layer for the length,
- the characteristic viscous timescale τ_ν for the time,
- the characteristic viscous velocity ν/d for the velocity,
- the imposed difference temperature ΔT for the temperature,
- $\rho(\nu/d)^2$ for the pressure,
- ϕ_0 for the electric potential,
- ϕ_0/d for the electric field.

The resulting equations read:

$$\vec{\nabla} \cdot \vec{u} = 0, \tag{2.26}$$

$$\frac{\partial \vec{u}}{\partial t} + (\vec{u} \cdot \vec{\nabla})\vec{u} = -\vec{\nabla} H + \Delta \vec{u} + Pr^{-1}\left(Ra\vec{e}_z - L\vec{\hat{g}}_e\right)\theta, \tag{2.27}$$

$$\frac{\partial \theta}{\partial t} + (\vec{u} \cdot \vec{\nabla})\theta = \frac{1}{Pr}\Delta\theta, \tag{2.28}$$

$$\vec{\nabla} \cdot \left[(1 - \gamma_e \theta)\vec{\nabla}\phi\right] = 0, \text{ where } \vec{E} = -\vec{\nabla}\phi. \tag{2.29}$$

The generalized pressure H is given by:

$$H = \left(\frac{\nu}{d}\right)^2 \left[\frac{P}{\rho_{ref}} + \frac{1}{2}\left(\frac{\partial \varepsilon}{\partial \rho}\right)_T \vec{E}^2 + \frac{1}{2}\frac{e\theta\varepsilon_{ref}\vec{E}^2}{\rho_{ref}}\right]. \tag{2.30}$$

Thermoelectric Rayleigh-Bénard convection

Chapter 3: Thermoelectric convection in horizontal rectangular cavities: Linear stability analysis

When the lower plate of a rectangular system is hotter than the upper plate, the fluid layer close to the cold plate is denser than the fluid close to the hot plate, leading to a thermally unstable stratification. For small values of ΔT, viscous dissipation and thermal diffusion dominate the Archimedean buoyancy and the fluid remains in stable equilibrium. Above a critical value $(\Delta T)_c$ which depends on fluid properties, the Archimedean buoyancy takes over the dissipative forces and convective motion sets in the fluid. When the top plate is hotter than the lower plate, such a configuration has a stable thermal stratification as the heavier fluid close to the cold plate is below the lighter fluid close to the hot plate. In both cases, the electric buoyancy intervenes in the base state destabilization. The present chapter addresses the effect of the dielectrophoretic buoyancy on the thermally stability of a dielectric fluid in three different situations: microgravity ($Ra = 0$), thermal stable configuration ($Ra < 0$) and thermally unstable configuration ($Ra > 0$).

3.1. Fluid configuration

We investigate the critical conditions of the thermoelectric convection in a Newtonian dielectric fluid layer bounded by two rigid horizontal plates maintained at different constant temperatures.

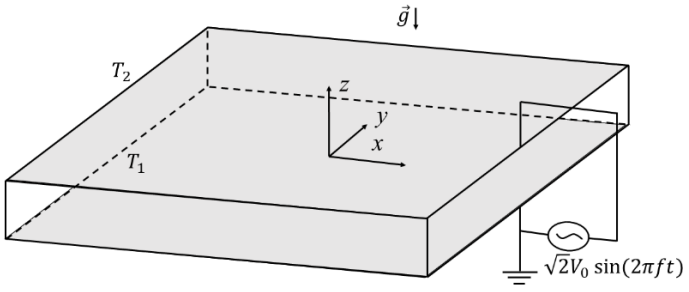

Figure 3.1: Horizontal dielectric fluid layer bounded by two parallel plates kept at different temperatures and subject to a high-frequency electric field.

We note T_1 the temperature of the lower plate and T_2 the temperature of the top plate so that the vertical temperature gradient across the dielectric fluid layer is $\Delta T = T_1 - T_2$. The flow is subject to an alternating electric field which arises from the applied electric voltage with an effective value V_0.

3.2. Base state of dielectric fluid in a horizontal cavity

For a small temperature difference ΔT and a low electric field, the fluid is in a quiescent state (conduction regime): $\vec{u} = (0,0,0)$. This state is invariant with respect to the translation in the horizontal plane and all dynamical variables change in the axial coordinate z only. This base state is governed by the following set of dimensionless equations derived from the system of equations (2.26)-(2.29):

$$\frac{dH_b}{dz} = Pr^{-1}(Ra - Lg_{eb})\theta_b, \text{ (3.1)} \tag{3.1.a}$$

$$\frac{d^2\theta_b}{dz^2} = 0, \tag{3.1.b}$$

$$\frac{d^2\phi_b}{dz^2} - \gamma_e\left(\theta_b\frac{d\phi_b}{dz} + \phi_b\frac{d\theta_b}{dz}\right) = 0. \tag{3.1.c}$$

The equation (3.1.a) shows that the basic electric gravity g_{eb} coupled with the basic temperature θ_b reduces the pressure gradient in the vertical direction. The parameter γ_e in equation (3.1.c) determines the coupling of the temperature and the electric field.

The integration of equations (3.1.a), (3.1.b), and (3.1.c) yields the temperature profile, the electric potential, and the pressure distribution of the base state

$$\left.\begin{aligned} \theta_b(z) &= -z, \\ \phi_b(z) &= ln\left(\frac{1+\gamma_e z}{1+\gamma_e/2}\right)\left[ln\left(\frac{2-\gamma_e}{2+\gamma_e}\right)\right]^{-1}, \\ E_b(z) &= -\frac{\gamma_e}{(1+\gamma_e z)\cdot ln\left(\frac{2-\gamma_e}{2+\gamma_e}\right)}, \\ H_b(z) &= \int Pr^{-1}(Ra - L\hat{g}_{eb})\theta_b dz. \end{aligned}\right\} \tag{3.2}$$

The base state is purely conductive and heat transfer occurs by thermal diffusion. From equations (2.8) and (3.2), the electric gravity in the base state g_{eb} is given by

$$g_{eb} = \bar{g}_e \cdot \hat{g}_{eb}, \tag{3.3}$$

where $\hat{g}_{eb} = -(1+\gamma_e z)^{-3}$ is the dimensionless basic electric gravity, and $\bar{g}_e$ is the characteristic electric gravity taken at mid-gap ($z = 0$) i.e.

$$\bar{g}_e = \frac{\varepsilon_{ref} e V_0^2 \gamma_e^3}{\alpha \rho d^3}\left[ln\left(\frac{1-\gamma_e/2}{1+\gamma_e/2}\right)\right]^{-2}. \tag{3.4}$$

The electric Rayleigh number defined using $\bar{g}_e$ reads:

$$L = \frac{\alpha \Delta T \bar{g}_e d^3}{\nu\kappa} = \gamma_e^4\left[ln\left(\frac{1-\gamma_e/2}{1+\gamma_e/2}\right)\right]^{-2} V_E^2. \tag{3.5}$$

The two control parameters L and Ra contain the temperature difference ΔT. In order to separate the effects of the temperature difference from those due to the electric field, we use the dimensionless potential V_E related to L by $V_E = \gamma_e^{-2} ln\left(\frac{1-\gamma_e/2}{1+\gamma_e/2}\right) L^{1/2}$.

The integration of the equation of H_b gives the analytic expression of the generalized hydraulic charge:

$$H_b(z) = -\frac{1}{2}\cdot\frac{Ra}{Pr} z^2 + \frac{L}{Pr}\cdot\frac{2\gamma_e z+1}{2\gamma_e^2(\gamma_e z+1)^2}. \tag{3.6}$$

Figure 3.3 shows the profiles of the base conductive flow for the different cases of thermal stratification of the fluid. The electric gravity is oriented from the low electric field region toward the zone of the high electric field; in the plane capacitor, the electric field is always larger at the

hot surface [26]. Figure 3.2 shows the orientation of the electric gravity in the base state depending on the heating direction. One can also observe that the sign of basic electric gravity changes when γ_e changes its sign by the curves presented in Figure 3.3 (c).

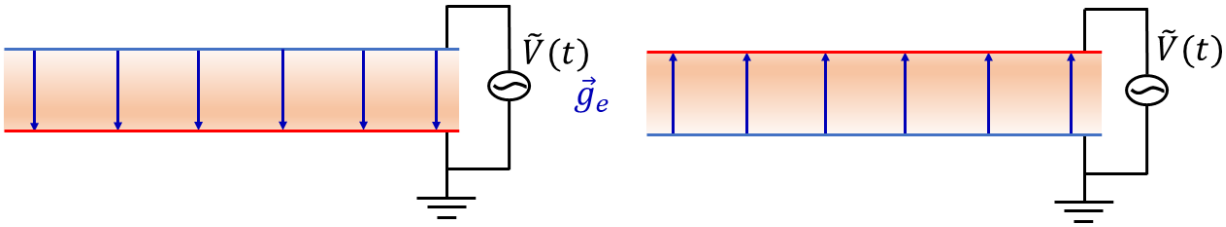

(a) (b)

Figure 3.2: Electric gravity generated by a high-frequency electric field in a dielectric fluid in a rectangular horizontal cavity with a vertical temperature gradient: (a) lower plate is hotter than the upper plate (thermal unstable stratification), (b) lower plate is colder than the upper plate (thermally stable stratification).

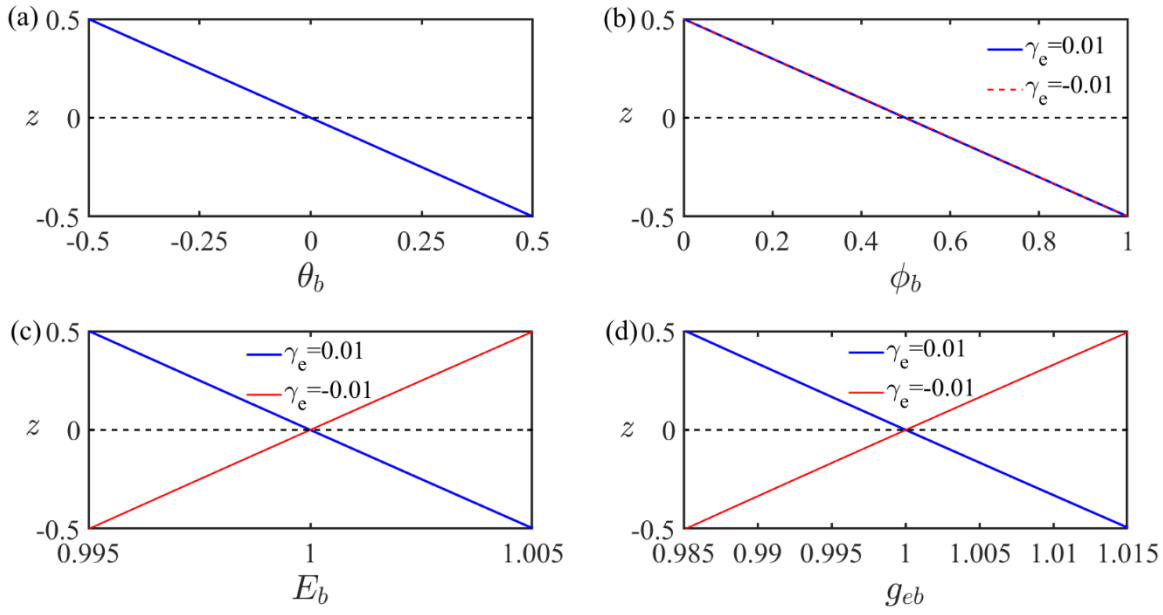

Figure 3.3: Base state : (a) Temperature profile θ_b, (b) Electric potential ϕ_b, (c) Electric field E_b, (d) Electric gravity g_{eb} for $\gamma_e = 0.01$ (blue curve) and $\gamma_e = -0.01$ (red curve).

3.3. Linearized equations and eigenvalue problem

The linear stability theory consists of the superposition of infinitesimal perturbations to the base state and then in the linearization of the resulting equations:

$$(u, v, w, \pi, \theta, \phi) = (0,0,0, H_b, \theta_b, \phi_b) + (u', v', w', \pi', \theta', \phi'), \tag{3.7}$$

where the prime denotes the perturbations.

3.3.1. Linearized equations

After subtraction of the base state, the system of linearized equations reads:

$$\left.\begin{aligned}
\frac{\partial u'}{\partial x} + \frac{\partial v'}{\partial y} + \frac{\partial w'}{\partial z} &= 0, \\
\frac{\partial u'}{\partial t} &= -\frac{\partial \pi'}{\partial x} + \frac{\partial^2 u'}{\partial x^2} + \frac{\partial^2 u'}{\partial y^2} + \frac{\partial^2 u'}{\partial z^2} - \frac{L}{Pr}\theta_b g'_{e_x}, \\
\frac{\partial v'}{\partial t} &= -\frac{\partial \pi'}{\partial y} + \frac{\partial^2 v'}{\partial x^2} + \frac{\partial^2 v'}{\partial y^2} + \frac{\partial^2 v'}{\partial z^2} - \frac{L}{Pr}\theta_b g'_{e_y}, \\
\frac{\partial w'}{\partial t} &= -\frac{\partial \pi'}{\partial z} + \frac{\partial^2 w'}{\partial x^2} + \frac{\partial^2 w'}{\partial y^2} + \frac{\partial^2 w'}{\partial z^2} + \frac{1}{Pr}\left(Ra - L g_{e_b}\right)\theta' - \frac{L}{Pr}\theta_b g'_{e_z}, \\
\frac{\partial \theta'}{\partial t} + w' \frac{d\theta_b}{dz} &= \frac{1}{Pr}\left(\frac{\partial^2 \theta'}{\partial x^2} + \frac{\partial^2 \theta'}{\partial y^2} + \frac{\partial^2 \theta'}{\partial z^2}\right), \\
0 = (1 + \gamma_e z)\Delta\phi' - \gamma_e &\left[\left(\frac{d^2\phi_b}{dz^2}\right)\theta' + \left(\frac{d\theta_b}{dz}\right)\left(\frac{d\phi'}{dz}\right) + \left(\frac{d\phi_b}{dz}\right)\left(\frac{\partial \theta'}{\partial z}\right)\right].
\end{aligned}\right\} \tag{3.8}$$

We have taken into account the perturbation of electric gravity which is induced by the perturbations of the temperature and of the electric field i.e. $\vec{g}_e = \vec{g}_{e_b} + \vec{g}'_e$.

The boundary conditions impose that perturbations vanish at the hot and the cold parallel plates:

$$u' = v' = w' = \pi' = \theta' = \phi' = 0 \text{ at } z = \pm 1/2. \tag{3.9}$$

3.3.2. Normal modes expansion

Since we consider a rectangular cavity with infinite horizontal extent, the base state is invariant in the plane (x, y) so that the perturbations can be developed in normal modes as follows

$$\begin{bmatrix} u'(x,y,z,t) \\ v'(x,y,z,t) \\ w'(x,y,z,t) \\ \pi'(x,y,z,t) \\ \theta'(x,y,z,t) \\ \phi'(x,y,z,t) \end{bmatrix} = \begin{bmatrix} U(z) \\ V(z) \\ W(z) \\ \Pi(z) \\ \Theta(z) \\ \Phi(z) \end{bmatrix} exp\big[st + i\big(k_x x + k_y y\big)\big] + c.c \tag{3.10}$$

where $s = \sigma + i\omega$ is the complex growth rate of the perturbations with σ the real growth rate and ω the frequency; $c.c.$ represents the complex conjugate; k_x and k_y are respectively the wavenumbers along the horizontal x and y directions. The perturbation $\vec{g}'_e$ is also expanded into normal mode:

$$\vec{g}'_e = \Big(G_{e_x}\vec{e}_x + G_{e_y}\vec{e}_y + G_{e_z}\vec{e}_z\Big) exp\big[st + i\big(k_x x + k_y y\big)\big]. \tag{3.11}$$

The vector $[U(z), V(z), W(z), \Pi(z), \Theta(z), \Phi(z)]^t$ represents the amplitudes of perturbations $(u', v', w', \pi', \theta', \phi')$. Substitution of (3.10) into the linearized equations (3.8) yields the following equations for the perturbations amplitudes:

$$\left.\begin{aligned} DW + i\big(k_x U + k_y V\big) = 0, \\ -ik_x\Pi + (D^2 - k^2)U - \tfrac{L}{Pr}\theta_b G_{e_x} = sU, \\ -ik_y\Pi + (D^2 - k^2)V - \tfrac{L}{Pr}\theta_b G_{e_y} = sV, \\ -D\Pi + (D^2 - k^2)W + \tfrac{1}{Pr}\big(Ra - L\hat{g}_{e_b}\big)\Theta - \tfrac{L}{Pr}\theta_b G_{e_z} = sW, \\ -D\theta_b U + \tfrac{1}{Pr}(D^2 - k^2)\Theta = s\Theta, \\ [(1 + \gamma_e z)(D^2 - k^2) + \gamma_e D]\Phi - \gamma_e(D^2\phi_b + D\phi_b D)\Theta = 0, \end{aligned}\right\} \tag{3.12}$$

where $D = \frac{d}{dz}$, k is the total wavenumber $k = \sqrt{k_x^2 + k_y^2}$. The components (G_{e_x}, G_{e_y}, G_{e_z}) of the normal mode of the electric gravity perturbation $\vec{g}'_e$ are given by:

$$\left.\begin{aligned} G_{e_x} = \mathrm{f}(\gamma_e)(ik_x D\phi_b D\Phi), \\ G_{e_y} = \mathrm{f}(\gamma_e)\big(ik_y D\phi_b D\Phi\big), \\ G_{e_z} = \mathrm{f}(\gamma_e) D(D\phi_b D\Phi), \end{aligned}\right\} \tag{3.13}$$

where $f(\gamma_e) \equiv \frac{1}{\gamma_e^3}\left[log\left(\frac{1-\gamma_e/2}{1+\gamma_e/2}\right)\right]^2$. Yoshikawa *et al.* [32] have shown that the basic electric gravity provides positive power to the perturbation (i.e. it enhances the instability), while the perturbation electric gravity produces a negative power i.e. it acts against the basic electric gravity [32].

3.3.3. Reduction to a 2-d thermal convection

The continuity equation for the perturbation $\vec{u}'$ suggests the introduction of the quantity $l\widehat{U} = k_x U + k_y V$ in order to reduce the number of equations in the system of equations (3.11). Elimination of the pressure from the set of perturbations equations (3.12) and the use of the relations (3.13) leads to the following system of coupled equations (3.14) for W, Θ, and Φ:

$$(D^2 - k^2 - s)(D^2 - k^2)W - \frac{k^2}{Pr}(Ra - L\hat{g}_{eb})\Theta + \frac{L}{Pr}f(\gamma_e)k^2 D\phi_b D\Phi = 0, \tag{3.14.a}$$

$$(D^2 - k^2 - sPr)\Theta = -PrW, \tag{3.14.b}$$

$$[(1 + \gamma_e z)(D^2 - k^2) + \gamma_e D]\Phi - \gamma_e(D^2\phi_b + D\phi_b D)\Theta = 0. \tag{3.14.c}$$

The elimination of the axial velocity component leads to the equations (3.15):

$$[(D^2 - k^2 - s)(D^2 - k^2)(D^2 - k^2 - sPr) + k^2(Ra - L\hat{g}_{eb})]\Theta - Lf(\gamma_e)k^2 D\phi_b D\Phi = 0, \tag{3.15.a}$$

$$[(1 + \gamma_e z)(D^2 - k^2) + \gamma_e D]\Phi - \gamma_e D(D\phi_b\Theta) = 0. \tag{3.15.b}$$

The system (3.15) contains the Rayleigh-Bénard convection as a limit case when $L = 0$ [33]. From the system of equations (3.15), one deduces immediately that stationary modes $(s = 0)$ are independent of Pr as in the Rayleigh-Bénard convection [33]. This was confirmed by the studies of Roberts [26] and Yoshikawa et *al.* [32]. In Roberts's work [26], the perturbative gravity terms were neglected.

3.3.4. Eigenvalue problem

The boundary conditions (3.9) impose that the complex amplitudes vanish at the horizontal surfaces:

$$U = V = W = \Pi = \Theta = \Phi = 0 \text{ at } z \pm 1/2. \tag{3.16}$$

The system of linearized equations (3.12) together with the boundary conditions (3.16) form an eigenvalue problem which can be written as follows:

$$\bar{\bar{L}}\vec{\Psi} = s\bar{\bar{M}}\vec{\Psi}, \tag{3.17}$$

where the vector $\vec{\Psi}$ represents the perturbation eigenvector

$$\vec{\Psi}(z) = [U \quad V \quad W \quad \Pi \quad \Theta \quad \Phi]^t. \tag{3.18}$$

The control parameters Ra, L, Pr, γ_e, and the solution of the conductive state enter the operator $\bar{\bar{\mathrm{L}}}$:

$$\bar{\bar{\mathrm{L}}} = \begin{bmatrix} ik_x & ik_y & D & 0 & 0 & 0 \\ D^2 - k^2 & 0 & 0 & -ik_x & 0 & -\frac{L}{Pr}\theta_b G_{ex} \\ 0 & D^2 - k^2 & 0 & -ik_y & 0 & -\frac{L}{Pr}\theta_b G_{ey} \\ 0 & 0 & D^2 - k^2 & -D & \frac{1}{Pr}(Ra - L\hat{g}_{eb}) & -\frac{L}{Pr}\theta_b G_{ez} \\ -D\theta_b & 0 & 0 & 0 & \frac{1}{Pr}(D^2 - k^2) & 0 \\ 0 & 0 & 0 & 0 & A & B \end{bmatrix}. \tag{3.19}$$

The quantities A and B are given by

$$A = -\gamma_e(D^2\phi_b + D\phi_b D), \quad B = (1 + \gamma_e z)(D^2 - k^2) + \gamma_e D.$$

The operator $\bar{\bar{M}}$ is given by:

$$\bar{\bar{M}} = \begin{bmatrix} 0 & 0 & 0 & 0 & 0 & 0 \\ 1 & 0 & 0 & 0 & 0 & 0 \\ 0 & 1 & 0 & 0 & 0 & 0 \\ 0 & 0 & 1 & 0 & 0 & 0 \\ 0 & 0 & 0 & 0 & 1 & 0 \\ 0 & 0 & 0 & 0 & 0 & 0 \end{bmatrix}.$$

The eigenvalue problem allows for the computation of the growth rate (s) of the perturbations as a function of their wavenumber (k_x, k_y) and of the control parameters (Ra, L, Pr, γ_e). Thus, solving the eigenvalue problem (3.17) is equivalent to finding the characteristic equation:

$$F(Ra, L, Pr, \gamma_e, \sigma, \omega, k_x, k_y) = 0 \text{ or } \quad s = f(Ra, L, Pr, \gamma_e, k_x, k_y). \tag{3.20}$$

3.3.5. Marginal stability

The linear stability analysis aims to determine the marginal perturbations for which $\sigma = 0$. Indeed, when $\sigma < 0$, disturbances are damped and the base state remains stable; whereas when $\sigma > 0$, the perturbations grow and the base state becomes unstable. The marginal states belong to the surface $\sigma(Ra, L, Pr, \gamma_e, k_x, k_y) = 0$ called marginal or neutral surface. The minimum of the neutral surface is the critical point which determines the onset of the instability. The onset of the thermoelectric convection is determined by

$$L_c = L_c(Ra, Pr, \gamma_e);\ k_{x_c} = k_{x_c}(Ra, Pr, \gamma_e); k_{y_c} = k_{y_c}(Ra, Pr, \gamma_e);\ \omega_c = \omega_c(Ra, Pr, \gamma_e).$$

The critical state appears as a stationary mode if $\omega_c = 0$ and as an oscillatory mode if $\omega_c \neq 0$.

In the present study, we fixed Pr, Ra and γ_e, and then determined the marginal stability curves $L = L(k_{x,} k_y)$.

3.3.6. Numerical method

The eigenvalue problem (3.17) is solved with an in-house code developed by Yoshikawa that uses the Chebyshev spectral collocation method. All unknown functions are expanded into the Chebyshev polynomial series and equations (3.17) are discretized using the Chebyshev-Gauss-Lobatto collocation points z_j where $j = 1,2, \ldots, N-1$ with N being the highest order of the considered Chebyshev polynomials [32]. To ensure the good convergence of solutions, we chose $N = 32$. The resulting discretized problem is then solved by the QZ-decomposition method to determine the eigenvalues and the eigenfunctions.

3.4. Results

The objective of the study is the determination of the critical conditions of thermoelectric convection in a dielectric fluid confined in a rectangular cavity for three situations : i) microgravity ($Ra = 0$), ii) a thermally unstable stratification of the fluid $Ra < Ra_c = 1708$ (threshold of the Rayleigh-Bénard convection) and iii) a thermally stable stratification ($Ra < 0$). We present results obtained for $Ra \in [\,-1.2 \cdot 10^4; 1708\,[$.

3.4.1. Marginal curves and critical parameters

Figure 3.4 illustrates the behavior of the marginal stability curves for $Pr = 1$, $Ra \in \{-500, 0, 500\}$. We determined the values of critical parameters L_c, k_c, ω_c presented in Table 3.1.

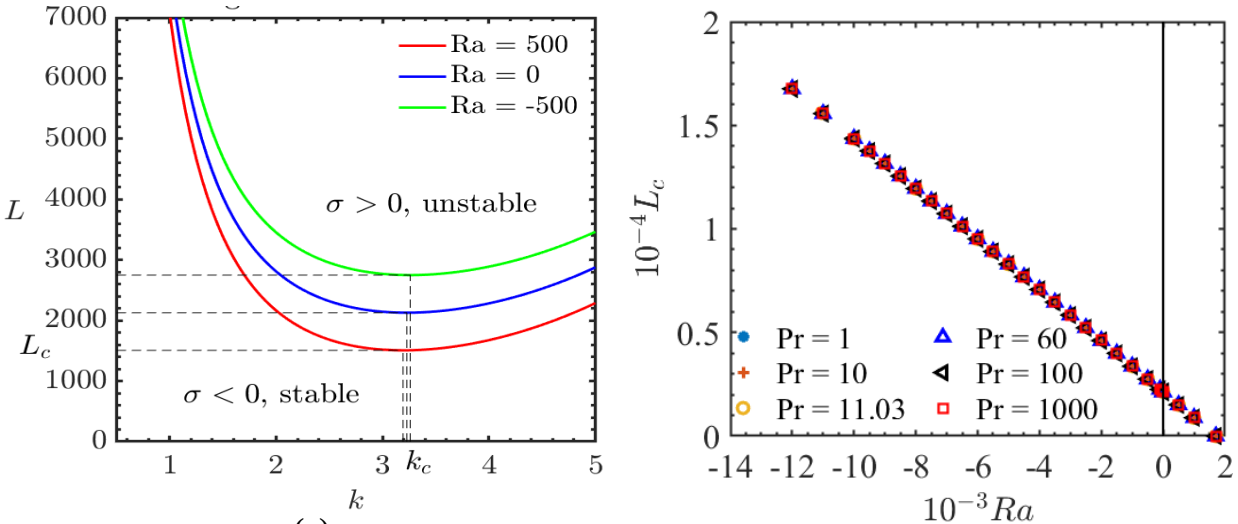

Figure 3.4: (a) Marginal stability curves for $Pr = 1$, and different values of Ra; (b) Variation of critical electric Rayleigh number L_c against Ra for various values of Pr.

In the microgravity, $g = 0$ (or $Ra = 0$), the conducting state becomes unstable when L reaches the value $L_c = 2128.6$. The corresponding critical modes are stationary ($\omega_c = 0$) and are called *electric modes* as they originate from the effect of the dielectrophoretic buoyancy. We recover the results of the previous studies [26,27,32]. For a fluid with thermally stable stratification ($Ra < 0$), the marginal stability curve lies above that of the microgravity case. The threshold of thermoelectric convection $L_c(Ra < 0) > L_c(Ra = 0)$.

For a fluid with thermally unstable stratification ($0 < Ra < 1708$), the marginal stability curve lies below that of the microgravity case, so that the threshold $L_c < L_c(Ra = 0)$. On Earth conditions, in a fluid with thermally unstable stratification, the thermoelectric convection is enhanced while in a fluid with thermally stable stratification, the thermoelectric convection is delayed. Even in the fluid with stable or unstable thermal stratification, the critical modes are induced by the dielectrophoretic buoyancy, that is why they are also called electric modes.

We have computed the critical parameters for 5 values of Pr corresponding to dielectric fluids with different diffusive properties (gas, light liquids, oils) and found that these parameters are independent of Pr within the numerical precision of the computations (Table 3.1, Figure 3.5). This is in agreement with the results of Stiles [27] and Yoshikawa *et al.* [32].

Table 3.1: Critical parameters for the thermoelectric convection for $Pr = 1$ and $Pr = 100$ and different values of Ra.

	$Pr = 1$			$Pr = 100$		
Case	Ra	L_c	k_c	Ra	L_c	k_c
Unstable Ssratification	1708	0	3.115	1708	0	3.115
	1000	883.518	3.161	1000	883.115	3.148
	500	1506.573	3.193	500	1506.535	3.191
Microgravity conditions ($g = 0$)	0	2128.694	3.228	0	2128.694	3.228
Stable stratification	−500	2749.868	3.260	−500	2749.857	3.259
	−1000	3370.074	3.294	−1000	3370.047	3.294
	−2000	4607.532	3.366	−2000	4607.547	3.365
	−4000	7070.302	3.516	−4000	7070.455	3.516
	−6000	9516.479	3.672	−6000	9516.995	3.672
	−8000	11945.940	3.830	−8000	11947.220	3.828
	−10000	14359.050	3.986	−10000	14361.600	3.983
	−12000	16756.340	4.134	−12000	16760.960	4.126

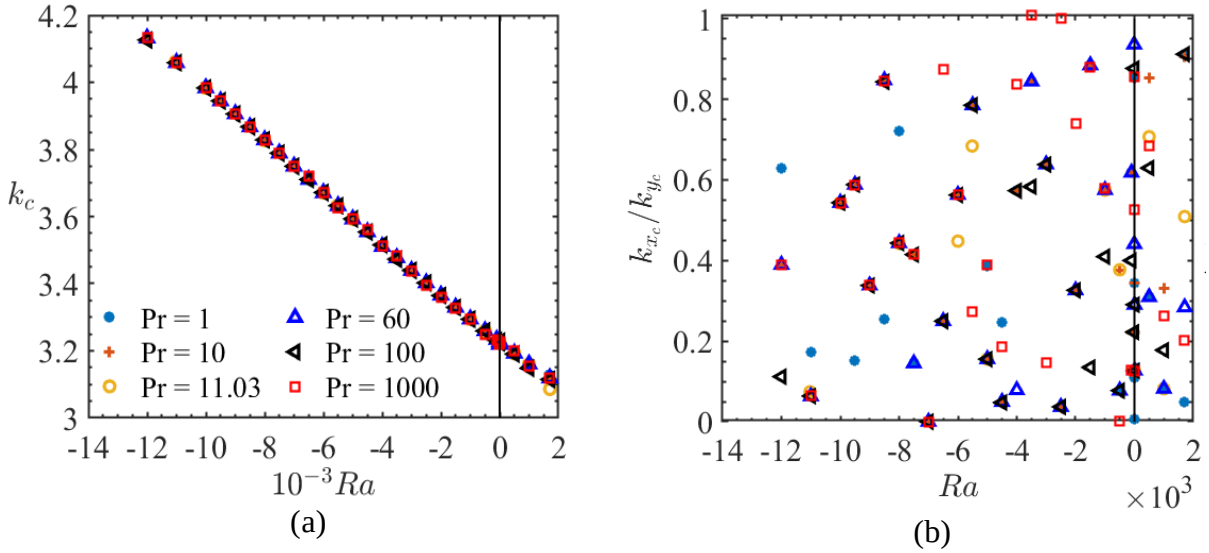

(a) (b)

Figure 3.5: Variation of critical parameters against Ra for various values of Pr: (a) critical electric Rayleigh number L_c, (b) critical wavenumber k_c.

The variations of the critical parameters (L_c, k_c) of thermoelectric convection in a rectangular cavity with Ra are plotted in Figure 3.4 (b) and Figure 3.5 in the range [-12000, 1708]; they are given by linear relationships:

$$L_c = L_c^0\left(1 - \frac{\mathrm{Ra}}{Ra_c^0}\right) \text{ and } k_c = k_c^0\left(1 - \alpha\frac{Ra}{Ra_c^0}\right), \tag{3.21}$$

where $L_c^0 = 2128.6, Ra_c^0 = 1708, k_c^0 = 3.228, \alpha = 0.042$. The relationships (3.21) estimate critical parameters by no more than 2% for L_c and 1.24% for k_c and they are in good agreement with results of Stiles [27]. Based on the variation of the ratio of wavenumbers as a function of the Ra in Figure 3.5 (b), one can conclude that the thermoelectric convective rolls appear with random angle in the horizontal plane.

3.4.2. Eigenfunctions of the critical states

Streamlines and flow fields of the critical state give insight into the shape of the flow. We presented, in Figure 3.6, the eigenfunctions of the critical electric mode under microgravity conditions ($Ra = 0$) for $Pr = 11.03$. This value of Pr corresponds to the liquid Novec 7200 used in the experiment performed during the Parabolic Flight Campaign (PFC VP139) held in Bordeaux in September 2018. Figures are plotted in both vertical planes $(x - z)$ and $(y - z)$; they show that the thermoelectric convection patterns are inclined in the horizontal $(x - y)$-plane with an angle of

about 83° with respect to the x direction. The thermo-convective flow is characterized by alternating cold (blue) and hot (red) zones which show counter-rotating convective rolls having about the size of the gap. Arrows represent velocity vectors and colors give the temperature perturbation. For the elucidation of the periodicity along the x direction, we set $l_x = 40$.

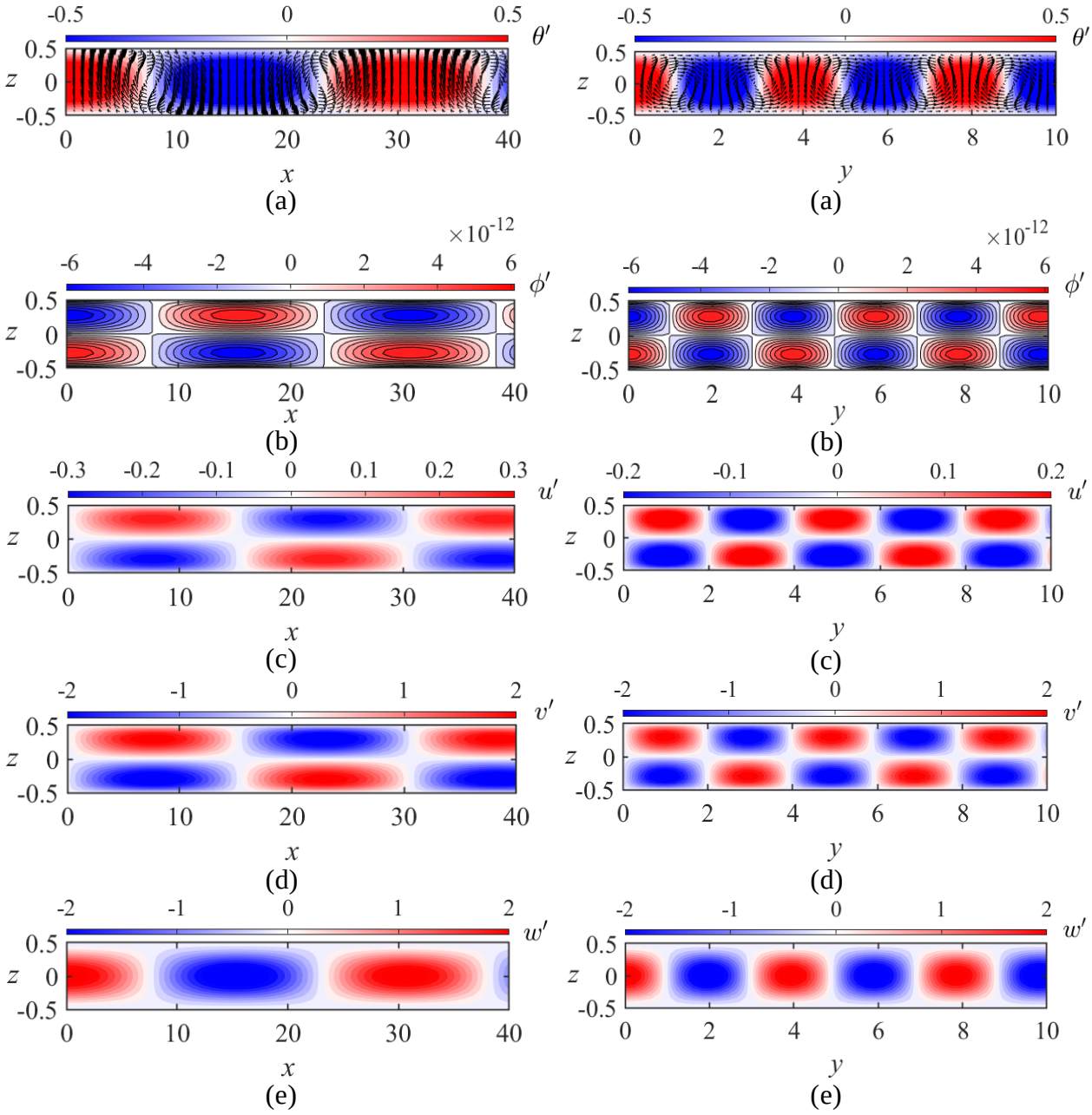

Figure 3.6: Eigenfunctions of the electric mode for $Pr = 11.03$, $Ra = 0$, and $L_c = 2128.69$. (a) the velocity fields and the temperature levels, (b) the electric potential ϕ', (c-d) the horizontal velocity components u' and v', and (e) the vertical velocity w'.

The cross-section $(y-z)$ of thermo-convective flow induced by the dielectrophoretic buoyancy in a fluid layer for $Pr = 65$ and $Ra = 500$ is presented in Figure 3.7. The flow is characterized by alternating cold (blue) and hot (red) zones which show counter-rotating convective rolls having about the size of the gap. Arrows represent velocity vectors and colors give the temperature perturbation in Figure 3.7 (a).

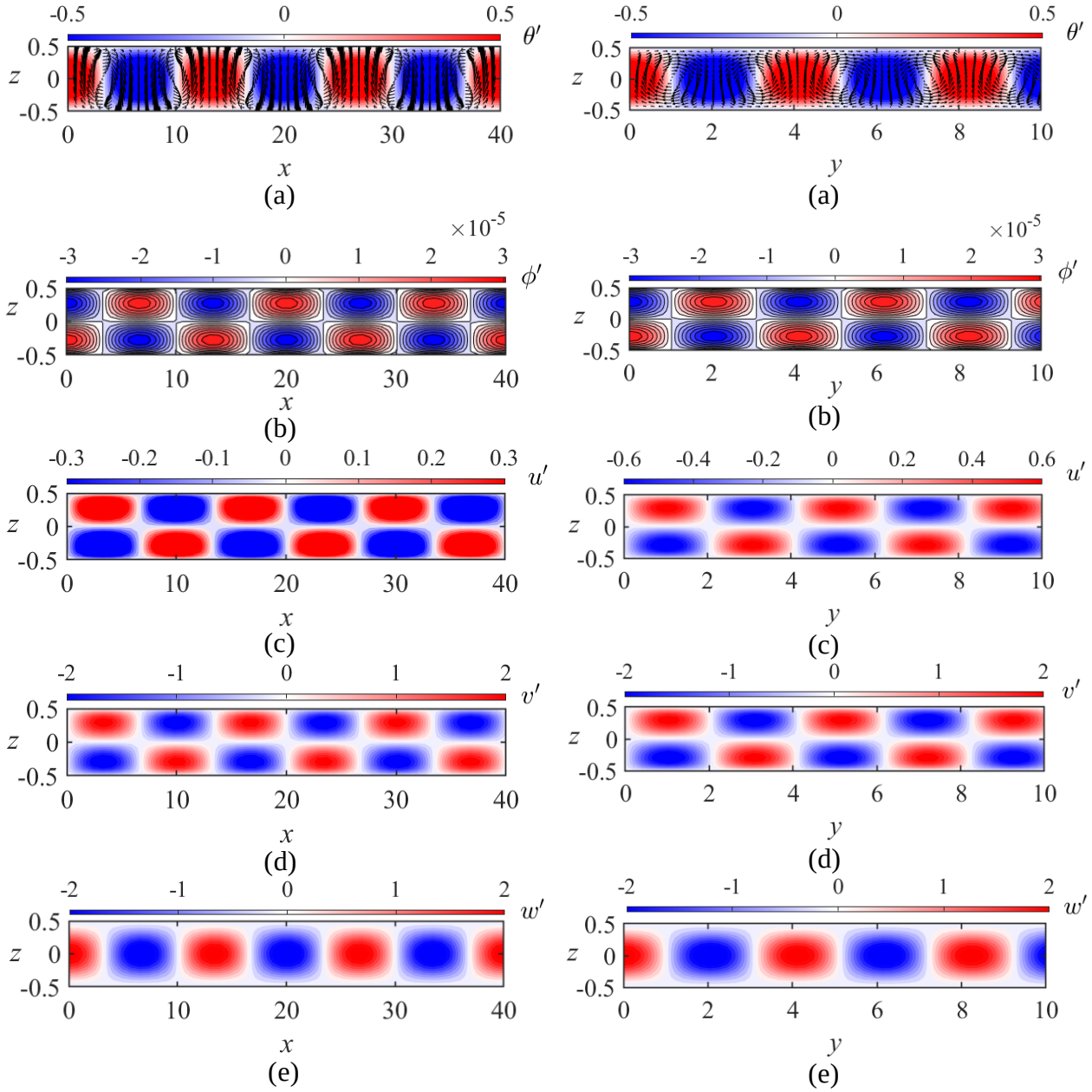

Figure 3.7: Eigenfunctions of the electric mode for $Pr = 65$, $Ra = 500$, and $L_c = 1706.57$. (a) the velocity fields and the temperature levels, (b) the electric potential ϕ', (c-d) the horizontal velocity components u' and v', and (e) the vertical velocity w'.

Figure 3.8 presents the instantaneous flow fields of the critical modes for $Pr = 65$, $Ra = -500$. It shows that the electric modes are inclined in the horizontal plane $(x - y)$.

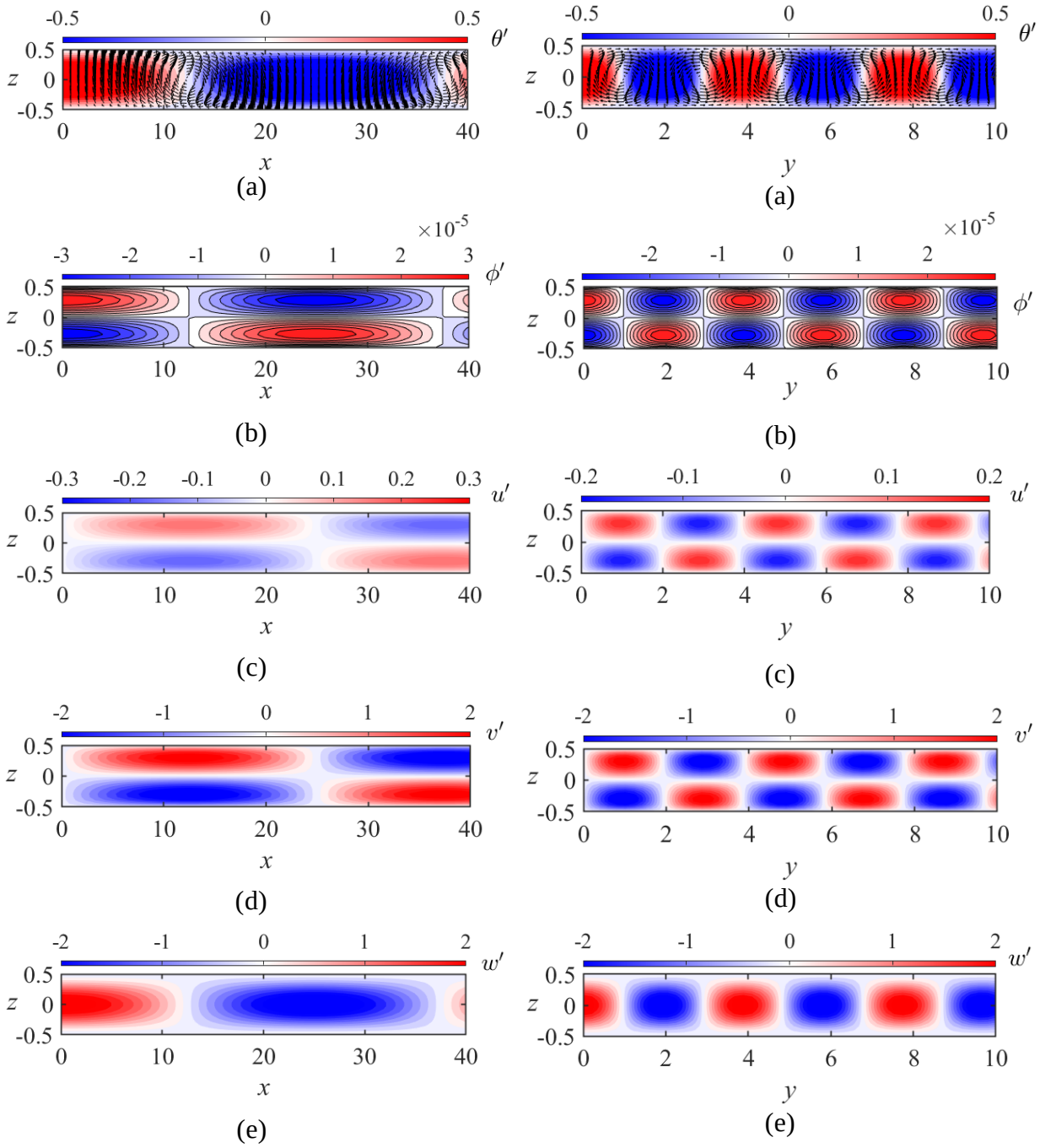

Figure 3.8: Eigenfunctions of the electric mode for $Pr = 65$, $Ra = -500$ and $L_c = 2749.89$. (a) the velocity fields and the temperature levels, (b) the electric potential ϕ', (c-d) the horizontal velocity components u' and v', and (e) the vertical velocity w'.

3.4.3. Energetic analysis at the threshold

The fluid stability is governed by the competition between Archimedean buoyancy, dielectrophoretic buoyancy, and viscous dissipation. To emphasize the contribution of each term to the energy balance at the onset of the thermoelectric convection, we have computed the power of each force in the equation of the kinetic energy (2.18). In the framework of the linear stability analysis, the time evolution of the kinetic energy of the perturbation is derived by taking the scalar product of the momentum equation with $\vec{u}'$. After decomposing the electric gravity into basic electric gravity and perturbative electric gravity, we integrate the resulting equation over the whole volume [32]:

$$\frac{dK}{dt} = W_{BEG} + W_{PEG} + W_G - D_\nu, \tag{3.22}$$

where K, W_G and D_ν are defined in (2.18), $W_{BEG} = -\frac{L_c}{Pr}\int \theta'\vec{u}' \cdot g_{eb}\, dV$ is the contribution of the basic electric gravity to the power of the dielectrophoretic force, and $W_{PEG} = -\frac{L_c}{Pr}\int (\theta_b \vec{u}') \cdot \vec{g}'_e\, dV$ is the contribution of the perturbed electric gravity to the power of the dielectrophoretic force.

In order to analyze the equation (3.22) at the onset of thermoelectric convection, let us introduce a new variable $\varphi = e^{st+ik_x x+ik_y y}$, so that we have $\varphi\varphi^* = e^{2\sigma t}$. The development of the velocity in normal modes $\vec{u}' = \hat{u}(z)e^{st+ik_x x+ik_y y} + c.c.$ yields $\vec{u}' = \hat{u}\varphi + \hat{u}^*\varphi^*$, and then $\vec{u}'^2 = \hat{u}^2\varphi^2 + 2\hat{u}\cdot\hat{u}^*\varphi\varphi^* + \hat{u}^{*2}\varphi^{*2}$. Therefore, we obtain the following formulae for the time variation of the kinetic energy of the perturbation

$$\frac{dK}{dt} = 2\sigma\, e^{2\sigma t}\int \hat{u}\cdot\hat{u}^* dV = 2\sigma \int \hat{u}\cdot\hat{u}^* e^{2\sigma t} dV = 2\sigma K,$$

Equation (3.22) leads to :

$$\sigma = \frac{W_{BEG}}{2K} + \frac{W_{PEG}}{2K} + \frac{W_G}{2K} - \frac{D_\nu}{2K}.$$

So the balance of powers from all forces intervening at the threshold of the thermos-convection reads:

$$\frac{W_{BEG}}{2K} + \frac{W_{PEG}}{2K} + \frac{W_G}{2K} - \frac{D_\nu}{2K} = 0. \tag{3.23}$$

Each power is computed using the eigenfunctions of critical mode.

The terms of the energy equation terms of a flow in a system heated from the bottom are presented in Figure 3.9 for $Pr = 11.03$. All terms were computed for different values of Ra below $Ra_c \approx 1708$ (vertical dashed line) in Figure 3.9. We observe that W_G increases when increasing Ra; while the contribution W_{BEG} of the basic electric gravity decreases with Ra. This diminution of the power W_{BEG} with Ra is due to the decrease of L_c with Ra as shown in equation (3.21). The two mechanisms driving the convection are Archimedean buoyancy and basic electric gravity buoyancy. The intersection of the curves of the powers from the Archimedean buoyancy and the dielectrophoretic buoyancy from the basic electric gravity related power graphs determines the point $Ra = Ra^* \approx 954$ where $W_G = W_{BEG}$. The dielectrophoretic buoyancy is the dominant term in thermoelectric convection generation when $Ra < Ra^*$; and the Archimedean buoyancy dominates when $Ra > Ra^*$. This suggests that in this later case, the thermo-convective structures are Rayleigh-Bénard cells which were favored by the dielectrophoretic buoyancy.

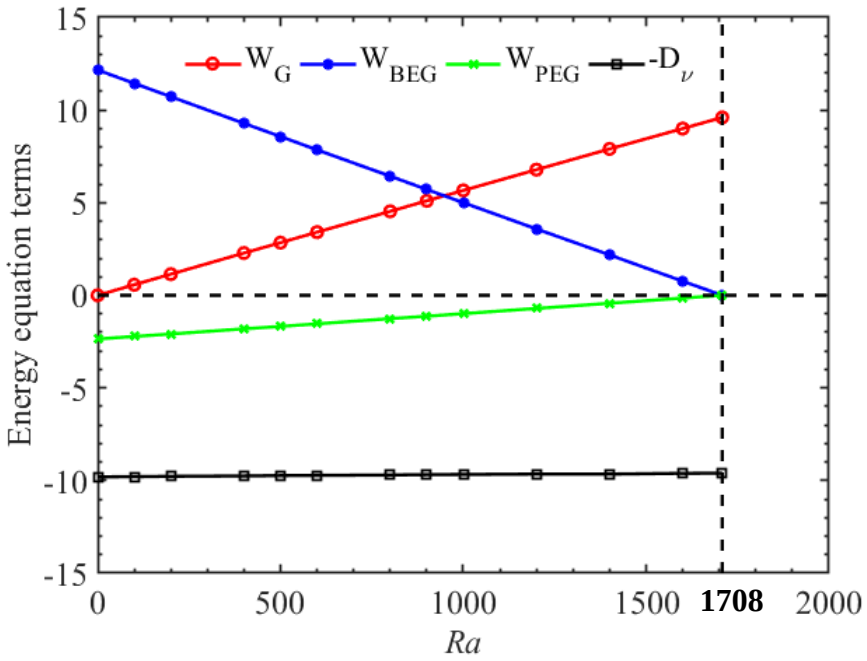

Figure 3.9: Different terms of the energy balance at the critical point (L_c, k_c) normalized by twice the kinetic energy plotted as a function of the Rayleigh number Ra.

Figure 3.10 shows the variation of the terms of the kinetic energy equation with $|Ra|$ at the threshold for a system heated from the top. One sees that the power W_{BEG} is the sole positive term in the energy equation. The contribution W_G and W_{PEG} are both negative, with the viscous dissipation term. Therefore, the dielectrophoretic force induced by the perturbative electric gravity

and the Archimedean buoyancy contributes to the stabilization of the system. Since $|W_G|$ and $|W_{PEG}|$ increase with $|Ra|$, the stabilization of the system is intensified with $|Ra|$; thus an intense electric potential is needed to induce thermoelectric convection.

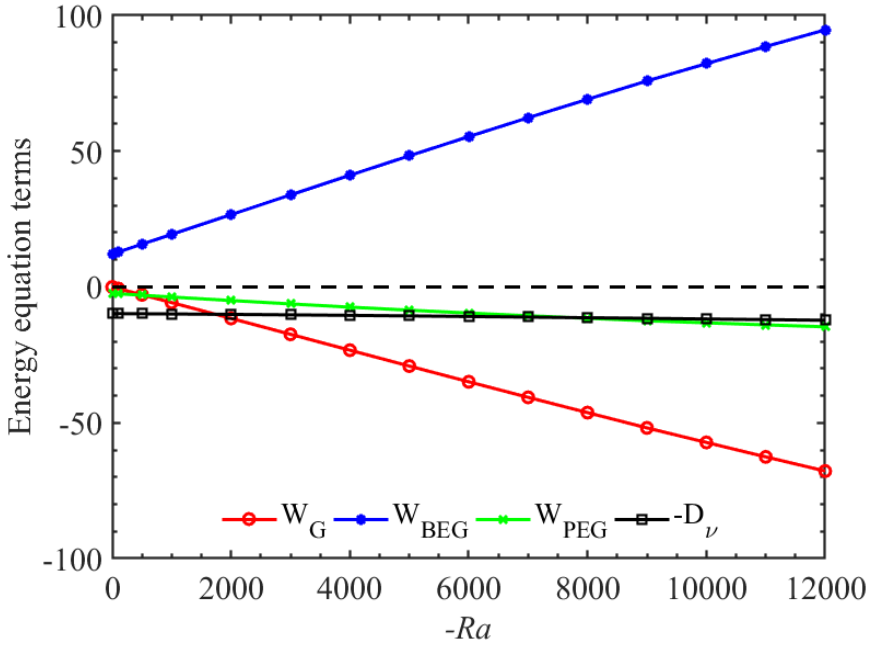

Figure 3.10: Different terms of the energy balance at the critical point (L_c, k_c) normalized by twice the kinetic energy plotted as a function $|Ra|$ for $Pr = 11.03$ (Novec 7200) for a system heated from the top.

The local kinetic energy $E_c = \frac{1}{2}\|\vec{u}'\|^2$, the local power of the basic electric gravity $w_{BEG} = -\frac{L}{Pr}(\theta'\vec{u}') \cdot g_{eb}$, the local power of the perturbed electric gravity $w_{PEG} = -\frac{L}{Pr}(\bar{\theta}\vec{u}') \cdot \vec{g}_e'$, and the local power of the Archimedian buoyancy $w_G = -\frac{Ra}{Pr}(\theta' w')$ are presented in Figure 3.11 for $Pr = 65$, and $Ra = 500$. One sees that w_G and w_{BEG} are both positive at the central zone $(z = 0)$ in both vertical $(x - z)$ and $(y - z)$ planes.

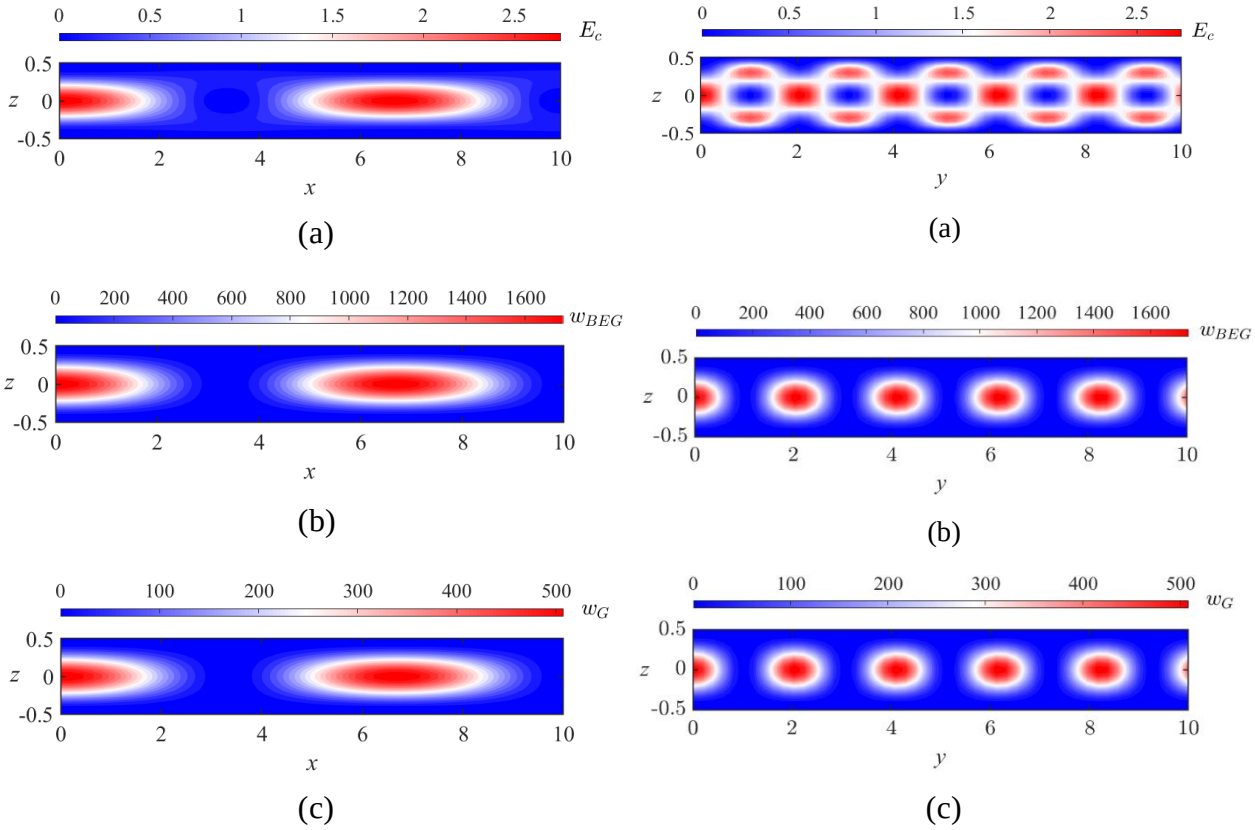

Figure 3.11: Cross-section of different local power terms at the threshold ($L_c = 1506.57$) for $Pr = 65$, $Ra = 500$, , and $\gamma_e = 1.92 \cdot 10^{-3}$: local kinetic energy (a), local power arising from the basic electric gravity (b), and the local power from the Archimedean buoyancy (c).

By integrating the energy terms over the horizontal x and y-directions, we obtain the energy evolution inside the gap. Results are presented in Figure 3.12. Curves represent the local variation along the z-axis of mass density of the kinetic energy of disturbances E_c, the power performed by the basic electric gravity w_{BEG}, and the power of the Archimedean buoyancy w_G. One can observe that w_{BEG} and w_G are maximum at the mid-gap $z = 0$. This shows that the effects of the Archimedean and dielectrophoretic buoyancies are maximum at zone $z = 0$ which corresponds to the active zone. Since w_{BEG} is larger than w_G, we confirm that thermoelectric convection is governed by basic electric gravity (Figure 3.11-Figure 3.12).

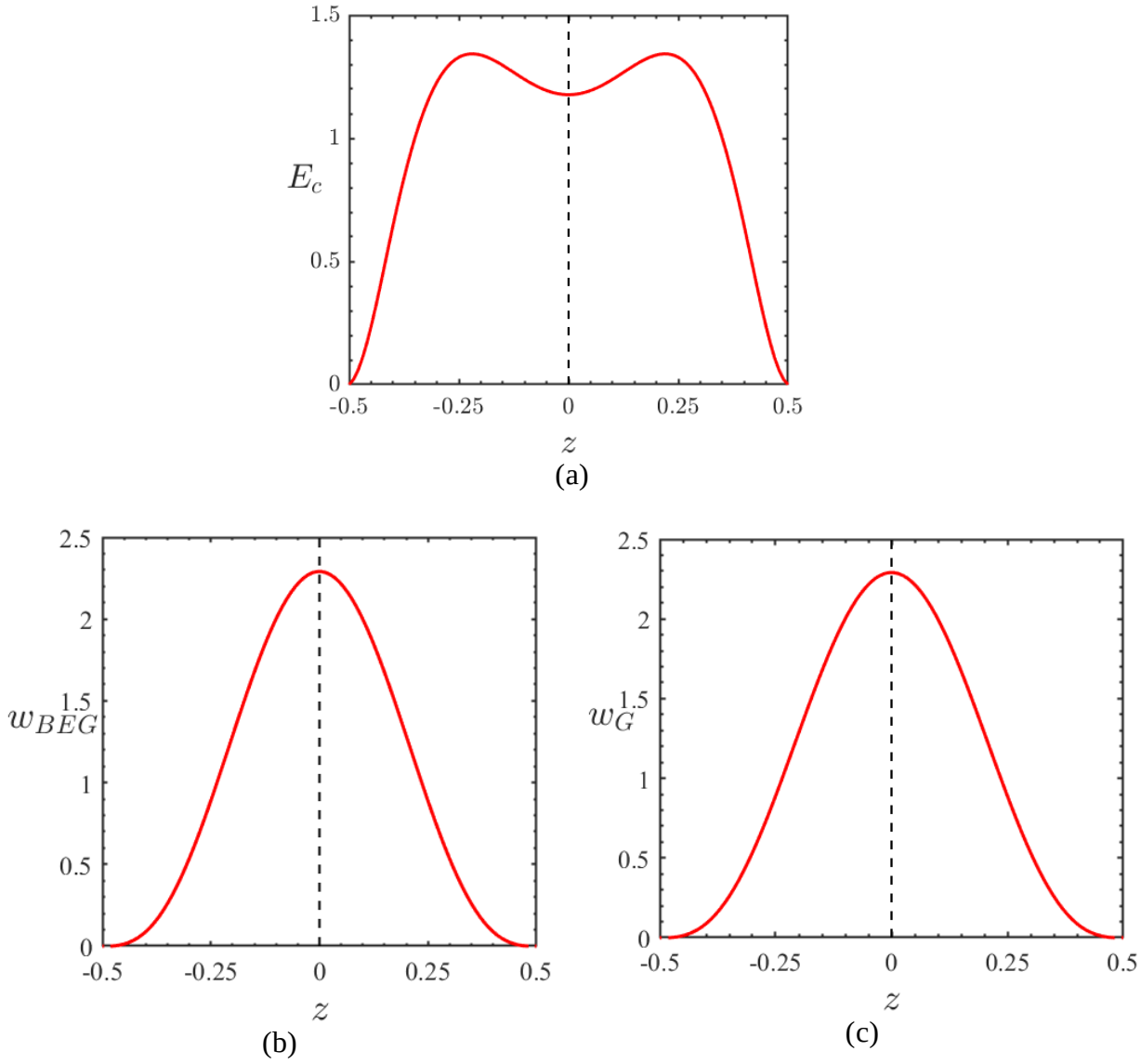

Figure 3.12: Profiles of local kinetic energy (a), local power generated by the basic electric gravity (b), and the local power performed by the Archimedean buoyancy (c) at the threshold ($L_c = 1506.57$) for $Pr = 65$, $Ra = 500$. The local kinetic energy is normalized by K, w_{BEG} by W_{BEG} and the local power of the Archimedean buoyancy w_G by W_G.

3.5. Partial Conclusion

The stability of a horizontal layer of a dielectric fluid subject to a vertical temperature gradient and to a vertical alternating electric field has been investigated. The dielectrophoretic force produced by the thermoelectric coupling changes the stability of the fluid layer when the electric Rayleigh number reaches the critical value $L_c(Ra)$ independently on Pr. We confirmed previous results from different authors on the threshold of the thermoelectric convection under microgravity conditions ($Ra = 0$) with critical modes formed of stationary counter-rotating vortices with a spatial periodicity in the horizontal plane.

When the fluid layer is heated from the top ($Ra < 0$), it has a thermally stable stratification and the thermoelectric convection is delayed. When the fluid layer is heated from the bottom ($0 < Ra < 1708$) it has a thermally unstable stratification and the thermoelectric convection occurs for lower values of the electric Rayleigh number $[L_c(0 < Ra < 1708) < L_c(Ra = 0) < L_c(Ra < 0)]$.

The energetic analysis showed that the power of the dielectrophoretic force due to basic electric gravity is the dominant term in energy generation. Its intensity is more important in the central part of the gap located at $z = 0$. The influence of Ra on the energy balance has also been analyzed. When the fluid layer is in thermally stable stratification ($Ra < 0$), the basic electric gravity is the only term generating the thermoelectric convection as in the microgravity conditions ($Ra = 0$). When the fluid is heated from the bottom, the dielectrophoretic buoyancy and the Archimedean buoyancy complement each other in the destabilization of the base state. We have found that the Archimedean buoyancy overcomes the dielectrophoretic buoyancy when Ra reaches the Ra^*. So we conclude that thermoelectric convection occurs for $Ra < Ra^*$ while for $Ra > Ra^*$, we have Rayleigh-Bénard convection enhanced by dielectrophoretic buoyancy.

Chapter 4: Numerical simulation of thermoelectric convection in a horizontal rectangular cavity

The present chapter addresses results from Direct Numerical Simulations (DNS) of thermo-electro-hydrodynamic instabilities in a horizontal rectangular cavity in microgravity and in thermally stable and unstable stratifications. We first determine the critical values of the electric Rayleigh number for given values of Pr and different values of Ra. Then, we use a weakly nonlinear analysis with the Landau-Stuart Equation (LSE) to determine the nature of the bifurcation from the base state to the first regime of thermoelectric convection. Different regimes of thermoelectric convection are computed by increasing L. The variation of the heat transfer coefficient Nu of thermoelectric convection with the control parameter L is determined for two values of Pr.

4.1. Numerical method

We consider a horizontal rectangular cavity with lengths $L_x = L_y = 10d$. According to linear stability analysis, such lengths allow having about 10 modes in the x-direction and 2 modes in the y-direction. The choice of the aspect ratio $\Gamma = L_x/d = 10$ is motivated by the study of Hartlep *et al.* [71]. With this value, the authors were able to observe the different instability modes present in a classical Rayleigh-Bénard convection during the transition to turbulence. The numerical code is an in-house code written by Dr. Kang [21,72–74]. In the Cartesian coordinates, we have used the finite volume method to discretize the dimensionless governing flow equations (2.26)-(2.29). The fluid domain is divided into many control volumes as shown in Figure 4.1. The second-order central difference scheme was used for spatial discretization. The Crank-Nicolson scheme was employed for time advancement for the second-order diffusion terms and the third-order of the Runge-Kutta for the convective terms and the other terms. The pressure in the momentum equation and the continuity equation are coupled using the fractional step method; so that the resulting Poisson equation is solved by a spectral method. The Preconditioned Biconjugate Gradient method

(PBCG) was utilized to solve the Laplace equation for the electric potential. The pressure, the temperature, and the potential are determined at the center of the control volume while the velocities are determined at each face of the control volume.

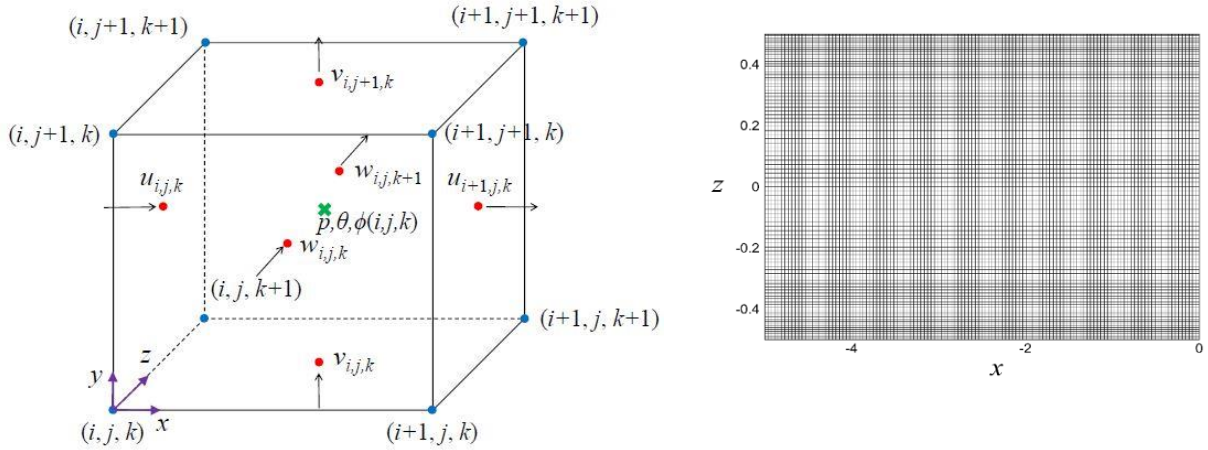

Figure 4.1: Control volume and grid system in the vertical $(x - z)$ plane.

The temperature and the electric potential are kept constant on the top and bottom walls. Since the no-slip condition was employed, we have utilized the Dirichlet boundary conditions at the horizontal solid surfaces located at $z = \pm 1/2$:

$$\vec{u} = 0;\ \theta = 1/2;\ \phi = 1 \text{ à } z = -1/2\,,$$

$$\vec{u} = 0;\ \theta = -1/2;\ \phi = 0 \text{ à } z = 1/2\,;$$

and the periodic boundary conditions for the velocity, the temperature, and the electric potential along the horizontal x and y directions:

$$\left.\begin{aligned} \vec{u}(x,y,z) &= \vec{u}(x \pm L_x/2, y \pm L_y/2, z), \\ \theta(x,y,z) &= \theta(x \pm L_x/2, y \pm L_y/2, z), \\ \phi(x,y,z) &= \phi(x \pm L_x/2, y \pm L_y/2, z). \end{aligned}\right\} \tag{4.1}$$

The computational grid cells in this study are chosen depending on the values. For example, we have adopted the grid cells with $256(x) \times 256(y) \times 64(z)$ for $Pr = 1$ with 64 points in the vertical direction (z). For large values of Prandtl number $Pr \gg 1$, the thermal boundary layer is smaller than the momentum boundary layer. Viscous and buoyancy forces are in balance in the thermal boundary layer and viscous and inertia are in balance in the larger viscous boundary layer.

Accordingly, we need to increase the grid point number along the vertical direction, for example, we have chosen $256(x) \times 256(y) \times 96(z)$ for $Pr = 65$. The grid refinement is uniform in the horizontal (x) and (y) directions, while more grid points are located near the walls in the vertical direction (z). To ensure the convergence of solutions, we have computed the mean values of the temperature and the velocity for the chosen grid cells. The obtained values are 1% less than those obtained with doubled grid points in each direction. This refinement corresponds to an optimal computation time.

For the visualization of the flow patterns, we plotted the iso-surfaces of the quantity Q [75]: $Q = -\frac{1}{2}\mathrm{tr}\left(\bar{\bar{S}}^2 + \bar{\bar{\Omega}}^2\right)$ where $\bar{\bar{S}}$ and $\bar{\bar{\Omega}}$ are the symmetric and the antisymmetric parts of the velocity gradient tensor $\vec{\nabla}\vec{u}$ respectively. Their components are given by

$$S_{ij} = \frac{1}{2}\left(\frac{\partial u_j}{\partial x_i} + \frac{\partial u_i}{\partial x_j}\right) \text{ and } \Omega_{ij} = \frac{1}{2}\left(\frac{\partial u_j}{\partial x_i} - \frac{\partial u_i}{\partial x_j}\right).$$

By introducing the quantities $T_{ij} = \frac{\partial u_j}{\partial x_i}$ and $T_{ji} = \frac{\partial u_i}{\partial x_j}$, the quantity Q reads [75]:

$$Q = -0.5 \cdot [T_{11}^2 + T_{22}^2 + T_{33}^2 + 2 \cdot (T_{21} \cdot T_{12} + T_{13} \cdot T_{31} + T_{23} \cdot T_{32})].$$

In our study, we have fixed the value of the thermoelectric coefficient $\gamma_e = 0.01$. For a given value of Pr, computations are started with random noise with an amplitude of about 10^{-5}. For given values of the Ra, the flow is computed for increasing the values of the applied electric potential above the threshold, i.e. $L > L_c$.

4.2. Conductive Base state

For small values of the electric potential i.e. $L < L_c(Ra)$, the fluid layer is at rest, and heat transfer is accomplished by conduction. The temperature obeys the Fourier law. The electric field is also linearly distributed along the vertical direction. The numerical code was tested by computing the numerical solution of the quiescent conductive state. Analytic and numerical solutions for $Pr = 1, Ra = 0$, and $L = 2100$ are plotted in Figure 4.2 and Figure 4.3. The temperature and the electric potential are invariant by translation along the y direction. Thus the behaviors of isotherms and equipotentials are the same in both vertical $(x - z)$ and $(y - z)$ directions.

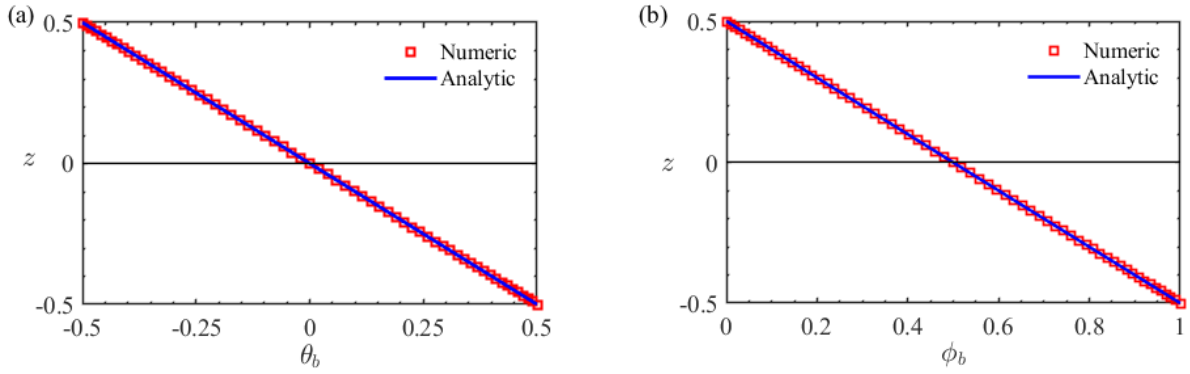

Figure 4.2: Analytic and numerical solution of the conductive base state for $Pr = 1, Ra = 0$ and $L = 2100$. Profiles of the (a) temperature and (b) the electric potential.

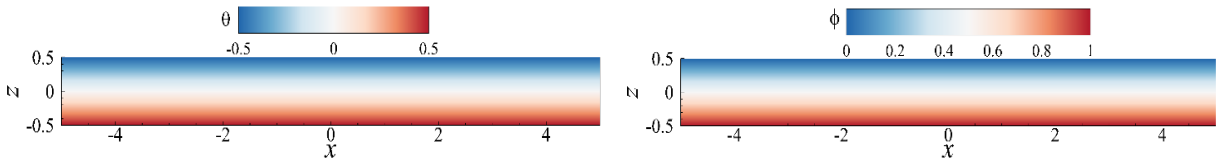

(a) (b)

Figure 4.3: Isotherms (a) and equipotential (b) of the quiescent base state in the (x, z) plane for $Pr = 1$, $Ra = 0$ and $L = 2100$.

4.3. Landau-Stuart equation

The linear stability analysis yields the critical parameters (threshold, critical wavenumber) of the thermoelectric convection but the mode amplitude can be obtained from DNS. Near the threshold, the amplitude can be chosen as the amplitude of either the vertical velocity or the temperature. The velocity component is aligned with the vertical temperature gradient and participates in the vertical advection of the temperature. The amplitude of the vertical velocity at the mid-gap reads:

$$A = \frac{1}{L_x L_y} \int_{-\frac{l_y}{2}}^{\frac{l_y}{2}} \int_{-\frac{l_x}{2}}^{\frac{l_x}{2}} |w(x, y, z = 0)| dx dy. \tag{4.2}$$

Near the threshold, the dynamics of the perturbed state are described by the nonlinear Landau-Stuart equation [76]:

$$\tau_0 \frac{dA}{dt} = \delta A - l|A|^2 A + g|A|^4 A, \tag{4.3}$$

where $\delta = (L - L_c)/L_c$ is the relative distance from the threshold, τ_0 is the characteristic time of the perturbations, l, and g are the nonlinear saturation coefficients. If the Landau coefficient l is positive, the bifurcation is supercritical and there is no need to take into account the higher-order terms in (4.3). When $l < 0$, the bifurcation is subcritical and the term of higher order is then needed for the saturation. In that case, one has to consider the sign of g in order to decide to limit the expansion to the 5th order ($g < 0$) or to continue to higher order if ($g > 0$).

The characteristic time $\tau_0 = \sigma_0^{-1}$ where σ_0 is computed from linear stability analysis. Indeed, in the neighborhood of the threshold, the growth rate σ obeys the following relation:

$$\sigma = \sigma_0 \delta + \sigma(O^2), \text{ with } \sigma_0 = \left(\frac{\partial \sigma}{\partial \delta}\right)\Big|_{L_c} = L_c \left(\frac{\partial \sigma}{\partial L}\right)\Big|_{L_c}. \tag{4.4}$$

It can be determined also from DNS in the linear phase of the curve $l\,n|A| = f(t) \approx \sigma_0 \delta t$. The coefficients l and g which determine the nature of the bifurcation from the base state to the thermo-convective regime given by the following formulae [72]

$$l = -\frac{df(|A|^2)}{d|A|^2}\Big|_{|A|^2=0} \text{ with } f(|A|^2) = \delta - l|A|^2 + g|A|^4; g = \frac{l}{2|A_m|^2}, \tag{4.5}$$

where A_m is the amplitude corresponding to the maximum of $f(|A|^2)$ in the case of subcritical bifurcation ($l < 0$).

4.4. Instability threshold and nature of bifurcation

4.4.1. Critical electric Rayleigh number L_c and nature of bifurcation

When the electric potential exceeds the critical value, a convective flow sets and its amplitude A defined in equation (4.2) grows exponentially in time until it gets saturated due to nonlinearities (Figure 4.4). The plots show that each amplitude curve contains three parts: the random noise near

$t = 0$, the linear growth phase and the nonlinear saturation phase. We analyze the linear growth and nonlinear saturation phases to determine the coefficients of the Landau-Stuart equation (4.3).

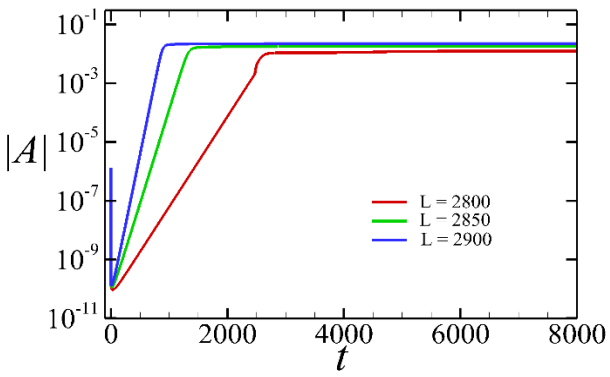

(a) $Ra = -500$

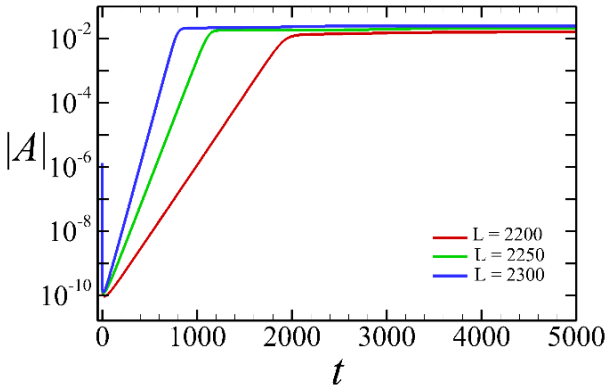

(b) $Ra = 0$

Figure 4.4: Temporal evolution of the amplitude of perturbations, until the saturation for $\delta < 0.03$ of a saturated perturbed flow for $Pr = 65, \gamma_e = 0.01$.

Since the LSA has shown that critical modes of the thermoelectric convection are stationary, the time evolution of A in the linear-growth phase is given by:

$$A(t) = Ce^{\sigma t}, \tag{4.6}$$

where the linear growth rate σ is real. The growth rate σ can be determined by using the exponential fit of the time evolution of the amplitude A or equivalently by the plot $\ln A(t) = \ln C + \sigma t$.

The slope of the amplitude depends on the value of L (Figure 4.4). The obtained values of σ are plotted as a function of the electric Rayleigh number L i.e. $\sigma(L)$ for the fixed values of the Rayleigh number Ra. The intersection of the line $\sigma(L)$ with the horizontal axis ($\sigma = 0$) determines the threshold of the thermoelectric convection L_c i.e. $L_c = L(\sigma = 0)$ as shown in Figure 4.5-a.

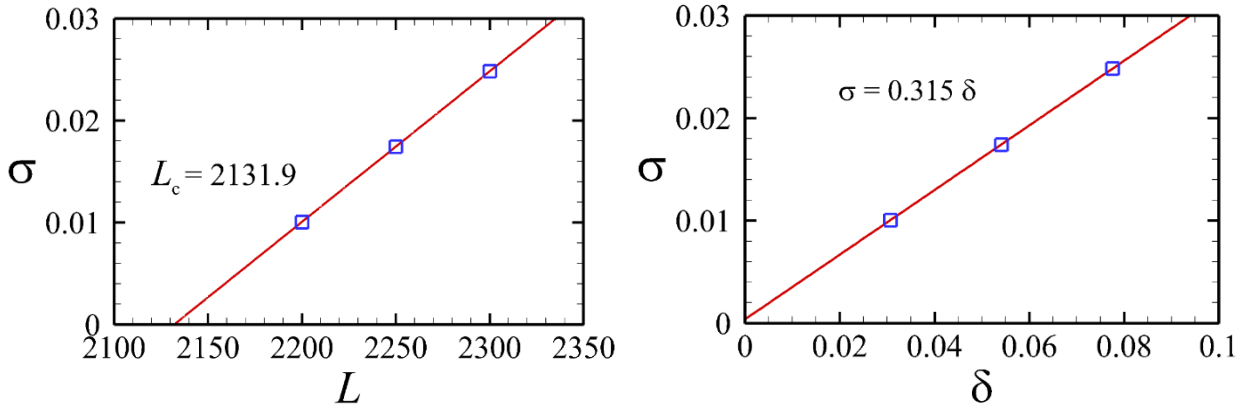

Figure 4.5: Growth rate σ plotted against a) the electric Rayleigh number L to determine L_c, and b) the criticality δ to determine the characteristic time τ_0 for $\gamma_e = 0.01$, $Pr = 65$, and $Ra = 0$.

Under a microgravity condition ($Ra = 0$), the critical electric Rayleigh number found by DNS is $L_c = 2131.9$ for $Pr = 65$ and $L_c = 2128.10$ for $Pr = 1$; these values are very close to the threshold obtained by the LSA ($L_c = 2128.6$). The evolution of the growth rate σ as a function of the reduced control parameter near the threshold is presented in Figure 4.5 (b). From the slope of the curve $\sigma = f(\delta)$, we can extract the characteristic time τ_0, defined in equation (4.4).

When the system reaches saturation we extracted the Landau constant l using equation (4.5). Figure 4.6 shows that the slope at the origin of the derivative of the logarithm of the amplitude is negative, therefore the Landau coefficient l is positive for $Pr \in \{1; 65\}$. We found that the bifurcation to thermoelectric convection is supercritical in microgravity and for different thermal stratification of the fluid layer. Table 4.1 gives values of L_c, τ_0, l for $Pr \in \{1; 65\}$ and different values of Ra. The characteristic time τ_{DEP} introduced in chapter 2 is made non-dimensional by the characteristic viscous time τ_v. Its non-dimensional form is computed at the threshold by the following formula $\tilde{\tau}_{conv}(Ra) = \sqrt{\frac{Pr}{L_c(Ra)}}$ and results are presented in Table 4.1.

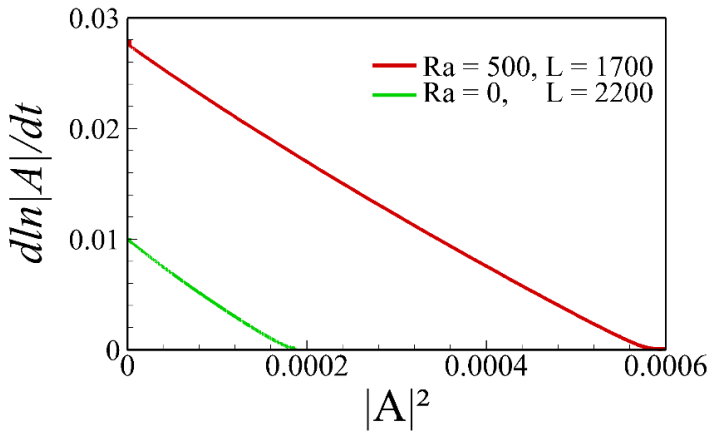

Figure 4.6: Variation of the $d(\ln|A|)/dt$ as a function of $|A|^2$ for $Pr = 65$: under microgravity conditions ($Ra = 0, L_c = 2131.9$); and unstable stratification case ($Ra = 500, L_c = 1507.95$).

Table 4.1: Values of the critical electric Rayleigh number L_c and the coefficients of the LSE for two values of Pr and different values of Ra.

Pr	Ra	-1000	-500	0	500	1000
1	L_c	3369.74	2749.06	2128.10	1504.65	883.38
	τ_0	0.044	0.055	0.073	0.105	0.179
	l	0.023	0.027	0.031	0.040	0.058
	$\tilde{\tau}_{conv}$	0.017	0.019	0.022	0.026	0.034
65	L_c	3375.81	2768.47	2131.90	1507.95	885.42
	τ_0	2.06	2.43	3.18	4.62	7.99
	l	99.73	111.13	130.10	157.12	245.06
	$\tilde{\tau}_{conv}$	0.139	0.153	0.175	0.208	0.271

Table 4.1 shows that the values of the characteristic time τ_0 and of the Landau coefficient l depend considerably on Pr. Under microgravity conditions, the values of τ_0 agree with those obtained in the case of the two-dimensional thermoelectric convection under microgravity conditions for $\gamma_e = 0.03$ [32]. This coefficient can be correlated using the same relationship of the classical Rayleigh-Bénard problem $\tau_0 = (Pr + 0.5117)/19.65$ [77] within a precision of 5%. The values given by Yoshikawa *et al.* [32] and Cross [77] are $\tau_0 \in \{0.078, 3.33\}$ for $Pr \in \{1; 65\}$.

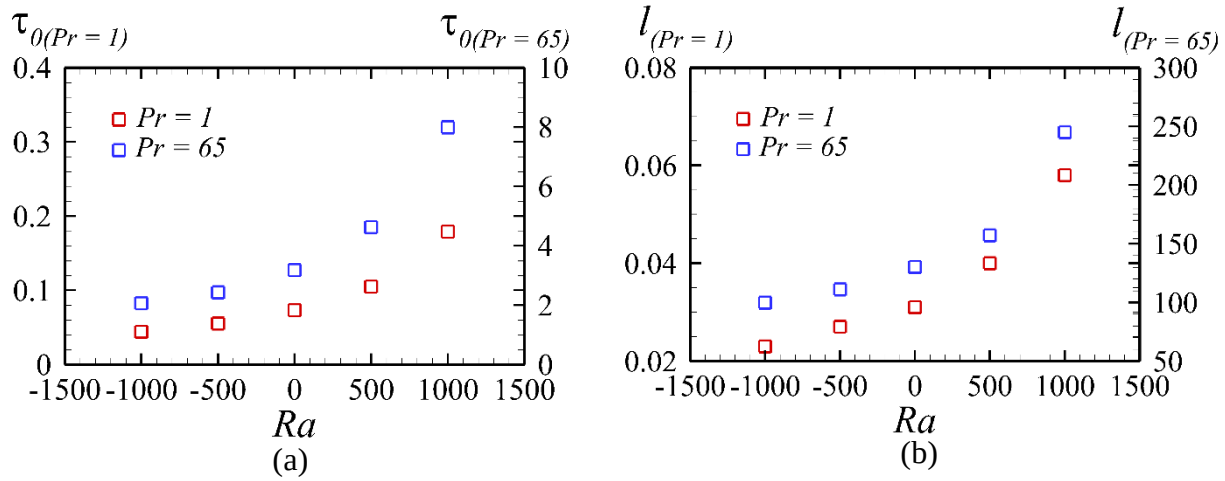

Figure 4.7: Variation of (a) τ_0 and (b) l as function of Ra for two values of Prandtl number Pr.

To illustrate the supercritical bifurcation, we have plotted the amplitude of the saturated thermo-convective flows as a function of L in Figure 4.8 for two values of the Prandtl number Pr under microgravity conditions.

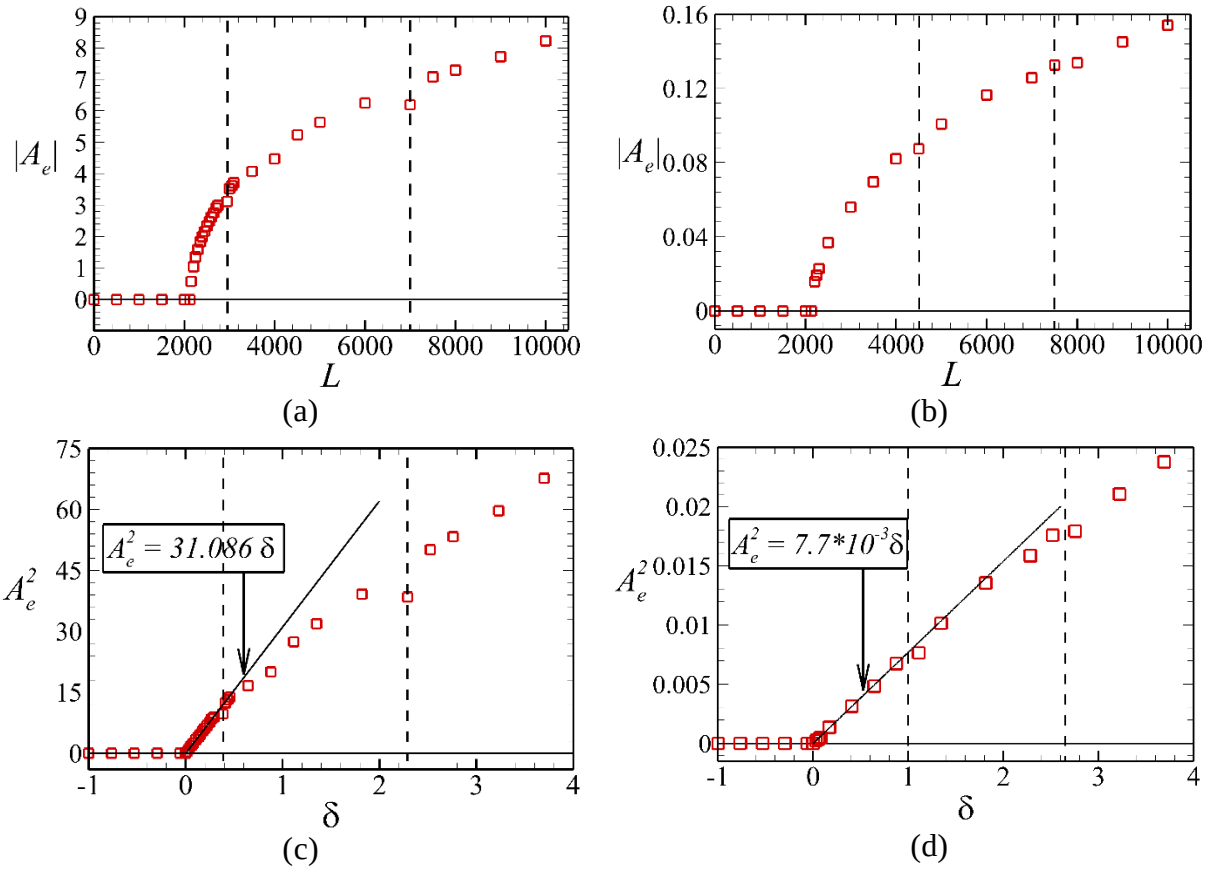

Figure 4.8: Variation of the amplitude $|A_e|$ of saturated regimes with L and A_e^2 as function of δ for $Ra = 0$, (a-c) $Pr = 1$, and (b-d) $Pr = 65$.

One sees that the amplitude of the convection increases with increasing the value of the electric Raleigh number L for both values of Pr. The slopes at the origin are about $S_1 = 5.4 \cdot 10^{-3}$ for $Pr = 1$ (Figure 4.8 (a)) and $S_2 = 7.1 \cdot 10^{-5}$ for $Pr = 65$ (Figure 4.8 (b)). We also notice that the amplitude $|A_e|$ changes with Pr while its global behavior as a function of the electric Rayleigh number L is the same for both Pr as shown on Figure 4.9. The changes in slopes of the curve of $|A_e|$ with L in Figure 4.8 (a) and (b) can be associated with the change of the flow regimes. Figure 4.8 (c-d) shows the variation of $A_e^2 = \frac{1}{l}\delta$ as function of δ; we then observe that the linear approximation in the LSE is only valid around the threshold for both values of Pr.Due to the important viscous effects for $Pr = 65$, the amplitude of thermoelectric convection regimes is much lower than that of the thermal convective instabilities occurring for $Pr = 1$.

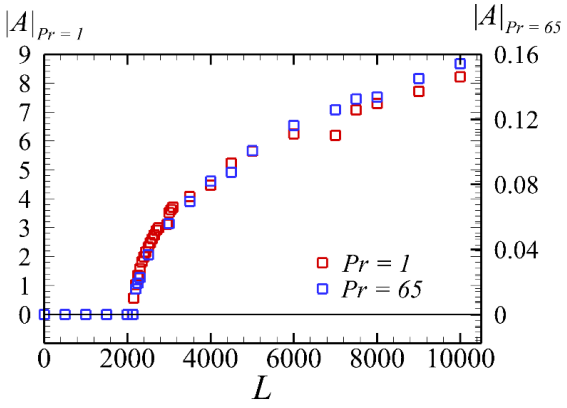

Figure 4.9: Variation of the amplitude $|A|$ of saturated regimes with the electric Rayleigh number L for $Ra = 0$, and $Pr = 1$ and $Pr = 65$.

4.5. Flow regimes for $Pr = 1$

We have seen from the previous section that the first bifurcation to the thermoelectric convection regime in the differentially heated fluid layer is independent of Pr for all values of Ra. In this section, the Prandtl number will be fixed at $Pr = 1$. To investigate the different thermo-convective regimes induced by the dielectrophoretic buoyancy, we performed numerical simulations for given values of Ra and electric Rayleigh number L ranging from L_c to 10^4. We stop computations at this value because of the limitation due to the breakdown voltage. For

example, the voltage corresponding to $L = 10\,000$ for the silicone oil (AK5) is about $V_0 = 38.6\ kV$. This value is under the predicted breakdown voltage given in Table 2.1.

4.5.1. Flow patterns under microgravity conditions ($Ra = 0$)

Dielectrophoretic instability occurs in the fluid layer under microgravity conditions when $L_c \approx 2132$. The thermoelectric convection appears in form of stationary straight convective rolls with an inclined axis in the $(x - y)$ plane. The analysis of the behavior of the flow above the threshold shows that the thermoelectric convective patterns remain stationary for $L_c < L < 3500$. We have plotted in Figure 4.10 (a), the amplitude of the averaged vertical velocity to monitor the evolution of thermoelectric convection. The stationarity of the rolls in the convective regime is evidenced by plotting the time evolution of the vertical velocity w_0 and the temperature θ_0 at the center of the rectangular cavity (Figure 4.10 (b)). Graphs reveal that w_0 and θ_0 converge to finite stationary values after the computational time exceeds 400 times the viscous time. An example of the first steady regime can be seen in Figure 4.11.

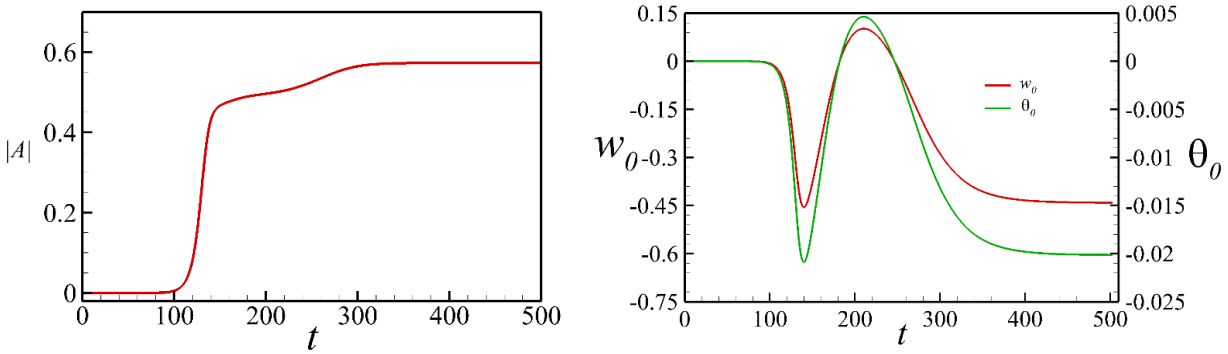

Figure 4.10: Time evolution of the (a) amplitude of averaged vertical velocity $|A|$ at the mid-gap $z = 0$; (b) vertical velocity w_0 and temperature θ_0 at the center of the rectangular cavity for $Pr = 1$ and $L = 2150$. Amplitudes and time are, respectively, normalized by the viscous velocity ν/d and the viscous time d^2/ν.

From linear stability analysis, we have shown that critical roll patterns are inclined in the plane horizontal $(x - y)$ plane. The wavenumber of patterns observed close to the threshold (Figure 4.11) is around $k = 3.204$ with $k_x = 0.628$ and $k_y = 3.142$. The value of $k = 3.204$ is close to that predicted in LSA which is about $k_c = 3.228$. The thermo-convective structures are tilted at an

angle of 78° to the x axis. This inclination angle changes randomly when L increases as shown in Figure 4.11 (a1) and (a2). The inclination angle of rolls in Figure 4.11 (a2) is about 53° with the $y-$direction. Snapshot of temperature distributions in Figure 4.11 (a) and (b) is taken at the mid-height position ($z = 0$) to show the patterns of thermo-convective structures.

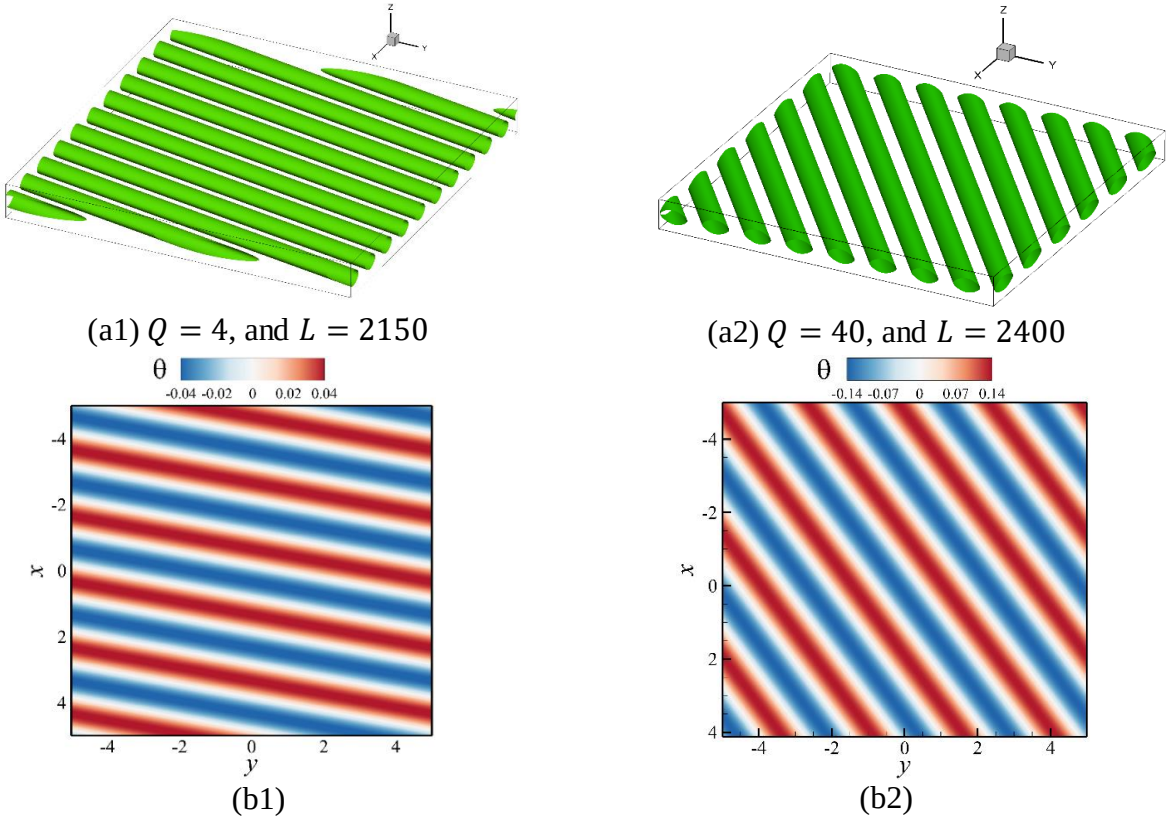

(a1) $Q = 4$, and $L = 2150$ (a2) $Q = 40$, and $L = 2400$

(b1) (b2)

Figure 4.11: (a) Vortical structures illustrated by iso-surfaces of Q, and (b) isotherms in the horizontal $(x - y)$ plane for $Pr = 1$, $\gamma_e = 0.01$, $Ra = 0$ and two values of L.

The instantaneous temperature fields together with the instantaneous velocity of flow on the vertical planes $(x - z)$ and $(y - z)$ are shown in Figure 4.12 for $L = 2400$. This flow regime is chosen in order to elucidate the periodicity in both horizontal directions. In the temperature distribution, blue represents cold zones and red corresponds to hot zones; the corresponding temperature perturbations are presented in Figure 4.12 (b). For low values of L around the threshold, we observe zones of high perturbation electric potential located alternatively near the hot and cold plates in Figure 4.12 (c). Figure 4.12 (f) shows an alternate of positive (red) and negative (blue) vertical velocity w zones; this illustrates the upward and downward motions of fluid particles that form vortices. The vertical vorticity components in both vertical $(x - z)$ and $(y - z)$ cross-sections are presented in Figure 4.13 for $L = 2400$. In both vertical planes, we

observe that the magnitude of the vertical vorticity component is lower than the magnitude of the horizontal vorticity components.

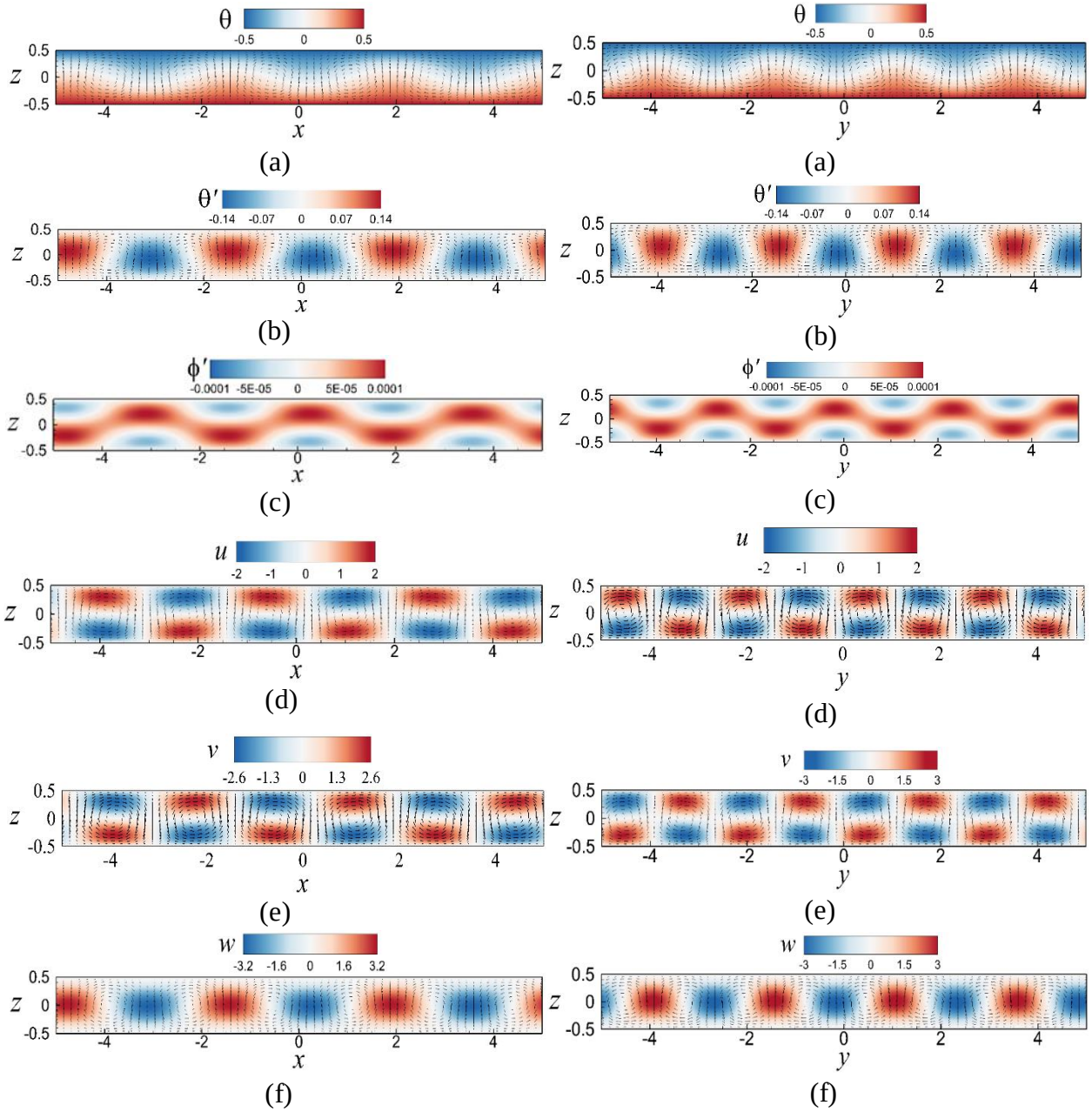

Figure 4.12: Instantaneous flow fields of saturated state in the plane $y = 0$, and in the plane $x = 0$ for $Pr = 1$, $\gamma_e = 0.01$, $Ra = 0$ and $L = 2400$. Vectors represent the velocity fields: (a) temperature distribution (color); (b) temperature perturbations; (c) electric potential perturbations; (d-e) horizontal velocity components u and v (color); and (f) vertical velocity component (color).

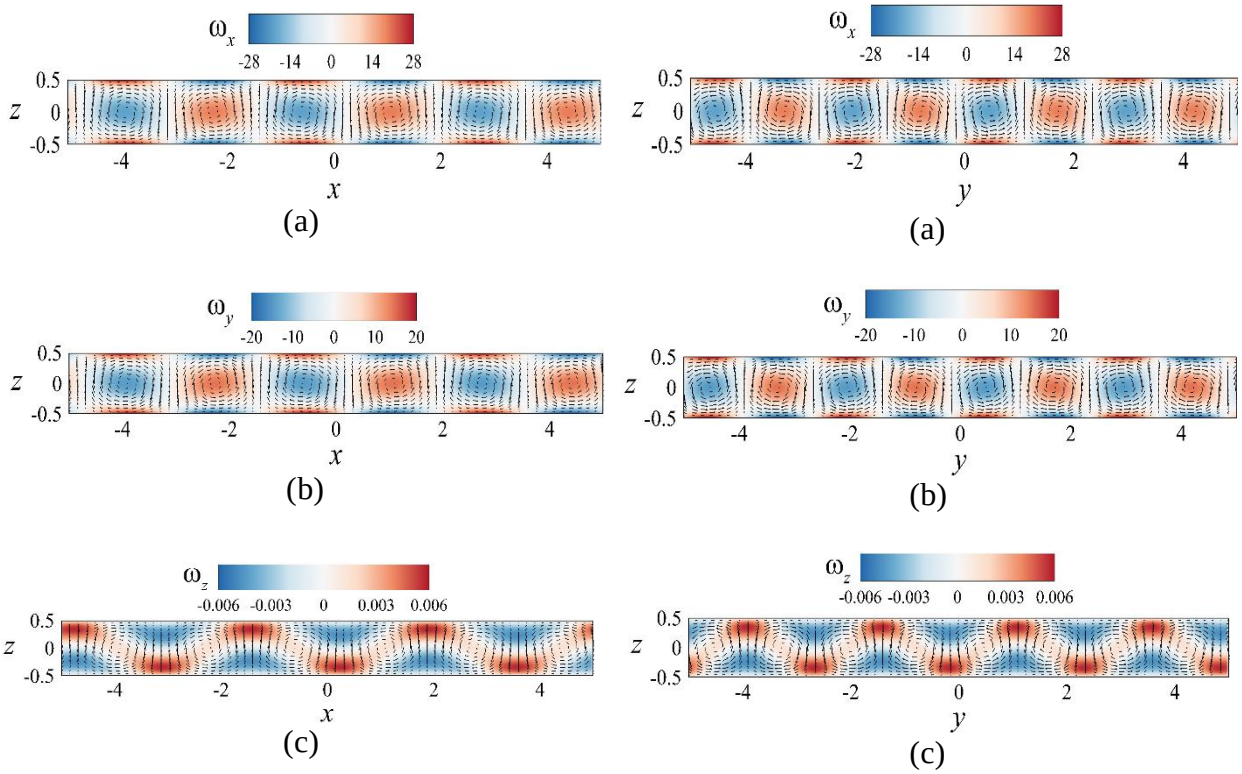

Figure 4.13: Vorticity components in the plane $y = 0$, and in the plane $x = 0$ for $Pr = 1$, $\gamma_e = 0.01$, $Ra = 0$ and $L = 2400$. Vectors represent the velocity fields: (a) and (b) horizontal vorticity components (color); and (c) vertical vorticity components (color).

When we increase the value of the electric Rayleigh number L, the straight rolls become deformed but remain stationary and then become time-dependent for a further increase of L. Figure 4.14 shows the instantaneous images of flow structures for $Ra = 0$ and $Pr = 1$ and different values of L. The convective patterns present some steady regimes with localized defects ($L \in \{3500; 5000\}$). The system of flow structures becomes time-dependent patterns for $L = 7000$ (periodic regime) and the disordered flow structures appear at $L = 10\,000$ as illustrated in Figure 4.15. The latter flow regime corresponds to the oscillatory spiral with defects and a zone of disordered rolls.

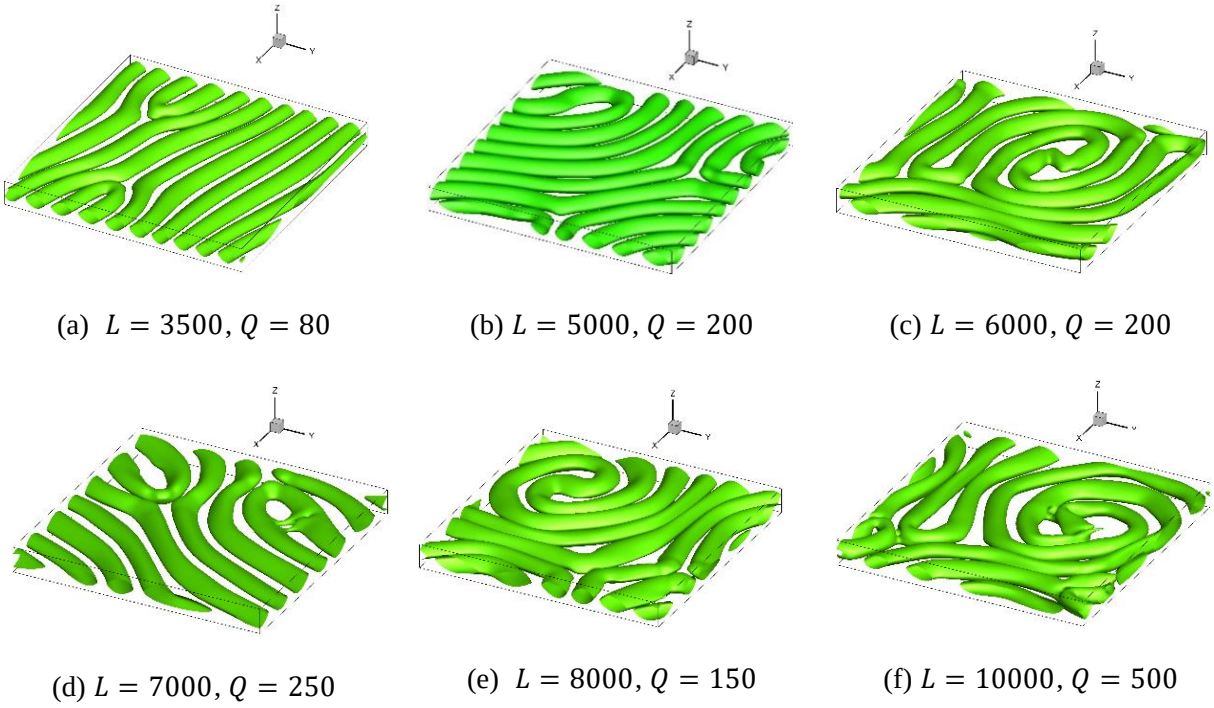

(a) $L = 3500, Q = 80$ (b) $L = 5000, Q = 200$ (c) $L = 6000, Q = 200$

(d) $L = 7000, Q = 250$ (e) $L = 8000, Q = 150$ (f) $L = 10000, Q = 500$

Figure 4.14: Instantaneous structures of isosurfaces of Q for $Pr = 1$ and different values of L under microgravity environment $Ra = 0$.

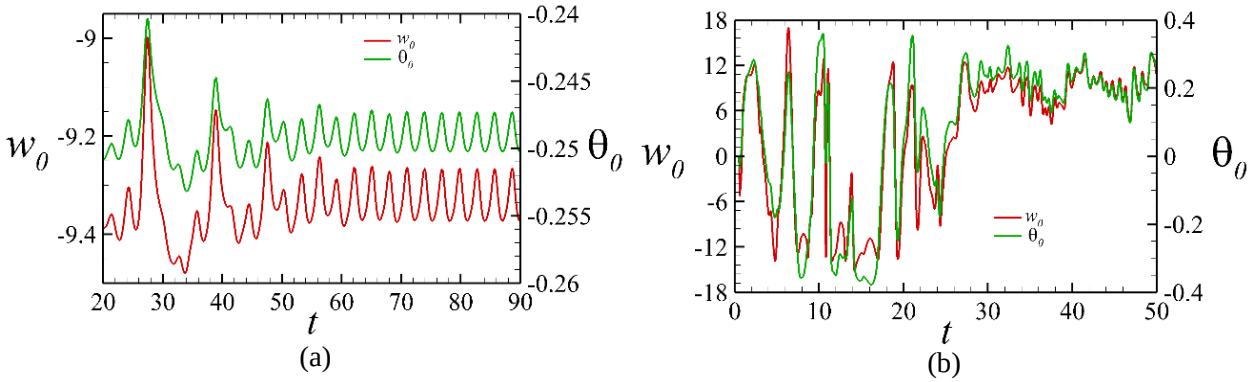

Figure 4.15: Time evolution of the vertical velocity w_0 and the temperature θ_0 at the cavity center $(x = y = z = 0)$ for $Ra = 0$, $Pr = 1$, $L = 7000$ (a) and $L = 10\,000$ (b).

Figure 4.16 shows the horizontal cross-sections of the instantaneous temperature distribution at the mid-gap $(z = 0)$ at different values of the electric Rayleigh number L. These snapshots (Figure 4.16) represent the convection patterns presented above in Figure 4.14.

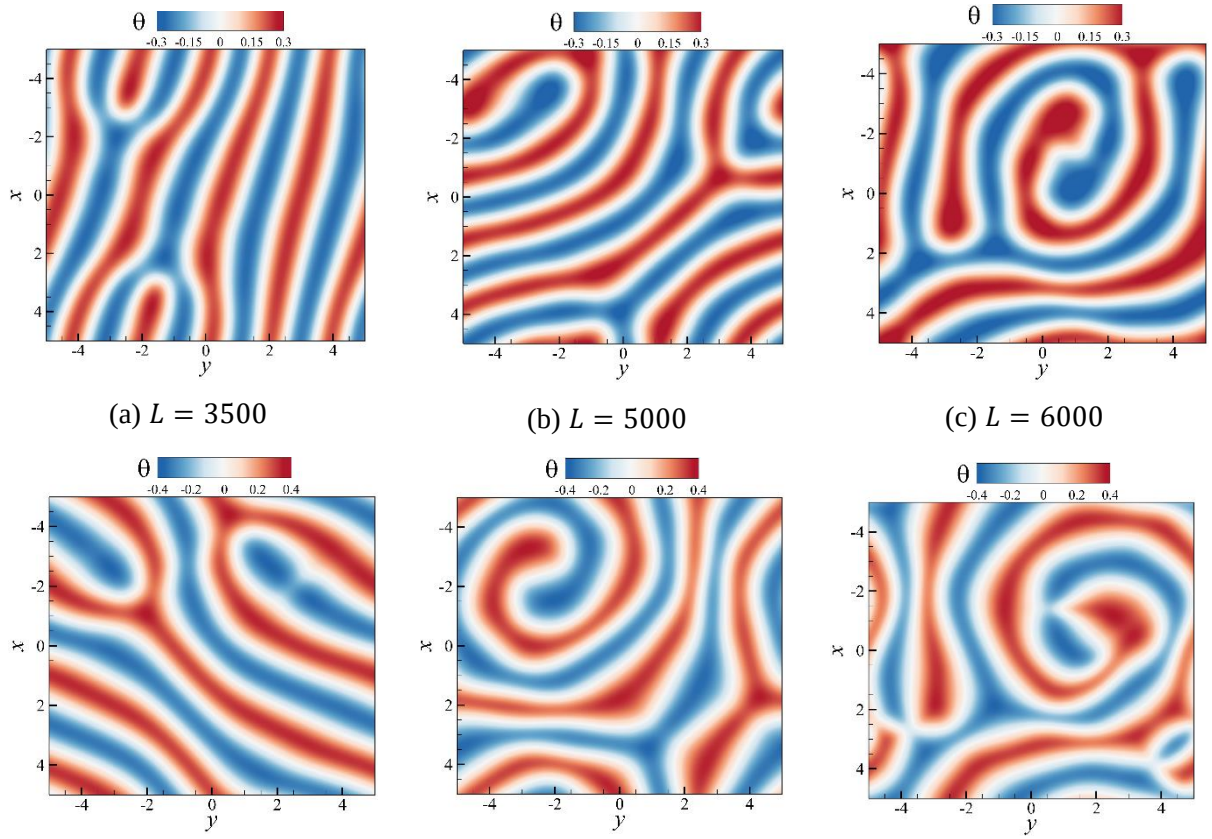

(a) $L = 3500$ (b) $L = 5000$ (c) $L = 6000$

(d) $L = 7000$ (e) $L = 8000$ (f) $L = 10\,000$

Figure 4.16: Screenshot of instantaneous thermo-convective flow in the horizontal $(x - y)$ plane at the mid-height $z = 0$ for $Ra = 0$, $\gamma_e = 0.01$, $Pr = 1$, and different values of the electric Rayleigh number $L > L_c$.

The coexistence of rolls and defects is characteristic of the classical Rayleigh-Bénard convection for $Pr \approx 1$ [35]. Figure 4.17 shows the deformation of isotherms of the convective regime in both vertical $(x - z)$ and $(y - z)$ planes at the mid-gap corresponding to $L = 10\,000$. The further increase of the electric Rayleigh number leads to the concentration of high perturbation electric potential at the central $z = 0$. The vorticity components of the perturbed flow for $L = 10\,000$ are shown in Figure 4.18.

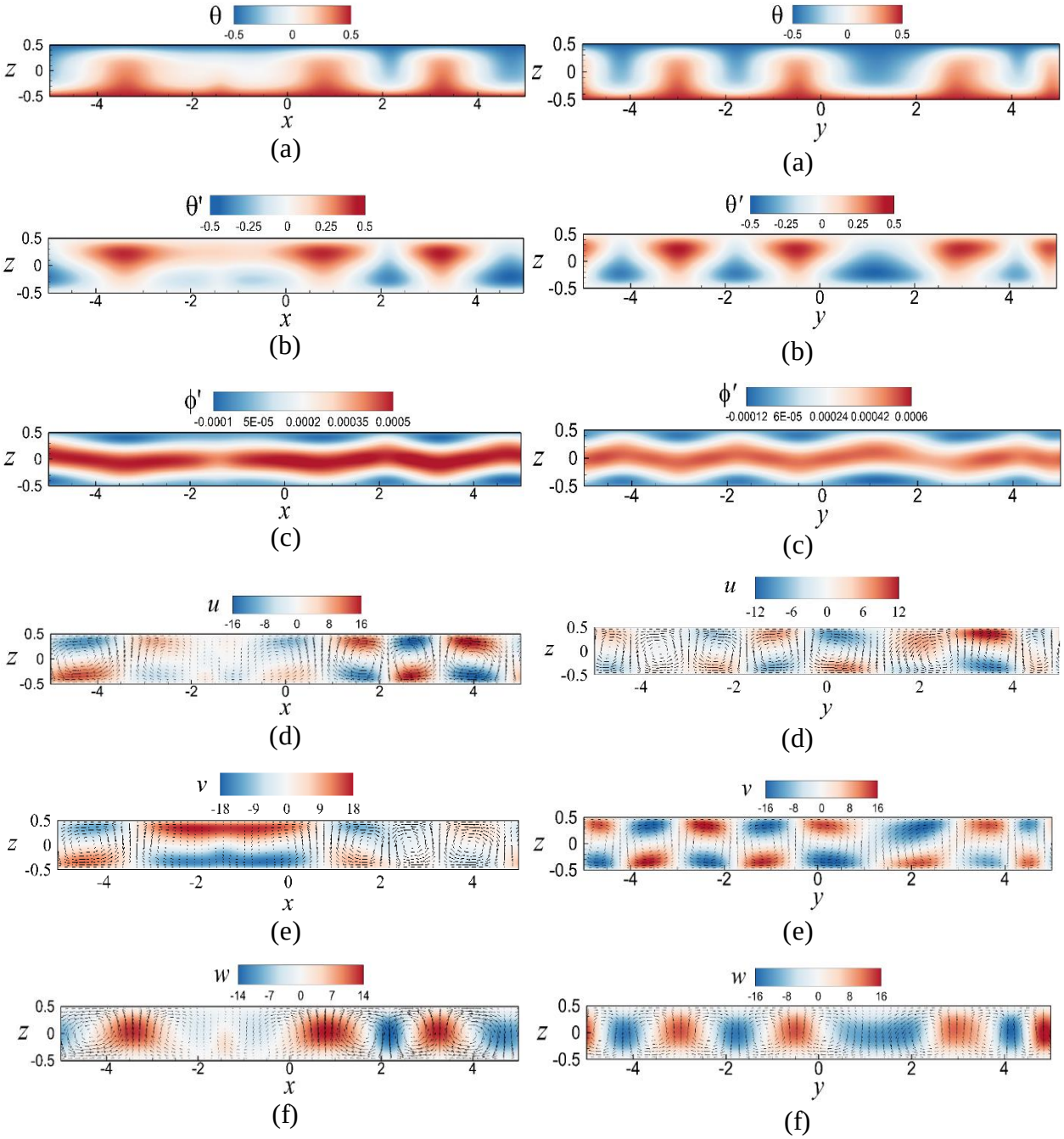

Figure 4.17: Instantaneous flow fields of the flow regime in the vertical planes for $Pr = 1$, $\gamma_e = 0.01$, $Ra = 0$ and $L = 10\,000$: (a) temperature distribution (color); (b) temperature perturbations; (c) electric potential perturbations; (d-e) horizontal velocity components u and v (color); and (f) vertical velocity component w (color). Vectors represent the velocity fields in (d-f) and snapshots are taken at $y = 0$ and $x = 0$.

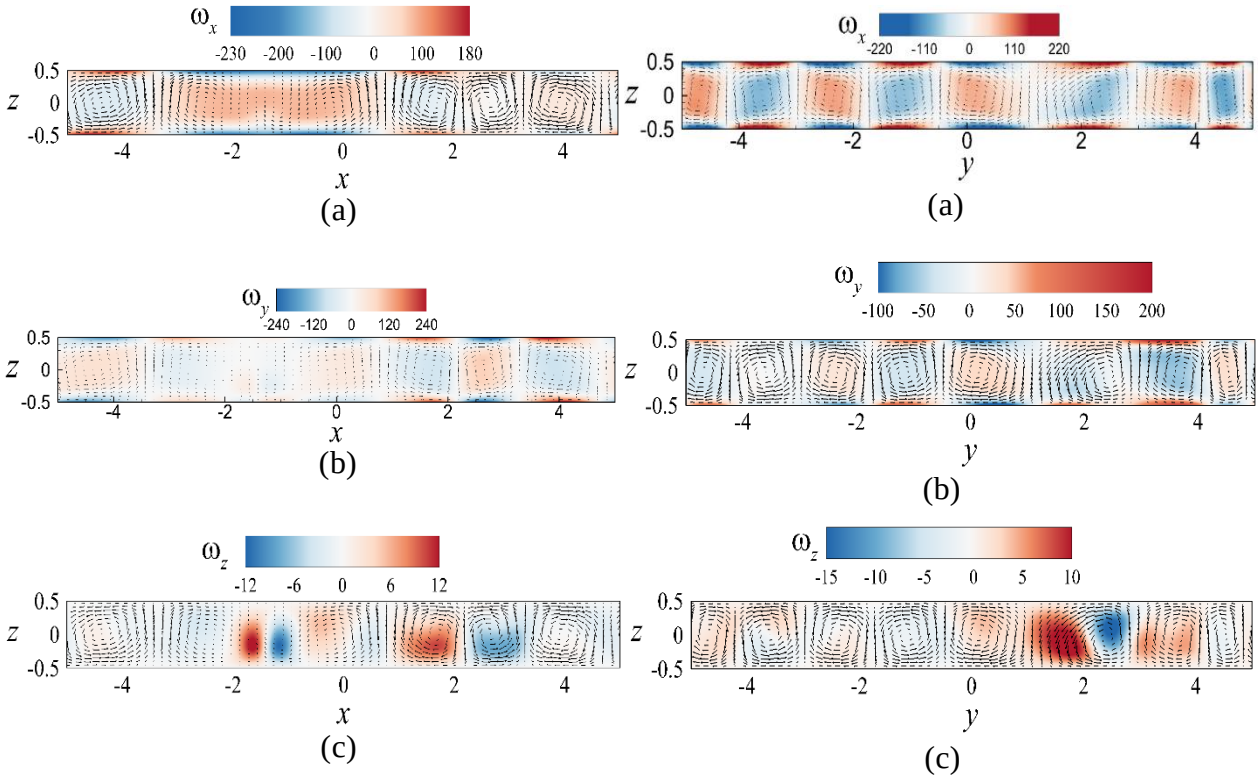

Figure 4.18: Vorticity components in the plane $y = 0$, and in the plane $x = 0$ for $Pr = 1$, $\gamma_e = 0.01$, $Ra = 0$ and $L = 10\,000$. Vectors represent the velocity fields: (a) and (b) horizontal vorticity components (color); and (c) vertical vorticity components (color).

4.5.2. Convective flow patterns under unstable stratification ($Ra > 0$)

When we apply low electric potential ($L < L_c(Ra)$) to a dielectric fluid layer heated from the bottom, the basic state is an unstable stratified state as long as the Rayleigh number Ra is lower than its critical value in the classical Rayleigh-Bénard problem ($Ra < Ra_c = 1708$). When $L \geq L_c(Ra)$, the effects of the electric buoyancy combined with the thermal buoyancy dominate the stabilizing viscous dissipation and thermal diffusion. Thus, counter-rotating thermo-convective cells occur in the cavity. Figure 4.19 shows the perturbed flow patterns for $Pr = 1$, $Ra = 500$ (i.e. the imposed temperature difference), and different values of L (i.e. increase in the electric voltage).

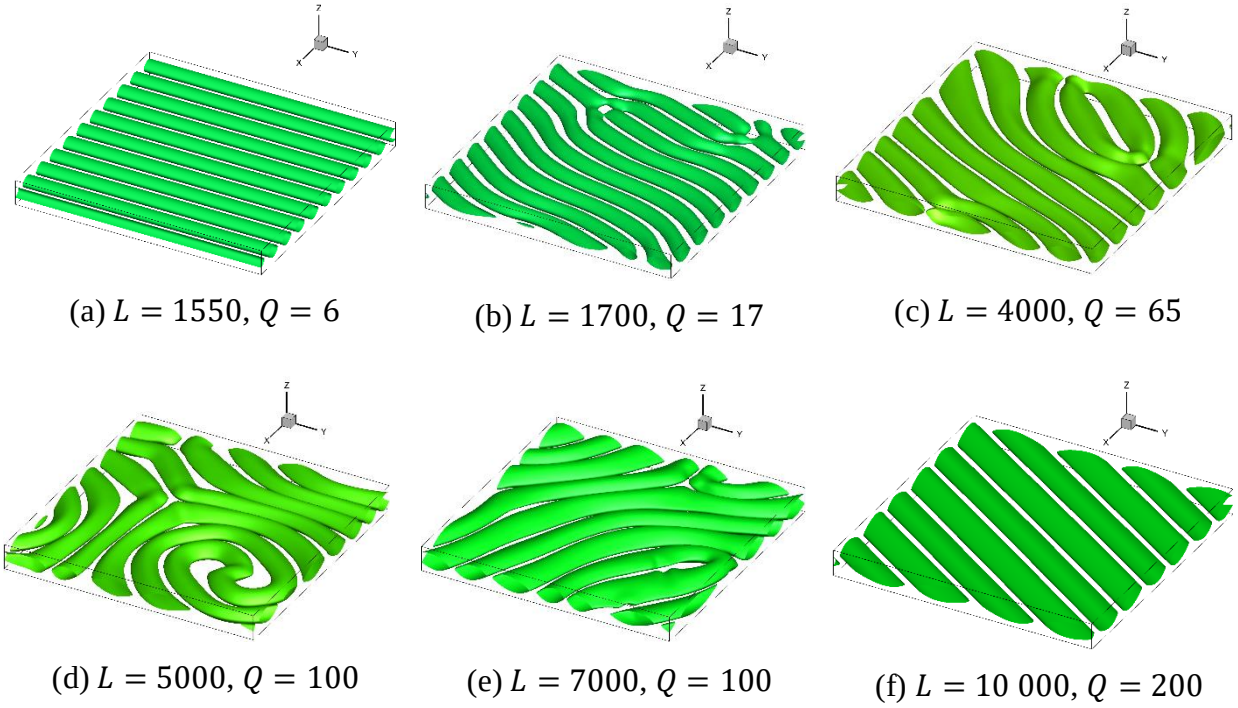

(a) $L = 1550$, $Q = 6$ (b) $L = 1700$, $Q = 17$ (c) $L = 4000$, $Q = 65$

(d) $L = 5000$, $Q = 100$ (e) $L = 7000$, $Q = 100$ (f) $L = 10\,000$, $Q = 200$

Figure 4.19: Instantaneous flow structures visualized by the isosurfaces of Q for $Pr = 1$, $Ra = 500$, and different values of L.

The thermo-convective structures, near the threshold, are aligned with the y-direction and have a wavenumber $k = 3.142$. The orientation of these rolls changes with the value of Ra. For example for $Ra = 1000$, the straight rolls are inclined in the $(x - y)$ horizontal plane ($k_x = 1.885$ and $k_y = 2.265$), but their total wavenumber remains unchanged ($k = 3.142$). As the value of L increases, the flow bifurcates to different complex regimes presenting many structures with defects

(Figure 4.19) similar to those observed in the Rayleigh-Bénard convection [35,78]. The spatio-temporal behavior of two regimes with dislocations is illustrated by the temperature distribution patterns presented in Figure 4.20-(a). These pictures are taken in the horizontal $(x-y)$ cross-section at the mid-height $z=0$. The time evolution of the vertical velocity and the temperature computed at the cavity center $(x=y=z=0)$ are presented in Figure 4.20-(b). One sees that the flow regime is steady for $L=1700$, while it bifurcates to an unsteady thermo-convective instability when $L=7000$.

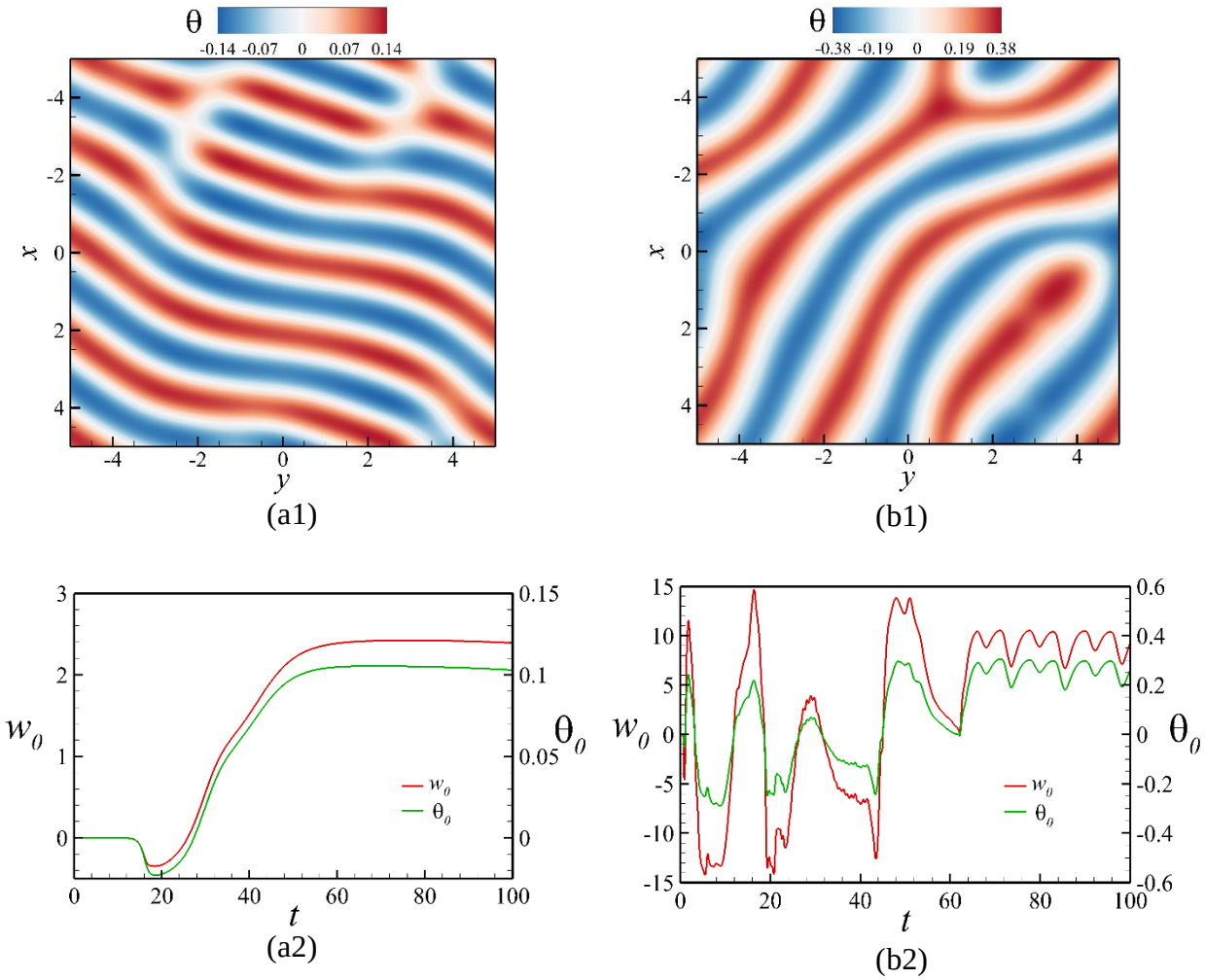

Figure 4.20: Isotherms of the flow regimes with defects in the $(x-y)$ plane and time variation of the vertical velocity w_0 and the temperature θ_0 at the cavity center $(x=y=z=0)$. Plots correspond to $Pr=1$, $Ra=500$ for (a) $L=1700$ and (b) $L=7000$.

For a better understanding of the flow regime with dislocations, the instantaneous flow fields, the temperature perturbation and the potential perturbation are presented in Figure 4.21 for $L=1700$.

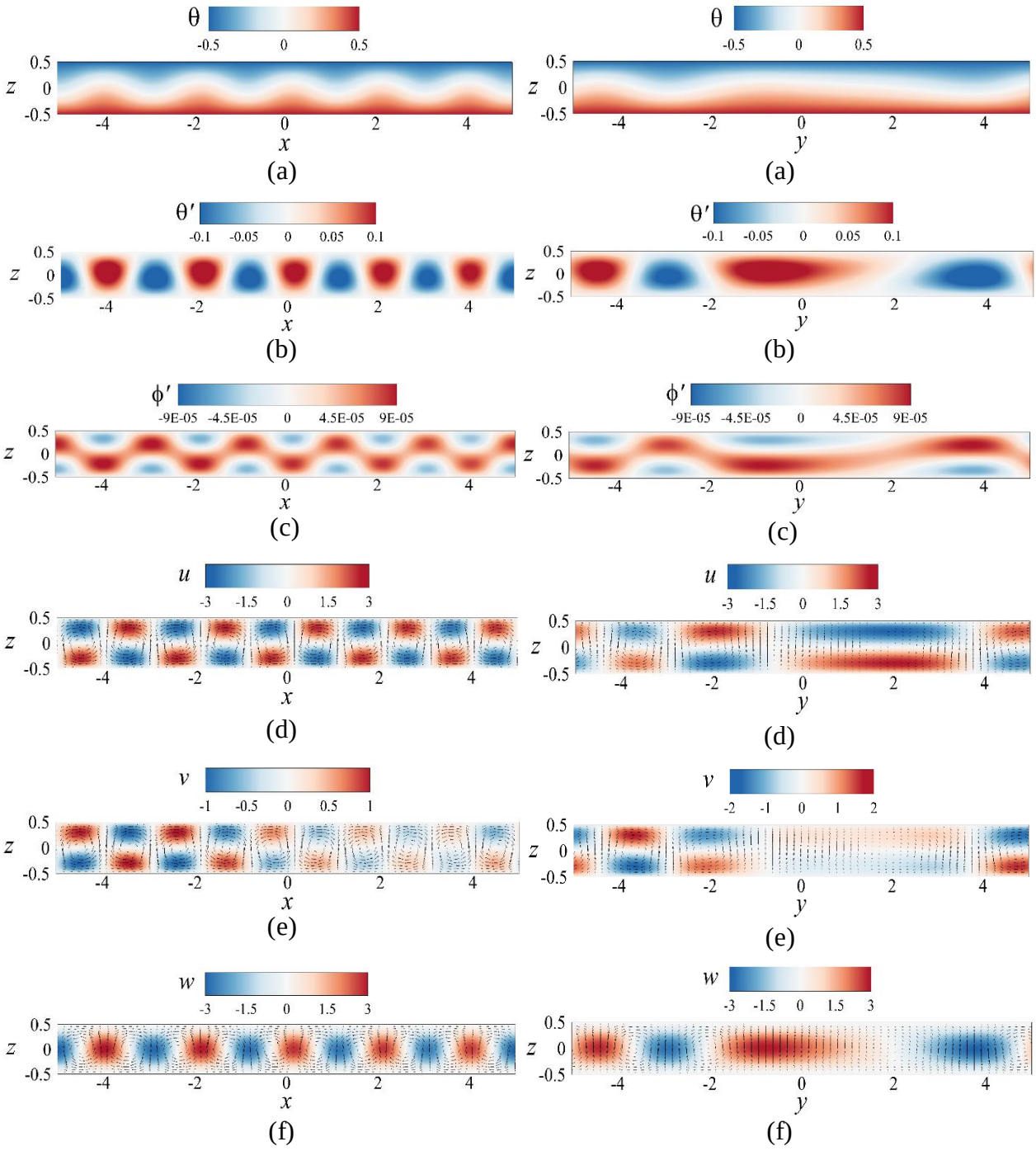

Figure 4.21: Instantaneous flow fields of the flow regime in the vertical planes for $Ra = 500$, $Pr = 1$, and $L = 1700$: (a) temperature distribution (color); (b) temperature perturbations; (c) electric potential perturbations; (d-e) horizontal velocity components u and v (color); and (f) vertical velocity component w (color). Vectors represent the velocity fields in (d-f).

The temperature distribution in both vertical planes are presented in Figure 4.21 (a) and the temperature and electric potential fluctuations are shown in Figure 4.21 (b) and (c). The temperature perturbations are located around the mid-height $z = 0$ for values of L near the threshold. Figure 4.22 shows the vorticity components in both vertical planes $y = 0$ and $x = 0$.

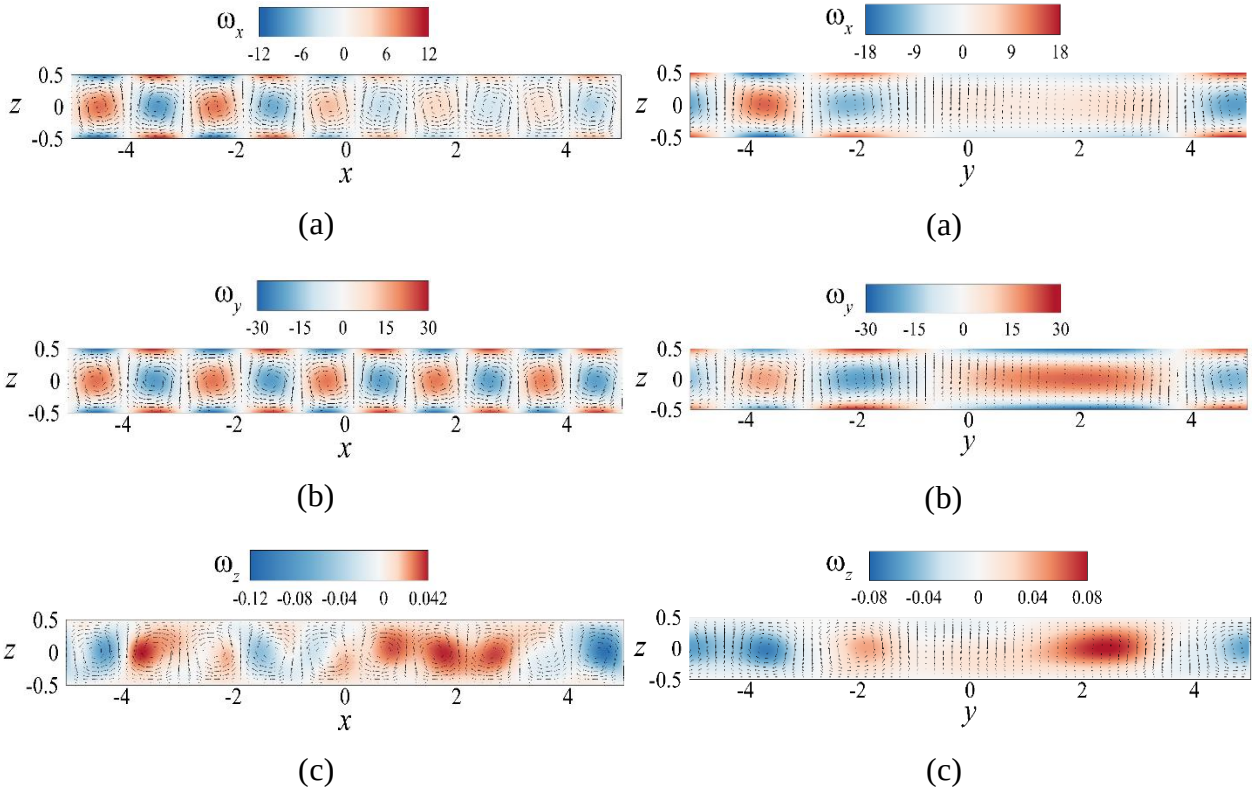

Figure 4.22: Vorticity components in the $(x - z)$ plane, and in the $(y - z)$ plane for $Pr = 1$, $Ra = 500$, and $L = 1700$. Vectors represent the velocity fields: (a) and (b) horizontal vorticity components (color); and (c) vertical vorticity components (color).

The instantaneous flow fields, the fluctuations in temperature and electric potential in the vertical cross-sections are presented in Figure 4.23 for $Ra = 500$ and $L = 7000$. Figure 4.23 (a) shows the considerable deformation of isotherms from those of previous steady thermo-convective regimes. One also sees that from Figure 4.23 (b), the temperature field perturbations predominates over the temperature field of the conductive base state when $L = 7000$. The vorticity components of this flow regime is presented in Figure 4.24.

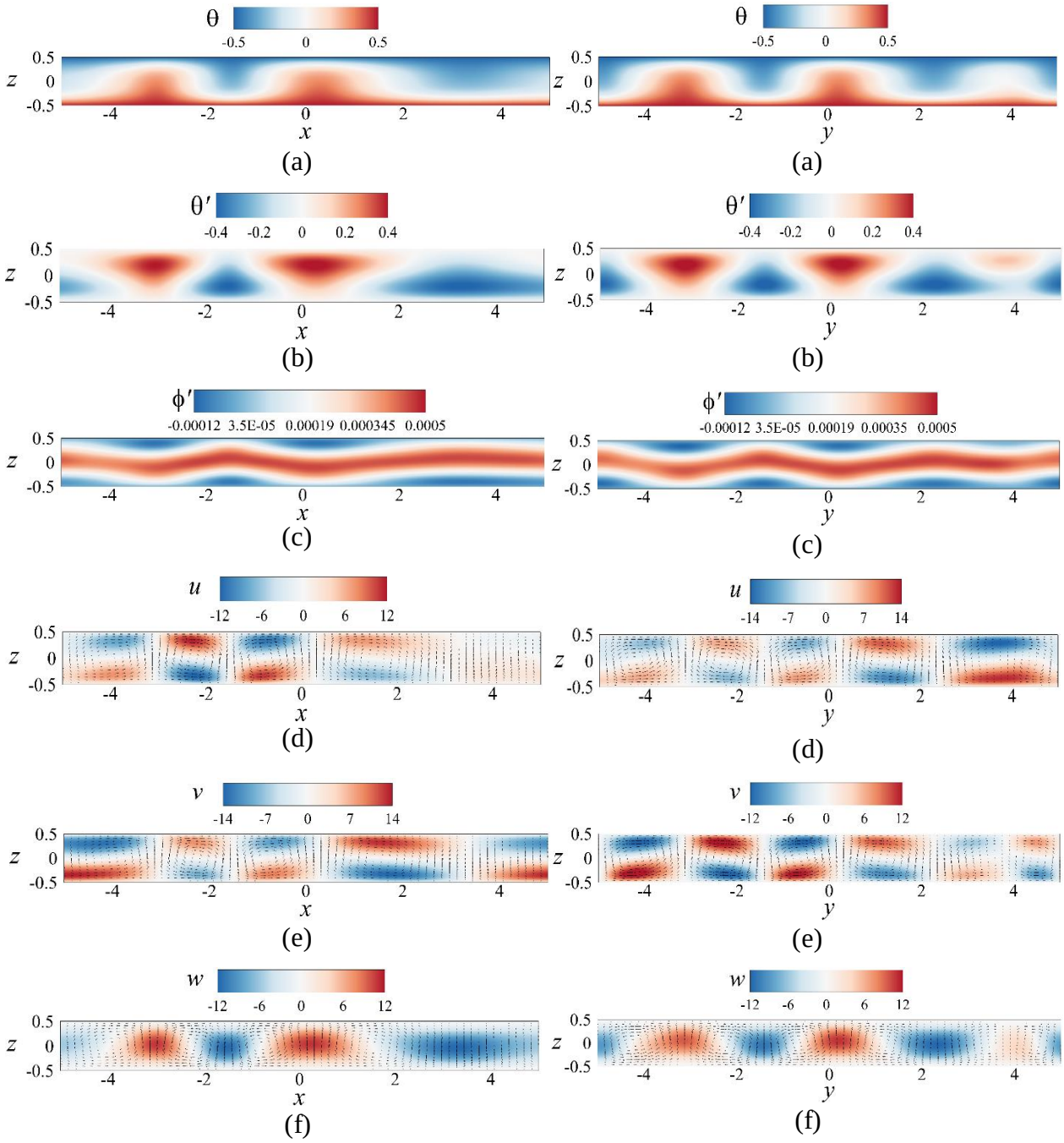

Figure 4.23: Instantaneous flow fields of the flow regime in the vertical planes for $Pr = 1$, $Ra = 500$, and $L = 7000$: (a) temperature distribution (color); (b) temperature perturbations; (c) electric potential perturbations; (d-e) horizontal velocity components u and v (color); and (f) vertical velocity component w (color). Vectors represent the velocity fields in (d-f).

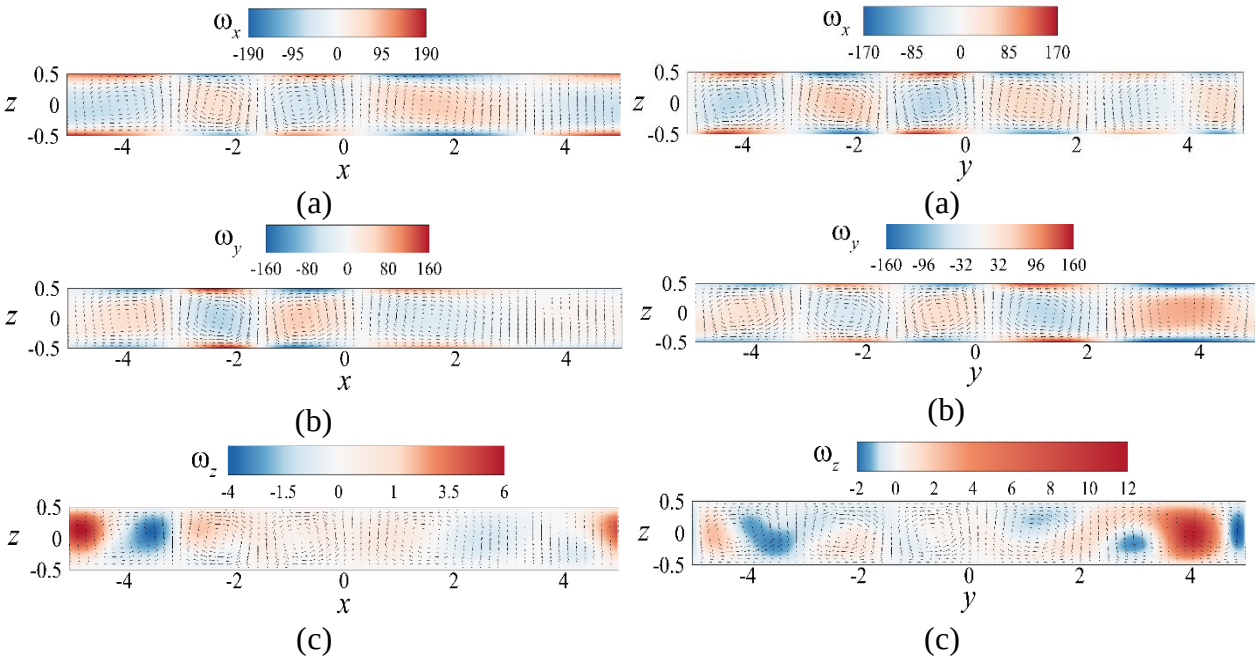

Figure 4.24: Vorticity components in the $(x-z)$ plane, and in the $(x-z)$ plane for, $Pr = 1$, $Ra = 500$, and $L = 7000$. Vectors represent the velocity fields: (a) and (b) horizontal vorticity components (color); and (c) vertical vorticity components (color).

The oscillatory flow is also present when we increase the Rayleigh number Ra i.e. the imposed temperature difference. When $Ra = 1000$, the thermoelectric convection set on with steady straight rolls which persist until $L = 1500$ ($L_c \approx 883$); then the flow bifurcates to stationary regimes with dislocations for $L\,\epsilon[2000:3500]$. The time-dependent thermo-convective structures appear at $L = 4000$, while the flow becomes again stationary with dislocations for $L = 4500$ and straight rolls at $L = 5000$. We have observed the oscillatory thermo-convective instability for values of the electric Rayleigh number lying in the range $L\,\epsilon[6000:9000]$; except for $L = 7000$ where the corresponding regime presents structures with defects.

For $Ra = 500$ and $Ra = 1000$, after the time-dependant regimes, the flow converges to a steady rolls regime when $L = 10\,000$ as shown in Figure 4.19-f. The size of these stationary thermo-convective rolls is larger than the size of rolls obtained in the neighborhood of the threshold ($L = L_c$). The corresponding wavenumbers of the patterns are $k_x = 1.885$ and $k_y = 1.257$; this confers a total wavenumber $k = 2.265$. Flow patterns of the corresponding steady regime can be observed on the isotherms deformation in the $(x-z)$ and $(y-z)$ vertical planes (Figure 4.25-(a)).

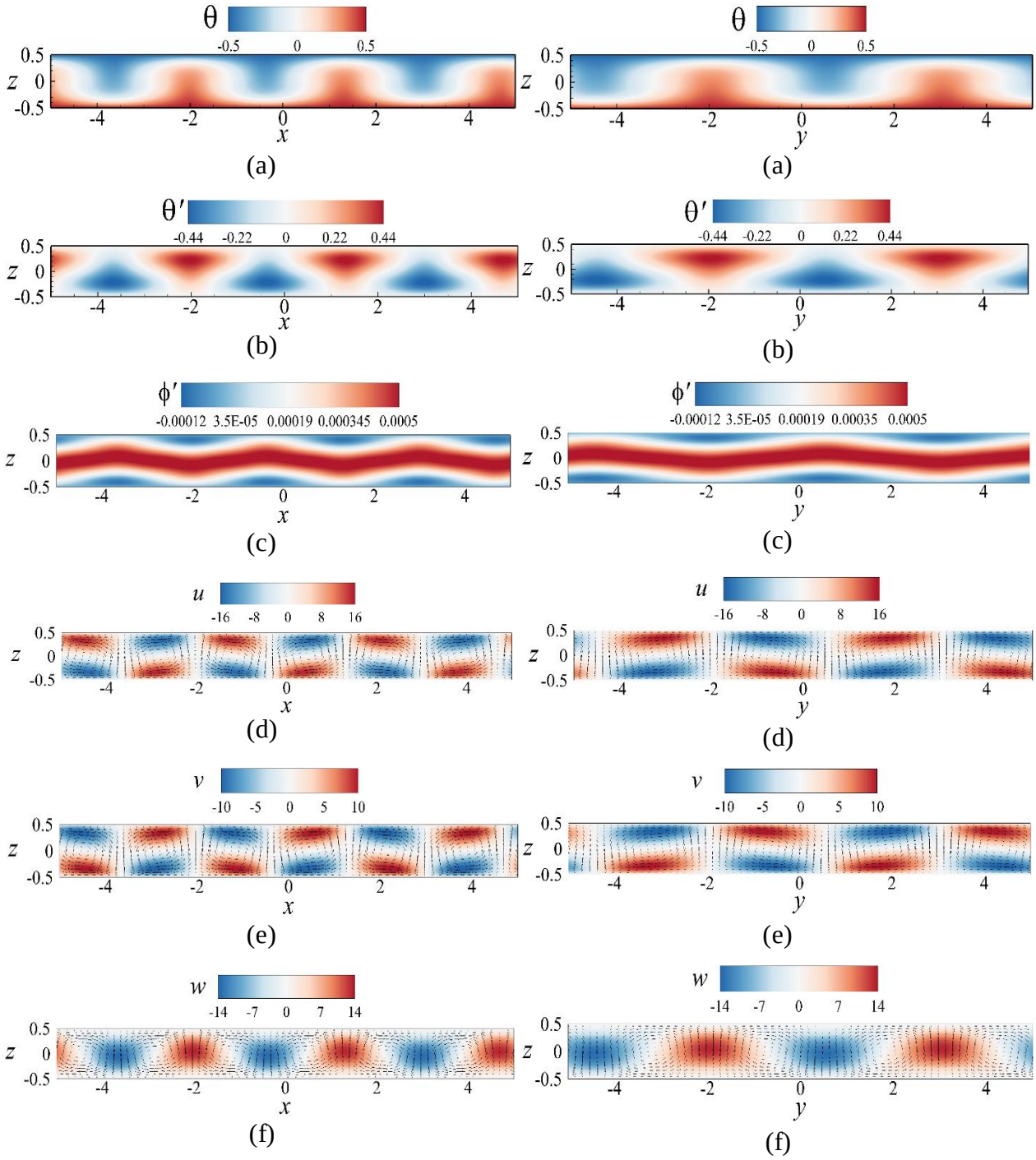

Figure 4.25: Instantaneous flow fields of the flow regime in the vertical planes for $Pr = 1$, $Ra = 500$ and $L = 10\,000$: (a) temperature distribution (color); (b) temperature perturbations; (c) electric potential perturbations; (d-e) horizontal velocity components u and v (color); and (f) vertical velocity component w (color). Vectors represent the velocity fields in (d-f).

Figure 4.25 shows that when $L = 10\,000$, thermo-convective rolls instability is characterized by the occurrence of thermal plumes which correspond to the detachment of the thermal boundary layer from the hot surface. The snapshots of the flow fields, presented in Figure 4.25, were taken in the vertical $(x - z)$ and $(y - z)$ cross-sections at, respectively, $y = 0$ and $x = 0$. Although the thermo-convective structures are characterized by straight rolls for values of L around the threshold and $L = 10\,000$, the isotherms are considerably different (Figure 4.21 and Figure 4.25). Figure 4.26 shows the vorticity components for $Pr = 1$, $Ra = 500$, and $L = 10\,000$.

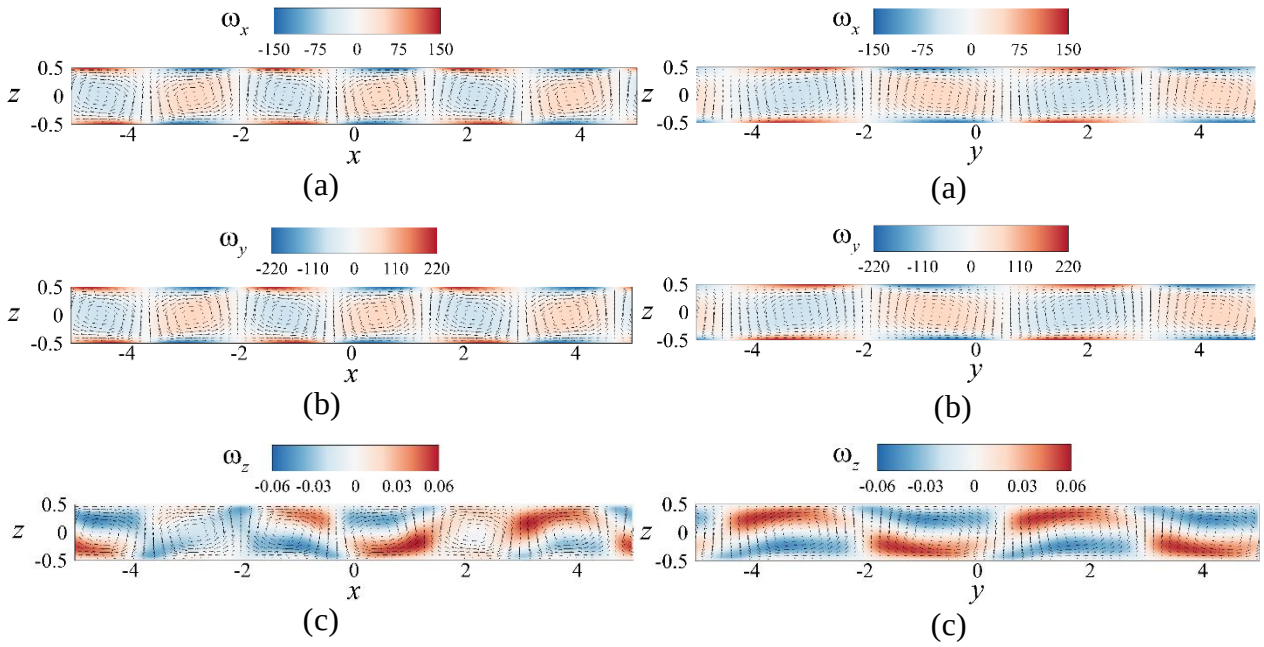

Figure 4.26: Vorticity components in the $(x - z)$ plane, and in the $(x - z)$ plane for $Pr = 1$, $Ra = 500$, and $L = 10\,000$. Vectors represent the velocity fields: (a) and (b) horizontal vorticity components (color); and (c) vertical vorticity components (color).

4.5.3. Convective flow patterns under stable stratification ($Ra < 0$)

When $Ra < 0$, thermal convection is set on trough stationary convective rolls when $L = L_c(Ra)$. For increasing values of $L \geq L_c(Ra)$, the obtained vortical structures are presented in Figure 4.27. The flow regimes around the threshold consist of stationary straight rolls as in the case of $Ra = 0$ and $Ra > 0$ as shown in Figure 4.27 (a). While increasing the value of L, a variety of complex convective patterns develop inside the dielectric fluid layer. Figure 4.27 (b) and (c) show some convective regimes generated by the dielectrophoretic force for $Ra = -500$ and moderate

values of L. One sees that the flow in the rectangular cavity bifurcates to thermo-convective flow structures with dislocations. The further increase of L leads to stationary straight rolls at $L = 7500$ and to a spiral defect regime from $L = 8\,000$.

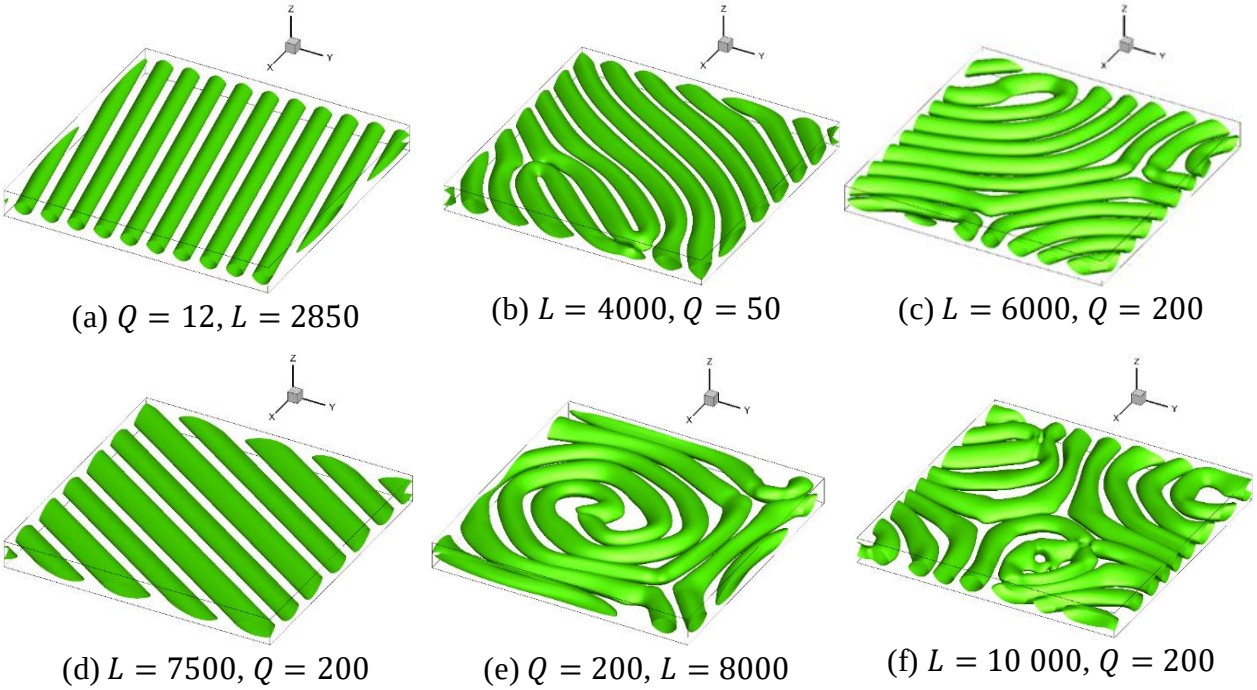

(a) $Q = 12, L = 2850$ (b) $L = 4000, Q = 50$ (c) $L = 6000, Q = 200$

(d) $L = 7500, Q = 200$ (e) $Q = 200, L = 8000$ (f) $L = 10\,000, Q = 200$

Figure 4.27: Instantaneous structures vortices visualized by the isosurfaces of Q for $Pr = 1$, $Ra = -500$ and different values of L.

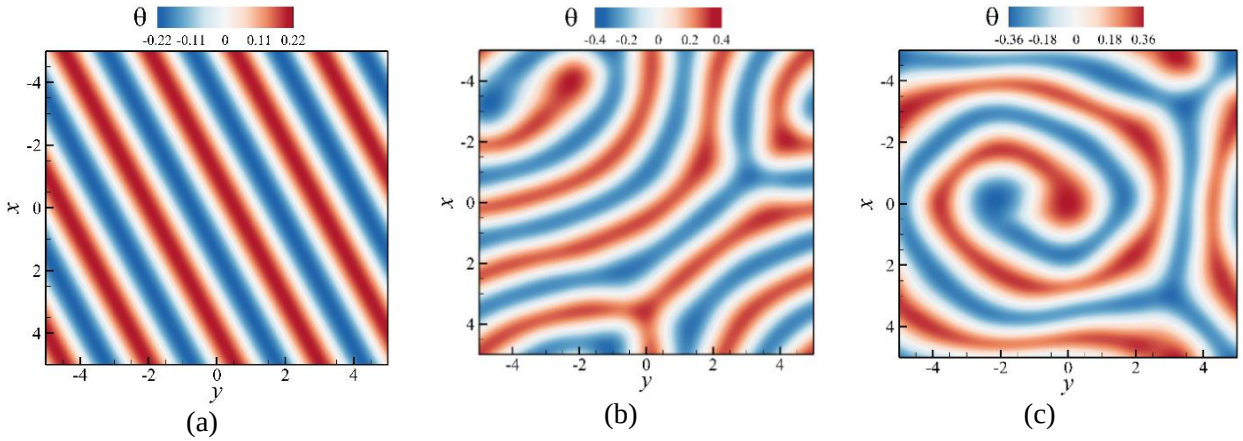

(a) (b) (c)

Figure 4.28: Temperature distribution of the flow regimes in the horizontal plane $z = 0$ for $Pr = 1$, $Ra = -500$, and different values of L: (a) $L = 2850$, (b) $L = 6000$ and (c) $L = 8000$.

Figure 4.28 shows the snapshots of temperature distributions in the horizontal $(x-y)$ plane for three different flow regimes. These flow regimes are chosen to analyze the behavior of the temperature of the uniform steady flow ($L = 2850$), the non-uniform steady flow ($L = 6000$) and the time-dependent flow regime ($L = 8000$).

For $L = 6000$, the saturated flow becomes stationary after a few computational times. The temporal evolution of the vertical velocity w_0 and the temperature θ_0, both taken at the center of the cavity, are presented in Figure 4.29 for (a) $L = 6000$ and (b) $L = 10\,000$. One sees that the flow regime at $L = 6000$ reaches a saturated state while the system does not saturate for $L = 10\,000$ in the range of the considered computational time.

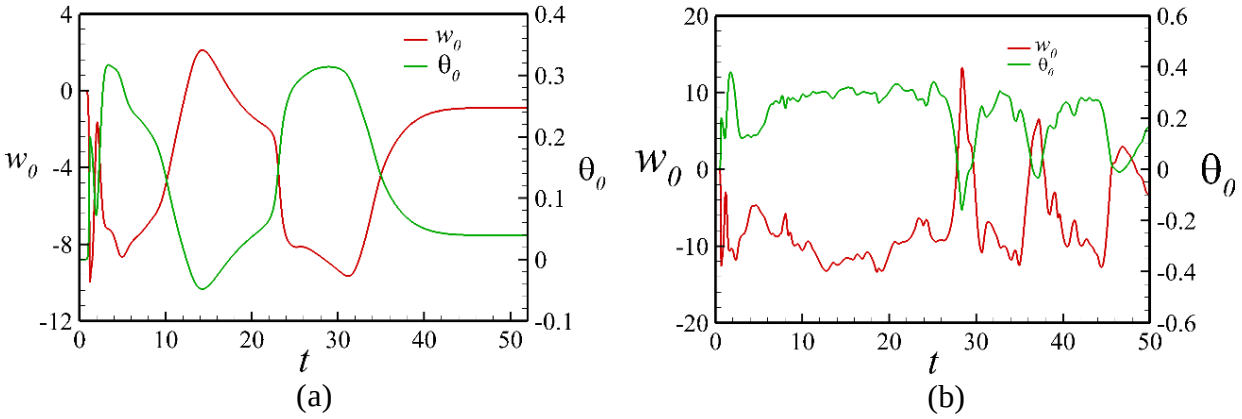

Figure 4.29: Time evolution of the vertical velocity w_0 and temperature θ_0 at the center of the cavity for $Pr = 1$, $Ra = -500$ and (a) $L = 6000$; (b) $L = 10\,000$.

The non-uniform unsteady flow regimes observed for $L \geq 8000$ present spiral defects with complex spatio-temporal dynamics as in the case of microgravity conditions ($Ra = 0$) and a system heated from below ($Ra = 500$) for $Pr = 1$ (Figure 4.27 (e)). The global movements of these spiral regimes are illustrated in Figure 4.29 (b).

The instantaneous flow fields captured in vertical cross-sections are presented in Figure 4.30 for $Ra = -500$ and $L = 6000$. A qualitative view of the temperature distribution is shown in Figure 4.29 (a), and the fluctuations in temperature and in electric potential are illustrated in Figure 4.30 (b) and (c). The vorticity components of this steady flow regime are shown in Figure 4.31.

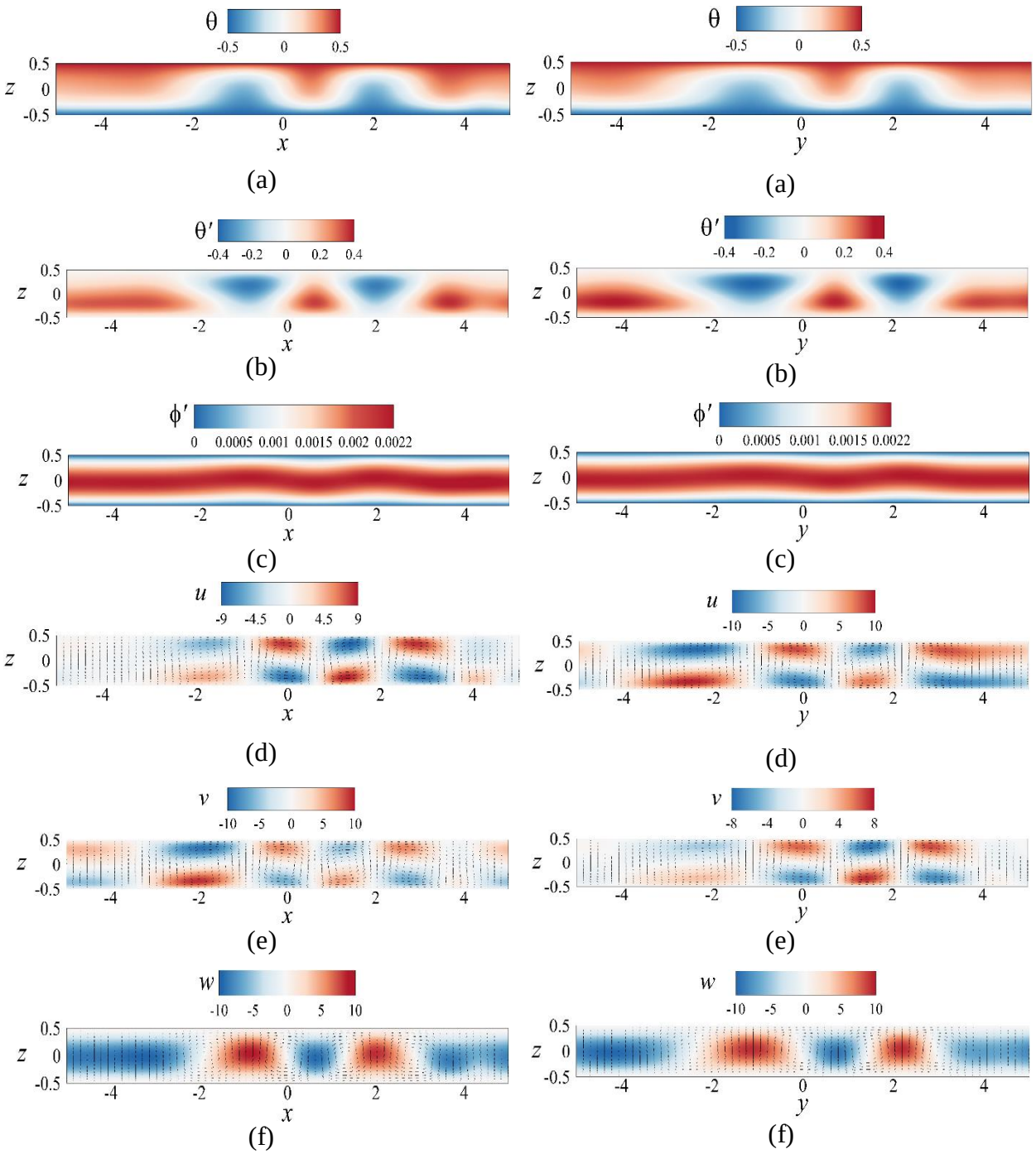

Figure 4.30: Instantaneous flow fields of the flow regime in the vertical planes for $Pr = 1$, $Ra = -500$ and $L = 6000$: (a) temperature distribution (color); (b) temperature perturbations; (c) electric potential perturbations; (d-e) horizontal velocity components u and v (color); and (f) vertical velocity component w (color). Vectors represent the velocity fields in (d-f).

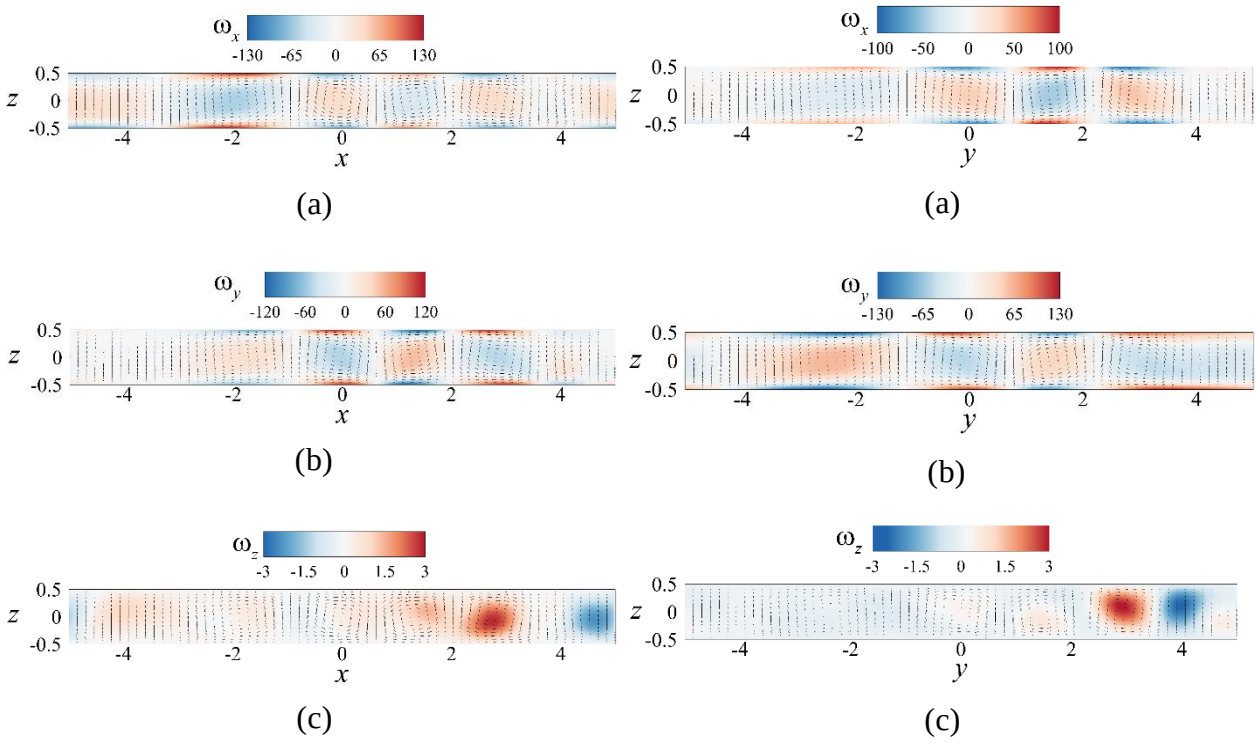

Figure 4.31: Vorticity components in the plane $y = 0$, and in the plane $x = 0$ for $Pr = 1$, $Ra = -500$, and $L = 6000$. Vectors represent the velocity fields: (a) and (b) horizontal vorticity components (color); and (c) vertical vorticity components (color).

The instantaneous flow fields and vorticity components of the time-dependent thermoelectric convection regime are presented in Figure 4.32 and Figure 4.33 for $Ra = -500$ and $L = 10\,000$. A diagram of the different thermo-convective flow regimes obtained in the horizontal rectangular cavity is shown in Figure 4.34 for $Pr = 1$. This sketch highlights the scenario of bifurcations that occurs in a system heated from the bottom ($Ra = 500$), from the top ($Ra = -500$), and under microgravity conditions ($Ra = 0$). In the value range of L under study, the sketch of the flow behaviors presents more bifurcation scenarios for $Ra = 0$. The flow regimes range from the stationary convective rolls ($L_c = 2128$) to the oscillating convective spiral defects ($L = 10\,000$). We observe that the flow in the rectangular cavity bifurcates towards a stationary rolls regime after the appearance of dislocations for all values of Ra. When $Ra = 0$, the reappearance of convective rolls without defects is observed for $L = 4000$, $L = 7000$ for $Ra = -500$, and $L = 10\,000$ for $Ra = 500$.

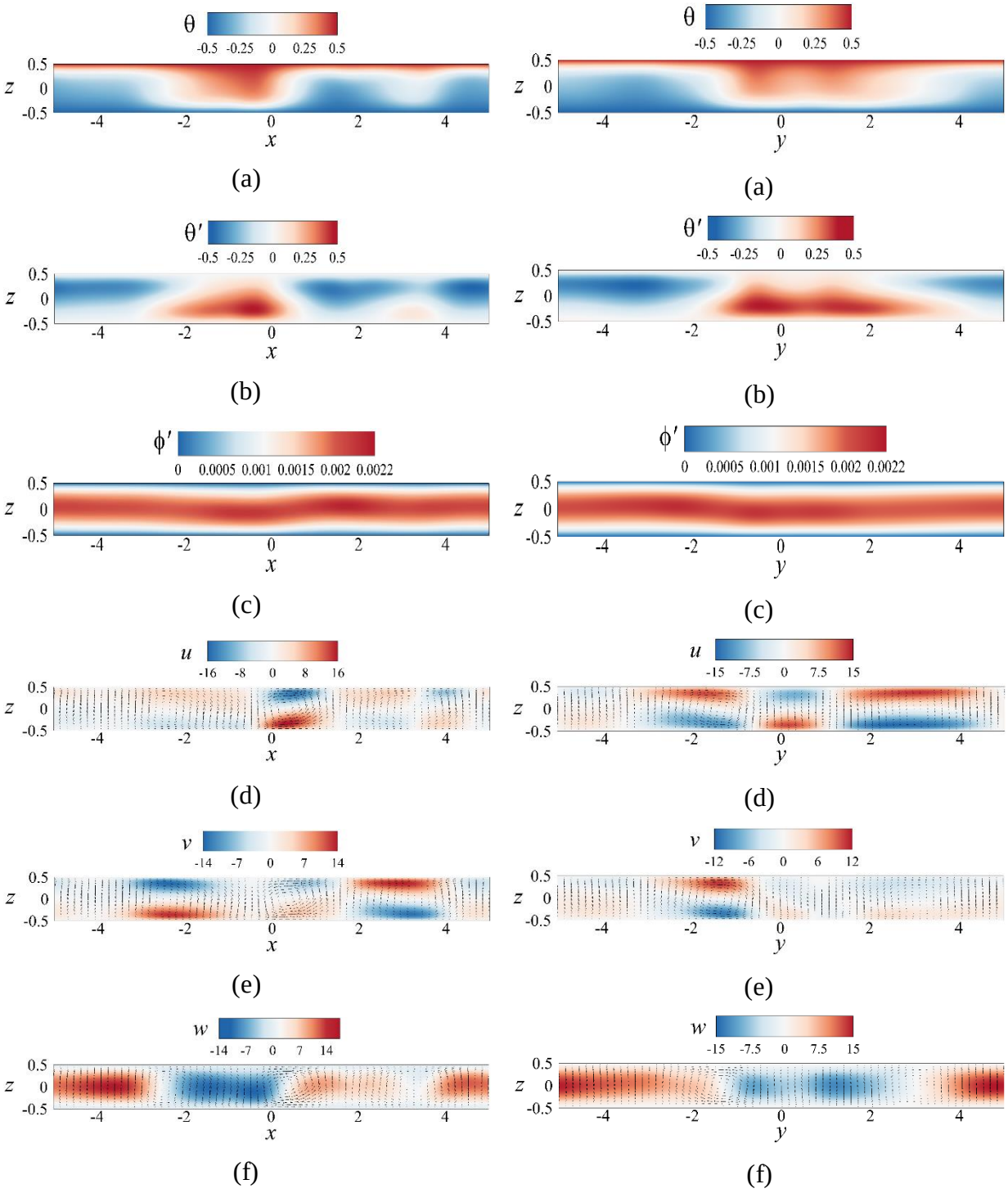

Figure 4.32: Instantaneous flow fields of the flow regime in the vertical planes for $Pr = 1$, $Ra = -500$ and $L = 10\ 000$: (a) temperature distribution (color); (b) temperature perturbations; (c) electric potential perturbations; (d-e) horizontal velocity components u and v (color); and (f) vertical velocity component w (color). Vectors represent the velocity fields in (d-f).

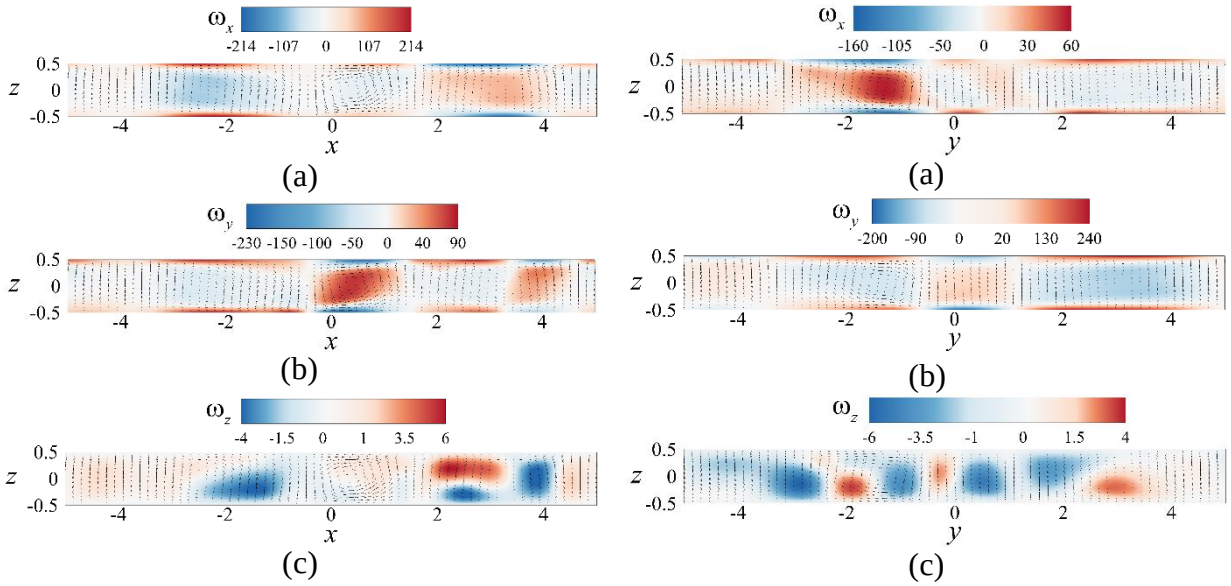

Figure 4.33: Vorticity components in the plane $y = 0$, and in the plane $x = 0$ for $Pr = 1$, $Ra = -500$, and $L = 10\,000$. Vectors represent the velocity fields: (a) and (b) horizontal vorticity components (color); and (c) vertical vorticity components (color).

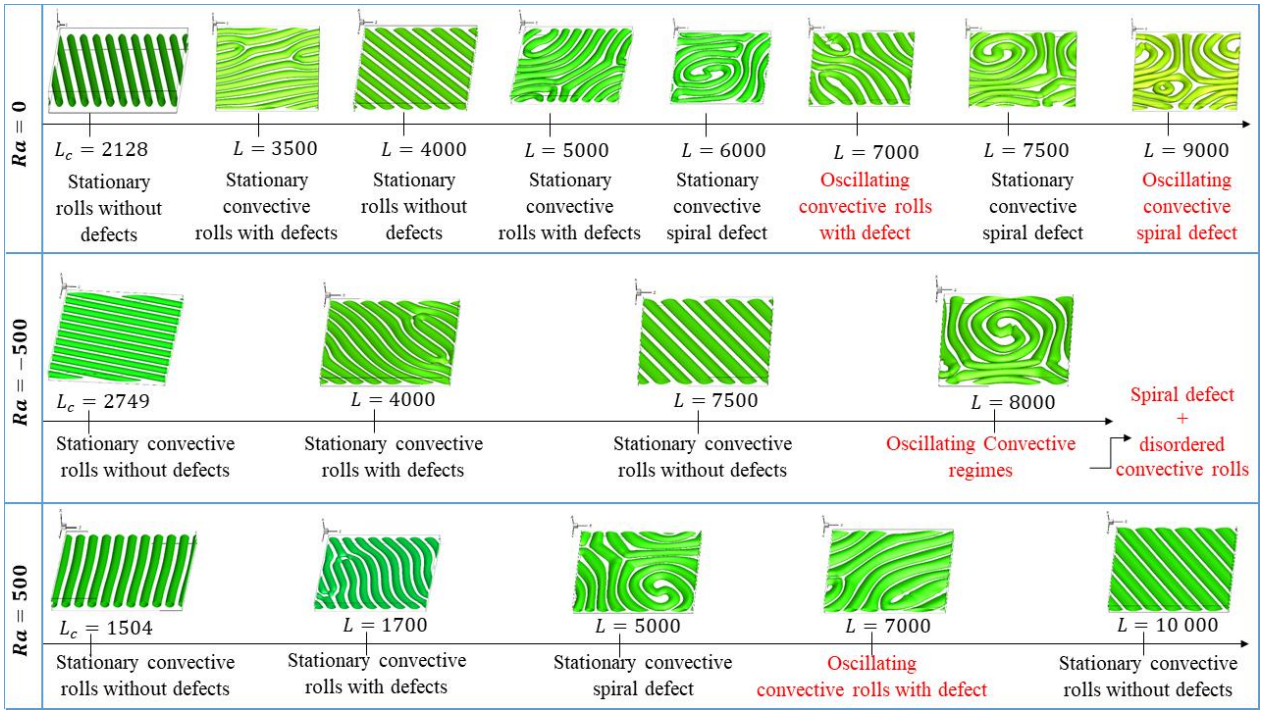

Figure 4.34: State diagram of the transitions for $Pr = 1$, $Ra \in \{-500, 0, 500\}$ and different increasing values of L.

4.6. Flow regimes for $Pr = 65$

4.6.1. Convective flow patterns under microgravity conditions ($Ra = 0$)

We have seen from the linear stability analysis that the first regime of thermoelectric convection consists of stationary convective rolls independently of the Prandtl number Pr. This has been confirmed by the patterns obtained by DNS around the critical point for $Pr = 65$ (Figure 4.35 and Figure 4.36). Sometime after launching computations with random noise, we can observe, from Figure 4.35 (a), that the amplitude of convection increases with time. The graph of $|A|$ present a zone of an exponential growth with time. By increasing the time, nonlinearities lead to the saturation of the system. The amplitude of the flow then converges to a constant value as shown in Figure 4.35 (a). Besides the graph of the amplitude A, Figure 4.35 (b) illustrates the saturation of the temperature and the vertical component of the velocity at the center of the cavity ($x = y = z = 0$). As for $Pr = 1$, in their saturated state, perturbations organize in form of stationary rolls (Figure 4.36).

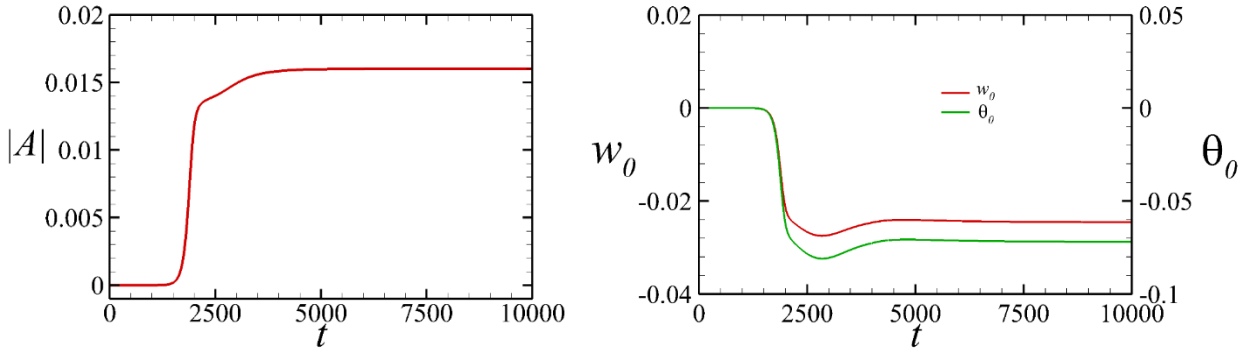

(a) (b)

Figure 4.35: Time evolution of the (a) amplitude of averaged vertical velocity $|A|$ at the mid-gap $z = 0$; (b) vertical velocity w_0 and temperature θ_0 at the center of the rectangular cavity for $Pr = 65$ and $L = 2200$ ($\delta = 0.032$). Amplitudes and time are, respectively, normalized by the viscous velocity ν/d and the viscous time d^2/ν.

Figure 4.36 shows the instantaneous rolls (a) and the temperature field θ determined at the mid-height $(z = 0)$ for $L = 2200$, and $Pr = 65$. Near the threshold, these thermo-convective patterns are independent of Pr. Just above the threshold, the vortices are periodic in both horizontal directions. The values of the corresponding wavenumbers are $k_x = 0.628$ and $k_y = 3$. The number of vortices is $N_x = L_x k_x/\pi = 2$, $N_y = L_y k_y/\pi = 10$. The total wavenumber is $k = \sqrt{k_x^2 + k_y^2} = 3.204$ which is close to the critical value obtained by the LSA ($k_c = 3.228$). This wavenumber is the same as that obtained for $Pr = 1$ and the inclination angle of rolls remains unchanged. This confirms that the nature of the dielectrophoretic instability is independent of the Pr.

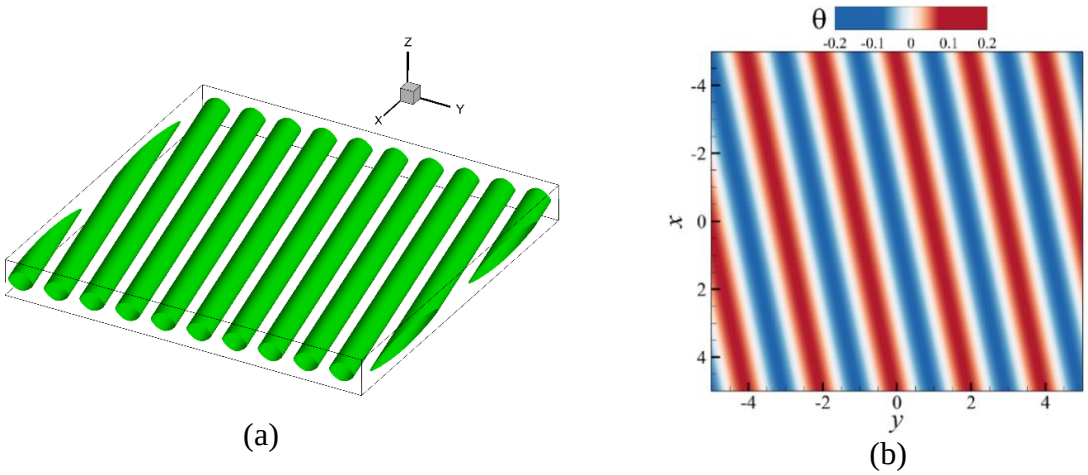

(a) (b)

Figure 4.36: Instantaneous flow field for $Ra = 0$, $Pr = 65$ and $L = 2200 > L_c$: (a) vortical structures of $Q = 0.008$, (b) temperature field levels. The temperature distribution is plotted at the mid-height $(z = 0)$ of the cavity.

Figure 4.37 shows the instantaneous flow fields, the temperature distribution, and the vorticity components of saturated stationary thermo-convective flow induced by the dielectrophoretic force in the $(x - z)$ and $(y - z)$ vertical planes. The deformation of the electric potential levels is presented in Figure 4.37 (b) for $Ra = 0$ and $L = 2200$. The corresponding vorticity components are shown in Figure 4.38.

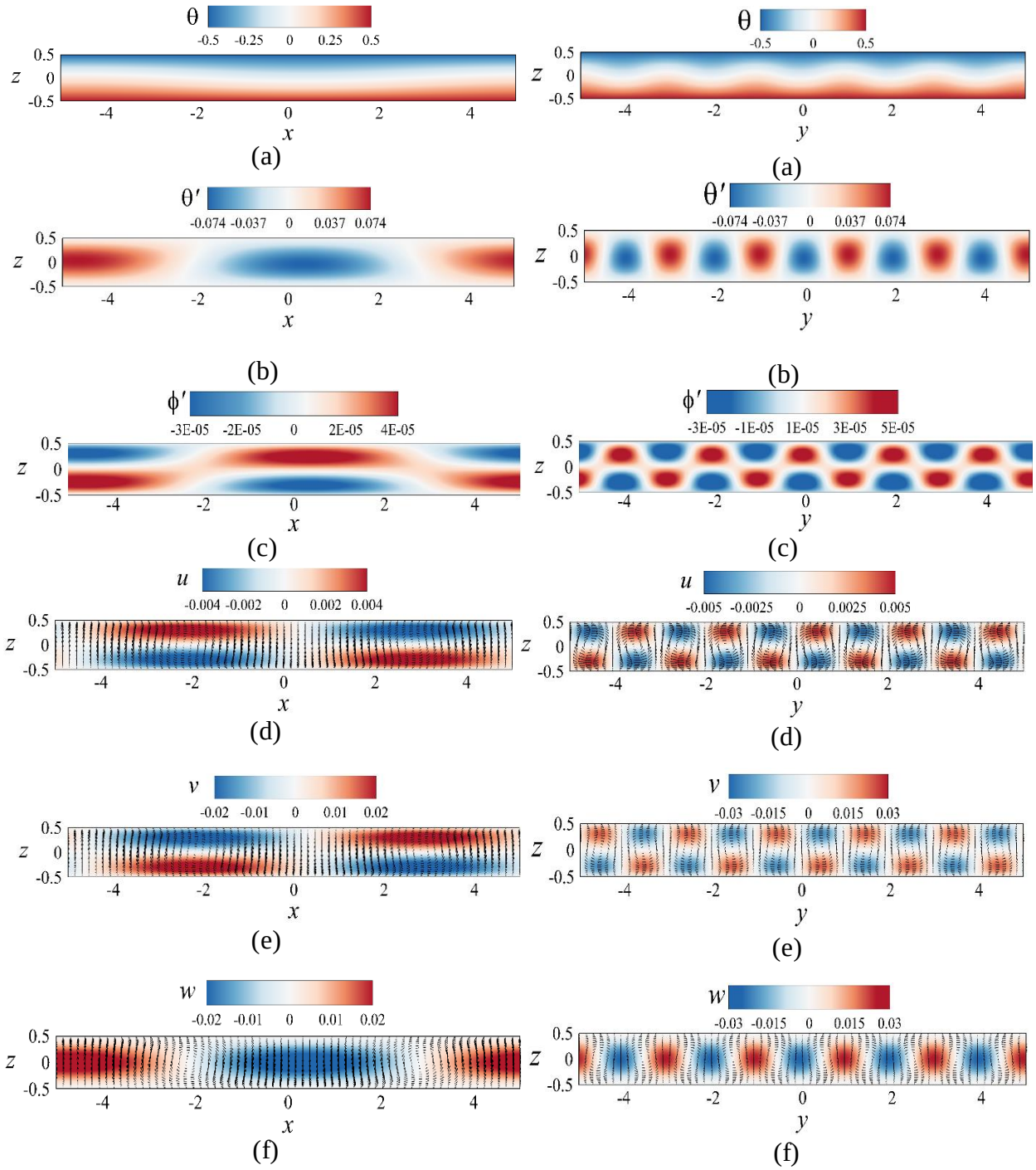

Figure 4.37: Snapshots of instantaneous saturated thermo-convective flow in the planes $y = 0$ and $x = 0$ for $Ra = 0$, $Pr = 65$ and $L = 2200$: (a) temperature distribution (color); (b) temperature perturbations; (c) electric potential perturbations; (d-e) horizontal velocity components u and v (color); and (f) vertical velocity component w (color). Vectors represent the velocity fields in (d-f).

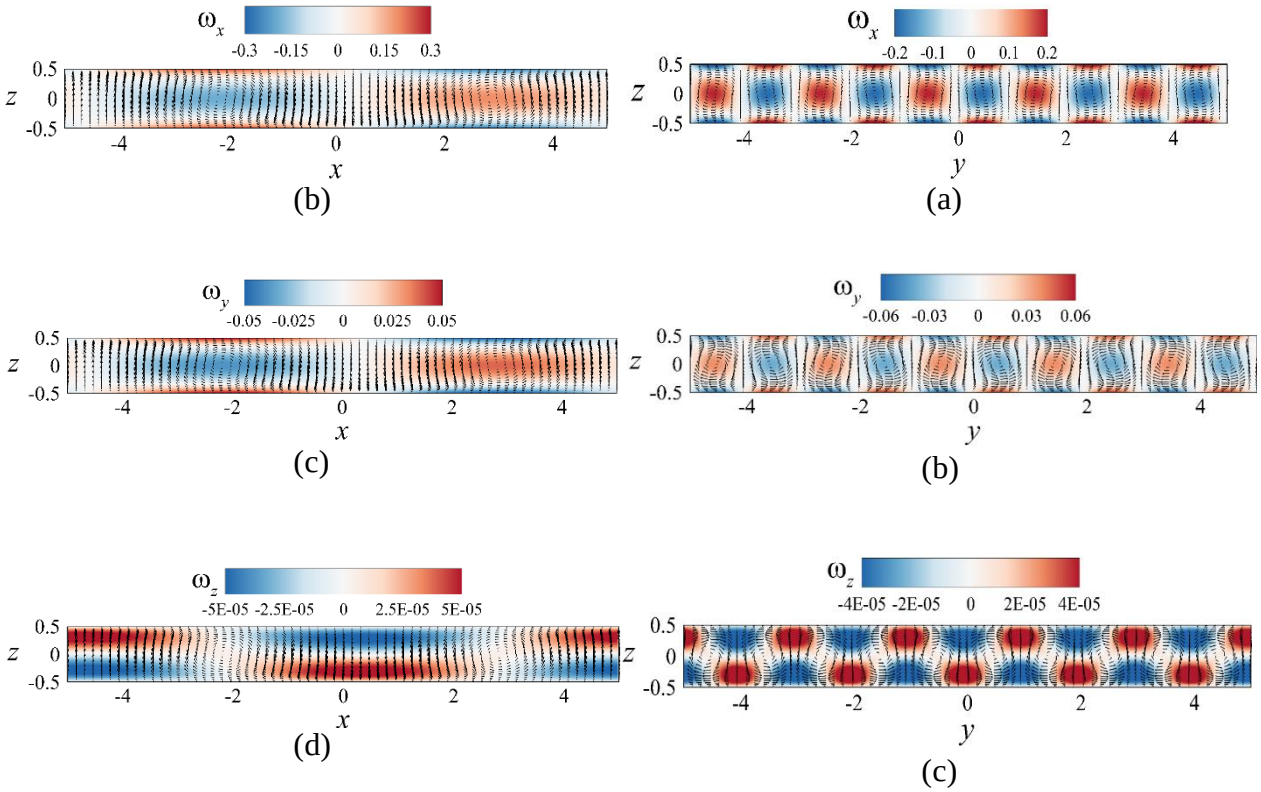

Figure 4.38: Vorticity components in the plane $y = 0$, and in the plane $x = 0$ for $Pr = 65$, $Ra = 0$, and $L = 2200$. Vectors represent the velocity fields: (a) and (b) horizontal vorticity components (color); and (c) vertical vorticity components (color).

In contrast with the independence of the first instability patterns on Pr, far from the threshold ($L > L_c$), the dynamics of the thermo-convective flows observed for $Pr = 65$ considerably differ from those of $Pr = 1$. Different types of thermo-convective structures are presented in Figure 4.39. We observed that the flow patterns are modulated from $L = 3\,500$; this modulation occurs along the roll axis and could be due to the periodic boundary conditions applied in the horizontal directions. As the value of L is increased, the spatial modulation of rolls increases. However, the flow regime is still time-independent.

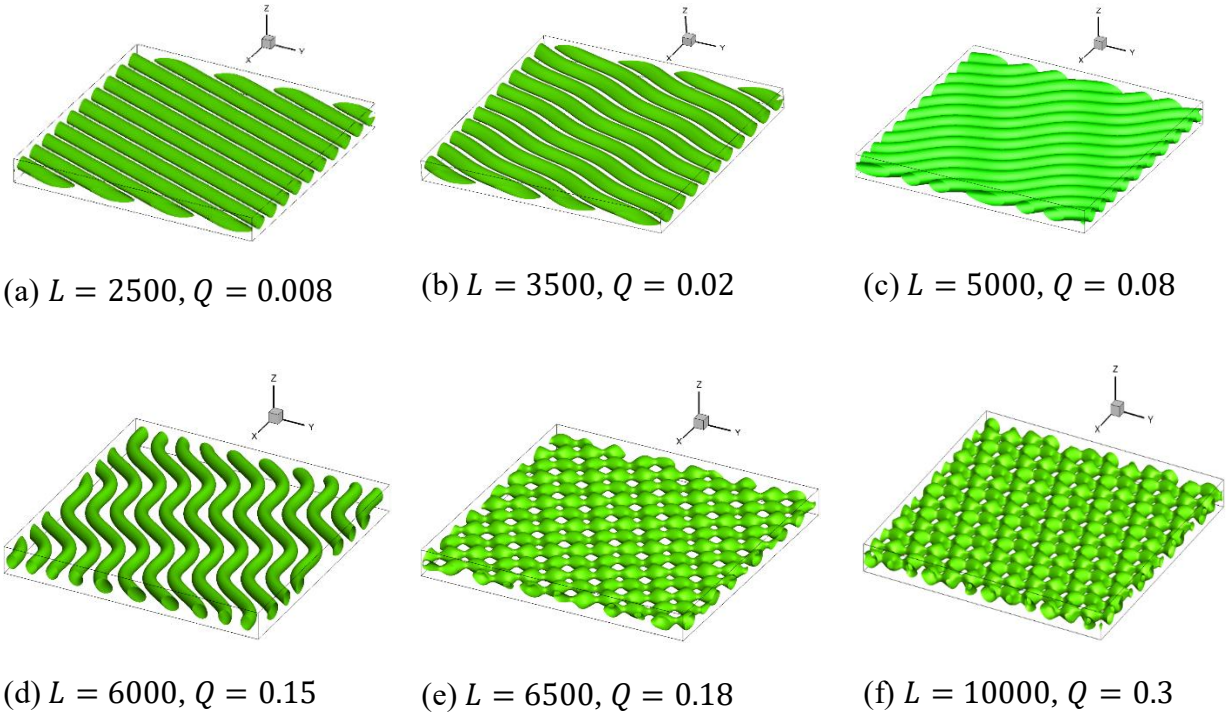

(a) $L = 2500, Q = 0.008$ (b) $L = 3500, Q = 0.02$ (c) $L = 5000, Q = 0.08$

(d) $L = 6000, Q = 0.15$ (e) $L = 6500, Q = 0.18$ (f) $L = 10000, Q = 0.3$

Figure 4.39: Instantaneous structures of isosurfaces of Q for $Pr = 65$ and different values of L in microgravity environment $Ra = 0$.

For $L = 6000$, the modulation along the rolls in the horizontal directions (Figure 4.39-d) resembles the zigzag instability observed in the Rayleigh Bénard convection [35]. For this regime, the instantaneous flow fields of modulated patterns are presented in Figure 4.40. The figure shows the instantaneous flow fields in the vertical $(x - z)$ and $(y - z)$ planes for $L = 6\,000$. The deformation of equipotentials increases with increasing the value of L (Figure 4.40, Figure 4.44). One sees that the perturbation electric potential is higher at the central zone $z = 0$. Furthermore, the vorticity components in both $(x - z)$ and $(y - z)$ vertical planes are presented in Figure 4.41. In contrast with the Rayleigh Bénard problem, the vertical vorticity ω_z does not have a relaxing behavior since it contains the source term arising from the electric buoyancy. However, its magnitude is lower than the magnitudes of the horizontal components ω_x and ω_y of vorticity.

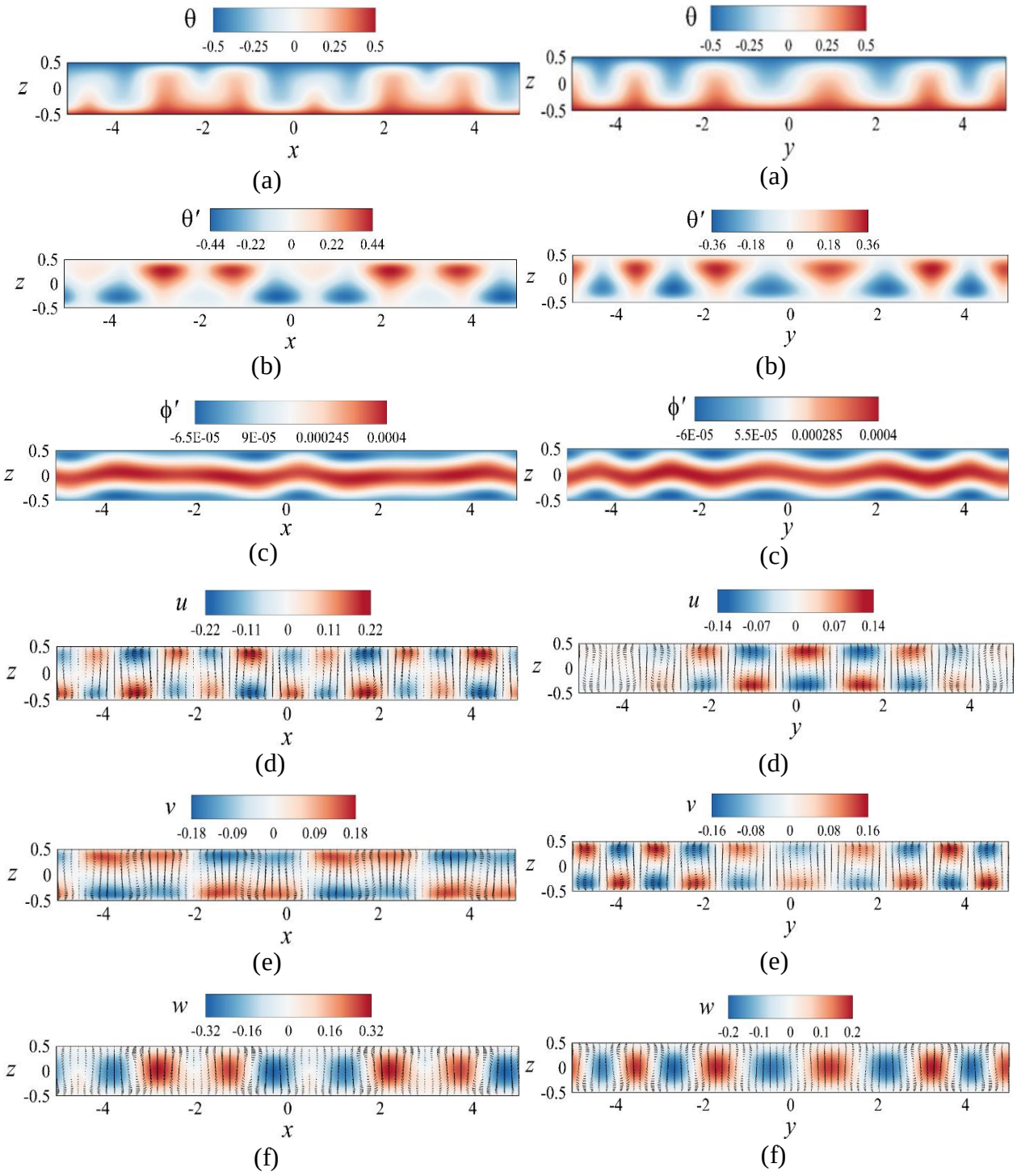

Figure 4.40: Instantaneous flow fields of the flow regime in the vertical planes for $Pr = 65$, $Ra = 0$ and $L = 6000$: (a) temperature distribution (color); (b) temperature perturbations; (c) electric potential perturbations; (d-e) horizontal velocity components u and v (color); and (f) vertical velocity component w (color). Vectors represent the velocity fields in (d-f).

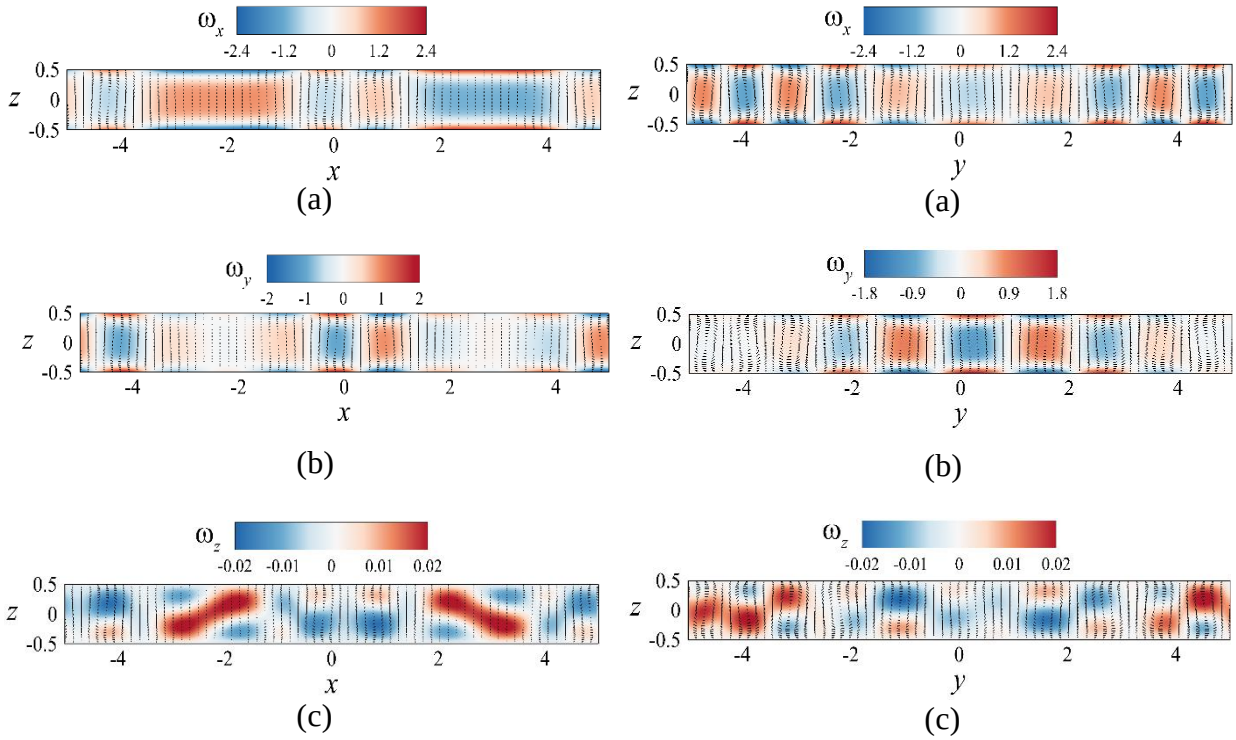

Figure 4.41: Vorticity components in the $(x - z)$ and $(y - z)$ vertical planes for $Pr = 65$, $Ra = 0$, and $L = 6\,000$.

At $L = 6\,500$, a new instability occurs and two perpendicular sets of rolls appear in the flow leading to stationary cross-roll patterns (Figure 4.39-e). Similar behavior of convective rolls has been reported in Rayleigh-Bénard convection as steady cross-roll convection [35,79,80]. This three-dimensional flow is due to the detachment of the thermal boundary layer from the horizontal plates. Indeed, this cross-roll instability presents square patterns in the horizontal $(x - y)$ plane as shown in Figure 4.42 which corresponds to the temperature distribution for $L = 6\,500$. The 3D time-independent flow regime is characterized by the thermal plumes in form of mushrooms in the vertical temperature distribution as illustrated in Figure 4.42. For this case, only the temperature distribution in all planes is presented.

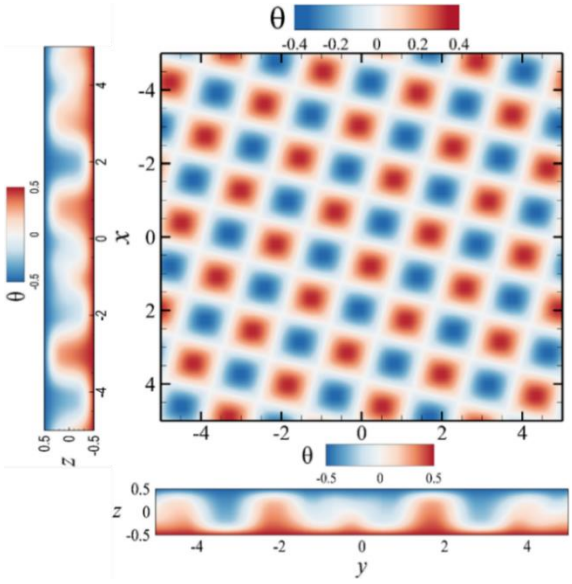

Figure 4.42: Illustration of the perturbed 3D flow by the temperature distribution in the $(x-y)$ horizontal plane $(z=0)$ and the vertical $(x-z)$ and $(y-z)$ cross-sections for $Ra=0$, $Pr=65$ and $L=6\,500$.

When the electric Rayleigh number reaches $L=9\,000$, the steady cross-roll instability presents defects as shown in Figure 4.43 (a). The screenshot of the temperature field in the horizontal slice, presented in Figure 4.43 (b), indicates that square cells are replaced by pentagons in certain locations especially near the corners.

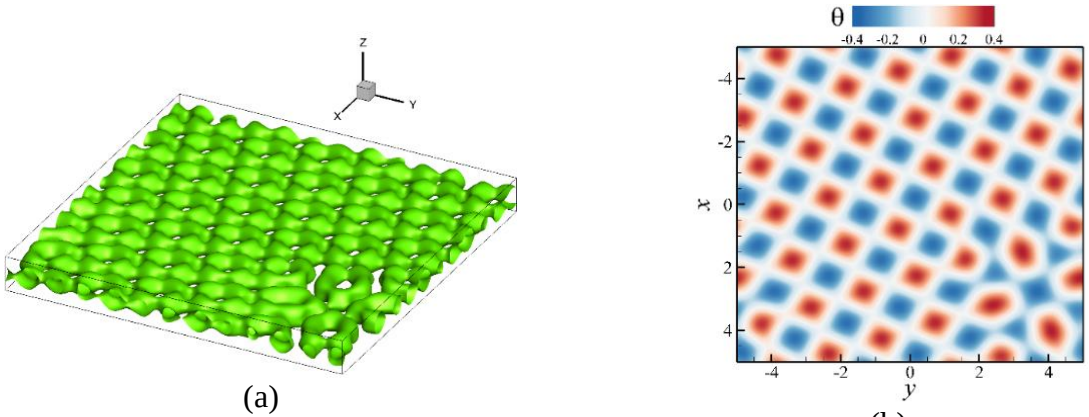

(a) (b)

Figure 4.43: Instantaneous flow field for $Ra=0$, $Pr=65$ and $L=9\,000$: (a) vortical structures of $Q=0.2$ and (b) isotherms. The temperature distribution is plotted at the mid-height $(z=0)$ of the cavity.

At $L=10\,000$, the defects of the cross-roll patterns (pentagons) disappear and the flow goes back to the instability regime presenting squares all over the flow. The instantaneous flow fields of

the square pattern regime for $Pr = 65$, $Ra = 0$, and $L = 10\,000$ are presented in Figure 4.44 for both vertical $(x - z)$ and $(x - z)$ cross-sections. The components of the vorticity are presented in Figure 4.45 for both vertical planes $x = 0$ and $y = 0$.

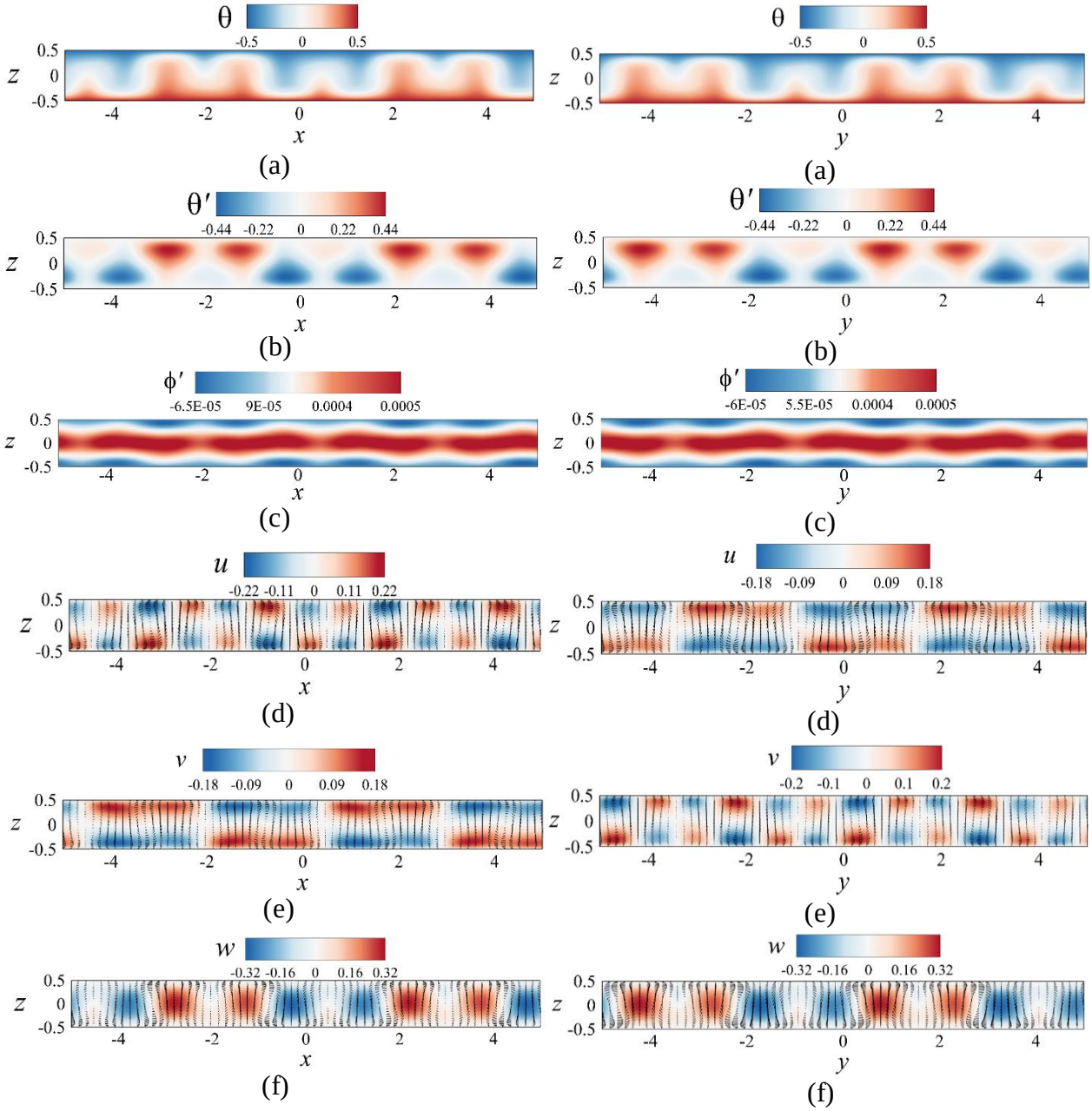

Figure 4.44: Snapshots of instantaneous saturated flow in the vertical planes for $Ra = 0$, $Pr = 65$ and $L = 10\,000$: (a) temperature distribution (color); (b) temperature perturbations; (c) electric potential perturbations; (d-e) horizontal velocity components u and v (color); and (f) vertical velocity component w (color). Vectors represent the velocity fields in (d-f).

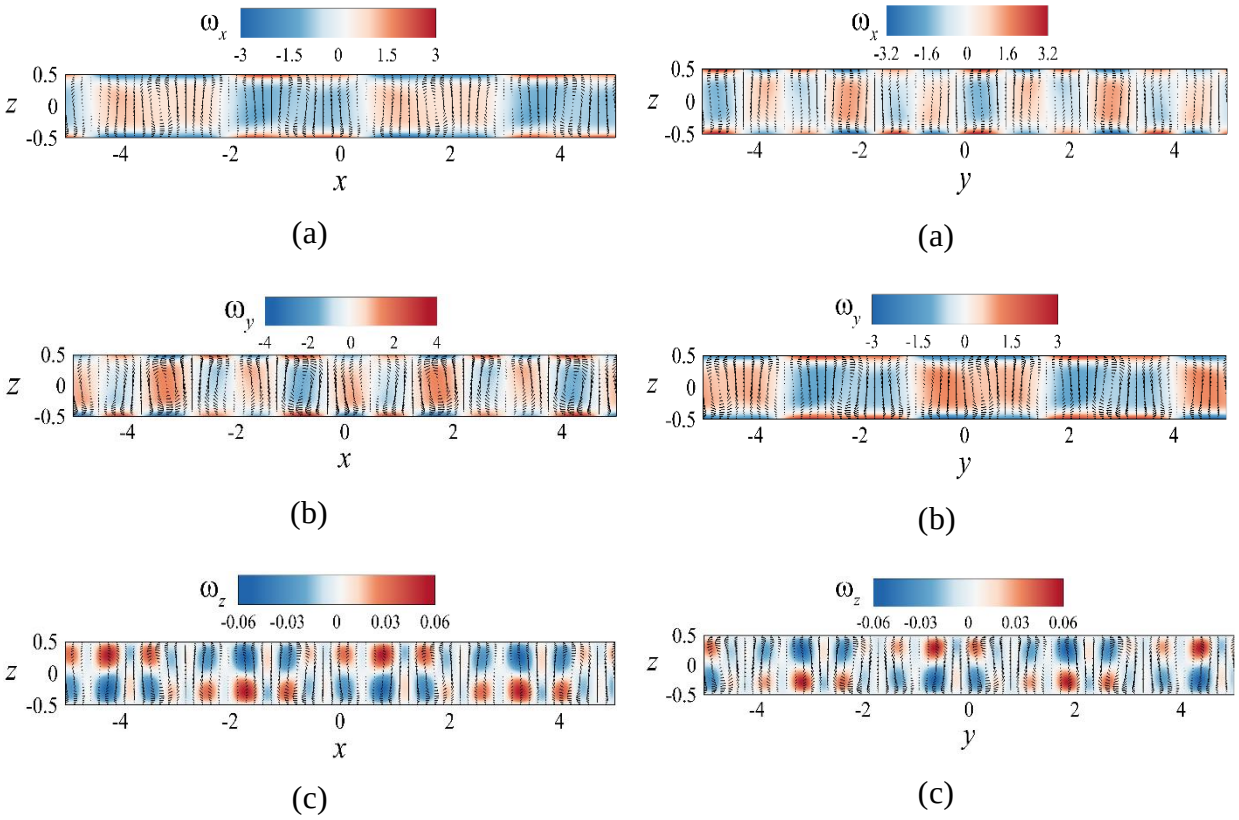

Figure 4.45: Vorticity components in the $(x - z)$ and $(y - z)$ vertical planes for $Pr = 65$, $Ra = 0$, and $L = 10\ 000$.

4.6.2. Convective flow patterns under unstable stratification ($Ra > 0$)

For $Pr = 65$ and $Ra > 0$, thermoelectric convection occurs in the fluid with straight inclined rolls having a wavenumber $k = 3.204$ as shown in Figure 4.46 (a1). When the electric Rayleigh number L is increased just above the threshold, we observe a new type of convective flow pattern with bending rolls.

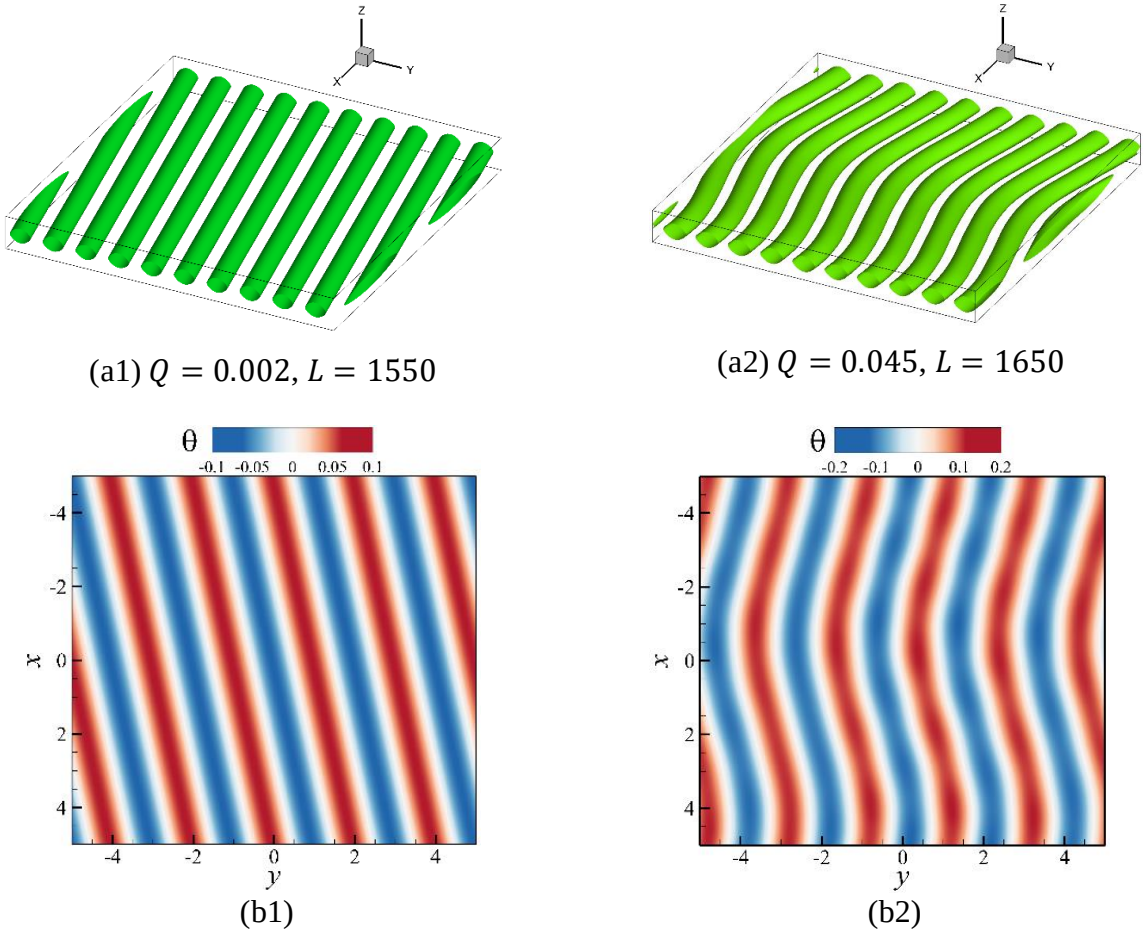

(a1) $Q = 0.002$, $L = 1550$ (a2) $Q = 0.045$, $L = 1650$

(b1) (b2)

Figure 4.46: (a) Vortical structures illustrated by iso-surfaces of Q, and (b) isotherms in the horizontal $(x - y)$ plane for $Pr = 65$, $Ra = 500$ and two values of L.

Figure 4.47 presents instantaneous vortical structures of different flow regimes for $Pr = 65$, $Ra = 500$ and different values of L. One sees that at $L = 4000$, the flow exhibits a steady three-dimensional regime. The steady thermo-convective flow presents vortices with bending at certain locations. The instantaneous flow structures for $L = 4000$ are displayed in Figure 4.47 (a).

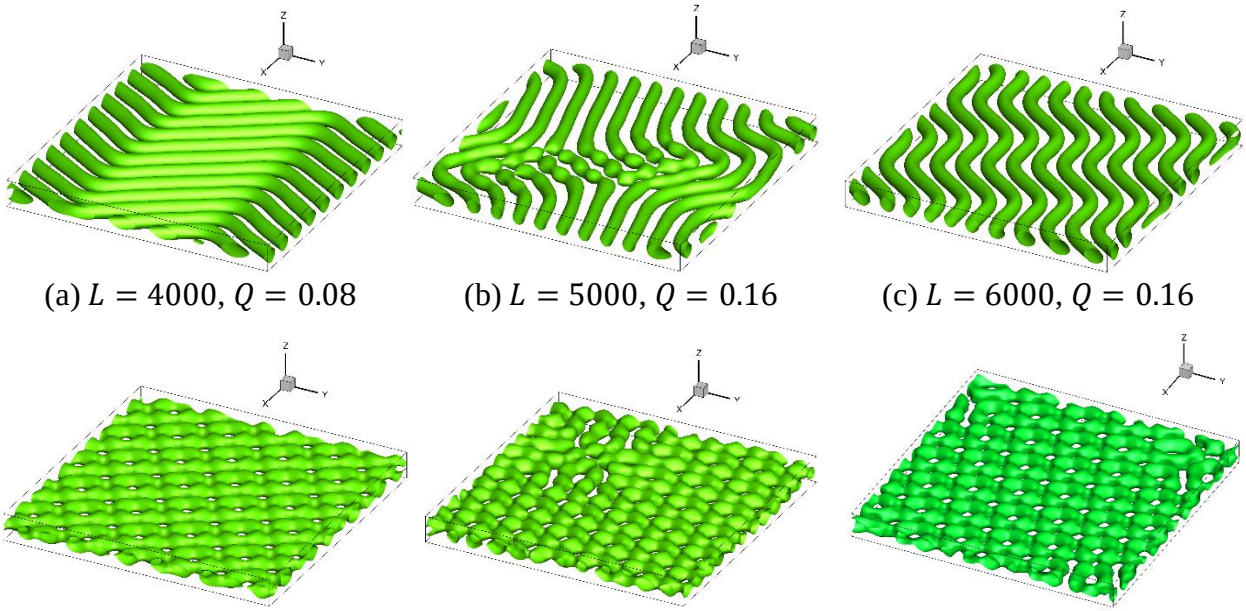

(a) $L = 4000$, $Q = 0.08$ (b) $L = 5000$, $Q = 0.16$ (c) $L = 6000$, $Q = 0.16$

(d) $L = 7000$, $Q = 0.16$ (e) $L = 8000$, $Q = 0.20$ (f) $L = 10\,000$, $Q = 0.16$

Figure 4.47: Instantaneous flow structures visualized by the isosurfaces of Q for $Ra = 500$, $Pr = 65$, and different values of L.

For $L = 5000$, the flow exhibits time-dependent thermo-convective rolls (Figure 4.47-(b)). The time evolution of the convection amplitude is presented in Figure 4.48-(a). We have also plotted the time variation of the vertical velocity and the temperature at the cavity center of this oscillatory regime in Figure 4.48-(b). Figure 4.49 shows the flow fields in the vertical $(x - z)$ and $(y - z)$ cross-sections. The temperature and the electric potential fluctuations are shown in Figure 4.49 (b) and Figure 4.49 (c).

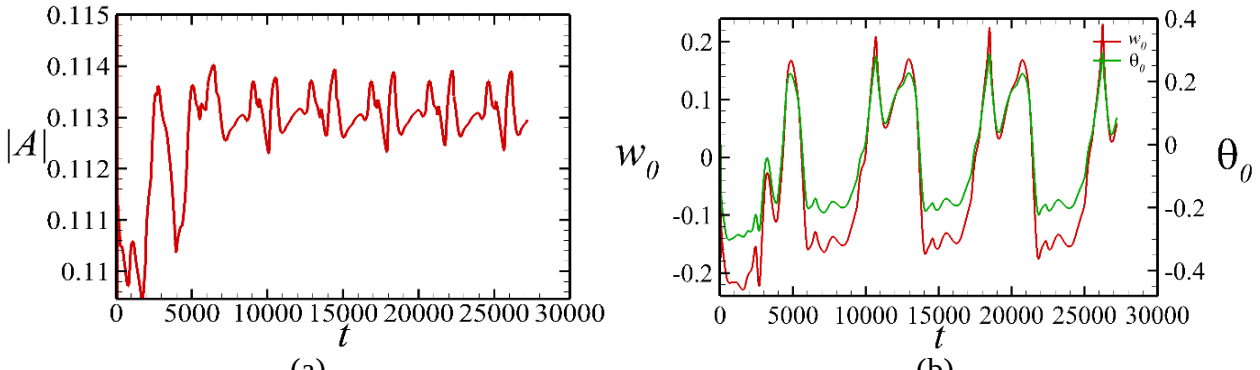

(a) (b)

Figure 4.48: Time evolution of (a) the amplitude of the averaged vertical velocity, (b) the vertical velocity w_0 and the temperature θ_0 at the cavity center $(x = y = z = 0)$ for $Ra = 500$, $Pr = 65$ et $L = 5000$.

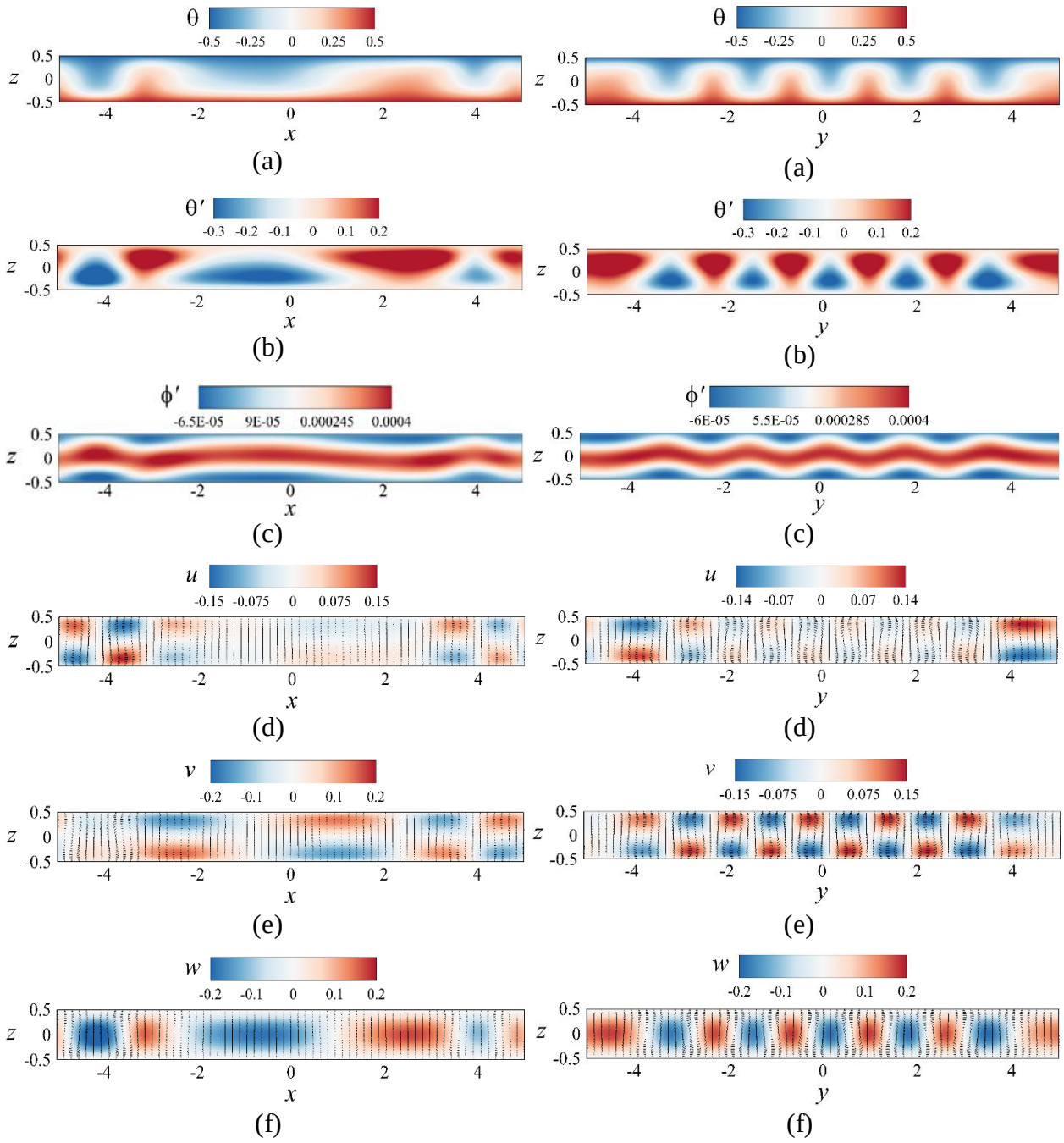

Figure 4.49: Snapshots of instantaneous saturated flow in the vertical planes for $Pr = 65$, $Ra = 500$, and $L = 5000$: (a) temperature distribution (color); (b) temperature perturbations; (c) electric potential perturbations; (d-e) horizontal velocity components u and v (color); and (f) vertical velocity component w (color). Vectors represent the velocity fields in (d-f).

All components of the vorticity in the vertical cross-sections are displayed in Figure 4.50 for a better illustration of the oscillating convective regime visualized in Figure 4.47 (b).

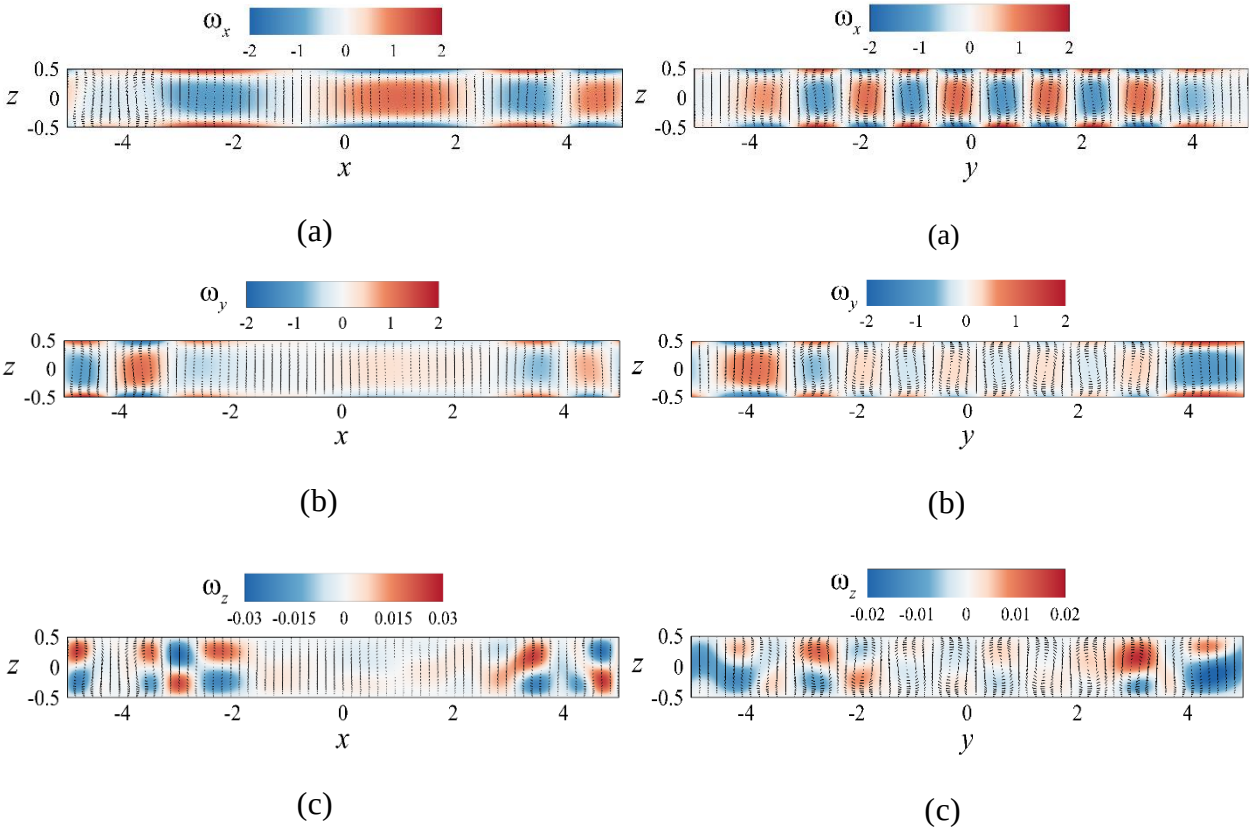

Figure 4.50: Vorticity components in the $(x - z)$ and $(y - z)$ vertical planes for $Pr = 65$, $Ra = 500$, and $L = 5000$.

The oscillating thermoelectric convection disappears when increasing the value of the electric Rayleigh number. For $L = 6000$, a three-dimensional stationary regime with modulated structures occurs in the system (Figure 4.47-c). A similar regime has already been observed under microgravity conditions ($Ra = 0$) for $Pr = 65$ and at the same value of L.

The increase of the value of L leads to the occurrence of steady cross-roll instability at $L = 7000$ (Figure 4.47-(d)). The flow presents square patterns similar to the patterns obtained under microgravity conditions for $Pr = 65$ and in the Rayleigh-Bénard convection [35]. A further increase of $L \geq 8000$ leads to the appearance of defects in the square patterns generating some zones with pentagons as shown by the temperature distribution presented in Figure 4.51.

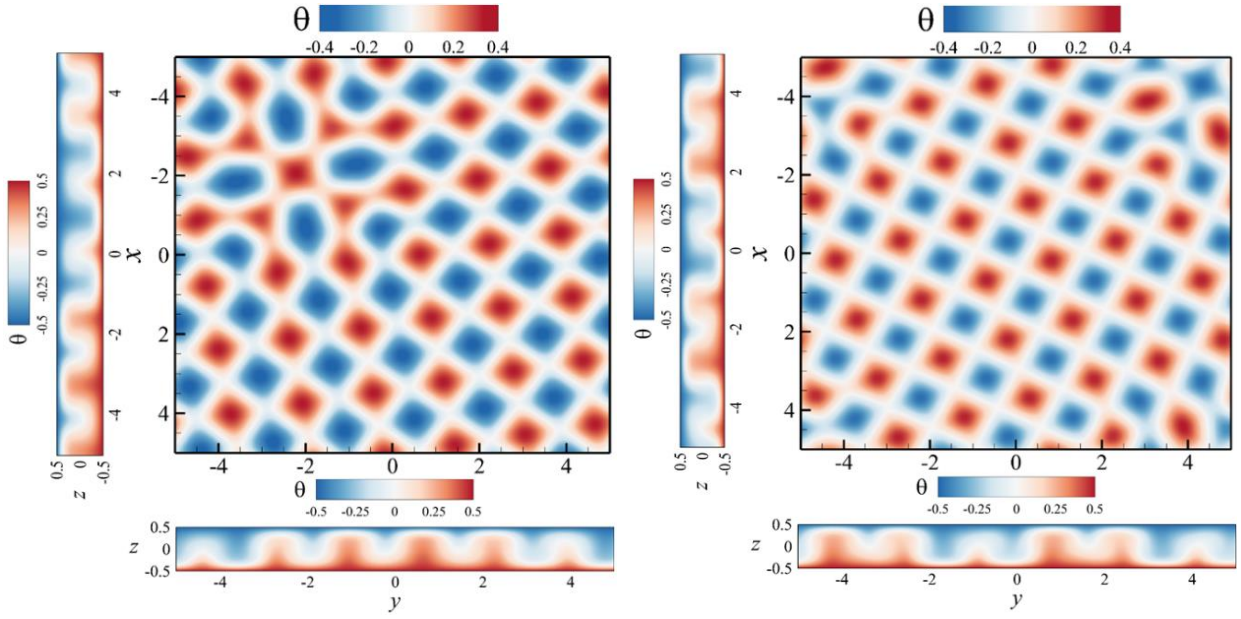

(a) (b)

Figure 4.51: Illustration of the perturbed 3D flow by the temperature distribution in the $(x - y)$ horizontal plane $(z = 0)$ and the vertical $(x - z)$ and $(y - z)$ cross-sections for $Pr = 65, Ra = 500$: (a) $L = 8000$ and (b) $L = 10\,000$.

We have to notice that thermoelectric convective states obtained for $Ra > 0$ are mostly similar to those obtained in microgravity $(Ra = 0)$. However, we have observed a window where an oscillatory regime (i.e. $L = 5000$) appears in the system and this instability could be deeply investigated.

4.6.3. Convective flow patterns for the stable stratification ($Ra < 0$)

For the present case, we have conducted numerical simulations for $Ra = -500$ and $L > L_c$. Figure 4.52 shows the different saturated thermoelectric convection regimes obtained for $Pr = 65$, $Ra = -500$ and different values of the electric Rayleigh number L. One sees that around the threshold, the thermoelectric instability is characterized by stationary inclined rolls. These straight vortices are modulated for $L \in \{2800, 4000\}$. The deformation of flow patterns in this range could be due to the periodic boundary conditions. At $L = 5500$, the cross-roll thermo-convective flow appears in the fluid layer (Figure 4.52-(d)).

When $L = 10\,000$, the regime of square patterns bifurcates to stationary flow patterns with defects as shown in Figure 4.52 (f). The defects are illustrated by the temperature distribution presented in Figure 4.53. These thermo-convective flow structures have already been observed in the ordinary Rayleigh-Bénard problem [35]. However, we did not observe an oscillatory solution in the case of the electric buoyancy-driven instability in a system heated from the top for $Pr = 65$.

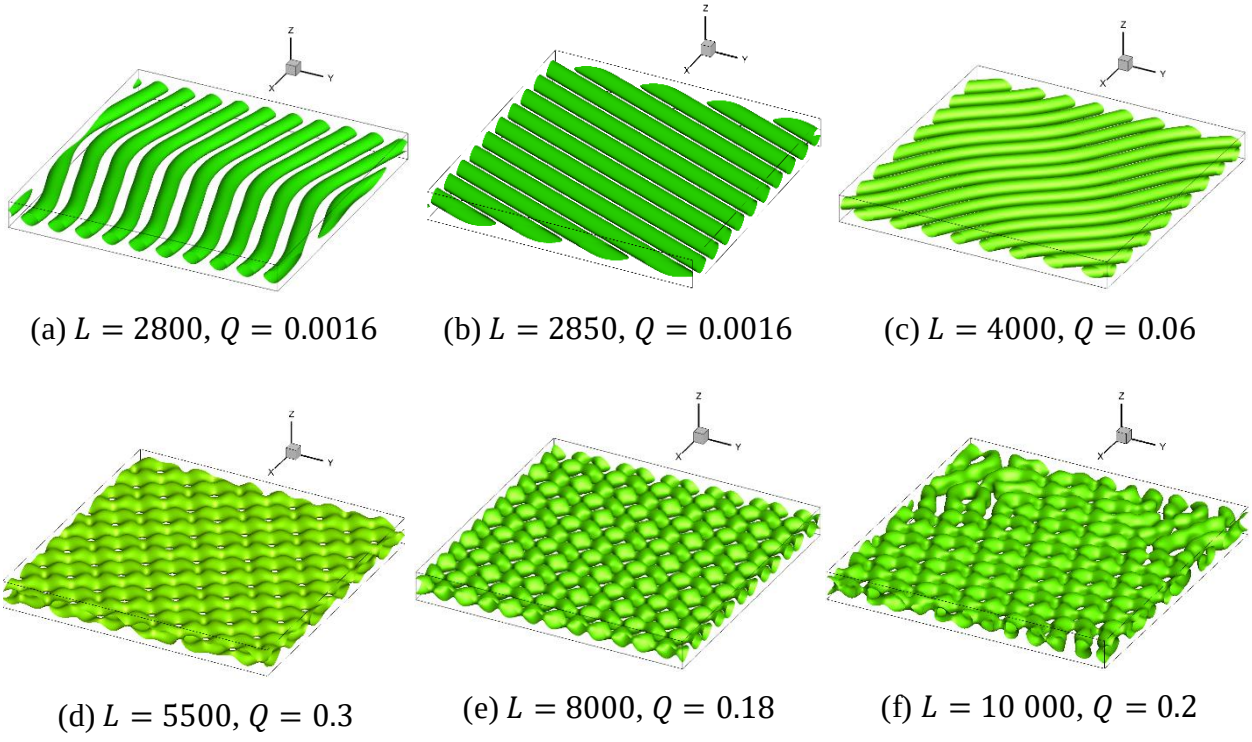

(a) $L = 2800$, $Q = 0.0016$ (b) $L = 2850$, $Q = 0.0016$ (c) $L = 4000$, $Q = 0.06$

(d) $L = 5500$, $Q = 0.3$ (e) $L = 8000$, $Q = 0.18$ (f) $L = 10\,000$, $Q = 0.2$

Figure 4.52: Instantaneous structures of vortices visualized by the isosurfaces of Q for $Ra = -500$, $Pr = 65$, and different values of L.

The temperature levels captured in the horizontal plane $(y-x)$ at the mid-height $z=0$ are presented in Figure 4.53 for the different observed regimes. The defects obtained in the thermo-convective regime that presents square patterns at $L=10\,000$ are illustrated in Figure 4.53 (f).

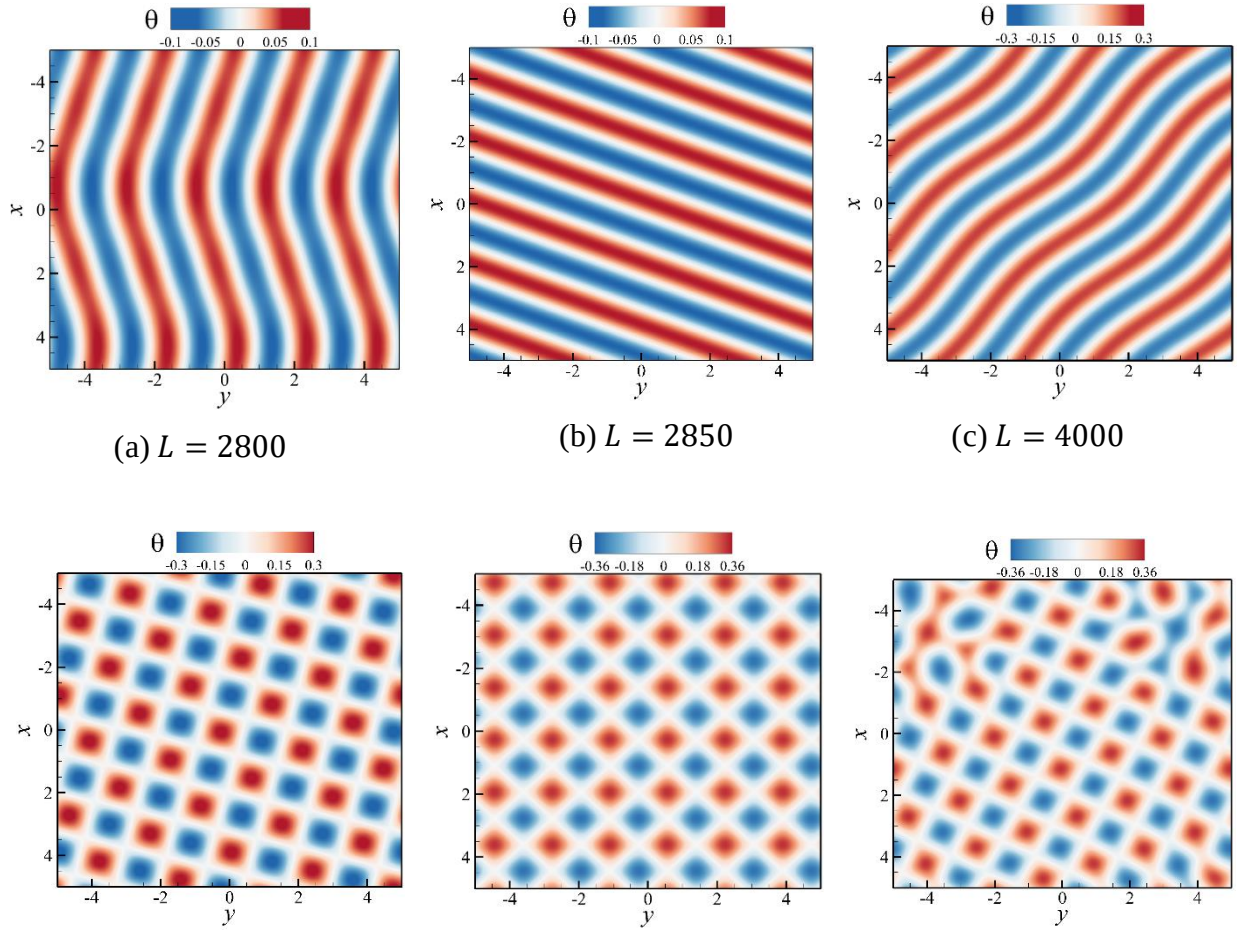

(a) $L=2800$ (b) $L=2850$ (c) $L=4000$

(d) $L=5500$ (e) $L=8000$ (f) $L=10\,000$

Figure 4.53: Instantaneous mid-gap temperature distribution in the horizontal $(x-y)$ plane for $Ra=-500$, $Pr=65$, and different values of L.

Figure 4.54 and Figure 4.55 show the patterns of the thermo-convective structures generated by the electric buoyancy around the threshold for $Ra=-500$ and $L=2800$. Snapshots are taken in the vertical slices to have a better insight in the vertical distribution of the temperature and flow behavior. We observe that the vertical components of vorticity are negligible compared to the horizontal components.

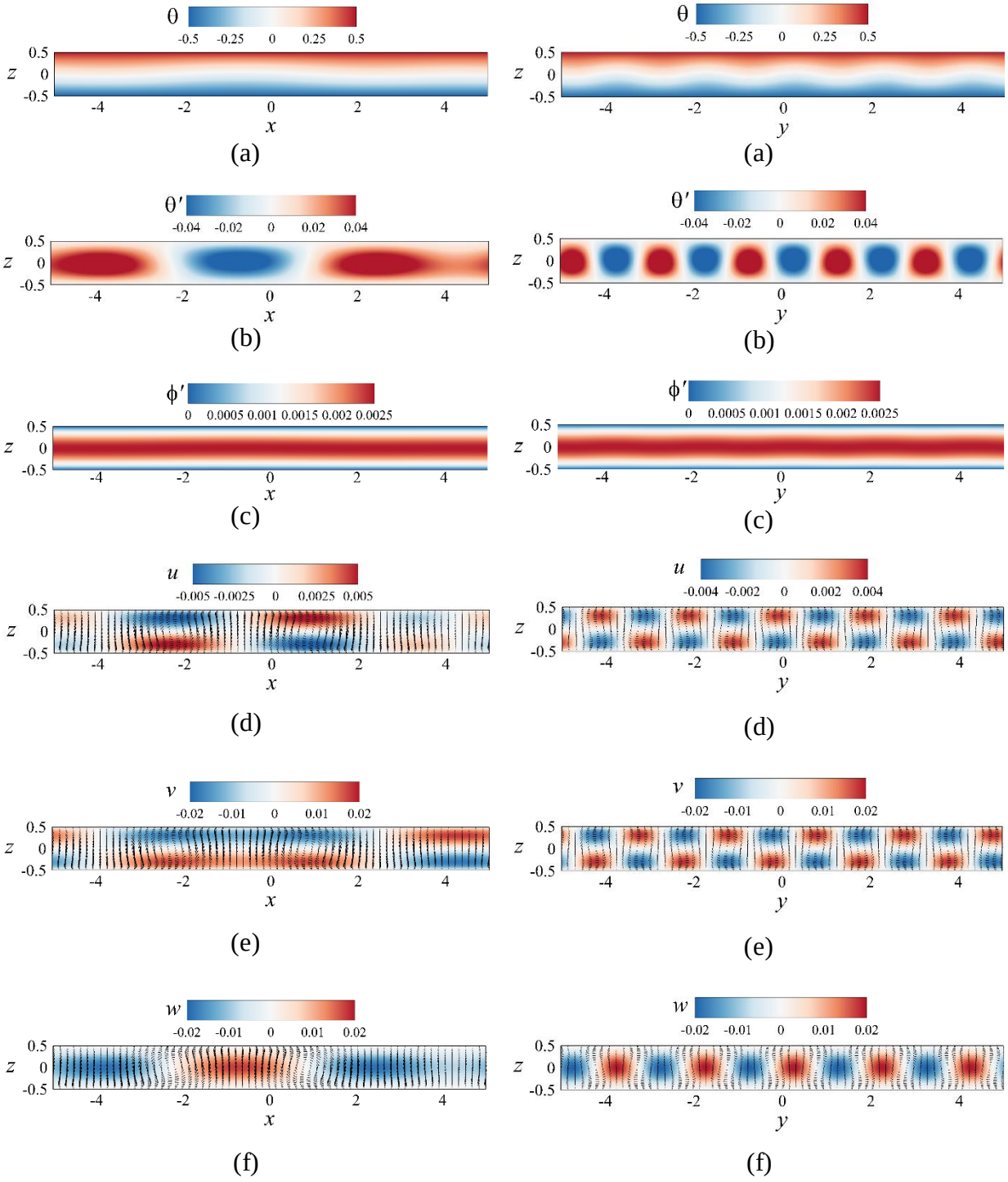

Figure 4.54: Snapshots of instantaneous saturated flow in the vertical planes for $Pr = 65$, $Ra = -500$, and $L = 2800$: (a) temperature distribution (color); (b) temperature perturbations; (c) electric potential perturbations; (d-e) horizontal velocity components u and v (color); and (f) vertical velocity component w (color). Vectors represent the velocity fields in (d-f).

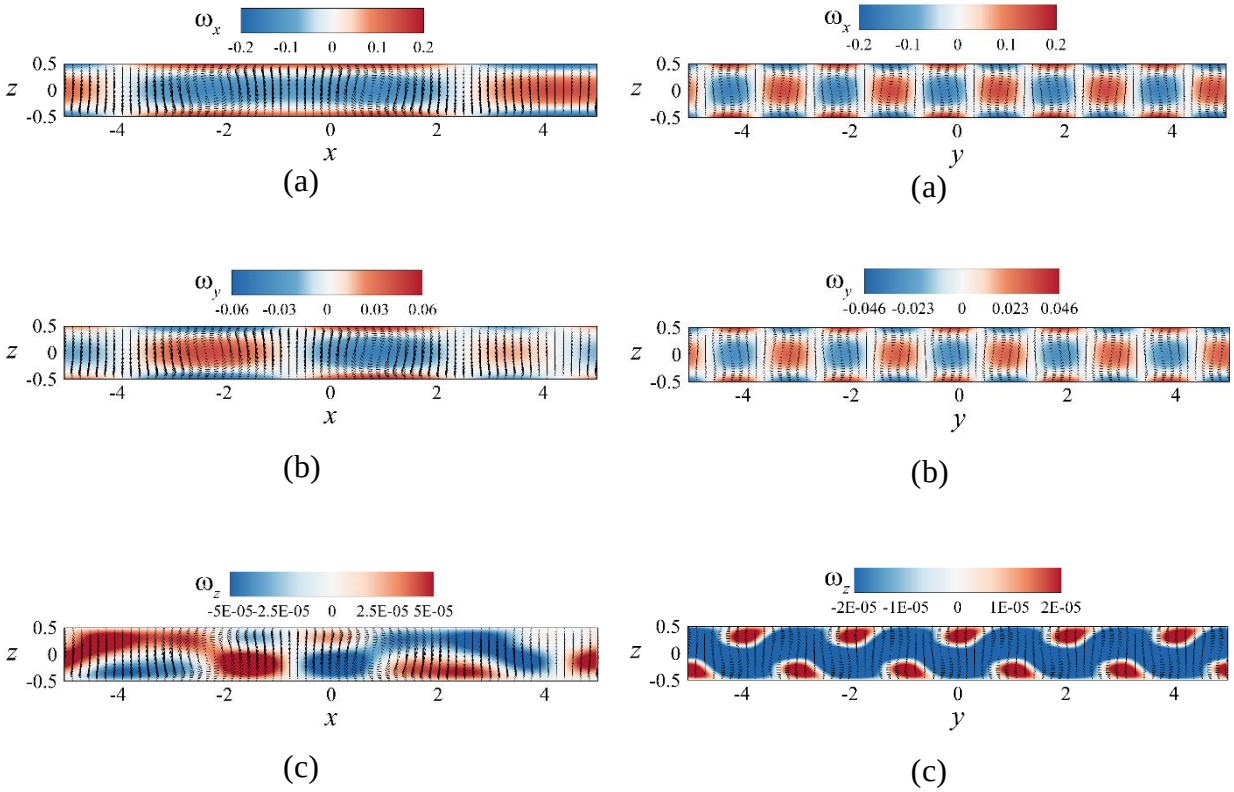

Figure 4.55: Vorticity components in the $(x - z)$ and $(y - z)$ vertical planes for $Pr = 65$, $Ra = -500$, and $L = 2800$.

Figure 4.52 and Figure 4.53 showed that the flow regime corresponds to a uniform steady flow presenting square patterns for $L = 8000$. The behavior of this square pattern regime in the vertical planes is illustrated in Figure 4.56 and Figure 4.57. We observe that the vertical vorticity components for $L = 8000$ are stronger than that of $L = 2800$. Figure 4.58 shows the bifurcation scenarios present in the thermoelectric convection in a rectangular cavity filled with silicone oil (i.e. $Pr = 65$) for $Ra \in \{-500, 0, 500\}$ and different values of L. The time dependent convective regime is obtained only for $Ra = 500$ and the modulated rolls regime are obtained at the same value of L for $Ra = \{0, 500\}$.

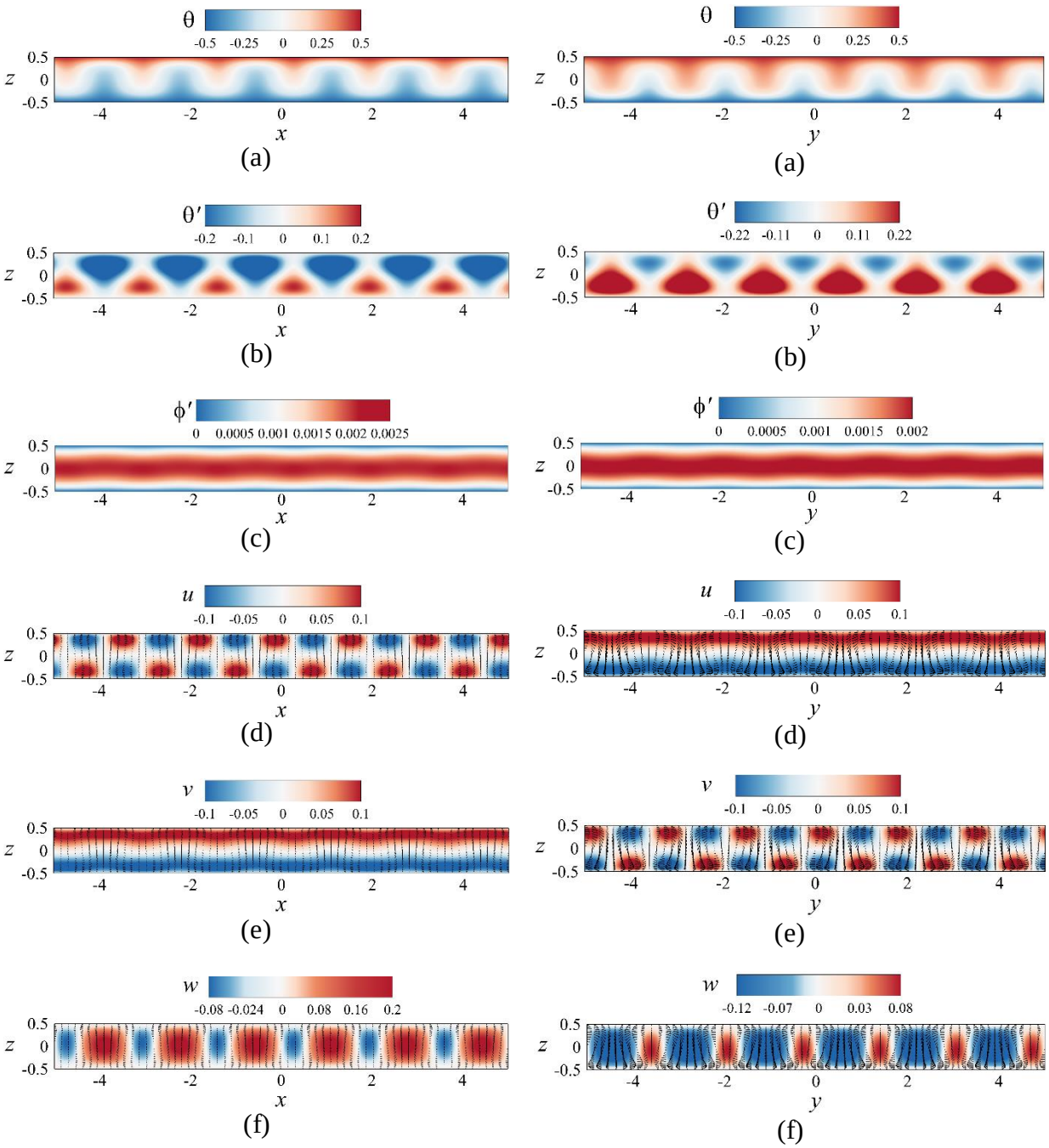

Figure 4.56: Snapshots of instantaneous saturated flow in the vertical planes for $Pr = 65$, $Ra = -500$, and $L = 8000$: (a) temperature distribution (color); (b) temperature perturbations; (c) electric potential perturbations; (d-e) horizontal velocity components u and v (color); and (f) vertical velocity component w (color). Vectors represent the velocity fields in (d-f).

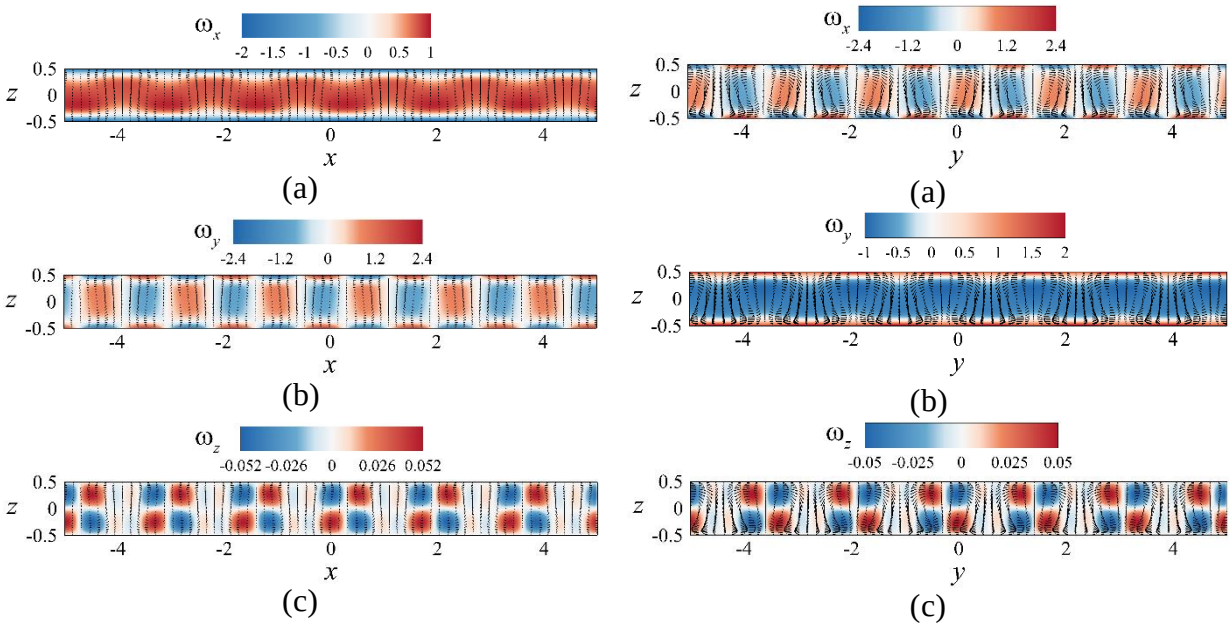

Figure 4.57: Vorticity components in the $(x - z)$ and $(y - z)$ vertical planes for $Pr = 65$, $Ra = -500$, and $L = 8000$.

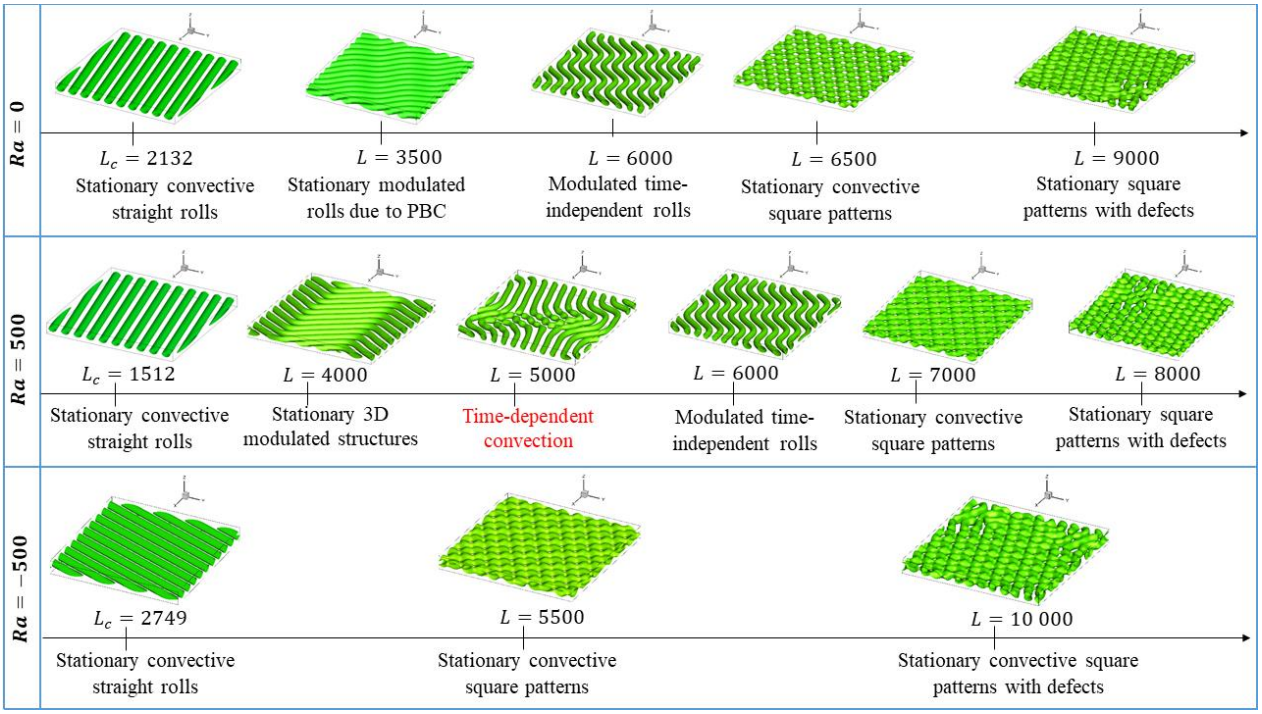

Figure 4.58: State diagram of the transitions for $Pr = 65$, $Ra \in \{-500, 0, 500\}$ and different increasing values of L.

4.7. Characterization of the heat transfer

In this section, we analyze the heat transfer associated with thermoelectric convection. When the fluid layer is at rest ($\vec{u} = 0$), the heat transport is only managed by conduction. However, when the electric Rayleigh number $L \geq L_c(Ra)$, thermo-convective rolls modify the heat transfer. The heat transfer is characterized by the transfer coefficient h or its dimensionless number called Nusselt number $Nu = hd/k$ where k is the thermal conductivity. The Nusselt number represents the ratio of the total heat flux (conduction + convection) to the heat flux by conduction. In this study, in order to compute the time-averaged Nusselt number in the rectangular cavity, we have used the following relation [81]:

$$Nu = \frac{1}{TL_xL_y}\int_0^T \int_{-L_y/2}^{L_y/2} \int_{-L_x/2}^{L_x/2} \left(Pr\theta w - \frac{\partial \theta}{\partial z}\right) dxdy\, dt, \tag{4.7}$$

where T is the total time.

The first term represents the heat exchange by convection, and the second is the heat exchange by conduction.

We have considered two types of dielectric fluids: gas with $Pr = 1$ and oils with $Pr = 65$. The latter corresponds to fluids used in some experiments performed or to be performed in parabolic flight experiments (see Appendix A). The variation of Nu as a function of the electric Rayleigh number L for three cases: $Ra < 0$, $Ra = 0$, and $Ra > 0$ is shown in Figure 4.59. In the conductive regime($L < L_c$), we have $Nu = 1$ and when thermo-convection sets in, i.e. when $\geq L_c$, $Nu > 1$ due to the transport of heat by thermoelectric convective rolls from the hot plate toward the cold one. As L increases, the intensity of thermo-convective rolls increases, and correspondingly the heat transfer increases.

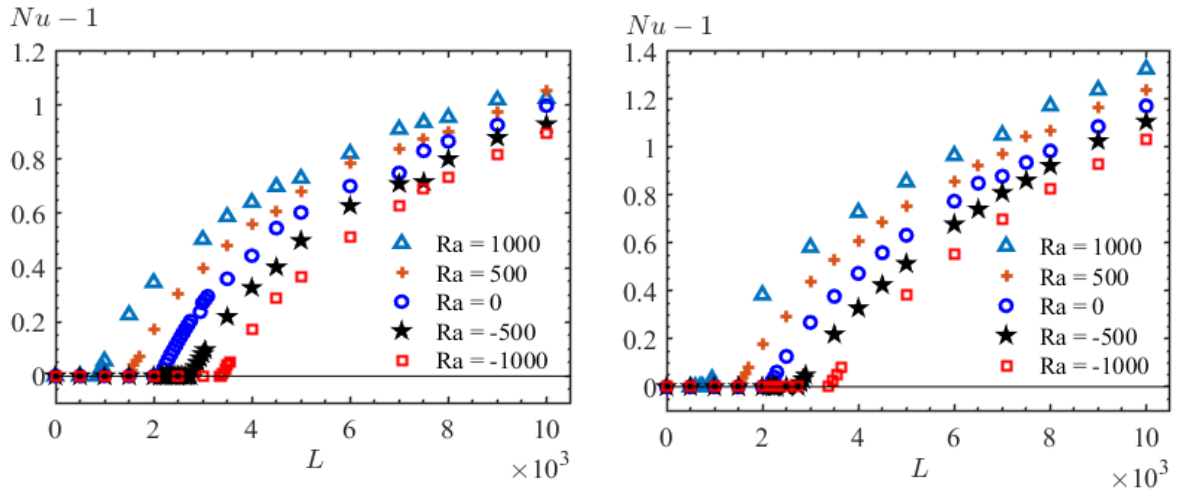

Figure 4.59: Variation of the Nusselt number Nu as a function of the electric Rayleigh number L and some values of Ra for (a) $Pr = 1$, and (b) $Pr = 65$.

In Figure 4.59 (a) and (b), we notice that

i) For each value of L, the heat transfer is larger for the unstable thermal stratification of the base state ($Ra > 0$) and lower for the stable thermal stratification ($Ra < 0$) than the heat transfer in microgravity ($Ra = 0$).

For a fixed value of the temperature difference ($Ra = const.$), we have fitted the Nusselt number with a linear function of the criticality $\delta = L/L_c - 1$ in the neighborhood of the threshold ($\delta < 0.1$):

$$Nu = 1 + C\delta \tag{4.8}$$

The value of the slope C varies with Ra and is independent of Pr. Table 4.2 shows that the coefficient C decreases with Ra. Under microgravity conditions where $Ra = 0$ i.e. $g = 0$, $C = 0.79$. This value is the same as the one obtained in previous studies [28,32] in the two-dimensional weakly non-linear analysis of the thermoelectric convection in microgravity for $Pr \geq 1$. Moreover, this slope is the same as in the Rayleigh-Bénard convection problem [82].

Since thermoelectric convection is analogous to the Rayleigh-Bénard convection, we have correlated the behavior of Nu at large values of L by the power law [81]:

$$Nu \sim L^{\gamma}, \tag{4.9}$$

with γ the power law exponent. The values of γ are sensitive to the thermal stratification of the base state i.e. they depend on Ra (Table 4.2). For large values of L, the heat transfer depends on Pr through the exponent γ i.e. $\gamma = \gamma(Pr)$.

Table 4.2: Values of the slope C around the threshold ($\delta < 0.1$) and the values of γ for Pr $\in \{1; 65\}$, and different values of Ra.

Ra	C	γ	
		$Pr = 1$	$Pr = 65$
- 1000	1.02	0.44	0.53
- 500	0.91	0.35	0.46
0	0.79	0.33	0.41
500	0.61	0.28	0.37
1000	0.43	0.21	0.33

In the turbulent Rayleigh-Bénard convection, the power law in (4.9) is examined in terms of kinematic and thermal energy dissipation rates. Based on the decomposition of these dissipation rates into boundary layers and bulk contributions, Grossman and Lohse [81] established four regimes. In our case, for $Pr = 1$ and $Ra = 0$, the exponent $\gamma = 0.33$ of the scaling power law agrees with that of the regime IV_u of the classical Rayleigh-Bénard problem for large values of Ra and Pr [81]. In that regime, both thermal and viscous dissipations are dominated by the bulk, and they found $\gamma = [0.28 - 0.33]$ depending on the dissipation regime and independently of the aspect ratio. For a system heated from the top $Ra < 0$, γ increases considerably with increasing $|Ra|$ as in the case of the Rayleigh-Bénard problem with oscillating body force [5]. When $Ra = 1000$, the value of the power constant $\gamma = 0.21$. This value corresponds to that of the regime II_u in the

Rayleigh-Bénard problem sketched by Grossman and Lohse [81]. It should be noticed that in practice, the values of L are limited by the breakdown voltage V_{BD} of dielectric liquids (Table 2.1) which corresponds to the rupture of the dielectric nature of the fluid. In general, silicone oils have high dielectric strength but the breakdown potential is reduced by the presence of impurities or droplets of water or air bubbles. Therefore, we cannot reach high values of L that correspond to turbulent thermo-convective flows.

For $Pr = 65$ under microgravity conditions, the value of the exponent is $\gamma = 0.41$. This value does not enter the range of the RBC power-law scaling predicted by Grossman and Lohse [81] for the classic turbulent flows with a smooth lower plate. But it agrees with that obtained in the modified RB flow using rough plates, to modify the height of the boundary layers, where $\gamma = 0.3 - 0.5$ depending on the height of a roughness element [6]. This result also agrees with that obtained in the case where a direct heating source is introduced in the bulk of the system [83] or adding an oscillating body force to the momentum equation [5] to enhance the heat transport by increasing the value of the exponent γ. Zou and Yang [84] have found the same result by separating numerically the dynamic boundary layer from the thermal one. All articles cited above for the comparison correspond to modified turbulent Rayleigh-Bénard convection flows for the enhancement of heat transport. Indeed, we can highlight that dielectrophoretic buoyancy is an alternative to the heat transfer enhancement without any modification of the roughness of the plates or any introduction of intrusive material in the bulk of the fluid layer. Despite that, the dielectrophoretic force in rectangular cavities remains less efficient than the classical or modified Rayleigh-Bénard convection in the range of control parameters studied here.

We have introduced a new parameter called the modified electric Rayleigh number L'. This dimensionless number, encompassing the two control parameters L and Ra, was defined taking into account the instability thresholds of the Rayleigh-Bénard problem ($L = 0$; $Ra_c^0 = 1708$) and the thermoelectric convection under microgravity conditions ($Ra = 0$; $L_c^0 \approx 2129$):

$$L' = Ra + (Ra_c^0 / L_c^0) \cdot L. \tag{4.10}$$

For any given couple $(Ra; L)$, the behavior of convection to heat transfer i.e. the quantity $Nu - 1$ can be plotted as a function of the modified Rayleigh number L'. In Figure 4.60-(a), we observe that all the curves are almost collapsed for $Pr = 1$. In addition, Figure 4.60-(b) illustrates the

evolution of the Nusselt $Nu - 1$ as function of the modified Rayleigh number L' for $Pr = 65$. The curve shows that, as in the case of $Pr = 1$, the thermoelectric convection problem can be reduced to a simple Rayleigh-Bénard problem with L' as a control parameter independently of Pr. The global thermoelectric convection threshold ($L = L_c$) corresponds to values of L'_c lying between 1704 (for $Ra = -1000$) and 1709 (for $Ra = 1000$) whatever the value of the Rayleigh number $Ra < Ra_c$. This brings the generalized problem of the thermal convection induced by the electric buoyancy back to a classic Rayleigh-Bénard problem with L' as the unique control parameter.

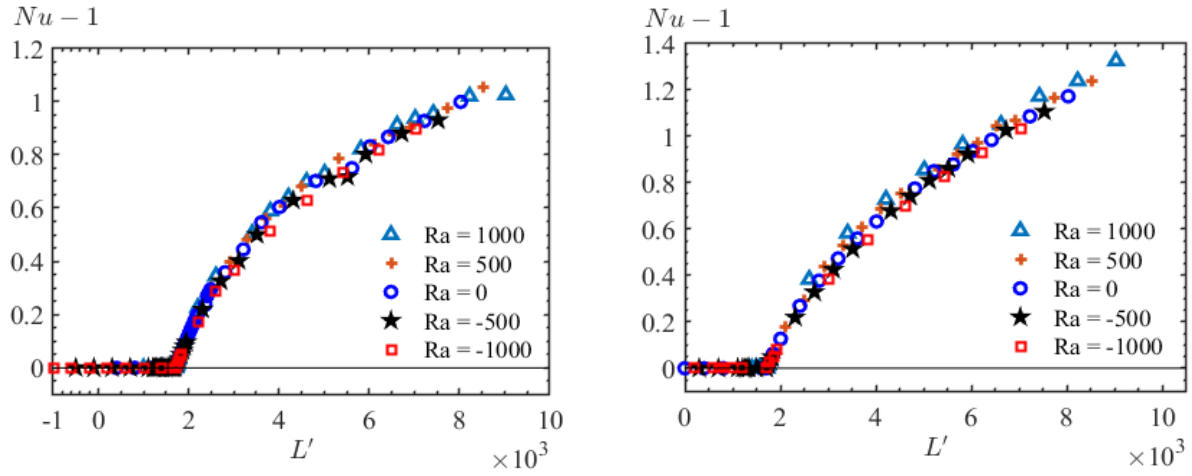

Figure 4.60: Variation of the Nusselt number Nu as a function of the modified Rayleigh number L' for some values of Ra and (a) $Pr = 1$, and (b) $Pr = 65$.

The unification of the Rayleigh Bénard thermoelectric convection problem by introducing the modified Rayleigh number $L' = Ra + (Ra_c^0/L_c^0)L$ requires the definition of an effective electric gravity g_{eff}:

$$L' = \frac{\alpha \Delta T d^3 g_{eff}}{\nu \kappa}. \tag{4.11}$$

Using the definition of the electric Rayleigh number, we can express the effective gravity of the unified problem as follows:

$$g_{eff} = g \cdot sign(\Delta T) + C g_e, \tag{4.12}$$

where the constant $C = Ra_c^0/L_c^0 = 0.8024$ and the electric gravity is $g_e = g_{e_b} + g'_e$. This definition of g_{eff} in equation (4.12) shows that the Earth's gravity stabilizes the system when

heated from the top (g_{eff} is diminished); while the total gravity is augmented when the system is heated from the bottom. The introduction of the effective gravity g_{eff} provides the possibility to simulate the thermoelectric convection patterns that could be generated in low-gravity environments (such Moon or Mars). One knows that the gravity of the Moon is 6 times smaller than the Earth's gravity and that of Mars is about 3 times smaller. Based on the equation (4.12), the gravity g can be diminished by the term of the electric gravity g_e such that to recover Mars or Moon gravity conditions. This shows the possibility to simulate the thermoelectric convection problem in varying gravity conditions.

For example, we consider a rectangular cavity filled with a dielectric liquid, heated from the top and subject to an alternating electric potential under terrestrial conditions. The effective value of the electric potential needed to realize an experiment that approximate the Moon or Mars gravity conditions can be computed as follows:

$$V_0 = \sqrt{\frac{1}{B \cdot C}\left(\tilde{g}_{eff} + g\right)}, \text{ with } B = \frac{\varepsilon_{ref} e}{\alpha \rho d^3} \gamma_e^3 \left[ln\left(\frac{1-\gamma_e/2}{1+\gamma_e/2}\right)\right]^{-2}; \tag{4.13}$$

where the quantity $\tilde{g}_{eff}$ is the effective electric gravity which corresponds to the gravity of the Moon $\tilde{g}_{eff}^{Moon} = \frac{1}{6} g$ or the gravity of Mars $\tilde{g}_{eff}^{Mars} = \frac{1}{3} g$. The values of V_0 for different dielectric liquids are presented in Table 4.3 for a system with gap size $d = 5\ mm$ and an applied temperature difference $\Delta T = 5\ K$. An experiment performed considering these parameters would approximatively correspond to experiments realized under Mars or Moon gravity conditions.

Table 4.3: Values of the effective electric potential necessary for the simulation of thermoelectric convection on Mars or on the Moon under terrestrial conditions.

Dielectric Fluids	AK5 (25°C)	AK0.65 (25°C)	Novec 7200 (25°C)	1-Nonanol (20°C)	Pure water (25°C)
γ_e	0.0053	0.0065	0.0195	0.0148	0.0230
V_0^{Moon} [kV]	114.31	105.51	28.81	36.08	2.28
V_0^{Mars} [kV]	122.20	112.80	30.80	38.57	2.43

4.8. Partial conclusion

Previous studies on the thermoelectric convection in the horizontal dielectric fluid were performed by Stiles *et al*. [28] and Yoshikawa *et al*. [32] considering a weakly non-linear analysis. Stiles have analyzed the dependence $Nu(Ra)$ for a wide range of $|Ra|$. He found a coefficient $C \approx 0.8$ for $Pr = 10$ under microgravity conditions. Yoshikawa *et al*. [32] recovered the same value by employing a two-dimensional weakly non-linear analysis, and they took into account the thermoelectric coupling effects on the threshold. Moreover, they found that C was independent of Pr around the threshold.

We have performed a numerical study of the thermoelectric convection induced by the dielectrophoretic force in a horizontal fluid layer, which can be heated from the top or the bottom. Results show that the critical electric Rayleigh number L_c depend on the value of the Rayleigh number Ra, while the corresponding instability consists of straight stationary rolls whatever the value of Ra as predicted by the linear stability analysis. Under microgravity conditions, different patterns are found in the dielectric fluid between two horizontal plates for different given values of the electric Rayleigh number L above the threshold. Thermal convection is set on with steady stationary rolls; and when L increases, the primary rolls are deformed and merge into complex patterns. The pattern regimes are similar to the structures generated by the Archimedean buoyancy in the Rayleigh-Bénard problem and they are characterized by a slow spatio-temporal modulation. The Nusselt number Nu, which characterizes the heat transfer, grows with increasing the intensity of the electric potential. This shows that dielectrophoretic buoyancy can be used in the generation of thermo-convective flows in microfluidic devices or in microgravity.

The analogy between the thermoelectric convection generated by the electric buoyancy under microgravity conditions and the ordinary Rayleigh-Bénard convection is presented in Figure 4.61. The sketch on the left shows the thermo-convective regimes for $Pr \in [1,65]$ under microgravity conditions ($Ra = 0$). As we already mentioned above (Chapter 3), the onset of the thermoelectric convection in a microgravity environment ($Ra = 0$) is delayed due to the dissipative nature of the perturbed part of electric gravity independently of Pr. However, the time-dependent convection appears at $L = 7000$ as in the case of the Rayleigh-Bénard convection for $Pr = 1$. When $Pr = 65$,

the steady cross-roll convection sets on at $L = 6500$. This value is lower than that obtained in the RBC where cross-roll instability appears at $Ra \approx 2.3 \cdot 10^4$.

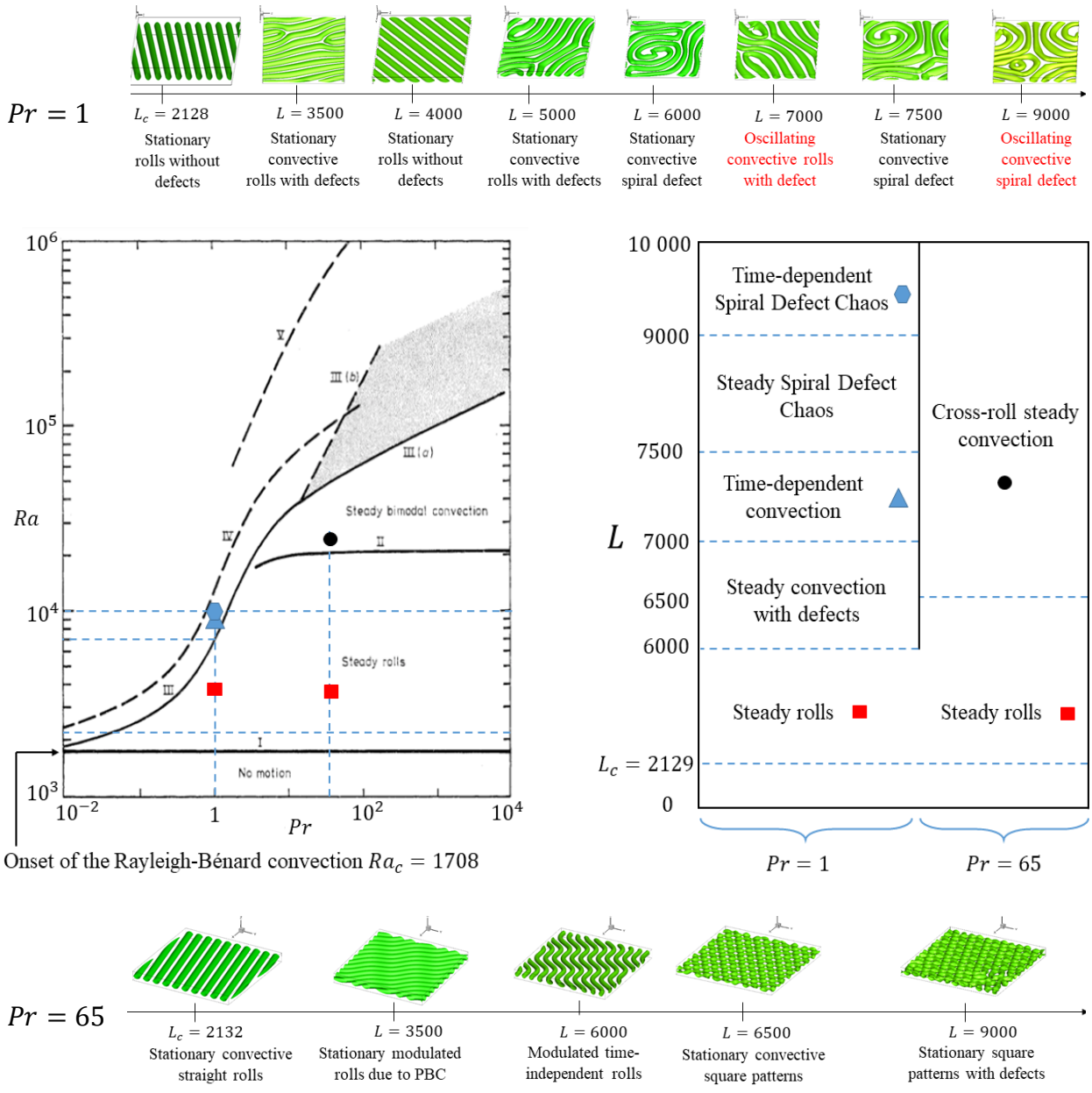

Figure 4.61: (a) The Busse diagram [35] shows the transitions in the Rayleigh-Bénard convection as a function of Ra and Pr: (I) steady rolls regime, (II) three-dimensional convection, (III) time-dependent convection, and (IV) turbulent convection. (b) Regimes of thermoelectric convection as a function of L under microgravity conditions ($Ra = 0$) for $Pr = \{1,65\}$.

Chapter 5: Thermoelectric convection in a vertical cavity filled with a dielectric fluid

In this section, we investigated the stability of a dielectric fluid layer in a vertical rectangular cavity subject to a horizontal temperature difference and an alternating electric potential. In such a configuration, the electric gravity is perpendicular to the Earth's gravity since it is oriented from the cold plate toward the hot plate. The main objective of this study is to perform a 3D linear stability analysis to determine the critical parameters and the nature of the critical modes and to predict critical modes that may occur in vertical rectangular cavities set during the g and hypergravity phases of parabolic flights when the power is not turned off. The study is inspired by the DNS results on columnar thermo-convective rolls in the vertical cylindrical annulus subjected to both Archimedean and electric buoyancies in Earth conditions [20,21,74].

5.1. Flow configuration

We consider a dielectric fluid inside a vertical rectangular cavity subject to a horizontal transverse temperature difference ΔT and a high-frequency electric potential that generates an electric field $\vec{E}$ (See Figure 5.1).

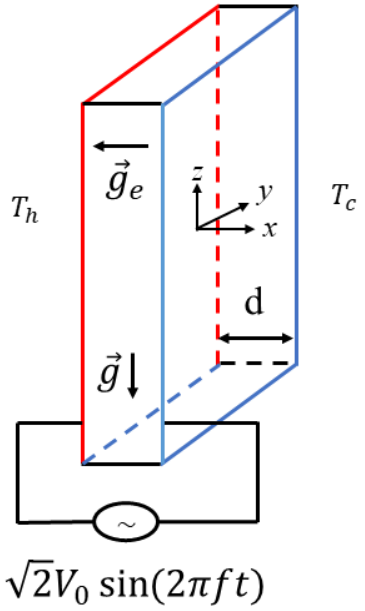

Figure 5.1: A vertical slot filled by a dielectric fluid, subject to a horizontal temperature gradient and an alternating electric field of effective voltage V_0.

The flow in the vertical slot can be described by the couple of equations (2.26)-(2.29) defined in Chapter 2. The vertical electrodes are uniformly kept at different temperatures T_c (cold) and T_h (hot). The reference temperature is defined as follows $T_{ref} = \frac{T_h + T_c}{2}$ and the temperature difference is $\Delta T = T_h - T_c$. The boundary conditions imposed on the electrodes are:

$$\left.\begin{aligned} u = v = w = 0, \theta = \frac{1}{2}, \phi = 1 \; at \; x = -1/2 \\ u = v = w = 0, \theta = -\frac{1}{2}, \phi = 0 \; at \; x = 1/2. \end{aligned}\right\} \tag{5.1}$$

5.2. Base state

For small temperature differences and weak electric voltage, the system of equations (2.26)-(2.29) with boundary conditions has a steady-state solution described by $\vec{u} = W_b(x)\vec{e}_z, \theta = \theta_b(x), \phi = \phi_b(x)$. In this state, the motions of fluid particles are aligned to isotherms, due to the shear flow, so the temperature field is determined only by heat conduction without any advection effect. The equations governing the basic state are [42]:

$$\left.\begin{aligned} \frac{d\pi_b}{dx} + \frac{L}{Pr}\theta_b g_{eb} = 0, \\ \frac{d^2W_b}{dx^2} + Gr\theta_b = 0, \\ \frac{d^2\theta_b}{dx^2} = 0, \\ (1-\gamma_e\theta_b)\frac{d^2\phi_b}{dx^2} - \gamma_e\frac{d\theta_b}{dx}\frac{d\phi_b}{dx} = 0. \end{aligned}\right\} \tag{5.2}$$

The solutions of these equations (5.2) subject to the boundary conditions (5.1) are:

- Basic velocity: $W_b = \frac{1}{6}Gr \cdot x\left(x^2 - \frac{1}{4}\right)$, where the Grashof number is $Gr = Ra/Pr$;
- Basic temperature profile: $\theta_b = -x$;
- Basic electric potential: $\phi_b = \ln\left(\frac{1+\gamma_e x}{1+\gamma_e/2}\right)\left[\ln\left(\frac{1-\gamma_e/2}{1+\gamma_e/2}\right)\right]^{-1}$;
- Basic electric field : $E_b = \frac{\gamma_e}{\ln\left(\frac{2-\gamma_e}{2-\gamma_e}\right)} \cdot \frac{1}{1+\gamma_e x}$.

From equation (2.8) and the solution of the basic electric field, the electric gravity of the base flow is obtained x: $g_{eb} = -[1+\gamma_e x]^{-3}$. The basic electric gravity remains the same as in the case of the horizontal configuration. Accordingly, the definition of the electric Rayleigh number remains the same as in the horizontal configuration: $L = \frac{\varepsilon_1 {\phi_0}^2 {\gamma_e}^4}{\rho\kappa\nu}\left[\ln\left(\frac{1-\gamma_e/2}{1+\gamma_e/2}\right)\right]^{-2}$.

Fluid particles move upward near the hot electrode and downward near the cold electrode. The vorticity of the base flow is given by:

$$\vec{\omega}_b = -\frac{dW_b}{dx}\vec{e}_y = -\frac{1}{6}Gr\left(3x^2 - \frac{1}{4}\right)\vec{e}_y. \tag{5.3}$$

The pressure distribution is then obtained by straightforward integration of the first equation of the set of (5.2) and it reads:

$$\pi_b(x) = \frac{L}{Pr} \cdot \frac{2\gamma_e x+1}{2\gamma_e^2(\gamma_e x+1)^2}.$$

The profiles of the axial velocity W_b, vorticity ω_b, temperature θ_b, electric potential ϕ_b, and the electric field are shown in Figure 5.2. We can observe, from Figure 5.2(e), that intensity of the electric field of the base state is stronger at the hot plate.

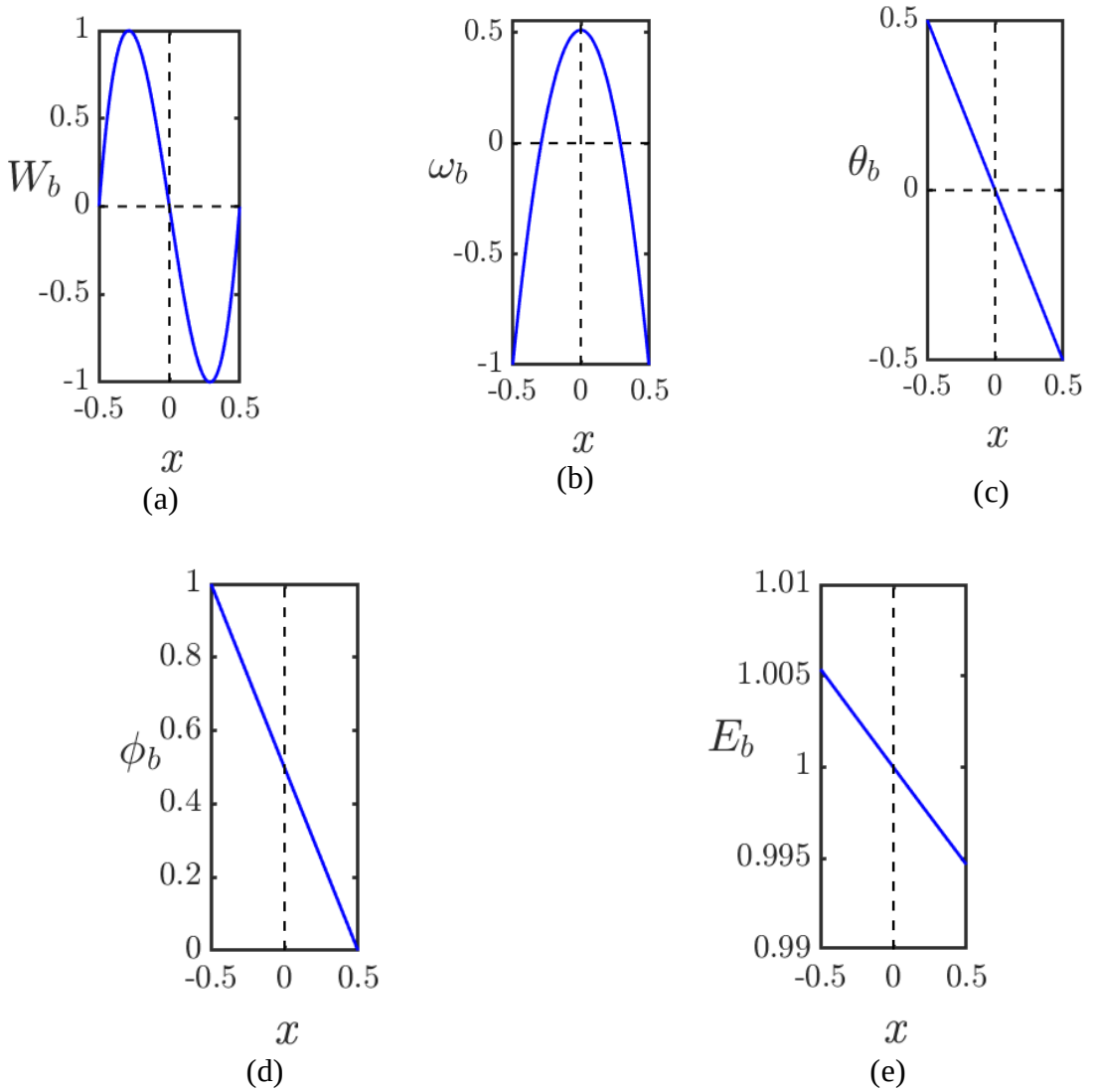

Figure 5.2: Profiles of velocity (a), vorticity (b), temperature (c), electric potential (d), and electric field (e) of the base state flow for $Ra = 800$.

5.3. Linear stability equations

To analyze the stability of the flow, we superimpose to the base flow infinitesimal perturbations and we linearize the resulting equations. Since the system is assumed infinite along the horizontal direction y and the vertical direction z, the perturbations are developed into normal modes as follows :

$$\begin{bmatrix} u'(x,y,z,t) \\ v'(x,y,z,t) \\ w'(x,y,z,t) \\ \pi'(x,y,z,t) \\ \theta'(x,y,z,t) \\ \phi'(x,y,z,t) \end{bmatrix} = \begin{bmatrix} U(x) \\ V(x) \\ W(x) \\ \Pi(x) \\ \Theta(x) \\ \Phi(x) \end{bmatrix} exp\big[st + i\big(k_y y + k_z z\big)\big] + c.c$$

The complex amplitudes $[U(x), V(x), W(x), \Pi(x), \Theta(x), \Phi(x)]$ of normal modes then satisfy the following equations:

$$\left.\begin{array}{c} DU + i\big(k_y V + k_z W\big) = 0, \\ [s - (D^2 - k^2) + ik_z W_b]U = -D\Pi - LPr^{-1}\big(g_{eb}\Theta + \theta_b G_{e_x}\big), \\ [s - (D^2 - k^2) + ik_z W_b]V = -ik_y \Pi - LPr^{-1}\theta_b G_{e_y}, \\ [s - (D^2 - k^2) + ik_z W_b]W + DW_b U = -ik_z \Pi + Pr^{-1}\big(Ra\Theta - L\theta_b G_{e_z}\big), \\ U = [s - Pr^{-1}(D^2 - k^2) + ik_z W_b]\Theta, \\ [(1 + \gamma_e x)(D^2 - k^2) + \gamma_e D]\Phi - \gamma_e [D^2\phi_b + D\phi_b D]\Theta = 0, \end{array}\right\} \quad (5.4)$$

where $k^2 = k_y^2 + k_z^2$ with k_y and k_z, the wavenumbers along y and z respectively; and the operator $D = d/dx$. The quantity s is the complex growth rate of perturbations. The linear stability system of equations (5.4) contains the base flow velocity component, temperature, and electric field. Thus, three types of modes can be excited in such a system: hydrodynamic modes, thermal modes, or electric modes. The present study aims to determine the conditions of the excitation of these different modes.

The boundary conditions for the perturbations are:

$$U = V = W = \Pi = \Theta = \Phi = 0 \text{ at } x \pm 1/2. \quad (5.5)$$

In the system of equations (5.4), we have taken into account perturbations in the electric gravity.

5.4. Results of linear analysis

5.4.1. Marginal stability curves

We computed the growth rate $s = s(Ra, L, Pr, k_y, k_z)$ with varying Ra for fixed other parameters and then we determined a marginal condition for Ra, where the real part $\sigma = Re(s)$ of the fast-growing mode changes its sign. The determination of marginal conditions for different values of wavenumbers yields a marginal stability hypersurface $Ra = Ra(L, Pr, k_y, k_z)$ or $L = L(Ra, Pr, k_y, k_z)$. The problem contains three control parameters that participate in the selection of critical modes: for a fixed Pr and $L < L_c$, the critical modes may be either hydrodynamic ($Pr < 12.45$)or thermal modes ($Pr > 12.45$). For fixed Pr and Ra, the critical modes may be electric modes which are monitored by L. For given values of the control parameters (L, Pr), the global minimum $Ra = Ra_c$ of the marginal surface gives a critical condition $(k_{yc}, k_{zc}, Ra_c, \omega_c)$.

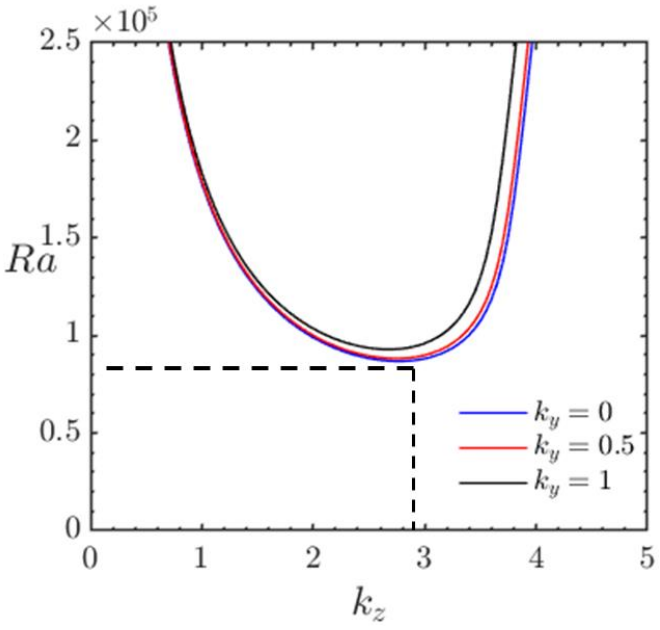

Figure 5.3: Marginal stability curves for $Pr = 11.03$ and $L = 0$.

Figure 5.3 gives the marginal stability curve for $Pr = 11.03$ when no electric field is applied $(L = 0)$; the liquid is the Novec 7200 used in experiments. Curves correspond to marginal states for three different values of k_y. The lowest curve corresponds to the mode with

$Ra_c = 8.683 \cdot 10^4, k_c = 2.765, k_y = 0$ and $\omega_c = 0$; the critical mode is then stationary hydrodynamic transverse mode.

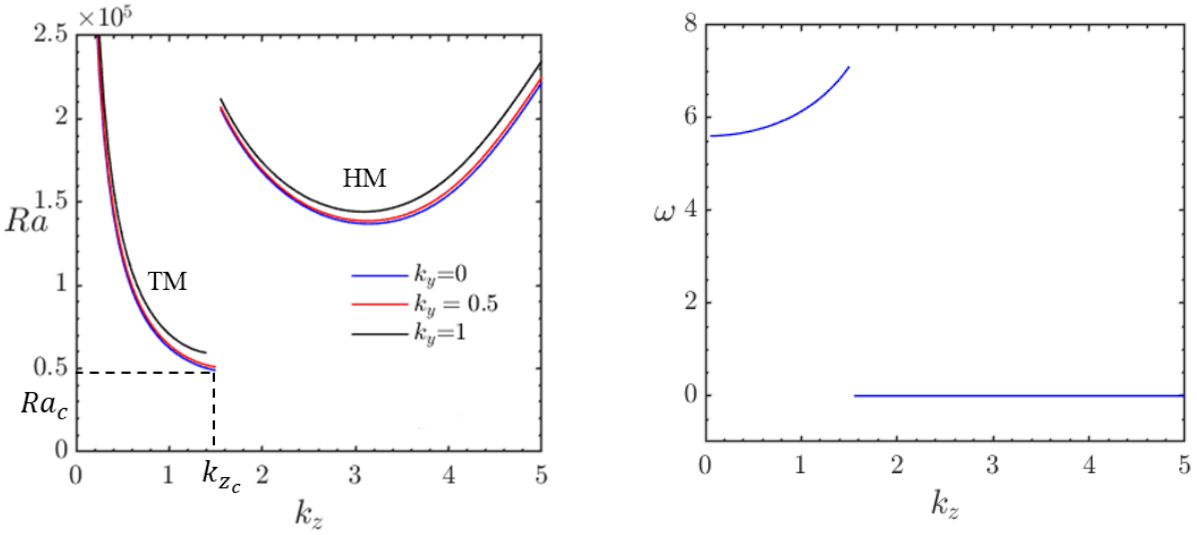

(a) (b)

Figure 5.4: (a) Marginal stability curves for $Pr = 20$ and $L = 170$ - the lowest curve ($k_y = 0$) is the marginal state; and (b) the frequency that corresponds to the marginal state.

Figure 5.4 shows three marginal stability curves for $Pr = 20$, $\gamma_e \ll 1$, and low values of the electric potential. The system is stable below the blue curve ($\sigma < 0$), while it becomes unstable in the zone under the marginal curve ($\sigma > 0$). The lowest point of the blue curve gives then the critical gravitational Rayleigh number Ra_c, the critical wavenumber k_c and the critical frequency ω_c. Two branches are observable in Figure 5.4 (a): Thermal Mode (TM) and Hydrodynamic Mode (HM). Curves illustrate that the TM is the lowest one for $Pr = 20$. The values of critical parameters are tabulated in Appendix C for different values of Pr and L. To investigate the occurrence of the electric modes, we fix $Ra < Ra_c$ and vary L i.e. we look for the hypersurface $L = L(Ra, Pr, k_y, k_z)$.

5.4.2. Critical modes

The critical conditions are determined for different values of $Pr\epsilon$ [0.3, 10^4]. The critical modes are hydrodynamic, thermal, or electric, depending on the values of the parameters (L, Ra, Pr). The hydrodynamic modes (HM) appear in fluids with $Pr < 12.45$ in form of stationary transverse convective rolls which are periodic along the z-direction with the wavenumber ($k_z \approx 2.8$) and are invariant in the y-direction ($k_y = 0$). Their critical parameters $(Gr_c = Ra_c/Pr, k_c)$ weakly depend on Pr [39,42,57].

The thermal modes (TM) appear in fluids with $Pr > 12.45$ in form of oscillatory ($\omega \neq 0$) horizontal convective rolls. Like hydrodynamic modes, thermal modes have periodicity along the z-direction ($k_z \neq 0$) and are invariant in the y-direction. Since thermal modes are oscillatory, we have computed the corresponding phase velocity:

$$c = \omega_c/k_c. \tag{5.6}$$

This critical phase velocity c of thermal convective rolls decreases with Pr as shown in Table 5.1. The critical phase velocity must be smaller than the maximum of the base flow velocity computed at the threshold value $W_b^{max} = \sqrt{3}\, Gr_c/216$ which should be the velocity of perturbations in inviscid homogeneous parallel shear flows [85].

Table 5.1 gives the critical values of HM and TM for different values of Pr. We have also introduced the values of W_b^{max} for HM for completeness, their weak variation is due to the weak variation in Gr_c. Following the analysis of Gershuni-Zhukhovitskii [39], we found that the critical value Gr_c of thermal modes decreases with Pr following the law $Gr_c = A/\sqrt{Pr}$, $A = 9400$ (Table 5.1). Table 5.2 also shows the critical parameters of the transverses instabilities (HM & TM) for two values of the Prandtl number Pr.

Table 5.1: Critical parameters for different values of Pr and $L = 0$.

Modes	Pr	Ra_c	Gr_c	k_c	ω_c	c	W_b^{max}
HM	0.3	2370	7896	2.73	0	0	63.35
	1	7940	7.940	2.81	0	0	63.69
	10	$7.73 \cdot 10^4$	7730	2.83	0	0	61.90
TM	20	$4.86 \cdot 10^4$	2430	1.53	28.88	18.66	102.05
	60	$5.94 \cdot 10^4$	992	2.33	18.64	7.86	40.96
	100	$7.46 \cdot 10^4$	746	2.40	14.67	6.04	31.24
	500	$1.71 \cdot 10^5$	342	2.63	7.51	2.84	14.16
	1000	$2.46 \cdot 10^5$	246	2.68	5.53	2.04	10.41
	10000	$8.93 \cdot 10^5$	89	2.33	1.64	0.72	3.71

For low values of the electric potential, the electric Rayleigh number has almost no effect on the critical parameters (Gr_c, k_c, ω_c). When L reaches $L_c \approx 2128.6$, we observe the switch from the thermal or hydrodynamic modes to the electric mode (EM) due to the dielectrophoretic buoyancy which dominates the action of the torque of the Archimedean buoyancy. The electric mode occurs in form of vertical vortices (i.e. with an axis parallel to the z −axis) and they are periodic along the y-direction i.e. $k_z = 0$. The critical wavenumber is $k_c = k_{y_c} \approx 3.2$. We found that the threshold of the electric modes is independent of the diffusive properties of the dielectric fluid i.e. of Pr (Table 5.3) as in the case of the thermoelectric convection in microgravity. The threshold of the electric modes is also independent of the Archimedean buoyancy i.e. $L = L_c(Ra) = 2128.6;\ \forall\, Ra < Ra_c$.

Surprisingly, in the Earth's gravity, we have found that the threshold of the thermoelectric convection in a vertical cavity is $L_c(Ra) = 2128.6$ (within the numerical precision of 0.03%). The critical modes are electric and they consist of stationary vertical convective rolls, i.e., columnar vortices with a periodicity in the y-direction ($k_{y_c} \approx 3.23$) and invariant in the z-direction ($k_z =$

0). This result is in contrast with the results of Takashima & Hamabata [58] and Tadie Fogaing [42] who assumed that perturbations were two-dimensional in the $x-z$ plane and missed the modes in the y-direction. Indeed, they found the same value of $L_c(Ra) = 2128.7$, but their critical modes were transverse (i.e. with $k_{z_c} = 3.23, k_y = 0$).

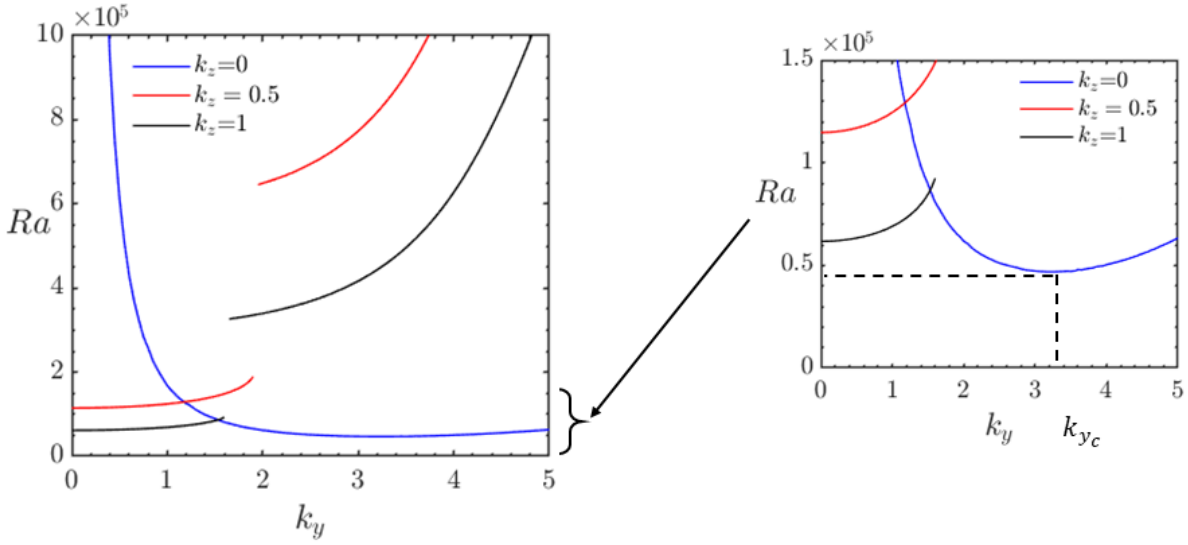

Figure 5.5: Marginal stability curves for $Pr = 20$ and $L = 2128.6$; the lowest curve ($k_z = 0$) is the marginal state.

We have presented in Figure 5.5 the marginal stability curves for $Pr = 20$ when $L = 2128.6$. The corresponding critical mode is an electric mode with the following corresponding $k_{z_c} = 0$ and $k_{y_c} \neq 0$. This shows that the electric mode has periodicity in the $y-$direction i.e columnar mode.

Table 5.2: Critical parameters for $Pr = 5$ (Hydrodynamic Modes) and $Pr = 15$ (Thermal Modes).

k_{z_c}	k_y	Gr_c	Ra_c	γ_e	L	ω_c
Hydrodynamic modes ($Pr = 5$)						
2.77	0.00	7860.50	39302.510	$1.97 \cdot 10^{-2}$	0	0
2.77	0.00	7820.37	39101.825	$1.96 \cdot 10^{-2}$	682.525	0
2.77	0.00	7780.24	38901.215	$1.95 \cdot 10^{-2}$	1358.460	0
Thermal modes ($Pr = 15$)						
1.083	0.00	4018.998	$6.03 \cdot 10^{4}$	10^{-2}	0	-33.16
1.083	0.00	4001.975	$6.00 \cdot 10^{4}$	10^{-2}	1047.821	-32.97
1.083	0.00	3999.909	$5.997 \cdot 10^{4}$	10^{-2}	1152.033	-32.95
1.083	0.00	3997.718	$5.996 \cdot 10^{4}$	10^{-2}	1256.104	-32.93
1.083	0.00	3995.492	$5.989 \cdot 10^{4}$	10^{-2}	1360.056	-32.91
1.083	0.00	3993.261	$5.989 \cdot 10^{4}$	10^{-2}	1463.898	-32.90
1.083	0.00	3991.067	$5.987 \cdot 10^{4}$	10^{-2}	1567.647	-32.88
1.083	0.00	3988.866	$5.983 \cdot 10^{4}$	10^{-2}	1671.287	-32.86
1.083	0.00	3986.625	$5.979 \cdot 10^{4}$	10^{-2}	1774.804	-32.84
1.083	0.00	3984.428	$5.976 \cdot 10^{4}$	10^{-2}	1878.236	-32.82
1.083	0.00	3982.238	$5.973 \cdot 10^{4}$	10^{-2}	1981.567	-32.80

Table 5.3: Critical parameters for $Pr = 5$ and $Pr = 15$ (Electric Modes).

k_z	k_{y_c}	Gr	Ra	γ_e	L_c
Columnar vortices ($Pr = 5$)					
0.00	3.20	7601.92	38009.610	$1.90 \cdot 10^{-2}$	2125.067
0.00	3.20	6960.40	34802.010	$1.74 \cdot 10^{-2}$	2128.582
0.00	3.23	6088.03	30440.155	$1.52 \cdot 10^{-2}$	2128.583
0.00	3.25	2414.12	12070.600	$6.04 \cdot 10^{-3}$	2128.373
0.00	3.23	1169.71	5848.530	$2.92 \cdot 10^{-3}$	2128.691
0.00	3.23	737.40	3687.002	$1.84 \cdot 10^{-3}$	2128.692
0.00	3.23	507.37	2536.871	$1.27 \cdot 10^{-3}$	2128.687
0.00	3.23	357.24	1786.187	$8.93 \cdot 10^{-4}$	2128.695
0.00	3.24	245.81	1229.046	$6.15 \cdot 10^{-4}$	2128.769
0.00	3.20	154.94	774.702	$3.87 \cdot 10^{-4}$	2128.475
Columnar vortices ($Pr = 15$)					
0	3.229	4062.810	$6.09 \cdot 10^{4}$	$1.02 \cdot 10^{-2}$	2128.147
0	3.229	2707.844	$4.06 \cdot 10^{4}$	$6.77 \cdot 10^{-3}$	2128.681
0	3.229	1621.816	$2.43 \cdot 10^{4}$	$4.05 \cdot 10^{-3}$	2128.357
0	3.230	804.816	$1.21 \cdot 10^{4}$	$2.01 \cdot 10^{-3}$	2128.660
0	3.231	529.493	$7.9 \cdot 10^{3}$	$1.32 \cdot 10^{-3}$	2128.159
0	3.254	389.840	$5.85 \cdot 10^{3}$	$9.75 \cdot 10^{-4}$	2128.354
0	3.246	304.246	$4.56 \cdot 10^{3}$	$7.61 \cdot 10^{-4}$	2128.087
0	3.237	245.802	$3.69 \cdot 10^{3}$	$6.15 \cdot 10^{-4}$	2128.705
0	3.245	202.681	$3.04 \cdot 10^{3}$	$5.07 \cdot 10^{-4}$	2128.780
0	3.250	169.067	$2.54 \cdot 10^{3}$	$4.23 \cdot 10^{-4}$	2127.964
0	3.192	141.912	$2.13 \cdot 10^{3}$	$3.55 \cdot 10^{-4}$	2128.673
0	3.230	119.071	$1.79 \cdot 10^{3}$	$2.98 \cdot 10^{-4}$	2128.545

The thresholds of the different modes obtained in the vertical slot for different values of Pr are shown in the $L - Ra$ plane in Figure 5.6. One observes that the critical parameters of HM and TM do not exhibit any significant variation with L, meaning that these modes are not sensitive to the electric field intensity, except in the case of low values of $Pr \leq 0.3$. For these low values of Pr, the threshold of HM decreases as L increases before reaching the value L_c. We are not aware of dielectric fluids with such low values of Pr, so that this result may not have any practical relevance. The electric modes obtained in the vertical slot are similar to columnar vortices obtained in cylindrical annulus under combined effects of dielectrophoretic and Archimedean buoyancies found by Meyer *et al*. [20] and numerically investigated later by Kang and Mutabazi [21,74]. The electric modes in the cylindrical annulus in microgravity are stationary and helical; moreover, their threshold is a function of the radius ratio [65].

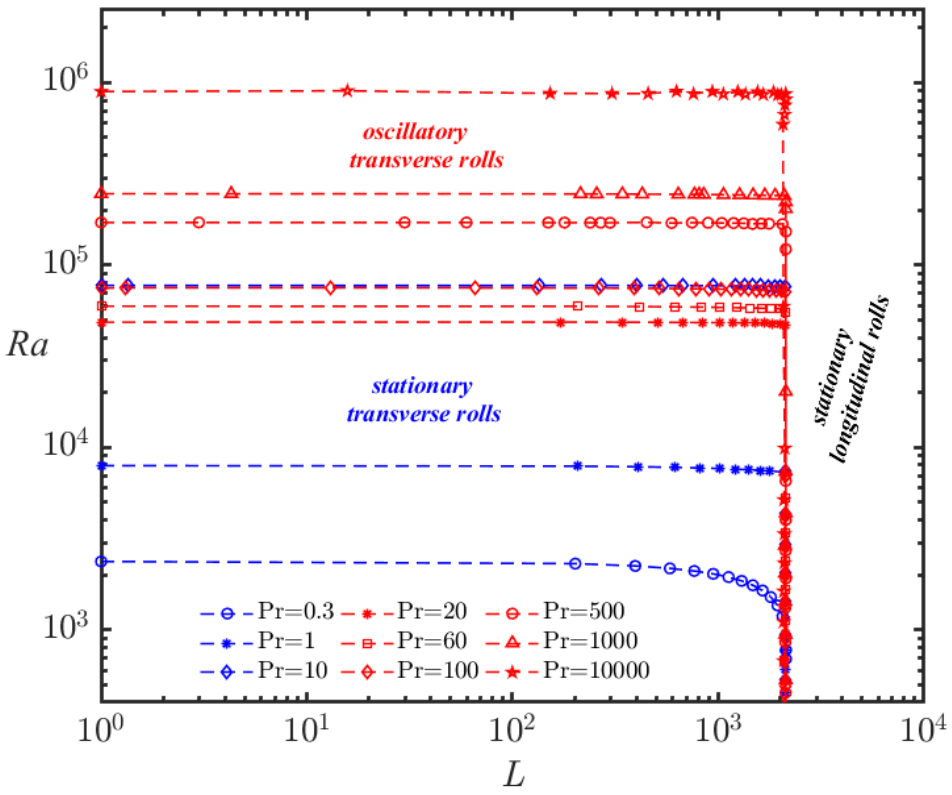

Figure 5.6: Variation of the threshold of the critical modes in the plane (L, Ra) for $Pr \in [0.3, 10^4]$. Blue lines correspond to HM, and red lines represent TM. EM has a unique threshold represented by the vertical line located at $L_c = 2128.6$.

In the absence of an electric field ($L = 0$), we found the ordinary problem of natural convection in a vertical slot. Figure 5.7 shows the critical values of the wavenumber (k_c) and the frequency (ω_c) respectively, for different values of L. The critical parameters (k_c,ω_c) and the phase velocity c are independent of the value of L for weak values of the electric field. Close to the threshold $L \approx L_c = 2128.6$ the electric field has a weak effect on the wavenumber k_c. This is due to the mechanism of switching from transverse modes to the columnar vortices in which the perturbations have to reorganize themselves.

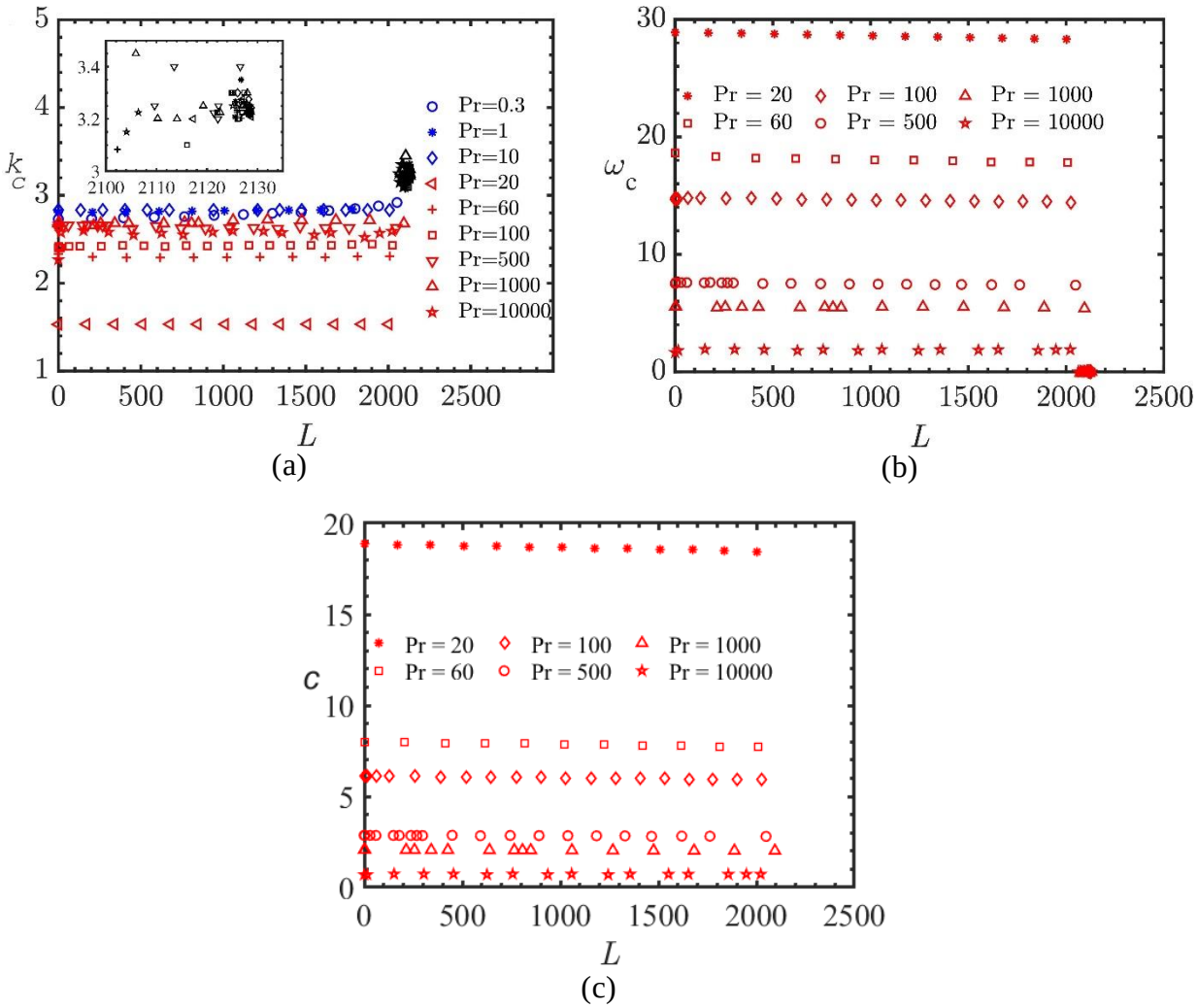

Figure 5.7: Variation of critical parameters (k_c, ω_c) with the electric Rayleigh number L for different values of Prandtl number Pr: (a) critical wavenumber (k_c); (b) critical frequency (ω_c); (c) phase velocity. Blue points correspond to HM (stationary modes), red points correspond to TM modes (oscillatory modes), and black points to EM (stationary modes).

5.4.3. Perturbation flow fields at the critical point

In this study, we did not enter into details about the transition from stationary modes to oscillatory modes. A rigorous explanation of the distinction of hydrodynamic from thermal modes can be found in the literature [36,40]. In particular, it was shown that HM originates from Kelvin-Helmholtz instability of the base profile $W_b(x)$ leading to cat's eyes vortices which are inclined in the gap. An illustration of the possible solutions to the thermoelectric instability in a vertical slot at the threshold is presented in Figure 5.8. For hydrodynamic and thermal modes, the transverse velocity component $v' = 0$ while for the electric modes there is no vertical velocity component $(w' = 0)$. Velocity fields (u', w'), temperature perturbation θ', and perturbed electric potential ϕ' of critical hydrodynamic modes are displayed in Figure 5.9 and Figure 5.10. One observes strong variations in temperature perturbations θ' (hot and cold zones) around the mid-plane $(x = 0)$. Velocity fields and isotherms of convective rolls of HM have inclined cross-sections due to the basic shear flow. The description of the flow structure in HM can be found in Lee and Korpela [40]. The transverse velocity u' and the axial velocity w' contours of HM do not depend on the Prandtl number Pr; while isotherm patterns and equipotentials change with Pr.

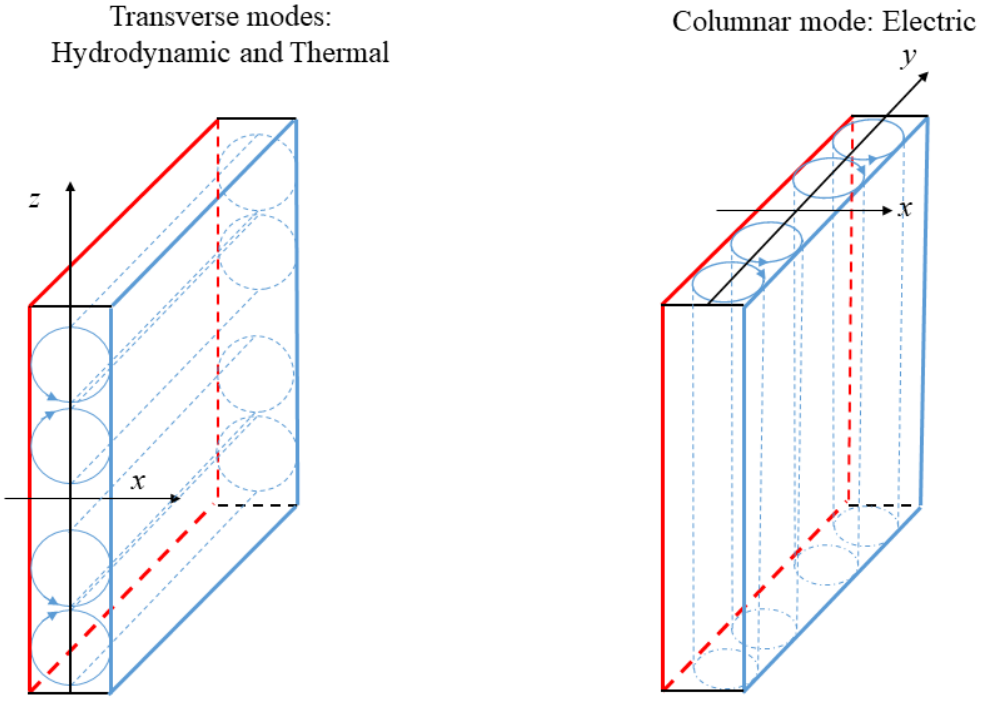

Figure 5.8: A schematic illustration of different critical modes occurrence.

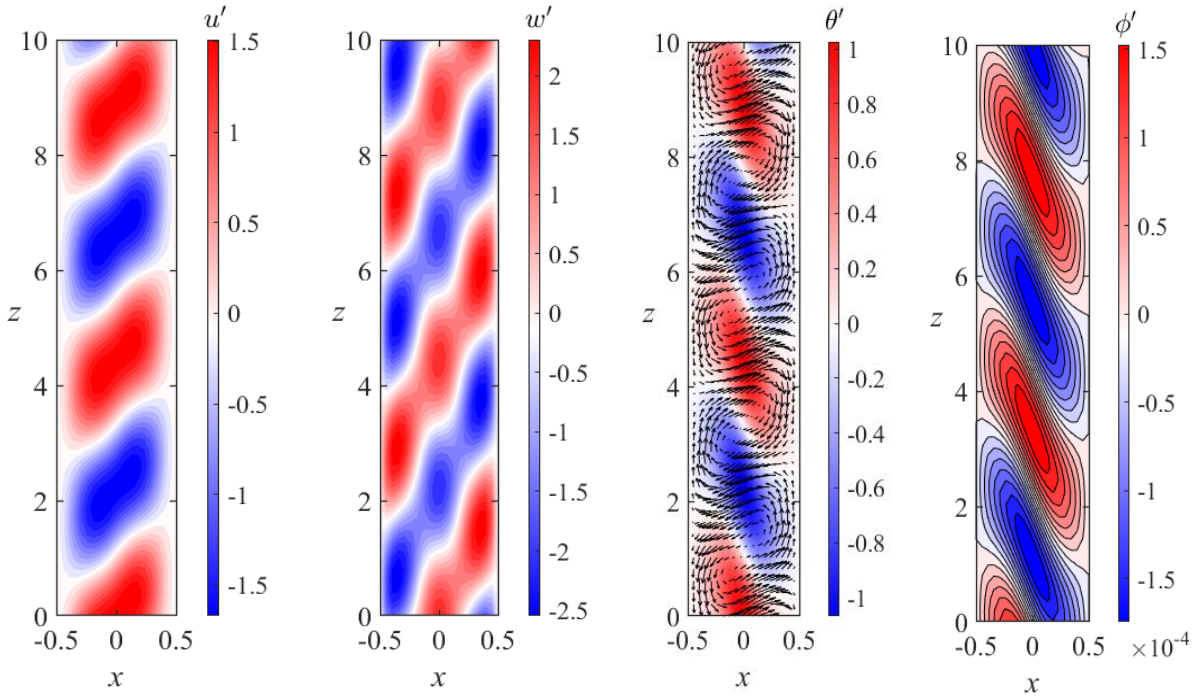

Figure 5.9: Perturbation flow fields of critical hydrodynamic mode for $Pr = 1$, $L = 1461.76$, $Ra_c = 7.52 \cdot 10^3$ and $\gamma_e = 1.89 \cdot 10^{-2}$. (a) Perturbation velocity component along the x-direction u'; (b) the axial perturbation velocity w'; (c) Velocity vectors and isotherm patterns θ'; and (d) the electric potential perturbation ϕ' of the perturbations.

Figure 5.10 shows the eigenfunctions of the dielectric liquid (Novec 7200).

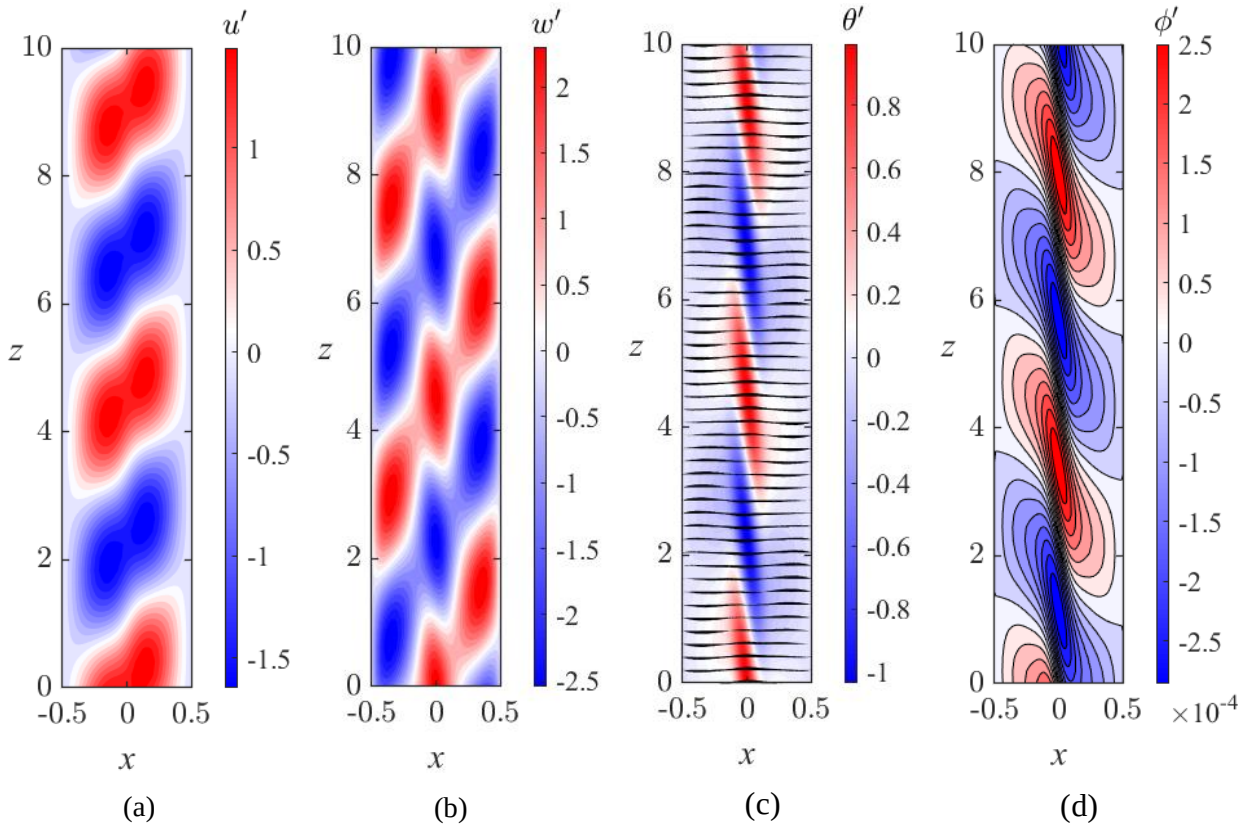

Figure 5.10: Perturbation flow field of critical hydrodynamic mode for $Pr = 11.03$, $L = 0$, $Ra_c = 8.683 \cdot 10^4$and $k_{z_c} = 2.765$. (a) Perturbation velocity component along the x-direction u'; (b) the axial perturbation velocity w'; (c) Velocity vectors and isotherm patterns θ'; and (d) the electric potential perturbation ϕ' of the perturbations.

Figure 5.11 and Figure 5.12 show the flow fields of oscillatory critical thermal modes. We can highlight that TM has velocity and temperature fields different from HM. Indeed, strong variations in temperature perturbations θ' (hot and cold zones) in TM occur near the hot wall. Streamlines and isotherms of convective rolls of TM have an almost squared section and the size of rolls depends on the Pr. The equipotential lines show the difference in the flow behavior between HM and TM. For both hydrodynamic and thermal modes, the transverse velocity u' and the perturbation temperature θ' are in phase.

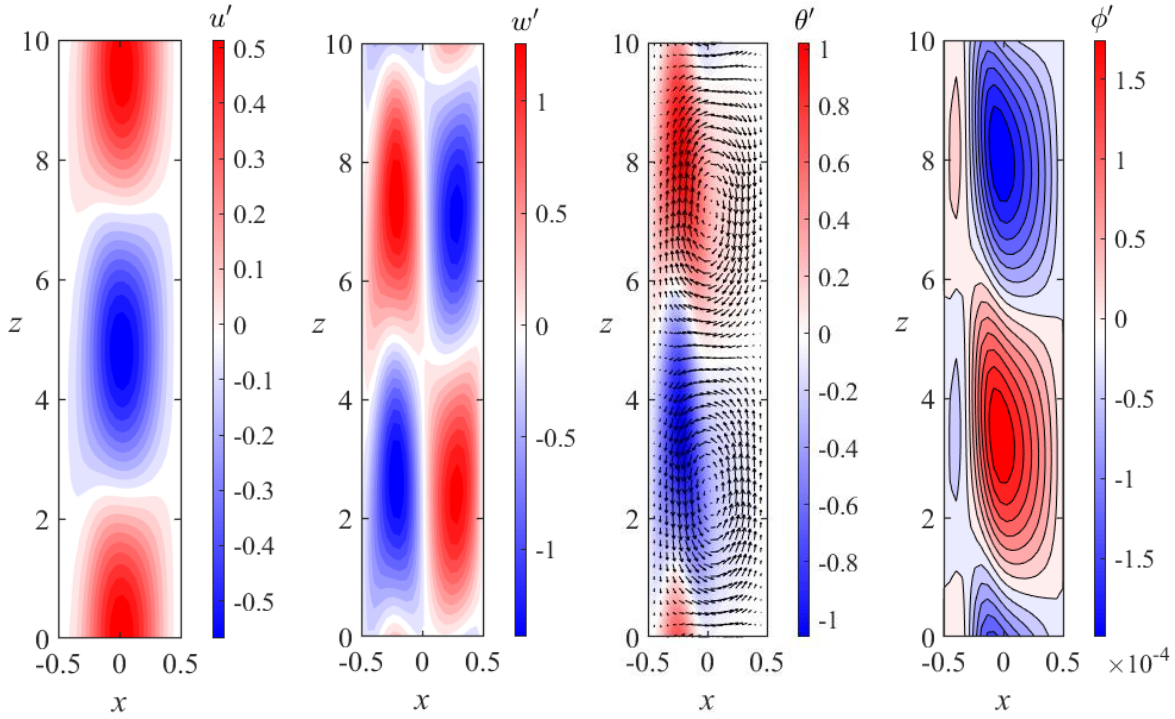

Figure 5.11: Perturbation flow field of critical thermal mode for $Pr = 20$, $L = 1655$, $Ra_c = 4.74 \cdot 10^4$, $k_{z_c} = 1.67$ and $\gamma_e = 6 \cdot 10^{-3}$. (a) Perturbation velocity component along the x-direction u'; (b) the axial perturbation velocity w'; (c) Velocity vectors and isotherm patterns θ'; and (d) the electric potential perturbation ϕ' of the perturbations.

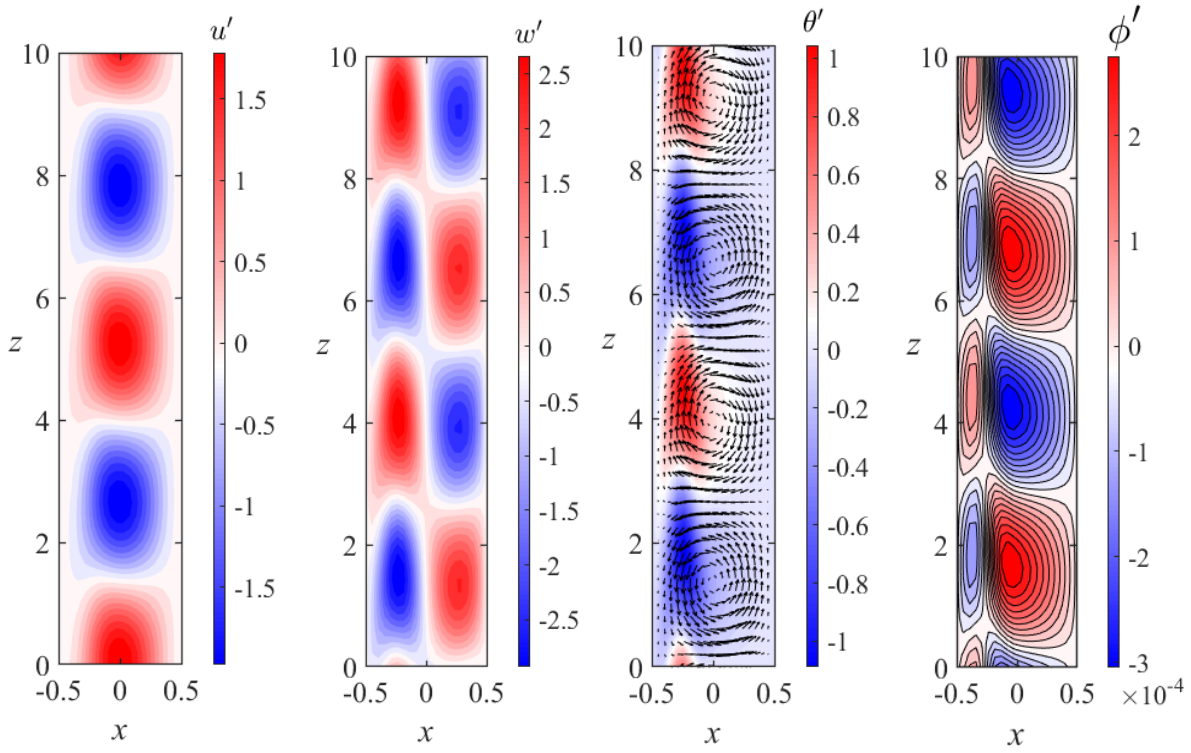

Figure 5.12: Perturbation flow field of critical thermal mode for $Pr = 100$, $L = 1282$, $Ra_c = 7.34 \cdot 10^4$ and $\gamma_e = 1.84 \cdot 10^{-3}$; (a) Perturbation velocity component along the x direction u'; and (b) the axial perturbation velocity w′; (c) Velocity vectors and isotherm patterns θ'; and (d) the electric potential perturbation ϕ' of the perturbations

The electric mode is invariant along the vertical direction and its velocity field has only two velocity components (u', v'). Figure 5.13 and Figure 5.14 show the perturbed flow of the critical electric mode for $Pr = 10$, $Ra = 2536.56$, and $\gamma_e = 6.34 \cdot 10^{-4}$. The velocity distributions (u', v') are presented in Figure 5.13; the temperature perturbation θ', the velocity vectors and equipotential in Figure 5.14. The hot and cold zones in convective vortices of the electric mode are located at the mid-plane $x = 0$. Figure 5.15 and Figure 5.16 show the averaged values of the egenfunctions of an critical electric mode inside the gap for $Ra = 0$.

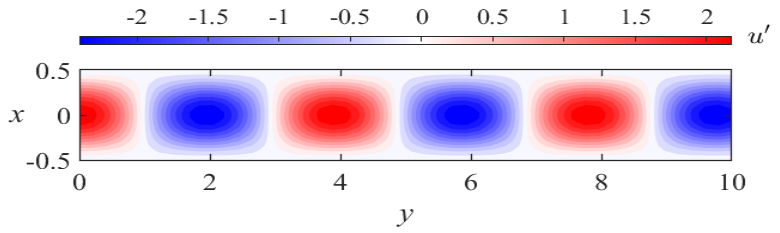

(a)

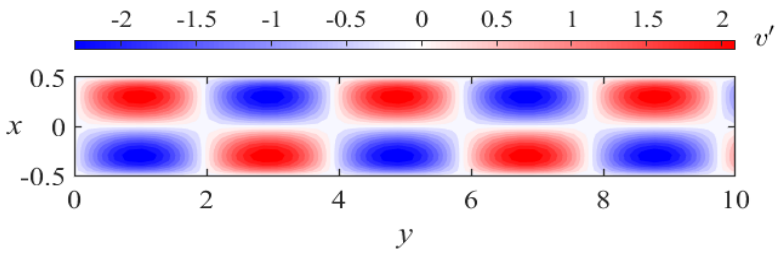

(b)

Figure 5.13: Perturbation velocity u' (a), and v' (b) at the threshold $L_c = 2128.6$ for $Pr = 10$, $Ra = 2536$ and $\gamma_e = 6.34 \cdot 10^{-4}$.

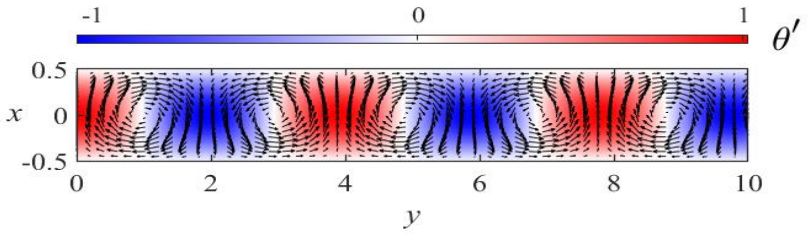

(a)

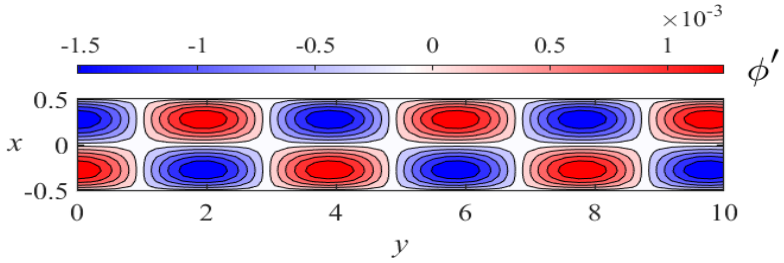

(b)

Figure 5.14: Flow fields of the critical electric mode for $Pr = 10$ and $Ra = 2536$: (a) streamline and isotherm patterns of the perturbations at the critical state (arrows represent velocity vectors); (b) equipotential lines.

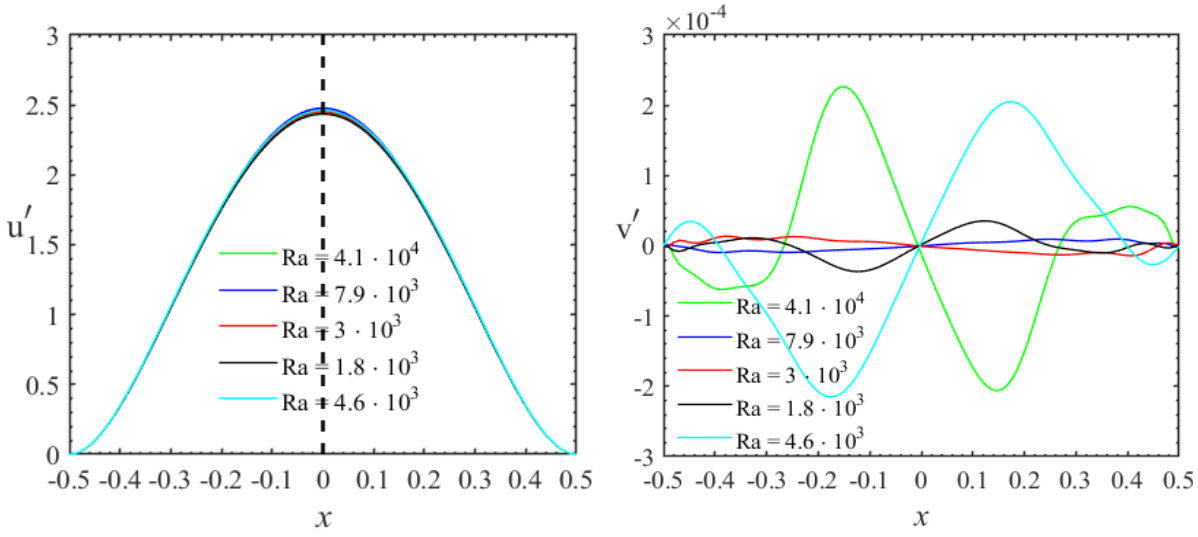

(a) (b)

Figure 5.15: Profile of perturbation amplitudes of velocity (u', v') for electric modes corresponding to $Pr = 15$ and different values of Ra and γ_e at the threshold ($L_c \approx 2129$).

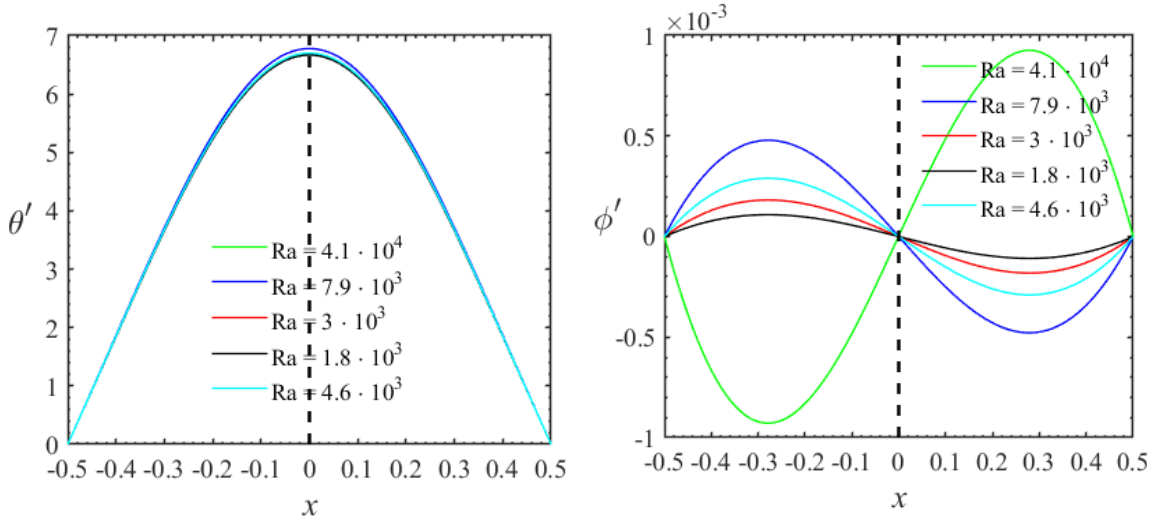

(a) (b)

Figure 5.16: Profile of temperature perturbation θ' (a) and the perturbation of electric potential ϕ' corresponding to $Pr = 15$ and different values of Ra and γ_e at the threshold ($L_c \approx 2129$).

5.5. Energetic analysis of the perturbed flow at the threshold

The base flow in the vertical cavity is characterized by a large convective cell. At the threshold, this base flow contributes to the total kinetic energy evolution of the perturbed flow due to the basic shear flow velocity W_b. The balance equation can be written as follows:

$$\frac{dK}{dt} = W_{sh} + W_G + W_{BEG} + W_{PEG} - D_v, \tag{5.7}$$

where $W_{sh} = -\int \frac{dW_b}{dx} u'w' \, dV$ is the power generated by the shear from the base flow. $W_G = \frac{Ra}{Pr}\int \theta' w' \, dV$ is the power of the Archimedian buoyancy; the base flow also contributes to the perturbed flow through the electric gravity $\vec{g}_{eb}$ and basic temperature θ_b. Their contributions are given by the power terms : $W_{BEG} = -\frac{L}{Pr}\int \theta' u' g_{eb} \, dV$ and $W_{PEG} = -\frac{L}{Pr}\int \theta_b \left(\overrightarrow{u'} \cdot \overrightarrow{g_e'}\right) dV$, power produced by g_{eb} and by the basic temperature combined with the perturbed electric gravity respectively. The local values of K, W_{sh}, W_G, W_{BEG}, and W_{PEG} are given by their density $E_c = \frac{1}{2}(u'^2 + v'^2 + w'^2)$, $w_{sh} = -\frac{dW_b}{dx}(u'w')$, $w_G = Gr(\theta' w')$, and $w_{BEG} = -\frac{L}{Pr} \cdot (\theta' u' g_{eb})$.

Since the dielectrophoretic effects predominate when the electric Rayleigh number reaches $L_c \approx 2129$, we will first analyze the effect of the electric Rayleigh number $(L < L_c)$ on the energy balance for transverse critical modes (hydrodynamic modes and thermal modes). Then, we will analyze the effect of the gravitational Rayleigh number Ra on the different terms of energy equation for electric modes.

We have presented in Figure 5.17 the density of the kinetic energy E_c of perturbations, the density of power of the Archimedean buoyancy w_G, the density of the power of the basic vorticity w_{sh}, and the density of power of the basic electric gravity w_{BEG} at the threshold for electric mode. One sees that for hydrodynamic modes, the distribution of the kinetic energy illustrates the inclination of HM cells (Figure 5.17 a). The power produced by the Archimedean buoyancy w_G presents positive zones at the central line of the cavity $(x = 0)$ and negative zones near the walls. The power density from the shear by the base flow w_{sh} is positive and strong at the active central zone $(x = 0)$ where the vorticity is maximum; and presents alternating positive and negative zones along the electrodes (Figure 5.17 c). The power density w_{BEG} shows that the power of the

dielectrophoretic buoyancy arising from the basic electric gravity is also strong in the central axis and follows approximately the same behavior as the Archimedean buoyancy (Figure 5.17 d).

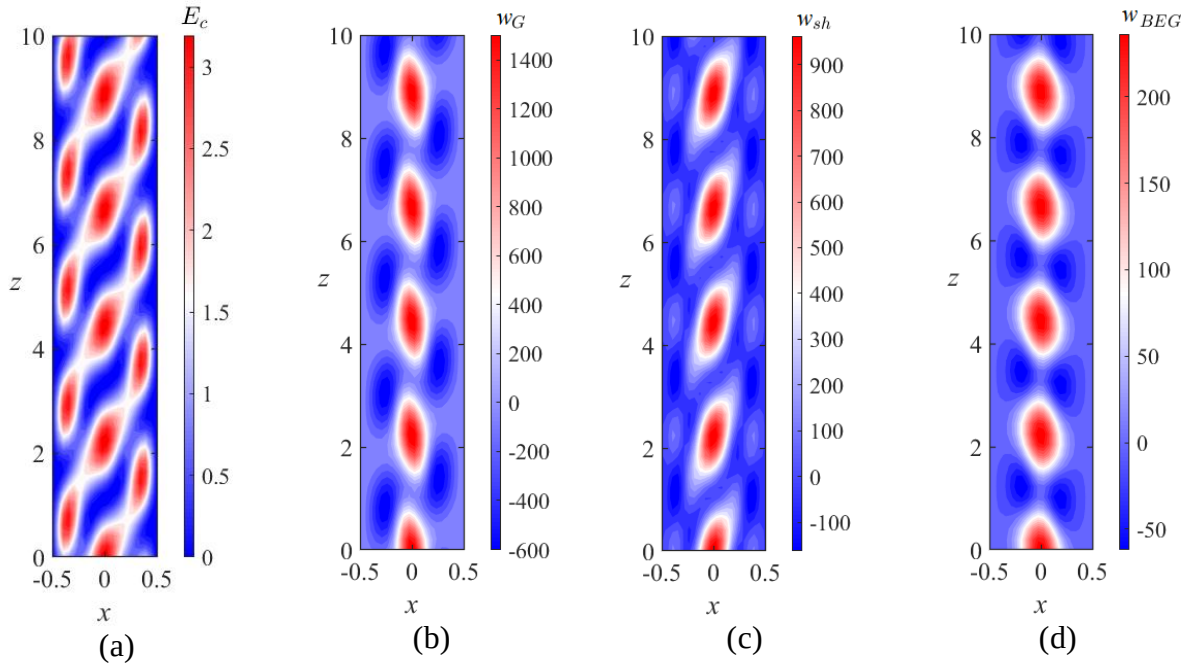

Figure 5.17: The contours of kinetic energy density and the densities of different power terms of the energy transfer at the critical point for $Pr = 1$, $Ra_c = 7.52 \cdot 10^3$ (Hydrodynamic mode), $L = 1462$, and $\gamma_e = 1.89 \cdot 10^{-2}$.

For thermal modes, the density of the kinetic energy of perturbations contains intense zones, in red, near the vertical electrodes (Figure 5.18 a). The density of energy produced by the Archimedean buoyancy w_G, which is the dominant energy generation source in TM, is concentrated at the left hot wall (Figure 5.18 b). The powers performed by the basic vorticity w_{sh} and the basic electric gravity w_{BEG} are also presented in Figure 5.18 (c, d). The active zone (where w_{BEG} is more intense) which was located at $x = 0$ for hydrodynamic modes, is shifted near the hot surface for thermal modes. The results obtained in this study are similar to the classical thermal modes [42].

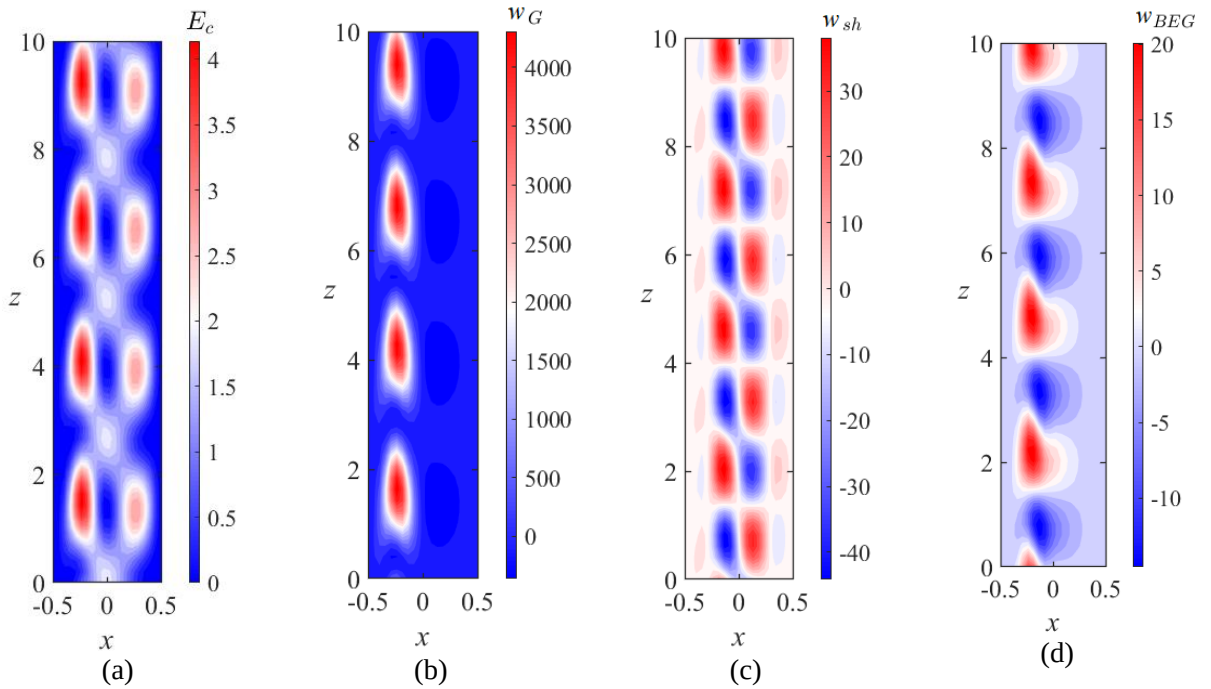

Figure 5.18: The contour of kinetic energy and different power terms of the energy transfer at the critical point for $Pr = 100$, $Ra_c = 7.34 \cdot 10^4$ (Thermal mode), $L = 1282$, and $\gamma_e = 1.84 \cdot 10^{-3}$.

Figure 5.19 shows the variation of the different powers in the energy equation as a function of L for hydrodynamic modes (a) and thermal modes (b). We observe that W_{sh} and W_G are both positives; the base flow and the Archimedean buoyancy give power to the perturbed flow whatever the value of the electric Rayleigh number L for both hydrodynamic and thermal modes. They contribute to the destabilization of the conducting base state. Figure 5.19 (a) shows that $W_{sh} > W_G$ i.e. the hydrodynamic effect predominates over the Archimedean buoyancy in the generation of the convection; while in Figure 5.19 (b) the Archimedean buoyancy produces more power than the basic shear flow $W_G > W_{sh}$. The viscous dissipation D_v due to the shear near the vertical walls dissipates the kinetic energy of the dielectric fluid. For both hydrodynamic and thermal modes, the electric field does not affect energy transfer to flow perturbation. Because w_{BEG} and w_{PEG} are identically zeros, the electric gravity plays no role and Ra_c is independent of L.

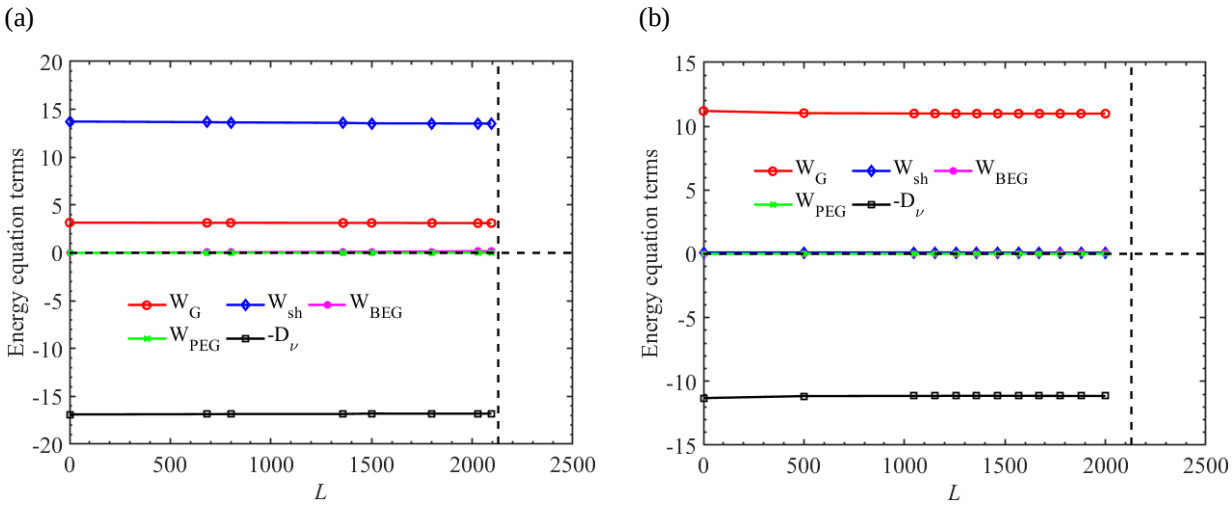

Figure 5.19: Different terms of the energy balance at the critical point (Ra_c, k_c) normalized by twice the kinetic energy plotted as a function of the electric Rayleigh number L: hydrodynamic mode (a) $Pr = 5$, $\gamma_e = 0.02$, and $Ra_c \approx 3.95 \cdot 10^4$; (b) thermal mode $Pr = 15$, $Ra_c \approx 6.15 \cdot 10^4$, and $\gamma_e = 0.01$. All terms were computed for different values of L below the critical value $L_c \approx 2129$. The vertical dashed line corresponds to the threshold $L = L_c$.

Figure 5.20 shows the powers of different energy transfer mechanisms of the perturbed flow, at the critical conditions (L_c, k_c) of the electric mode, plotted as function of Ra. All power terms of the energy equation are independent of Ra. The power W_G from the Archimedean buoyancy and the power W_{sh} from the shear in the base flow do not contribute to the energy transfer from the base state to perturbations whatever the value of Pr. The power generated by the basic electric gravity g_{eb} combined to the temperature perturbation θ' is positive $W_{BEG} > 0$. The power W_{PEG} from the perturbative gravity is negative whatever the value of the Rayleigh number Ra, it contributes to the energy dissipation as does the viscous dissipation D_v. The dielectrophoretic buoyancy arising from the basic electric gravity and the temperature perturbation is then the sole source term of destabilization leading to the thermoelectric convection. Therefore L_c is independent of Ra for electric modes.

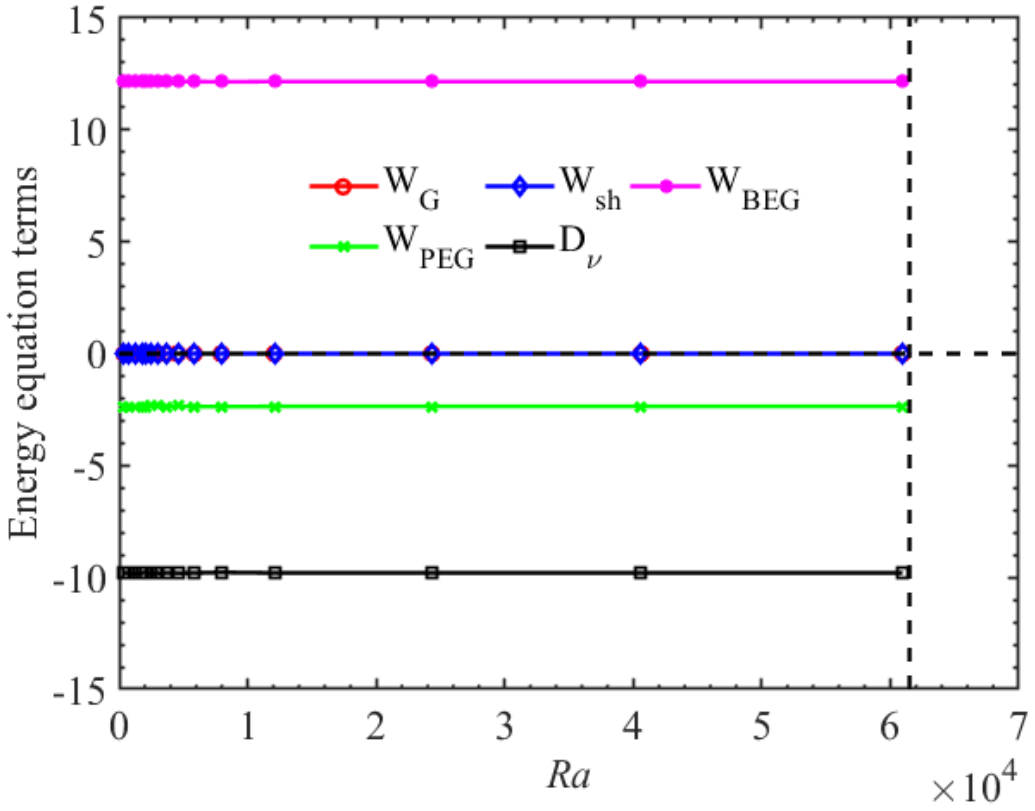

Figure 5.20: Different terms of the energy balance at the critical point (L_c, k_c) normalized by twice the kinetic energy plotted as a function of the gravitational Rayleigh number Ra for an electric mode ($Pr = 15$ and $L_c \approx 2129$). All terms were computed for different values of Ra below the critical value $Ra_c \approx 6.15 \cdot 10^4$. The vertical dashed line corresponds to the threshold.

Since the basic electric gravity is the term that destabilizes the base flow by injecting energy into the system, we plotted the contour of its power density w_{BEG} in the (x, y) plane. The contour of the density of perturbation kinetic energy E_c and the power density of the basic electric buoyancy w_{BEG} inside the gap are presented in Figure 5.21. The power density $w_{BEG} \geq 0$ everywhere and presents maximum values of alternating zones at the central plane of the gap ($x = 0$).

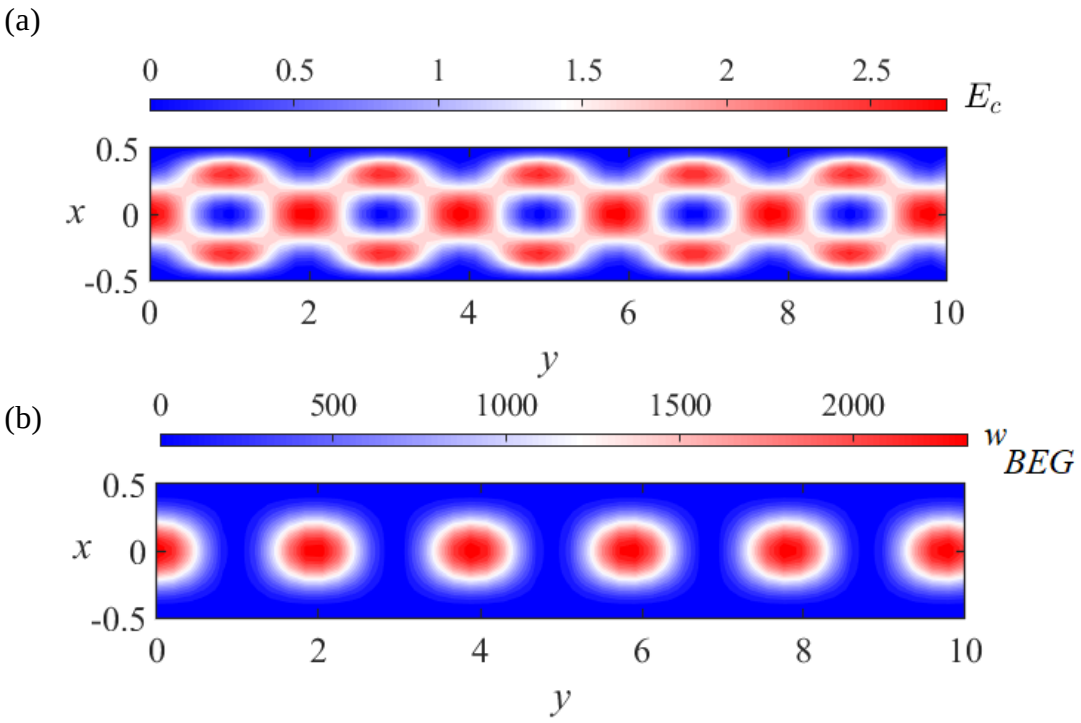

Figure 5.21: Local kinetic energy E_c (a), and power produced by the basic electric gravity w_{BEG} (b) at the threshold for $Pr = 10$, $Ra = 2536$ and $\gamma_e = 6.34 \cdot 10^{-4}$.

Figure 5.22 shows the local energy production w_{BEG} by the basic electric gravity g_{eb} combined with the perturbation temperature θ' inside the gap for different values of the gravitational Rayleigh number Ra and γ_e. The power density w_{BEG} is averaged along the y-direction and profile reveals that the energy production is maximum at the mid-gap ($x = 0$). The local average kinetic energy evolution E_c is presented in Figure 5.23. Arround the mid-gap ($x = 0$), the curves of w_{BEG} and E_c are weakly sensitive to Ra.

Table 5.4: Values of Ra and γ_e corresponding to the graphs below.

Ra	$4.1 \cdot 10^4$	$7.9 \cdot 10^3$	$4.6 \cdot 10^3$	$3 \cdot 10^3$	$1.8 \cdot 10^3$
γ_e	0.0068	0.0013	0.0008	0.0005	0.0003

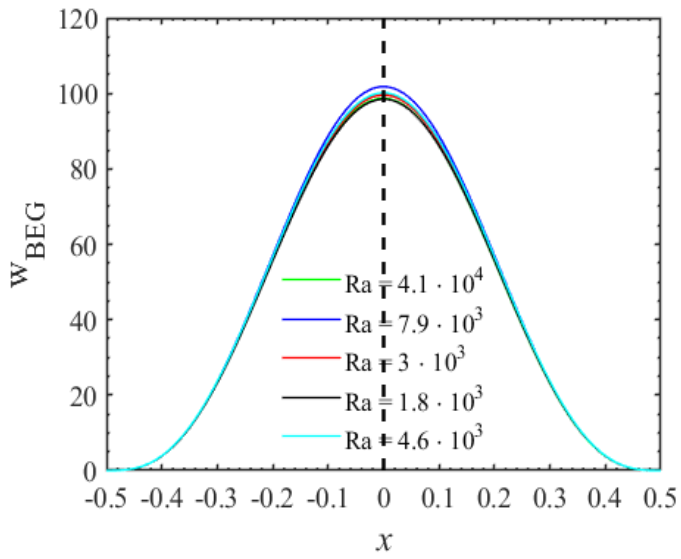

Figure 5.22: Profile of the local work performed by the dielectrophoretic buoyancy due to the basic electric gravity, normalized by W_{BEG} for $Pr = 15$ and $L \approx 2129$, corresponding to columnar modes.

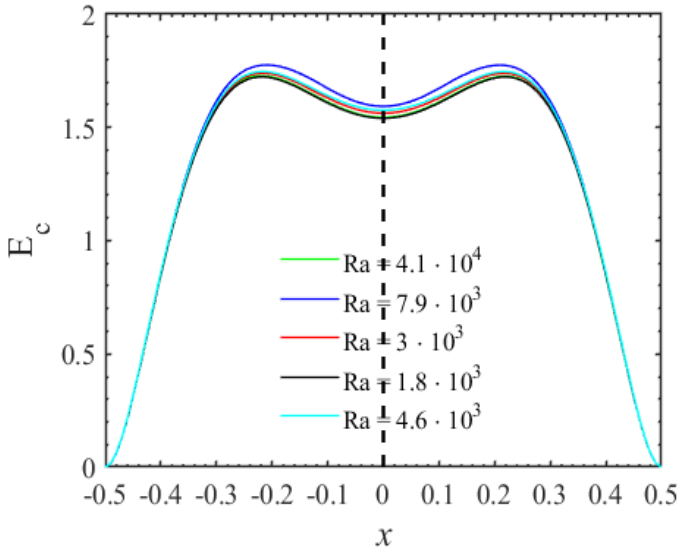

Figure 5.23: Local kinetic energy E_c evolution in the x-direction for Prandtl number $Pr = 15$, and $L \approx 2129$ that corresponds to electric modes.

5.6. Discussion

5.6.1. Comparison with previous studies

Our study concerned the investigation of the thermoelectric convection generated by the electric buoyancy in a vertical slot differentially heated and subject to a horizontal electric field. This problem has been investigated by Takashima and Hambata [58], and Tadie Fogaing [42]. In both studies, the authors performed linear stability analysis by assuming the validity of Squire's theorem and considered only two-dimensional perturbations in the vertical $(x-z)$ plane. They found three modes in that vertical plane; but the variations of the critical parameters Gr_c and k_c with L were not accurate. In particular, they found the co-existence of two critical modes when L exceeds a certain value L_c^s depending on the value of Pr. The couples of critical coexisting modes are either Electric Mode and Hydrodynamic Mode or Electric Mode and Thermal Mode. Accordingly, Gr becomes a double-valued function of L. In addition, they found that the critical electric mode should be oscillatory depending on Pr and γ_e.

Our results showed that the problem of thermoelectric convection in the vertical slot has only two solutions: hydrodynamic or thermal transverse rolls ($k_y = 0$ and $k_z \neq 0$) and electric columnar modes ($k_y \neq 0$ and $k_z = 0$) [86]. However, we did not find any inclined convective rolls in the $(y-z)$ plane ($k_y \neq k_z \neq 0$). The critical parameters of the hydrodynamic and thermal modes are independent of the electric intensity except for hydrodynamic modes in the fluids with small values of $(Pr \leq 0.3)$ when $L > 200$ where the threshold decreases and reaches the value $Ra_c = 0$ when $L = L_c$ i.e. at the threshold of the electric mode (EM).

The diagram of states in Figure 5.6 is different from the one obtained by Takashima and Hamabata or by Tadie Fogaing [86]. The marginal stability curve of the electric modes found by the authors has negative curvature.

5.6.2. Reduction to a 2-d convection

Observation of the linearized equations (5.4) suggests transforming it into a system with two-dimensional perturbations. For that, we introduce a transverse velocity $\widehat{W}$ into the continuity

equation which becomes $l\widehat{W} \equiv k_y V + k_z W$. The resulting system of perturbed flow equations reads:

$$\left.\begin{array}{c} DU + il\widehat{W} = 0 \\ [s - (D^2 - k^2) + ik_z W_b]U = -D\Pi - LPr^{-1}\left(g_{eb}\Theta + \theta_b G_{e_x}\right) \\ [s - (D^2 - k^2) + ik_z W_b]l\widehat{W} = -ik^2\Pi + k_z(RaPr^{-1}\Theta - DW_b U) - LPr^{-1}l\hat{G}\theta_b \\ U = [s - Pr^{-1}(D^2 - k^2) + ik_z W_b]\Theta \\ 0 = [(1 + \gamma_e x)(D^2 - k^2) + \gamma_e D]\Phi - \gamma_e(D^2\phi_b + D\phi_b D)\Theta \end{array}\right\} \quad (5.8)$$

where $l\hat{G} \equiv k_y G_{e_y} + k_z G_{e_z}$. The axial wavenumber (k_z) is coupled with the vertical velocity W_b of the base flow. Our problem is then reduced to a two-dimensional flow with velocity components $\left(U, \widehat{W}\right)$. In this case, three solutions are possible:

$k_y = 0$ and $k_z \neq 0 \rightarrow$ transverse solutions with axes parallel to the y axis i.e. periodic in the $z-$direction,

$k_y \neq 0$ and $k_z = 0 \rightarrow$ columnar solutions with axes parallel to the z axis i.e. periodic in the $y-$direction,

$k_y \neq 0$ and $k_z \neq 0 \rightarrow$ oblique solutions with periodicity in both $y-$ and $z-$directions.

The strong influence of k_z in (5.8) makes the Squire theorem non-applicable to the present problem [87]. Focusing on the critical electric modes, we can set the axial wavenumber $k_z = 0$ in the system of equations (5.8) and use the expressions of the temperature of the base state and the perturbative gravity to write the resulting equations:

$$\begin{array}{c} [(D^2 - k^2 - s)(D^2 - k^2 - Pr\, s)(D^2 + k^2) + Lk^2 g_{eb}]\Theta = -Lk^2 CD\phi_b D\Phi, \\ [(1 + \gamma_e x)(D^2 - k^2) + \gamma_e D]\Phi - \gamma_e(D^2\phi_b + D\phi_b D)\Theta = 0. \end{array} \quad (5.9)$$

Electric modes are then described by the temperature field and the electric potential. Since the base flow velocity W_b does not appear in the system of equations (5.9), the critical parameters of the electric modes are not affected by W_b. One sees that the equations of the classic Rayleigh-Bénard problem can be found by neglecting the perturbative electric gravity (i.e. $D\Phi = 0$) in the right-hand side of the first equation of the system (5.9). Moreover, the electric modes are stationary ($s = 0$); thus their independence on Pr is explained by the fact that Pr disappears from equations (5.9) at the threshold.

5.6.3. Comparison with stationary vertical cylindrical annulus

Recently Meyer [59] investigated the effects of the dielectrophoretic force in vertical stationary cylindrical annulus on the Earth conditions. The temperature difference is imposed by heating the inner cylinder and they introduced the parameter $\delta = \gamma_a/\gamma_e$ ($\gamma_a = \alpha\Delta T$) that gives the fluid properties.

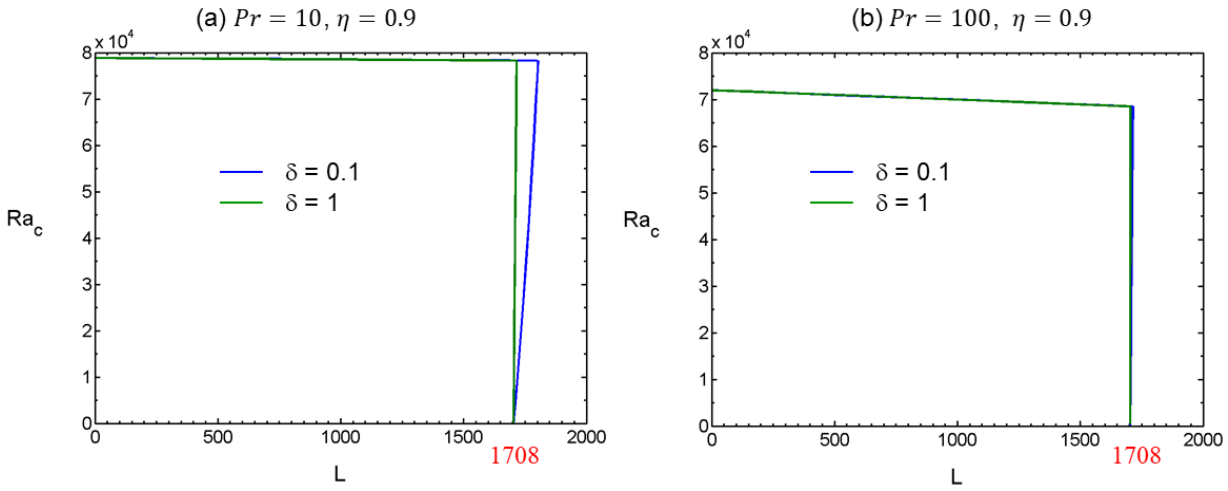

Figure 5.24: Variation of the critical Rayleigh number Ra as a function of the electric Rayleigh number L for two different values of the Prandtl number Pr in a vertical cylindrical annulus with a radial temperature gradient [59].

Under microgravity conditions, the critical electric mode induced by only the electric buoyancy in a cylindrical annulus consists of helical modes. However, in laboratory experiments and for low values of $L < L_c$, two critical modes have been detected depending on the Pr as in the case of the vertical cylindrical cavity [59]: Hydrodynamic modes which originate from the shear arising from the axial base flow, and Thermal modes which are produced by the Archimedean buoyancy and slightly dependent on the radius ratio η. It has been shown that η affects the nature of critical modes obtained. When the electric potential reaches a certain critical value $L_c(\eta)$, the hydrodynamic or thermal modes disappear and the stationary columnar mode appears. Figure 5.24 shows the behavior of the critical Rayleigh number Ra_c with the electric Rayleigh number L for a fixed aspect ratio $\eta = 0.9$ and two given values of Pr. We can observe that for both values of Pr, the columnar vortices occur when L reaches $L_c \approx 1708$ independently of δ. This result motivated the three-

dimensional analysis of the thermoelectric convection in vertical cavities in the presence of Archimedean and electric buoyancies.

In the present study, we considered three-dimensional perturbations. Results have been resumed in the stability diagram in the plane (L, Ra) together with the wavenumber $k_c(L)$ and the frequency $\omega_c(L)$. The threshold of the electric mode is independent of Pr; this represents a universal property of the electric mode which was established for different geometrical configurations (horizontal fluid layer, cylindrical annulus, spherical shell) [18]. This investigation also revealed that the electric modes manifest in form of stationary columnar rolls in contrast with the previous investigations [32,58] where 2D perturbations were assumed to lead to transverse rolls. We then highlighted three independent critical modes in the flow of dielectric fluid in a vertical slot: transverse $(\vec{k} = k_z \vec{e}_z)$ HM or TM depending on Pr and vertical EM $(\vec{k} = k_y \vec{e}_y)$.

The present study has allowed clarifying the nature of the electric modes observed in the cylindrical annulus. Indeed, in the microgravity conditions, the threshold increases with the radius ratio, and in the zero-curvature limit, $L_c \to 2128.6$. The critical electrical mode occurs in form of stationary helical vortices [32,88]. In the Earth conditions, as Gr increases, the threshold of electrical modes decreases and the helical vortices become columnar vortices [20,21]. The helical nature of the electric mode in the cylindrical annulus is due to the curvature and it becomes unstable and bifurcates to columnar vortices. A similar result was found recently by adding a global body rotation which transforms the helical vortices into columnar vortices [73].

5.7. Partial conclusion

Linear stability analysis of the convective cell of dielectric fluid in a vertical slot induced by a horizontal temperature gradient has been performed for different values of high-frequency electric field intensity. The flow is controlled by the Prandtl number, the Rayleigh number, and the electric Rayleigh number. For small electric field intensity, the convective cell becomes unstable against either stationary hydrodynamic or oscillatory thermal modes depending on the Prandtl number Pr, when the Rayleigh number Ra exceeds critical values Ra_c. These modes occur in form of transverse vortices with a periodicity in the vertical direction and they are insensitive to the electric field intensity. For a fixed value of the temperature difference below its critical value, the convective cell can be destabilized by electric-driven perturbations when the electric Rayleigh

number L reaches the critical value L_c which is independent of the diffusive properties of the fluid. The resulting electric mode consists of a pattern of stationary vertical vortices with a periodicity in the horizontal plane. The energetic analysis of the critical electric modes shows that the dielectrophoretic force due to the basic electric gravity injects energy into the system while the one due to the perturbative part stabilizes the flow. The energy balance is completely independent of the Rayleigh number Ra.

Chapter 6: General conclusions and perspectives

In this thesis work, the thermoelectric convection, generated by the coupled effect of temperature gradient and an alternating electric field, in a rectangular cavity filled with dielectric fluid has been investigated in Earth's gravity and under a microgravity environment. To perform these studies, we have used different tools: linear stability analysis, numerical simulations, and experiments in parabolic flight. Two configurations of the rectangular cavity were considered: the horizontal configuration which generalizes the classical Rayleigh-Bénard problem, and the vertical cavity. We have investigated the stability of the fluid against three-dimensional perturbations. The control parameters are the gravitational Rayleigh number Ra, the Prandtl number Pr, the thermoelectric coupling parameter γ_e, and the electric Rayleigh number L. For both cases, we have performed linear stability analysis to determine the critical parameters. An energy analysis has permitted us to identify the main mechanisms which drive thermoelectric convection and the particular role of the dielectrophoretic force.

For the horizontal cavity, we have used the Landau-Stuart equation to determine the supercritical nature of the bifurcation from the base state to the thermoelectric convection and the DNS to follow the evolution of thermoelectric convective structures for high values of the electric Rayleigh number L. The effects of the dielectrophoretic buoyancy have been investigated for three situations: the microgravity condition ($Ra = 0$), stable thermal stratification ($Ra < 0$), and unstable thermal stratification ($0 \leq Ra \leq Ra_c = 1708$).

We found that the electric buoyancy destabilizes the base state when the electric Rayleigh number L reaches the critical value $L_c(Ra)$ which is independent of the diffusive nature of the dielectric fluid (Pr). Under microgravity conditions $g \approx 0$ i.e. $Ra = 0$ the electric buoyancy is the sole source of instability, and the critical electric Rayleigh number is $L_c \approx 2128$. The resulting convective motions consist of stationary rolls with wavenumber q_c that depend on Ra. We then established the variation of critical parameters (L_c, q_c) with the Rayleigh number Ra. The energy analysis at the threshold showed that the dielectrophoretic buoyancy due to the basic electric gravity is the dominant term in the kinetic energy equation; thus the destabilization of the flow is due to the dielectrophoretic buoyancy.

Using Direct Numerical Simulations (DNS), we found that the increase of the electric Rayleigh number L beyond the threshold showed a complexification of the thermo-convective patterns with the occurrence of defects and unsteadiness. The dynamics of these patterns, far from the threshold $L > L_c$, is sensitive to the value of the Prandtl number Pr. The development of these thermo-convective structures is similar to that obtained in the Rayleigh-Bénard problem. The contribution of the dielectrophoretic buoyancy to the heat transfer is analyzed by computing the Nusselt number Nu for all saturated regimes. This number, which is the dimensionless measure of the heat transfer coefficient increases as a function of the applied electric potential when $L \geq L_c(Ra)$ for all cases. In the neighborhood of the criticality, the value of the averaged Nusselt number Nu is independent of Prandtl number Pr. However, Nu becomes sensitive to Pr for large values of L. We have generalized the thermoelectric convection problem in horizontal cavities by introducing a new control parameter called modified Rayleigh number L' which combines both the electric gravity and Earth gravity and yields an effective gravity g_{eff} which can be varied by tuning the electric gravity.

We have performed linear stability analysis in a vertical rectangular cavity subject to a horizontal temperature gradient and a horizontal alternating electric field. The base state consists of a shear flow arising from the ascending motion near the hot plate and descending flow near the cold one. The linear stability analysis showed the existence of three critical modes depending on the values of Ra, Pr, and L: Hydrodynamic Mode (HM), Thermal Mode (TM), and Electric Mode (EM). For low values of the electric Rayleigh number $L < L_c = 2128.6$, the critical mode is HM when $Pr < 12.45$ and TM for $Pr > 12.45$. HM is characterized by stationary transverse rolls and TM by oscillatory transverse rolls. The electric field has nearly no effect on HM and TM as long as $L < L_c$. However, when $L \geq L_c$, the critical mode becomes electric mode (EM) characterized by stationary vertical columnar vortices. These vortices are similar to those obtained in the cylindrical annulus. The energetic analysis showed that the Ra and the Pr do not affect the energy transfer to the critical electric modes.

As a perspective of the present study, it should be interesting to make a deeper analysis of the thermo-convective patterns computed in the present work in the horizontal rectangular cavity in order to push more in detail the comparison with the Rayleigh-Bénard convection. The DNS of thermoelectric convection in the vertical slot should be the next priority for the preparation of future parabolic flight experiments.

Scientific manifestations

Some results from the present work have been published in scientific journals and presented at national and international conferences. Here Below, I have listed three published articles and different oral communications presented at national and international conferences.

Publications

- E. B. Barry, H.N. Yoshikawa, C. Kang, A. Meyer, M. Meier, O. Crumeyrolle1, C. Egbers and I. Mutabazi, Effect of the weak Archimedean buoyancy on thermoelectric convection in a planar capacitor, CRAS – Comptes Rendus de l'Académie des Sciences (2022 Submitted).
- P. Szabo, M. Meier, A. Meyer, E. Barry, V. Motuz, I. Mutabazi, C. Egbers, PIV and shadowgraph measurements of thermo-electrohydrodynamic convection in a horizontal aligned differentially heated annulus at different gravity conditions, Exp. Therm. Fluid Sci. 129, 110470 (2021).
- E. Barry, H. Yoshikawa, C. Kang, I. Mutabazi, Transfert de chaleur par convection thermoélectrique dans des cavités rectangulaires horizontales, Entropie Thermodyn. – Énerg. – Environ. – Économie 2, (2021).
- E. B. Barry, H. N. Yoshikawa, C. Kang, I. Mutabazi, Critical modes of the thermoelectric convection instabilities in a vertical slot, Microgravity Sci. Technol. 33, 16 (2021).

Communications and posters

- E. B. Barry, H. N. Yoshikawa, C. Kang, I. Mutabazi, Modélisation des régimes d'écoulements générés par champ électrique et transfert de chaleur dans une huile de silicone en micropesanteur, GDR-MFA, Carry – Le Rouet (2021).
- E. B. Barry, C. Kang, H. N. Yoshikawa, I. Mutabazi, Generation of thermoelectric convection instabilities in a dielectric fluid layer, ICTW21, Online (2021).
- E. B. Barry, H. N. Yoshikawa, C. Kang, I. Mutabazi, Transfert de chaleur par convection thermoélectrique dans des cavités rectangulaires horizontales, SFT–2021, Belfort and Virtual (2021).

- E. B. Barry, H. N. Yoshikawa, C. Kang, I. Mutabazi, Modélisation de la convection thermoélectrique dans une cavité rectangulaire, JC2 – CNES, Online (2020).
- E. B. Barry, H. N. Yoshikawa, C. Kang, I. Mutabazi, Thermoelectric convection in a rectangular cavity, LOMC – Le Havre (2020).
- E. B. Barry, H. N. Yoshikawa, C. Kang, I. Mutabazi, Modes d'instabilités de convection thermoélectrique dans une cavité rectangulaire verticale, GDR – MFA, La Rochelle (2019).
- E. B. Barry, H. N. Yoshikawa, C. Kang, I. Mutabazi, Linear stability analysis of thermoelectric convection in a vertical rectangular cavity with a horizontal temperature gradient and a high-frequency voltage, LIA – ISTROF, Cottbus – Germany (2019).
- E. B. Barry, H. N. Yoshikawa, C. Kang, I. Mutabazi, Thermo-electro-hydrodynamic instabilities in a vertical rectangular cavity: Linear stability analysis, ELGRA, Granada –Spain (2019).

Appendix A: Experimental study of thermoelectric Rayleigh-Bénard convection in rectangular cavities

To validate the numerical work on the thermoelectric convection in rectangular cavities, we performed some experiments under microgravity conditions, during a Parabolic Flight Campaign (PFC VP139) held in Bordeaux in September 2018. The campaign has been supported by the French spatial agency CNES (Centre National d'Études Spatiales) through its subsidiary company Novespace in charge of the parabolic flights. The experiments have been performed in collaboration with the German TEHD team of Dr. Martin Meier, TEHD-project leader at the Department of Aerodynamics and Fluid Mechanics of the Brandenburg University of Technology in Cottbus (head: Prof. Dr. C. Egbers) which designed and built the experimental setup appropriate for parabolic flight campaigns. Since 2010, the German team has performed 12 parabolic flight campaigns on this topic [22,23,61,89]. Recently Marcel Jongmanns [20] defended his thesis dealing with flow control by the dielectrophoretic force in a cylindrical cavity. The experimental setup used for this work is the same except for the rectangular cavity cell, which was also designed, developed, and built by the BTU team.

The system under study consists of two rectangular cavities filled with dielectric liquids: one in the horizontal configuration and another in the vertical configuration. Since we have investigated the thermoelectric convection induced by the dielectrophoretic force, both systems are differentially heated and subject to a high-frequency electric field produced by the application of an electric potential. The flow in the rectangular cavities is visualized using the Background Oriented Schlieren (BOS) method [90–94] which is based on the density variation of the fluid due to the temperature difference.

A.1. Experimental apparatus

A.1.1. General description

All the experimental materials are packaged in two racks depending on their functionality. The first rack called the experiment rack is composed of one box containing the rectangular cavities, the metrology equipment, and the cooling and heating systems. It also contains a high-voltage generator and an electronic box that includes connectors, fuses, and power plugs. The second rack called the control rack accommodates a computer, a monitor, a keyboard, a data acquisition card, the main fuse box with an emergency stop, and a system of two input/output connector blocks. The two racks are connected by a system of cables and the whole experiment is connected to the aircraft laboratory power plug. In addition to the security button provided by Novespace, the experiment is equipped with an emergency stop to cut off the electric alimentation if any electrical problem arises.

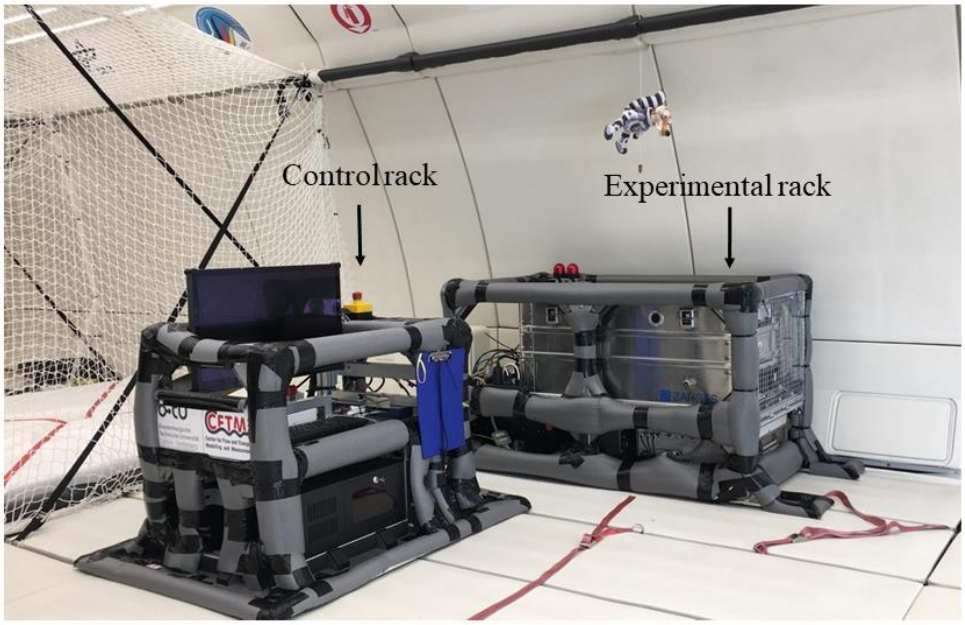

Figure A.1: Experimental apparatus composed of the control rack and the experiment rack loaded inside the laboratory part of Zero-G Aircraft.

A.1.2. Rectangular cavities

The system under study consists of two rectangular cavities, in different configurations, filled with a dielectric liquid. These experimental cells are characterized by their lengths, widths, and depths. In both horizontal and vertical configurations, the total height and the total width are fixed; only the depth can be changed, allowing the regulation of the gap size. The experiment cells are composed of three compartments: two chambers for the heating and the cooling process, and the gap cavity. Cover and view plates and the gap plate are made of polymethylmethacrylate (PMMA) to guarantee electrical and thermal insulation. The gap cavity includes two plates of borosilicate glass, which is known for its resistance to high temperatures. The interior of those plates is recovered by a thin Transparent Conductive Oxide (TCO) coating which serves the application of the electric potential by connecting one plate to the high voltage generator and the second plate to the ground. The outer part which represents the pressure frame of the experimental cells is made of aluminum (AlMgSi0.5). A schematic description of the rectangular cavity is presented in Figure A.2. This rectangular cavity can be placed horizontally or vertically in the experiment box.

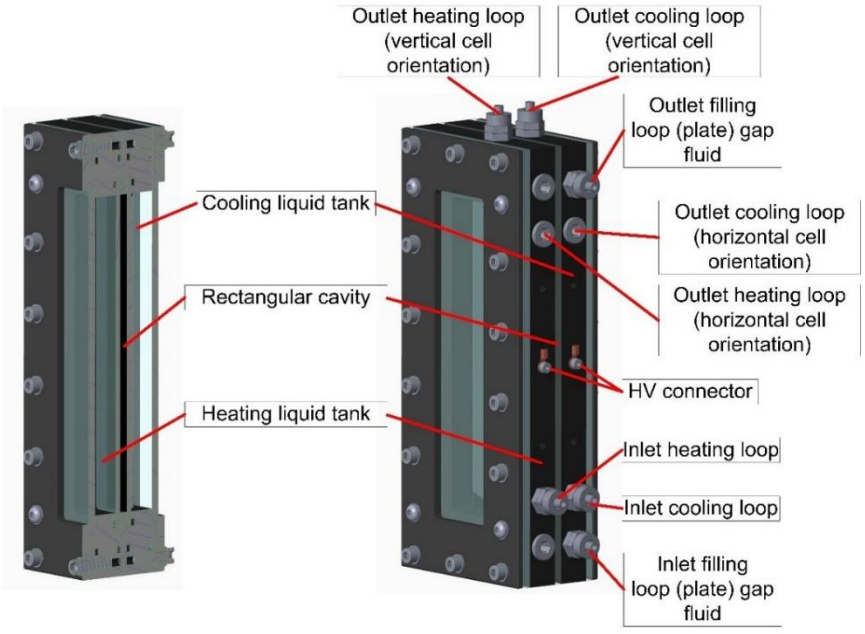

Figure A.2: Description of the rectangular cavity designed and built by the German team in Cottbus (LAS, BTU Cottbus). The figure on the left represents a cut through the middle of the cell.

The temperature difference inside the gap is imposed by fixing a heating loop on one face and a cooling loop on the other face. The liquid used for the heating and cooling loops is silicone oil (AK5) from Wacker Chemie. Both heating and cooling chambers are connected to different reservoirs, where temperatures are set according to two different methods. The two reservoirs are made of polyoxymethylene (POM). The temperature in the cooling system is controlled by a heat exchanger with a Peltier element fixed outside of the experimental box. The Peltier controller can provide temperatures inside the cooling liquid until about 10 °C under the ambient temperature outside of the box. A heating box with heating cartridges, containing temperature sensors, was utilized to heat the liquid (AK5) inside the heating loop. A power supply of 24 V DC provides a power of 100 W to the heating system. The dimensions of experiment cells are tabulated in Table A.1. Cell A represents the horizontal rectangular cavity and cell B is the vertical cavity.

Table A.1: Characteristics of the rectangular cavity.

Experiment cells		
	Cell A	Cell B
Dimensions of cells		
Total height	280 mm	280 mm
Total width	120 mm	120 mm
Total deep	65 mm	70 mm
Dimensions of the cavity (gap)		
Total height	200 mm	200 mm
Total width	40 mm	40 mm
Total deep	5 mm	10 mm

A couple of heating and cooling systems can generate inside the gap a temperature gradient up to 30 °C. Thermocouples fixed to the inlets and outlets of the heating and cooling loops allow reading the imposed temperature difference across the gap by taking the averaged value between the entrance and the output. The high voltage generator can deliver an alternative peak voltage $V_{peak} =$

$\sqrt{2}V_0$ up to 10 kV with various frequencies f. The peak voltage V_{peak} corresponds to ϕ introduced in previous chapters.

A.1.3. Choice of working dielectric fluid

Based on the linear stability analysis, the onset of the thermoelectric convection in parallel plates under microgravity conditions depends on the value of the electric Rayleigh number L. The critical value of the electric Rayleigh number is $L_c = 2128.6$ in an infinite extended system under microgravity conditions. The corresponding critical electric potential is then determined by the following formula: $V_{0c} = V_i \cdot \gamma_e^{-2} \left[\log\left(\frac{2-\gamma_e}{2+\gamma_e}\right)\right]\sqrt{L_c}$, where V_i (equation (2.24)) is the intrinsic electric potential of the dielectric liquid that we use.

As we are limited by a maximum value of the peak voltage equal to 10 kV in a parabolic flight situation, we have chosen the dielectric liquid with the lowest curve as shown in Figure A.3 (a).

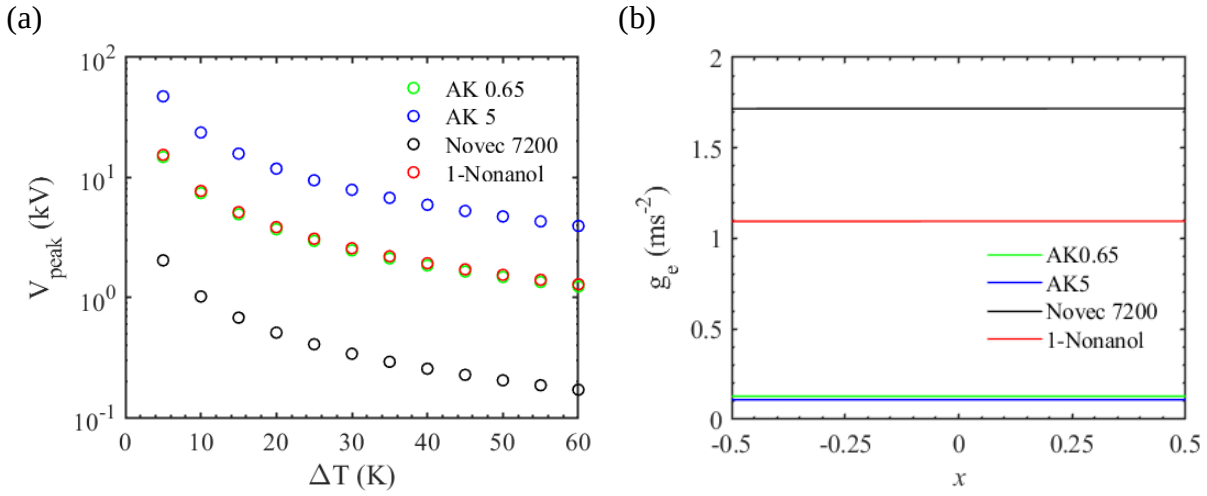

Figure A.3: a) Critical values of V_{peak} as a function of the temperature difference ΔT for some dielectric liquids; b) the corresponding basic electric gravity of these liquids sandwiched between two parallel plates of thickness $d = 5\,mm$ for $V_{peak} = 10\,kV$ and $\Delta T = 10\,K$.

This figure gives the variation of the peak voltage as a function of the imposed temperature difference at the critical point ($L = L_c$) for different dielectric liquids. The gap of the experiment cells is then filled with the Novec 7200; which is a dielectric liquid characterized by a high value of electric permittivity. We have also plotted the basic electric gravity for different liquids in a

given system in Figure A.3 (b). One sees that the basic electric gravity curve is more important in Novec 7200.

The physical phenomena in the experimental cells are described in terms of the viscous diffusion time scale τ_ν, the thermal diffusion timescale τ_κ and the turnover time scale $\tau_c = \tau_{DEP} = \sqrt{\frac{\tau_\nu \tau_\kappa}{L_c}}$. The latter one is the necessary time for a fluid particle to complete a round trip in the convection roll over the gap. It characterizes the growth of the vorticity generated by the electric buoyancy. For the working fluid Novec 7200, the values of these characteristic timescales are presented in Table A. 2. This table also contains some dielectric liquids.

Table A. 2: Values of the characteristic timescales for a system of thickness $d = 5\ mm$ under microgravity conditions.

Working fluids	τ_e [s]	τ_ν [s]	τ_κ [s]	τ_c [s]
Novec 7200	2.6	58.14	641.03	4.18
AK5 (25°C)	23.9	5.00	323.00	0.87
AK0.65 (25°C)	19.3	38.46	294.46	2.31
1-Nonanol (20°C)		1.76	314.86	0.51

In the experiment under consideration, the turnover time τ_c is way smaller than the viscous and thermal diffusive times (τ_ν, τ_κ). Since the duration of the microgravity phase is about 22 s, one sees that this time is 5 times τ_c for the Novec 7200. The period of the applied alternating electric $T = 5 \cdot 10^{-3}$ s. This period T is smaller than all characteristic times, which is in harmony with the assumption that the alternating electric potential can be replaced by its effective stationary part.

A.2. Background Oriented Schlieren

The Background Oriented Schlieren technique (BOS) is used for the visualization of the flow inside the gap. The BOS technique is a non-intrusive method of fluid flows visualization, based on the capture of the refractive index variation due to the inhomogeneity in the fluid layer. It remains

one of the synthetic Schlieren techniques that also provides a quantitative measurement of the density changes in fluid flows by using a simple optical system [90]. As an expansion of the basic Schlieren technique, experimental studies have shown that the BOS technique has many applications. Some of them are the study of the sound wave of a gunshot, the shed vortex, the supersonic jet, the mixing turbulent jet, the measurement of the pressure field of a laser-induced underwater shock wave, or the axisymmetric supersonic flow over a cone-cylinder model [90–93]. Therefore, this technique represents an interesting measurement method for engineering in the Aeronautic and Aerospace industries.

The BOS system consists of a camera, a background pattern plate with random-dot patterns, a light source, and a computer for data processing. The homogeneous light source and the pattern plate are both mounted to the rectangular cavity for the vertical orientation and below for the horizontal configuration. The density gradient is created by the imposed temperature difference and the perturbation temperatures induced in the flow system when the base state is destabilized by the electric field. The experimental setup of the BOS technique is presented in Figure A.4.

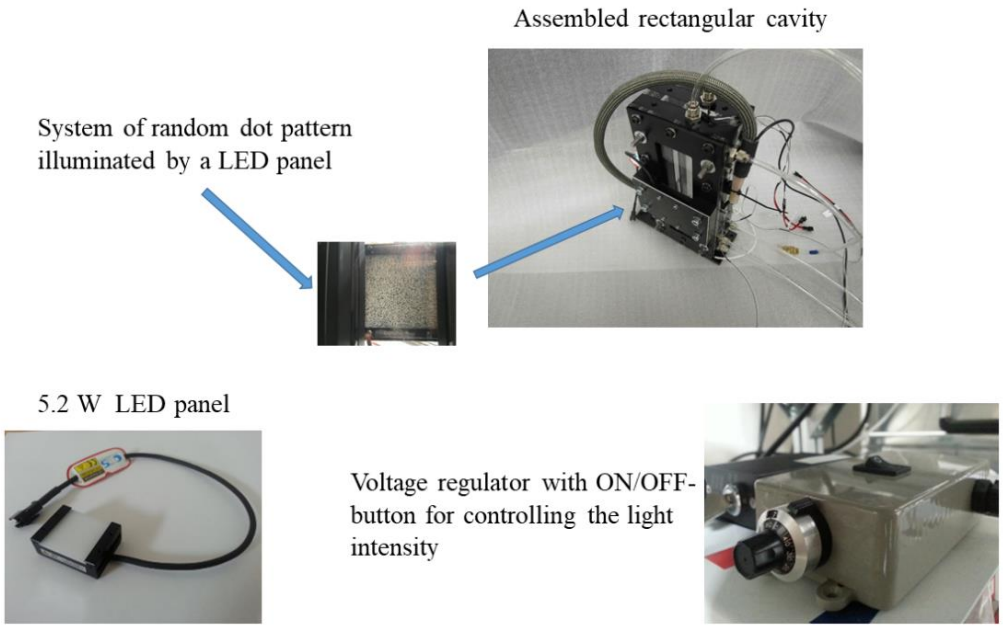

Figure A.4: Flow visualization experimental setup – Part of instruments of the BOS technique.

The basic principle of the BOS technique consists of placing an illuminated dot pattern in the background of the rectangular cavity and photographing the dot patterns through the fluid layer with a camera placed in front. Without the density gradient, the random structures on the

background dot patterns are undisturbed; while when the fluid layer is inhomogeneous, the light rays that the CCD camera perceives are deflected. We then take a reference image that corresponds to the one with no applied temperature difference and no applied electric potential. Indeed, the comparison between the two pictures of the background pattern gives the phase difference which can be translated into an apparent displacement field (shift) [94]. The shifting field (displacement field) is determined by the cross-correlation method used in PIV. The divergence of this displacement field is directly related to the density gradient. The result of the BOS algorithm represents the displacement field measured in mm. An illustration of the BOS technique is presented in Figure A.5.

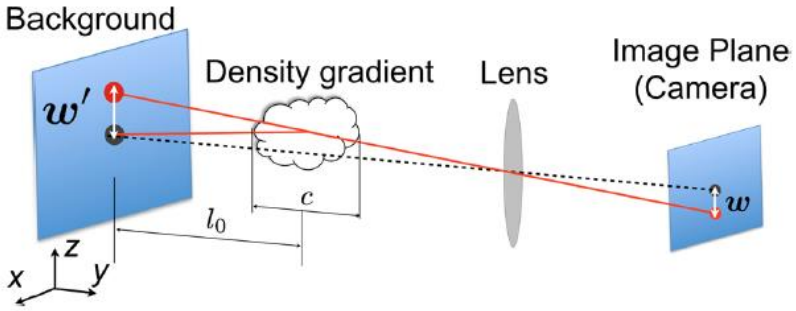

Figure A.5: Schematic representation of the principle of the BOS technique [91]. The zone of density gradient of width c represents the gap of the rectangular cavity.

A.3. Parabolic Flight Campaign (PFC)

Parabolic flight is one of the methods offering access to a microgravity environment. The first objectives of the parabolic flight campaigns were dedicated to the training of astronauts. The extension of parabolic flights to scientific studies allowed researchers to experience microgravity effects on different physical phenomena. For example, it allows the investigation of the fluid flows under three different gravity phases: $1g$, $0g$, and $1.8g$. The realization and the characteristics of the parabolic maneuvers are presented in Figure A.6.

Before the beginning of a parabola, the plane has a steady horizontal flight at an altitude of 6000 m. In this phase, we are submitted to normal gravity ($1g$) and the speed of the plane is about

820 km/h. Then, the pilots pitch the airplane up until reaching the injection at about 50° nose-up angle with the horizontal. Due to the centrifugal force arising from the airplane's upward inclination, a strong apparent gravity or hypergravity $(1.8g)$ is established during 20 s.

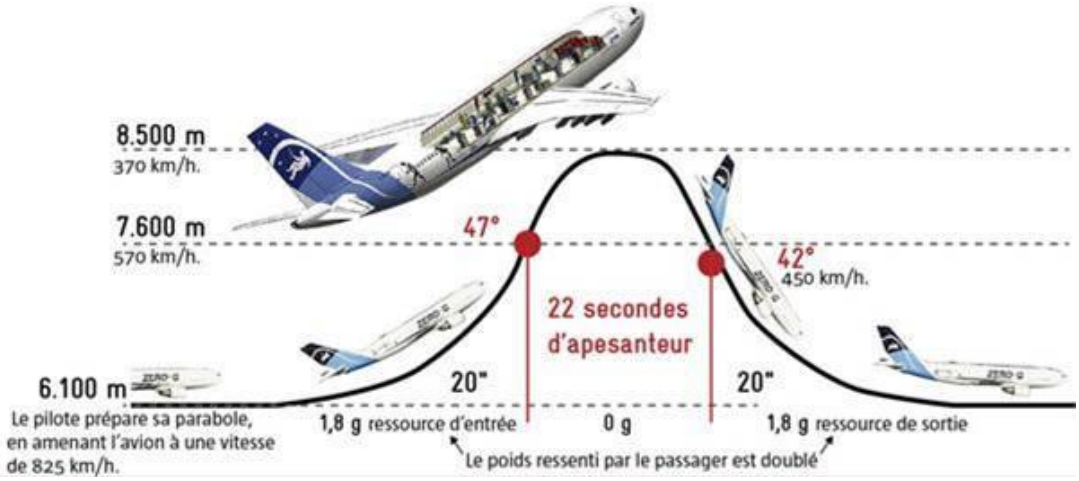

Figure A.6: The airbus A310 Zero-G and the sketch of the five phases for the realization of one parabola. Courtesy of NOVESPACE.

At the end of this hypergravity phase, the regimes of the aircraft engines are significantly reduced, so that to compensate for the resistance of air. In that case, the aircraft is only subject to its weight and that of the passengers and experiences. After 5 seconds of the transitory phase, the plane enters into the microgravity phase with a parabolic trajectory for 22 seconds. This corresponds to 11 seconds of upwards free fall and 11 seconds of downward free fall. The parabola injection altitude is 7600 m and the accuracy of the weightlessness is about $\pm 0.02g$. This precision on the microgravity quality is sufficient to assume that the fluid flow experiences only electric gravity when the potential is applied. At the end of this phase, a second hypergravity phase is encountered for 20 seconds before recovering the initial horizontal steady flight. Figure A.7 shows the time variation of the different components of acceleration during a whole parabola. Since the parabolic flight campaign is composed of 30 parabolas of experiments, the cumulative duration of weightlessness is about 11 minutes.

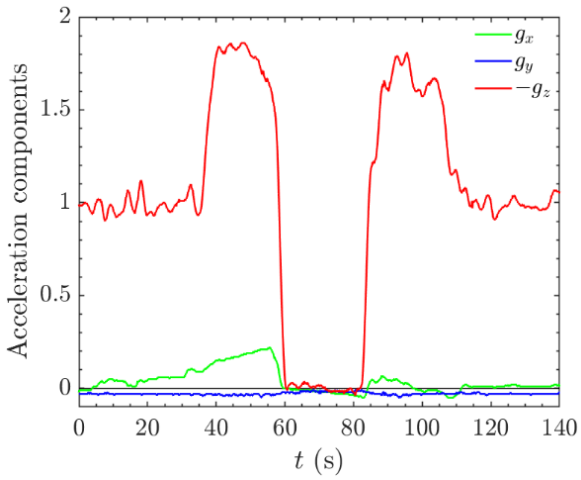

Figure A.7: The evolution of the normalized acceleration with the time during the parabolic maneuver. All terms of acceleration are normalized by the value of the Earth's gravity.

A.4. Experimental results

Under microgravity conditions, electric gravity is the sole source that induces thermo-convective motions in the dielectric fluid layer. The base state is purely conductive. As the microgravity phase is preceded by the 1.8 g phase, the rectangular cavity, in the horizontal configuration, is heated from above to ensure a stable stratification of the fluid layer during this phase. During this parabolic flight campaign, we investigated the thermoelectric convection under microgravity conditions for horizontal and vertical rectangular cavities filled with the Novec 7200 and Nonanol. We faced a leaking problem for the experiment performed with Nonanol, therefore no results will be presented here for this liquid.

A.4.1. Horizontal Orientation

We have performed experiments by fixing the values of the temperature difference ΔT between the upper and lower plates, and varying the value of the applied electric potential V_{peak}. The system has an accelerometer that detects the microgravity phase. The control program can activate the heating system to set ΔT, and the electric potential V_{peak} is activated at the beginning of each microgravity phase. The voltage remains activated until the following hypergravity phase. In this report, we will present the data for $\Delta T = 7\ K$ and $10\ K$. The electric potential V_{peak} is increased

until $5\ kV$ for each fixed value of the temperature difference ΔT. Figure A.8 shows the divergence of the displacement field ($Div(\vec{x},\vec{y})$) for $\Delta T = 7\ K$ and different values of V_{peak}. Pictures are taken at the end of the microgravity phase (0 g) so that the patterns have time to develop in the flow. The first image corresponds to the case without electric potential and represents a reference image. For all values of the applied electric potential below $2\ kV$, no displacement field has been observed, this means that there is no thermo-convection. When we increase further the electric tension, we observe that some structures appear in the cavity for $V_{peak} = 2\ kV$. The corresponding electric Rayleigh number value for temperature difference $\Delta T = 7K$ is $L = 4010$. Therefore, we are above the critical value predicted by linear stability analysis as shown in Figure A.3 and numerical simulations ($L_c \approx 2129$). These patterns are inclined in the horizontal plane and are similar to those obtained in numerical simulations of thermoelectric convection in a Silicone oil ($Pr = 65$) under microgravity conditions for $L_c < L \leq 5000$. The correspondence between the electric Rayleigh number L and the electric voltage is given in Table A.3. Using the intrinsic potential V_i, we defined a dimensionless voltage $V_E = V_{peak}/\sqrt{2}V_i$; and the electric Rayleigh number is computed by the following formula: $L = \left[\gamma_e^2 / ln\left(\frac{2-\gamma_e}{2+\gamma_e}\right)\right]^2 \mathrm{V_E^2}$.

Table A.3: Control parameters for Novec 7200

ΔT (K)		7	10	15
γ_e		0.027	0.039	0.059
Vpeak (kV)	V_E	L	L	L
0	0	0	0	0
0.5	580	250	511	1150
1	1160	1000	2040	4600
1.5	1740	2250	4600	$1.03 \cdot 10^4$
2	2320	4010	8170	$1.84 \cdot 10^4$
3	3480	9010	$1.84 \cdot 10^4$	$4.14 \cdot 10^4$
5	5800	$2.50 \cdot 10^4$	$5.11 \cdot 10^4$	$1.15 \cdot 10^5$
10	$1.16 \cdot 10^5$	$1.00 \cdot 10^5$	$2.04 \cdot 10^5$	$4.60 \cdot 10^5$

As the potential V_{peak} increases, another type of pattern more disordered grows. For $V_{peak} = 3\ kV$ and $V_{peak} = 5\ kV$, the flow patterns generated by the electric gravity are more complex.

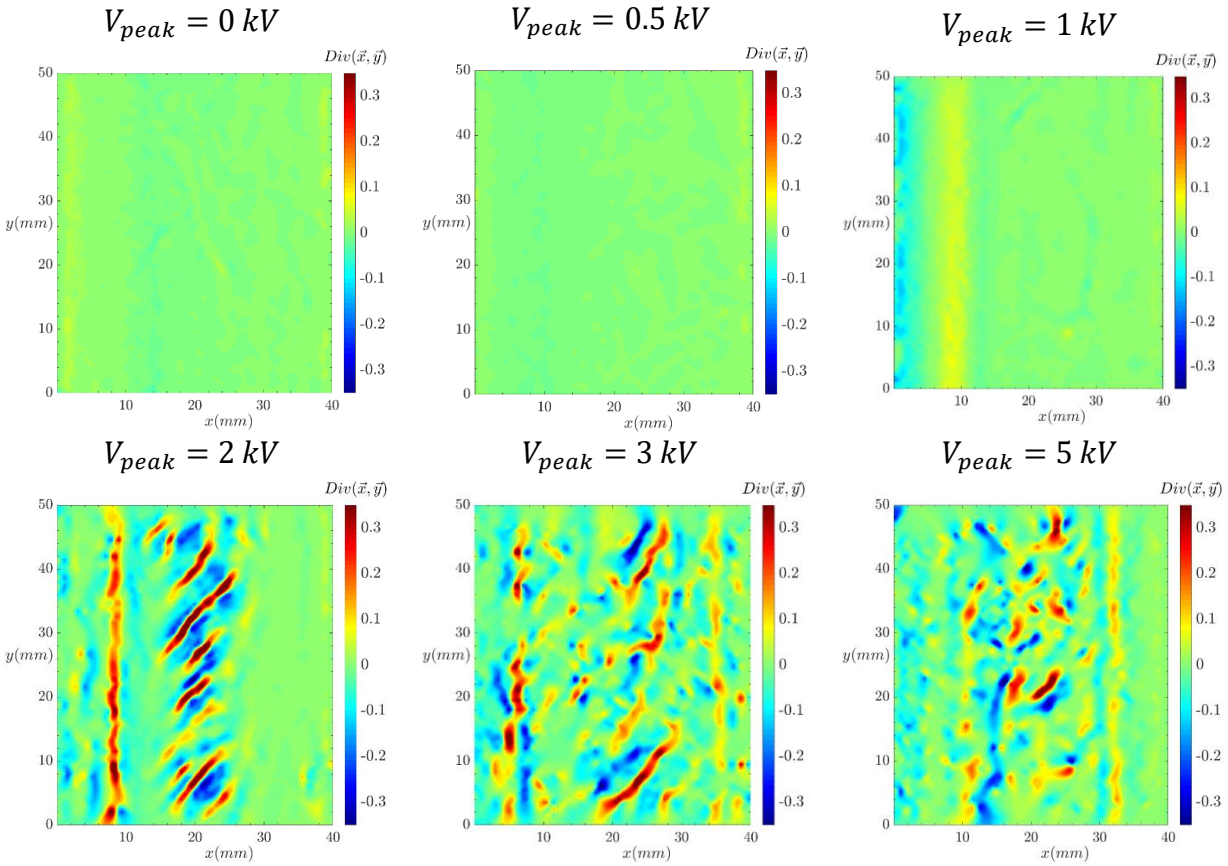

Figure A.8: Patterns of the divergence of the displacement vector ($Div(\vec{x},\vec{y})$) for the six first parabolas corresponding to $\Delta T \approx 7\ K$ and for different values of the V_{peak}.

For a better understanding of the fluid motions during the whole microgravity phase, we have plotted the space-time diagrams of the divergence of the displacement field at the fixed position $x = 20\ mm$. Results are presented in Figure A.9. The plot shows that for $\Delta T = 7\ K$, the perturbation induced by the application of the electric potential needs a certain time to grow and gives rise to some patterns.

The delay of occurrence and the nature of the observed structures depend on the value of V_{peak}. The higher the potential V_{peak} is, the sooner the structures appear. One sees that for $\Delta T = 7\ K$ and $V_{peak} = 2\ kV$, the flow is induced in the last 5 seconds before the end of the microgravity phase.

For the case where $V_{peak} = 3$ and $5\,kV$, movements are visible in the first half part of the microgravity phase. Especially for $V_{peak} = 5\,kV$ they are observed only 5 seconds after the beginning of the weightlessness phase. This time approximately coincides with the characteristic turnover time τ_c estimated above at 4.18 s for the Novec 7200 (Table A. 2).

$V_{peak} = 2\,kV$

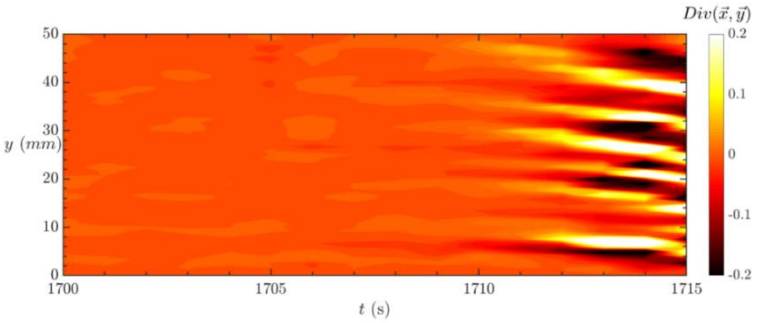

$V_{peak} = 3\,kV$

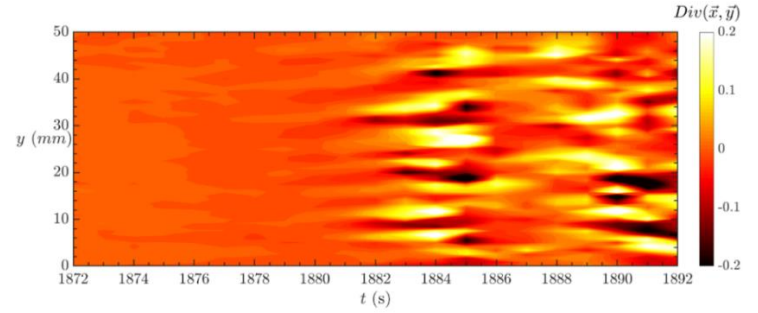

$V_{peak} = 5\,kV$

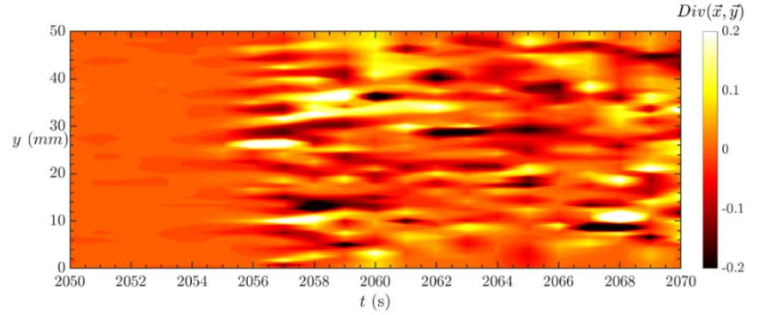

Figure A.9: Space-time diagram of the divergence of the displacement vector ($Div(\vec{x},\vec{y})$) during a weightlessness phase at $x = 20\ mm$. Snapshots correspond to a temperature difference $\Delta T \approx 7\ K$ and for different values of the applied electric potential V_{peak}.

Figure A.10 displays the flow patterns obtained for $\Delta T = 10\ K$ and different values of the electric potential. As in Figure A.8, the snapshots are taken at the end of the microgravity phase. These patterns are seen as signatures of thermoelectric convection in microgravity. In this case, the effect of the dielectrophoretic force on the fluid layer is visible at $V_{peak} = 3\ kV$; this value is larger than that obtained for $\Delta T = 7\ K$.

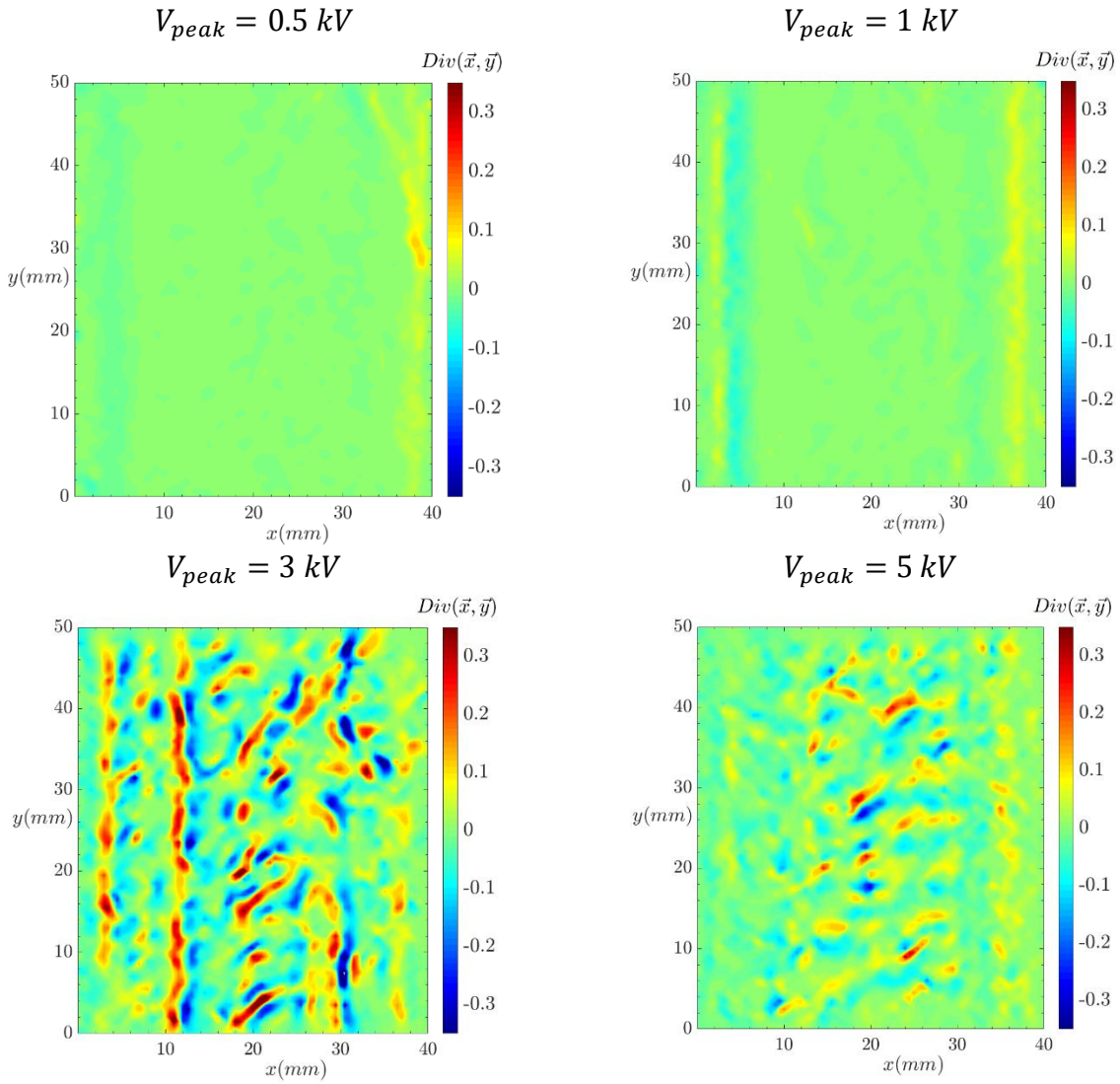

Figure A.10: Patterns of the divergence of the displacement vector ($Div(\vec{x}, \vec{y})$) for the six first parabolas corresponding to a temperature difference $\Delta T \approx 10\ K$ and for different values of the applied electric potential V_{peak}.

A qualitative description of patterns can be done with the space-time plots of the displacement patterns in Figure A.11. We can see from the plots that the dynamics of the formation of the instability patterns during the microgravity phase change with the applied potential.

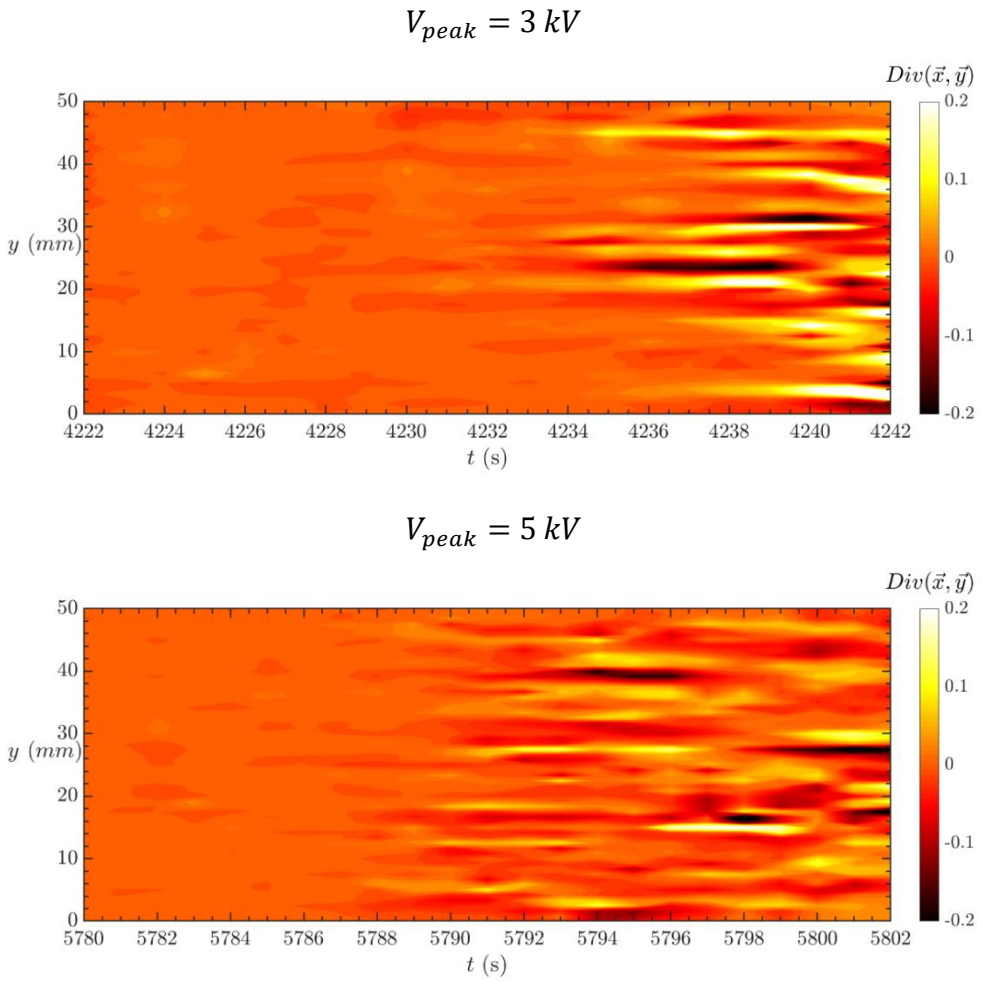

Figure A.11: Space-time diagram of the divergence of the displacement vector $(Div(\vec{x},\vec{y}))$ during a weightlessness phase at $x = 20\ mm$. Snapshots correspond to $\Delta T \approx 10\ K$ and for two values of V_{peak}.

On the space-time diagrams of the displacement vector in Figure A.9 and Figure A.11, we observe that the flow disturbances begin to grow sometime after the onset of the microgravity phase. To compute the growth rate of the thermoelectric instability, Meyer *et al.* [24] firstly

proposed to integrate the divergence of the displacement vector ($D = Div(\vec{x},\vec{y})$) over y at the mid-gap ($x = 20\ mm$):

$$\overline{D} = \frac{1}{L_y}\int |D(y,t)|\, dy. \tag{A.1}$$

After choosing the part of the curve $\overline{D}(t)$ that fit an exponential evolution, we modeled the integrated value of the displacement vector as $\overline{D}(t) = \widehat{D} \cdot Exp(\sigma t)$ where σ is the growth rate of perturbations and $\widehat{D}$ the amplitude of $\overline{D}$. σ corresponds then to the slope of the linear regression:

$$ln(\frac{\overline{D}}{\widehat{D}}) = \sigma t. \tag{A.2}$$

The time variation of the quantity $\overline{D}$ is plotted in Figure A.12 for a fixed value of ΔT and different values of V_{peak} above the threshold during the microgravity phase. The graphs show that the delay for perturbations to start growing decreases as the applied electric potential increases. For the extraction of σ, we have plotted in Figure A.13, the time evolution of $ln(\overline{D})$ corresponding to the quantities presented in Figure A.12. The instant $t = 0\ s$ in the figures corresponds to the beginning of the microgravity phase. The extracted values of σ for two experiments with the same control parameters are tabulated in Table A.4. We can observe that σ increases with increasing the electric potential for experiment 2. This behavior was expected; while for experiment 1, a decrease in the growth rate is observed for $V_{peak} = 3\ K$. This effect could be due to an artifact originating from the measurement technique.

Table A.4: Values of the growth rate for different values of the applied electric potential for two experiments. The temperature difference is fixed at $\Delta T = 7\ K$ for both experiments.

V_p (kV)	2	3	5
L	4010	9010	$2.5 \cdot 10^4$
σ_1 (first experiment) $[s^{-1}]$	0.70	0.59	1.1
σ_2 (second experiment) $[s^{-1}]$	0.41	0.49	0.53
$\sigma = (\sigma_1 + \sigma_2)/2\ [s^{-1}]$	0.56	0.54	0.81

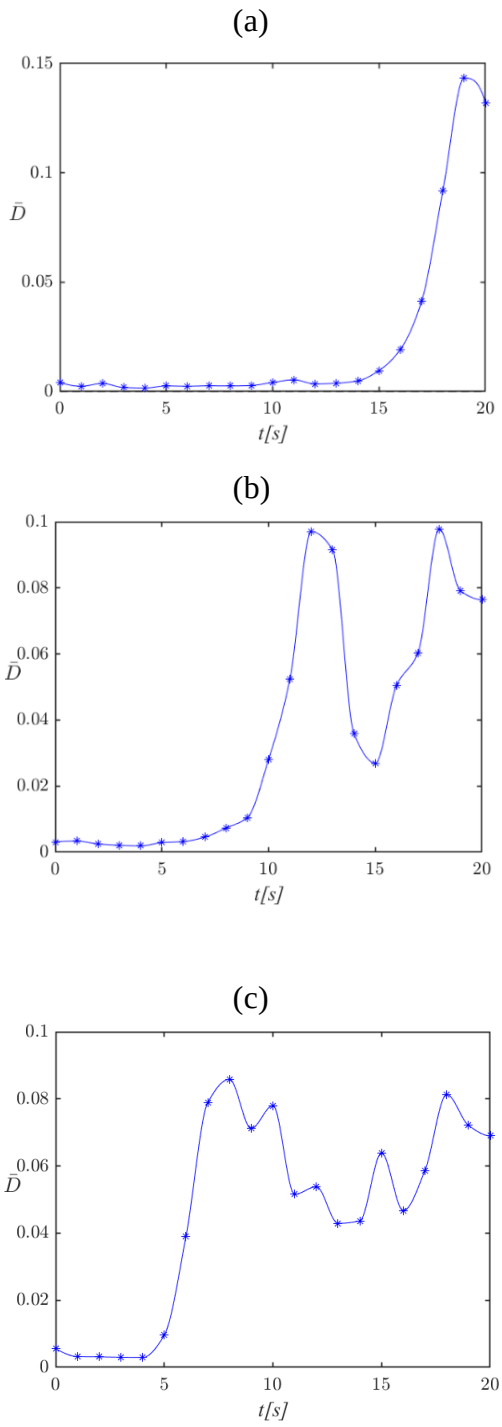

Figure A.12: Time evolution of $\bar{D}$ during a weightlessness phase at the mid-gap ($x = 20\ mm$) for $\Delta T = 7K$ and (a) $V_{peak} = 2\ kV$, (b) $V_{peak} = 3\ kV$, and (c) $V_{peak} = 5\ kV$.

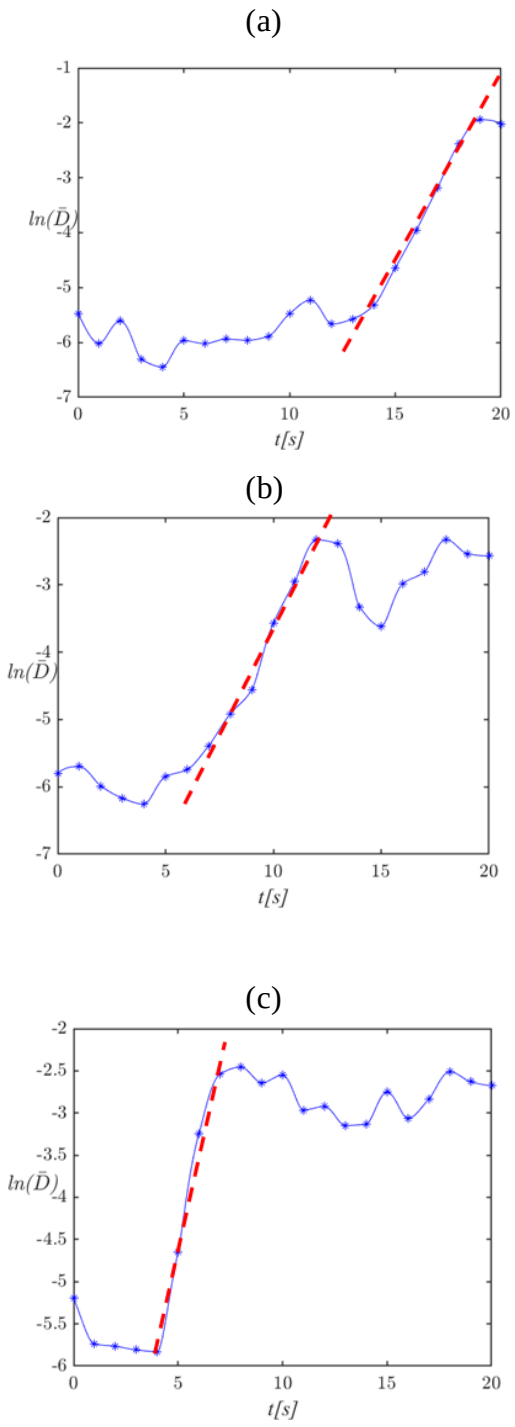

Figure A.13: Time evolution $ln(\bar{D})$ for $\Delta T = 7K$ and (a) $V_{peak} = 2\ kV$, (b) $V_{peak} = 3\ kV$, and (c) $V_{peak} = 5\ kV$.

A.4.2. Vertical Orientation

During our PFC campaign, the vertical rectangular cavity is filled with the dielectric liquid Novec 7200. For small values of L and $Ra \geq Ra_c$, the critical mode is hydrodynamic. During our experiment, the value of the Rayleigh number corresponding to a temperature difference $\Delta T = 7K$ is $Ra = 6.55 \cdot 10^6$ and $Ra = 9.36 \cdot 10^6$ for $\Delta T = 10K$ during the 1g phase of the parabola maneuver. So both values of Ra are above the critical value $Ra_c = 7.9 \cdot 10^4$ (without electric potential) marking the onset of hydrodynamic instability. Therefore, we would observe transverse rolls during the 1g phase which would be reinforced in the 1.8g; phase preceding the weightlessness phase. Figure A.14 shows the instantaneous flow structures for an applied temperature gradient $\Delta T \approx 7\ K$ and $V_{peak} \approx 0\ kV$. The snapshot is taken at the beginning of the microgravity phase. We can observe that the patterns of the divergence of the displacement are bent along the x-direction.

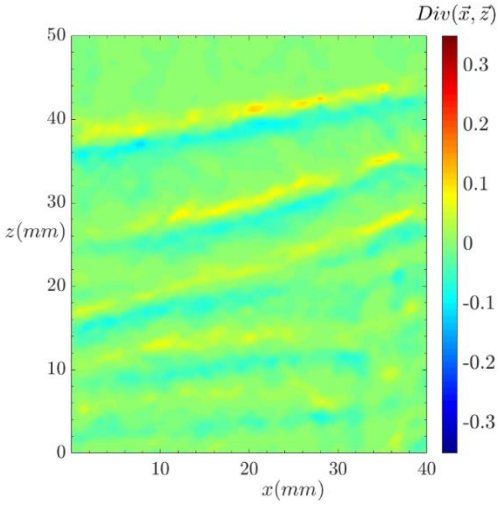

Figure A.14: Patterns of the divergence of the displacement vector ($Div(\vec{x},\vec{y})$) for the first parabola without the electric potential ($V_{peak} = 0$); The temperature difference is $\Delta T \approx 7\ K$.

In Figure A.15, we have presented the space-time diagram of the divergence of the displacement vector during the three phases of the parabola to have better insight into the behavior of the initial base flow. One observes that the transverse instability arising from the hydrodynamic effects during the 1g phase is reinforced during the hypergravity phase. The passage from the 1.8g to 0g phase is visible in the space-time diagram with a small deformation of the patterns. Despite this, the flow patterns persist during the first 18 s of the microgravity phase. At the end of

weightlessness, these structures are dissipated as shown in the space-time diagram and the passage to the hyper-gravity phase destroys completely the flow patterns. In the case of the vertical orientation, the obtained results were perturbed because of the alignment of the vertical cell with the plane direction. In this case, as the camera is placed perpendicularly to this direction, the flow is strongly affected by the hypergravity phases at the entrance and the exit of the weightlessness phase.

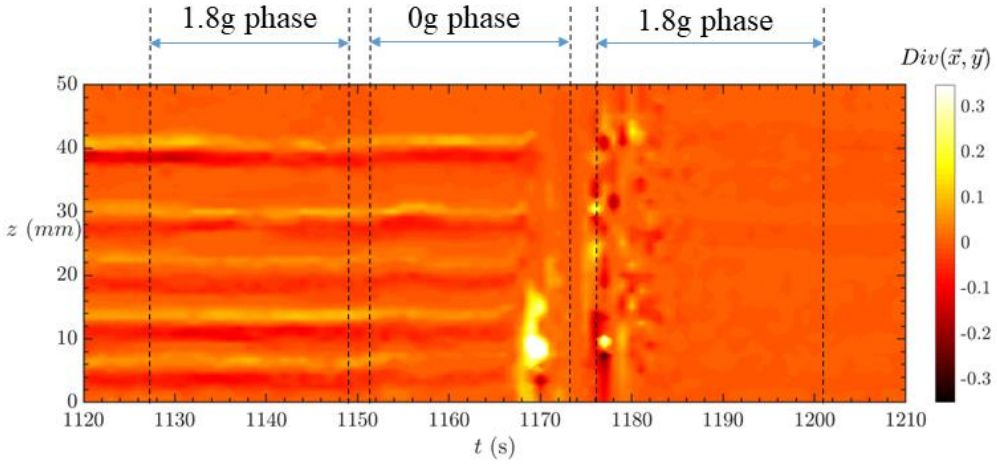

Figure A.15: Space-time diagram of the divergence of the displacement vector $(Div(\vec{x},\vec{y}))$ during a whole parabola at $x = 20\,mm$. Snapshots correspond to a temperature difference $\Delta T \approx 7\,K$ and no electric potential $V_{peak} = 0kV$.

In the absence of electric potential, the effect of microgravity (0g) dissipates the initial transverse structures; these patterns persist until the end of the microgravity phase. When the electric potential is applied, no significant visible effect of the dielectrophoretic on the initial transverse structures. This could be because the basic state of the system corresponds to an established flow regime during the two phases of 1g and 1.8g. Therefore, the duration of microgravity (22s) is not sufficient enough to destabilize this initial regime. However, we have observed the hydrodynamic modes and their persistence in the microgravity phase.

For a temperature difference $\Delta T = 10K$, the snapshots of the instantaneous flow structures at the end of the microgravity phase are presented in Figure A.16 for two values of the applied electric potential. The structures observed are inclined patterns. This deformation could be due to the inclination of the aircraft during the parabolic flight since the vertical cavity is aligned with the plane. The flow in the fluid is also affected by the acceleration component g_x which is not zero at the beginning and at the end of the microgravity phase as shown in Figure A.7.

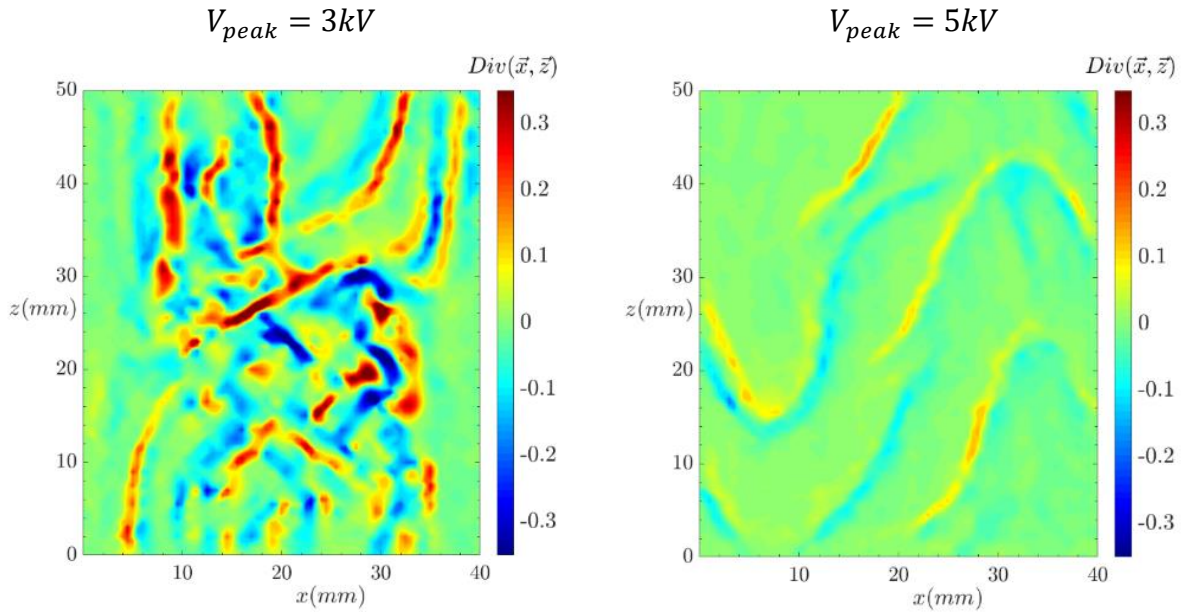

Figure A.16: Patterns of the divergence of the displacement vector ($Div(\vec{x}, \vec{y})$) for $\Delta T \approx 10\ K$ and different values of the electric potential V_{peak}.

Figure A.17 shows the space-time diagram of the flow during a microgravity phase for $\Delta T \approx 10\ K$ and two values of the electric potential $V_{peak} = 3kV$, and $V_{peak} = 5kV$. We can see a change in the flow patterns a few times after the beginning of the microgravity phase.

a- $V_{peak} = 3kV$,

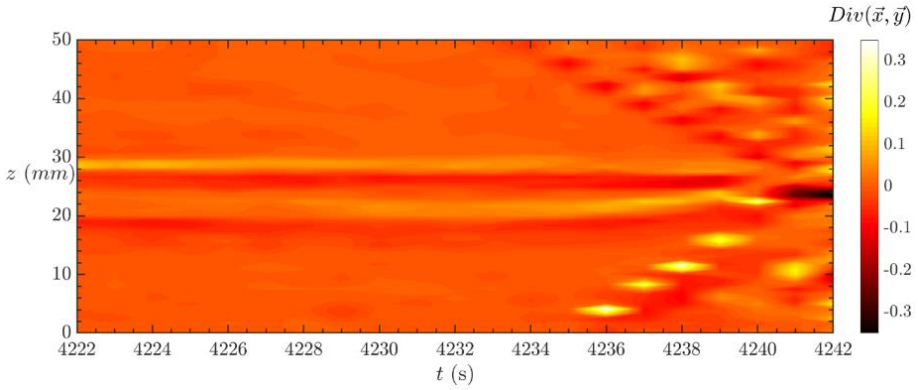

b- $V_{peak} = 5kV$

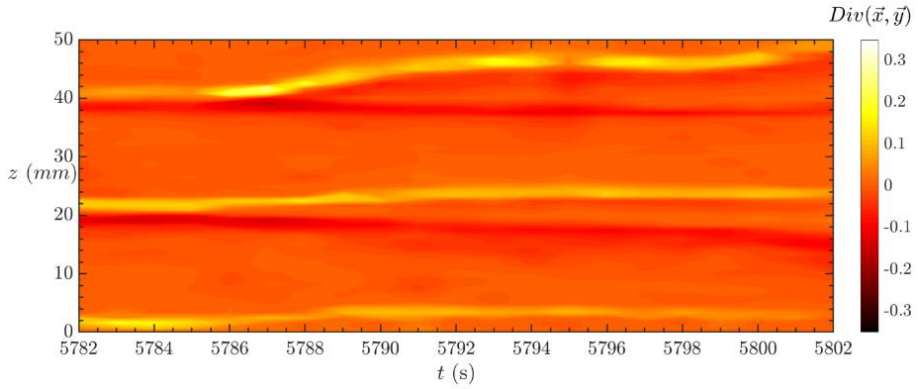

Figure A.17: Time evolution of the divergence of the displacement vector ($Div(\vec{x},\vec{y})$) at the mid-gap during a weightlessness phase. Snapshots correspond to $\Delta T \approx 10\,K$ and $V_{peak} = 3kV$ (a), and $V_{peak} = 5kV$ (b).

A.5. Partial Conclusion

During the parabolic flight campaign of September 2018, we investigated the effect of artificial electric gravity on a dielectric liquid layer in rectangular cavities in horizontal and vertical orientations. The evolution of the fluid is measured using the Background Orientation Schlieren technique.

Our investigations first concerned the horizontal orientation of the rectangular cell and heated from the top to ensure that the base state is stable and so no convective motions occur before the microgravity phase. For two fixed values of the temperature gradient, the value of the electric Rayleigh number is increased. The experiments performed during this campaign elucidated that thermo-convective motions are induced in the fluid during the microgravity phase. These motions consist of thermoelectric convective structures induced by dielectrophoretic buoyancy. For small temperature differences, flow patterns appear at a critical value of the electric potential which corresponds to that predicted by the linear stability. We also determined the growth rate of perturbations and showed that its value increases with the applied electric potential. Due to the limit of the weightlessness duration (22 s), we could not observe the establishment of a saturated state.

Concerning the vertical orientation, we investigated the fluid flow during the 1g, 1.8g, and 0g phases. We did not see any significant effect of the electric potential on the system due to the initial flow well established during the hypergravity phase. In addition, the system is affected by the horizontal component of the acceleration during the microgravity phase. A direct comparison between the BOS images and the original images showed that the BOS technique is not the best measurement technique for our experiment.

The experimental results obtained in the horizontal cavity validated the results from linear stability analysis and DNS. For future parabolic campaigns and DNS, it should be interesting to investigate the effects of the horizontal acceleration on the fluid, in particular, at the beginning and the end of the microgravity phase. The case of the vertical configuration may be studied in more detail to investigate the evanescence of the convective flow patterns in microgravity; the effect of the dielectrophoretic buoyancy in such a configuration may be investigated in the laboratory of LAS at BTU Cottbus.

Appendix B: Critical parameters of thermoelectric Rayleigh-Bénard convection

Values of critical parameters are given in the following tables for different values of Pr.

Table B.1: Critical parameters of electric modes for $Pr = 1$ and different values of Ra.

Ra	Gr	k_{y_c}	k_{x_c}	L_c	γ_e	k_c
1 000	1 000	0.258	3.150	883.518	2.5E-03	3.161
500	500	0.943	3.050	1 506.573	1.3E-03	3.193
10	10	1.050	3.050	2 115.838	1.5E-05	3.226
5	5	0.025	3.225	2 122.350	1.3E-05	3.225
0	0	2.074	2.456	2128.694	2.5E-05	3.228
-5	-5	0.348	3.200	2 134.796	-1.3E-05	3.219
-10	-10	2.100	2.450	2 140.696	2.5E-05	3.227
-100	-100	1.702	2.748	2 253.006	-2.5E-04	3.233
-500	-500	0.251	3.250	2 749.868	-1.3E-03	3.260
-1 000	-1000	1.642	2.856	3 370.074	-2.5E-03	3.294
-1 500	-1500	2.206	2.494	3 989.296	-3.8E-03	3.330
-2 000	-2000	1.044	3.200	4 607.532	-5.0E-03	3.366
-2 500	-2500	0.125	3.400	5 224.757	-6.3E-03	3.402
- 3 000	-3000	1.850	2.900	5 840.967	-7.5E-03	3.440
-3 500	-3500	2.244	2.656	6 456.150	-8.8E-03	3.477
-4 000	-4000	1.752	3.048	7 070.302	-1.0E-02	3.516
-4 500	-4500	0.855	3.450	7 683.412	1.1E-02	3.554
-5 000	-5000	1.298	3.350	8 295.480	-1.3E-02	3.593
-5 500	-5500	2.244	2.856	8 906.503	-1.4E-02	3.632
-6000	-6000	1.800	3.200	9516.479	-1.5E-02	3.672
-6 500	-6500	0.900	3.600	10 125.410	-1.6E-02	3.711
-7 000	-7000	0	3.750	10 733.300	-1.8E-01	3.750
-7 500	-7500	0.544	3.750	11 340.150	-1.9E-02	3.789
-8 000	-8000	2.244	3.106	11 945.940	-2.0E-02	3.832
-8 500	-8500	0.952	3.748	12 550.750	-2.1E-02	3.867
- 9 000	-9000	1.258	3.684	13 154.520	2.3E-02	3.893
-9 500	-9500	0.594	3.900	13 757.290	-2.4E-02	3.945
-10 000	-10000	1.906	3.500	14 359.050	-2.5E-02	3.985
-11 000	-11000	0.692	4.000	15 559.630	-2.8E-02	4.059
-12 000	-12000	2.202	3.498	16 756.340	-3.0E-02	4.134

Table B.2: Critical parameters of electric modes for $Pr = 10$ and different values of Ra.

Ra	Gr	k_{y_c}	k_{x_c}	L_c	γ_e	k_c
1000	100	0.992	3.000	883.505	2.5E-04	3.160
500	50	2.070	2.430	1 506.576	1.3E-04	3.192
10	1	0.400	3.200	2 116.260	2.5E-06	3.225
5	0.5	1.050	3.050	2 122.477	1.3E-06	3.226
0	0	0.694	3.151	2 128.693	2.5E-12	3.227
-5	-0.5	0.700	3.149	2 134.909	-1.1E-06	3.226
-10	-1	0.700	3.150	2 141.125	-2.5E-06	3.227
-100	-10	1.700	2.750	2 253.007	-2.5E-05	3.233
-500	-50	1.150	3.050	2 749.869	-1.3E-04	3.260
-1000	-100	1.642	2.856	3 370.078	-2.5E-04	3.294
-1500	-150	2.205	2.495	3 989.310	-3.8E-04	3.330
-2000	-200	1.045	3.200	4 607.553	-5.0E-04	3.366
-2500	-250	0.125	3.400	5 224.799	-6.3E-04	3.402
-3000	-300	1.850	2.900	5 841.035	-7.5E-04	3.440
-3500	-350	2.244	2.656	6 456.655	-7.5E-04	3.477
-4000	-400	1.748	3.050	7 070.454	-1.0E-03	3.516
-4500	-450	0.169	3.550	7 683.628	-1.1E-03	3.554
-5000	-500	0.552	3.550	8 295.769	-1.3E-03	3.593
-5500	-550	2.224	2.856	8 906.894	-1.4E-03	3.620
-6000	-600	1.801	3.198	9 516.988	-1.5E-03	3.670
-6500	-650	0.900	3.600	10 126.060	-1.6E-03	3.711
-7000	-700	0	3.750	10 734.110	-1.8E-03	3.750
-7500	-750	1.452	3.500	11 341.160	-1.9E-03	3.789
-8000	-800	1.550	3.500	11 947.210	-2.0E-03	3.828
-8500	-850	2.494	2.957	12 552.260	2.1E-03	3.868
-9000	-900	1.251	3.700	13 156.330	-2.3E-03	3.906
-9500	-950	2.000	3.400	13 759.430	-2.4E-03	3.947
-10000	-1000	1.902	3.500	14 361.580	-2.5E-03	3.983
-11000	-1100	0.258	4.050	15 563.060	-2.8E-03	4.058
-12000	-1200	1.502	3.850	16 760.900	-3.0E-03	4.133

Table B.3: Critical parameters of electric modes for $Pr = 60$ and different values of Ra.

Ra	Gr	k_{y_c}	k_{x_c}	L_c	γ_e	k_c
1000	16.67	0.258	3.150	883.514	4.2E-05	3.161
500	8.33	0.944	3.050	1 506.573	2.1E-05	3.193
10	0.17	0.406	3.194	2 116.236	4.2E-07	3.219
5	0.08	0.900	3.100	2 122.455	2.1E-07	3.228
-5	-0.08	1.302	2.952	2 134.896	-2.1E-07	3.226
-10	-0.17	2.200	2.350	2 141.046	-4.2E-06	3.219
-100	-1.67	1.700	2.750	2 252.972	-4.2E-06	3.234
-500	-8.33	0.252	3.250	2 749.868	-2.1E-05	3.260
-1000	-16.67	1.642	2.856	3 370.082	-4.2E-05	3.295
-1500	-25.00	2.206	2.494	3 989.309	-6.3E-05	3.330
-2000	-33.33	1.043	3.200	4 607.554	-8.3E-05	3.366
-2500	-41.67	0.125	3.400	5 224.799	-1.0E-04	3.402
-3000	-50.00	1.852	2.898	5 841.032	-1.3E-04	3.439
-3500	-58.33	2.244	2.657	6 456.258	-1.5E-04	3.477
-4000	-66.67	0.275	3.500	7 070.414	-1.7E-04	3.511
-4500	-75.00	0.175	3.550	7 683.629	-1.9E-04	3.554
-5000	-83.33	0.552	3.550	8 295.777	-2.1E-04	3.593
-5500	-91.67	2.244	2.856	8 906.898	-2.3E-04	3.632
-6000	-100.00	1.802	3.198	9 516.993	-2.5E-04	3.671
-6500	-108.33	0.898	3.600	10 126.050	-2.7E-04	3.710
-7000	-116.67	0	3.750	10 734.120	-2.9E-04	3.750
-7500	-125.00	0.544	3.750	11 341.160	-3.1E-04	3.789
-8000	-133.33	1.552	3.500	11 947.190	-3.3E-04	3.828
-8500	-141.67	2.500	2.950	12 552.270	-3.5E-04	3.867
-9000	-150.00	1.252	3.700	13 156.350	-3.8E-04	3.906
-9500	-158.33	2.000	3.400	13 759.450	-4.0E-04	3.945
-10000	-166.67	1.902	3.500	14 361.610	-4.2E-04	3.983
-11000	-183.33	0.256	4.050	15 563.100	-4.6E-04	4.058
-12000	-200.00	1.500	3.850	16 760.950	-5.0E-04	4.132

Table B.4: Critical parameters of electric modes for $Pr = 100$ and different values of Ra.

Ra	Gr	k_{y_c}	k_{x_c}	L_c	γ_e	k_c
1000	10	0.550	3.100	883.115	2.5E-05	3.148
500	5	1.700	2.700	1 506.535	1.3E-05	3.191
10	0.1	0.405	3.202	2 116.250	2.5E-07	3.227
5	0.05	0.900	3.100	2 122.407	1.3E-07	3.228
-5	-0.05	2.125	2.425	2 134.847	-1.3E-07	3.224
-10	-0.1	0.700	3.150	2 141.124	-2.5E-07	3.227
-100	-1	1.200	3.000	2 252.929	-2.5E-06	3.231
-500	-5	0.250	3.250	2 749.857	-1.3E-05	3.259
-1000	-10	1.248	3.048	3 370.047	-2.5E-05	3.294
-1500	-15	0.444	2.300	3 989.282	-3.8E-05	2.342
-2000	-20	1.043	3.199	4 607.547	-5.0E-05	3.365
-2500	-25	0.125	3.400	5 224.801	-6.3E-05	3.402
-3000	-30	1.850	2.900	5 841.036	-7.5E-05	3.440
-3500	-35	1.750	3.000	6 456.202	-8.8E-05	3.473
-4000	-40	1.748	3.050	7 070.455	-1.0E-04	3.516
-4500	-45	0.169	3.550	7 683.629	-1.1E-04	3.554
-5000	-50	0.551	3.550	8295.801	-1.3E-04	3.593
-5500	-55	2.244	2.856	8 906.917	-1.4E-04	3.632
-6000	-60	1.800	3.200	9 516.995	-1.5E-04	3.672
-6500	-65	0.898	3.600	10 126.070	-1.6E-04	3.710
-7000	-70	0	3.750	10 734.120	-1.8E-04	3.750
-7500	-75	1.452	3.500	11 341.170	-1.9E-04	3.789
-8000	-80	1.552	3.500	11 947.220	-2.0E-04	3.828
-8500	-85	2.494	2.956	12 552.270	-2.1E-04	3.868
-9000	-90	1.250	3.700	13 156.340	-2.3E-04	3.906
-9500	-95	2.000	3.400	13 759.450	-2.4E-04	3.945
-10000	-100	1.902	3.500	14 361.600	-2.5E-04	3.983
-11000	-110	0.258	4.050	15 563.090	-2.8E-04	4.058
-12000	-120	0.458	4.101	16 760.960	-3.0E-04	4.126

Table B.5: Critical parameters of electric modes for $Pr = 1000$ and different values of Ra.

Ra	Gr	k_{y_c}	k_{x_c}	L_c	γ_e	k_c
1000	1	0.800	3.050	883.279	2.5E-06	3.153
500	0.5	1.808	2.642	1 506.108	1.3E-06	3.201
10	0.01	0.400	3.200	2 116.073	2.5E-08	3.225
5	0.005	2.100	2.450	2 122.401	1.3E-08	3.227
-5	-0.005	2.100	2.450	2 134.790	-1.3E-08	3.227
-10	-0.01	1.500	2.850	2 141.037	-2.5E-08	3.221
-100	-0.1	0.407	3.206	2 252.950	-2.5E-07	3.232
-500	-0.5	0	3.250	2 749.842	-1.3E-06	3.250
-1000	-1	1.650	2.850	3 369.801	-2.5E-06	3.293
-1500	-1.5	2.199	2.498	3 989.026	-3.8E-06	3.328
-2000	-2	2.000	2.700	4 607.299	-5.0E-06	3.360
-2500	-2.5	2.400	2.400	5 223.821	-6.3E-06	3.394
-3000	-3	0.500	3.400	5 840.387	-7.5E-06	3.437
-3500	-3.5	2.475	2.450	6 456.232	-8.8E-06	3.482
-4000	-4	2.256	2.694	7 070. 295	-1.0E-05	3.514
-4500	-4.5	0.648	3.500	7 683.464	-1.1E-05	3.559
-5000	-5	1.301	3.349	8 295.788	-1.3E-05	3.593
-5500	-5.5	0.952	3.500	8 906.844	-1.4E-05	3.627
-6000	-6	1.800	3.200	9 516.955	-1.5E-05	3.671
-6500	-6.5	2.450	2.800	10 126.040	-1.6E-05	3.721
-7000	-7	0	3.750	10 734.080	-1.8E-05	3.750
-7500	-7.5	1.452	3.500	11 341.160	-1.9E-05	3.789
-8000	-8	1.552	3.500	11 947.220	-2.0E-05	3.828
-8500	-8.5	2.494	2.955	12 552.270	-2.1E-05	3.866
-9000	-9	1.252	3.700	13 156.340	-2.3E-05	3.906
-9500	-9.5	1.998	3.402	13 759.450	-2.4E-05	3.945
-10000	-10	1.898	3.502	14 361.620	-2.5E-05	3.983
-11000	-11	0.258	4.050	15 563.110	-2.8E-05	4.059
-12000	-12	1.502	3.850	16 760.980	-3.0E-05	4.133

Appendix C: Thresholds of hydrodynamic, thermal, and electric modes in the vertical rectangular fluid layer

Some numerical values of critical parameters are presented in this appendix. In the case of the flow in a vertical cavity, we showed the existence of three critical modes depending on the values of Ra, Pr, and L.

Table C.1: Critical values of hydrodynamic and electric modes for $Pr = 1$.

k_{z_c}	k_{y_c}	Gr_{cr}	γ_e	L	ω_c	Ra_c
2.81	0.00	7940.29	1.99E-02	0	-2.40E-04	7940.29
2.83	0.00	7558.95	1.89E-02	1332.85	-5.48E-03	7558.95
2.83	0.00	7520.10	1.88E-02	1461.76	-6.11E-03	7520.10
2.83	0.00	7481.07	1.87E-02	1590.15	-6.60E-03	7481.07
2.83	0.00	7441.79	1.86E-02	1718.07	-7.14E-03	7441.79
2.83	0.00	7402.19	1.85E-02	1845.57	-7.66E-03	7402.19
2.83	0.00	7362.41	1.84E-02	1972.75	-8.14E-03	7362.41
2.83	0.00	7322.25	1.83E-02	2099.62	-8.77E-03	7322.25
2.83	0.00	7318.22	1.83E-02	2112.29	-8.82E-03	7318.22
2.83	0.00	7314.18	1.83E-02	2124.97	-8.87E-03	7314.18
The transition from Hydrodynamic mode to Electric mode						
k_{z_c}	k_{y_c}	Gr	γ_e	L_c	ω_c	Ra_c
0.00	3.23	7307.51	1.83E-02	2128.56	-1.56E-06	7307.51
0.00	3.23	7279.12	1.82E-02	2128.56	-1.13E-06	7279.12
0.00	3.23	6962.25	1.74E-02	2128.57	-1.07E-06	6962.25
0.00	3.23	5838.09	1.46E-02	2124.89	-7.30E-07	5838.09
0.00	3.19	3682.11	9.21E-03	2125.86	-4.86E-07	3682.11
0.00	3.29	1784.42	4.46E-03	2126.59	-2.13E-07	1784.42
0.00	3.23	774.76	1.94E-03	2128.65	9.27E-07	774.76
0.67	3.18	376.23	9.41E-04	2133.71	-5.45E-05	376.23
0.67	3.17	299.62	7.49E-04	2131.89	-3.72E-05	299.62

Table C.2: Critical values of thermal and electric modes for $Pr = 20$.

k_{z_c}	k_{y_c}	Gr_{cr}	γ_e	L	ω_c	Ra_c
1.67	0.00	2415.74	6.04E-03	0.00	-7.75	48314.78
1.67	0.00	2403.85	6.01E-03	419.56	-7.70	48076.90
1.67	0.00	2399.24	6.00E-03	586.27	-7.70	47984.72
1.67	0.00	2396.95	5.99E-03	669.40	-7.68	47939.02
1.67	0.00	2392.18	5.98E-03	835.11	-7.66	47843.62
1.67	0.00	2387.43	5.97E-03	1000.19	-7.65	47748.56
1.67	0.00	2385.23	5.96E-03	1082.57	-7.65	47704.58
1.67	0.00	2368.94	5.92E-03	1654.50	-7.59	47378.78
1.67	0.00	2366.63	5.92E-03	1735.60	-7.58	47332.50
1.67	0.00	2364.32	5.91E-03	1816.56	-7.57	47286.30
1.67	0.00	2362.01	5.91E-03	1897.36	-7.56	47240.14
1.67	0.00	2359.72	5.90E-03	1978.03	-7.55	47194.46
1.67	0.00	2357.42	5.89E-03	2058.55	-7.55	47148.46
The transition from oscillatory thermal modes to stationary electric modes						
k_{z_c}	k_{y_c}	Gr	γ_e	L_c	ω_c	Ra_c
0.00	3.24	2343.95	5.86E-03	2128.76	1.22E-08	46878.94
0.00	3.23	2029.44	5.07E-03	2127.16	2.15E-08	40588.70
0.00	3.23	1216.23	3.04E-03	2128.12	-5.38E-08	24324.50
0.00	3.23	603.60	1.51E-03	2128.63	1.72E-07	12072.08
0.00	3.23	292.43	7.31E-04	2128.71	1.41E-07	5848.57
0.00	3.25	184.26	4.61E-04	2127.68	1.62E-07	3685.24
0.00	3.21	126.85	3.17E-04	2128.73	6.40E-08	2536.92
0.00	3.23	89.31	2.23E-04	2128.68	-3.02E-06	1786.17
0.00	3.24	61.45	1.54E-04	2128.67	-2.60E-06	1228.99
0.00	3.19	38.73	9.68E-05	2128.40	2.17E-05	774.67

Table C.3: Critical values of thermal and electric modes for $Pr = 100$.

k_{z_c}	k_{y_c}	Gr_{cr}	γ_e	L	ω_c	Ra_c
2.42	0.00	745.27	1.86E-03	0.00	3.71	74527.29
2.43	0.00	734.26	1.84E-03	1281.66	-3.64	73426.08
2.43	0.00	732.72	1.83E-03	1406.89	-3.64	73271.54
2.44	0.00	731.16	1.83E-03	1531.56	-3.64	73115.90
2.44	0.00	729.64	1.82E-03	1655.78	-3.63	72963.59
2.44	0.00	728.09	1.82E-03	1779.41	-3.63	72808.75
2.44	0.00	726.54	1.82E-03	1902.52	-3.62	72654.12
2.44	0.00	725.01	1.81E-03	2025.14	-3.61	72501.17
The transition from oscillatory thermal modes to stationary electric modes						
k_{z_c}	k_{y_c}	Gr	γ_e	L_c	ω_c	Ra_c
0.00	3.23	717.21	1.79E-03	2128.64	7.34E-08	71721.17
0.00	3.21	609.58	1.52E-03	2128.71	4.48E-08	60958.14
0.00	3.23	120.72	3.02E-04	2128.55	-1.74E-08	12071.61
0.00	3.23	58.48	1.46E-04	2128.34	7.38E-07	5847.56
0.00	3.25	36.86	9.22E-05	2128.30	6.35E-09	3686.32
0.00	3.24	25.37	6.34E-05	2128.60	2.18E-08	2536.77
0.00	3.23	17.86	4.47E-05	2128.63	7.56E-07	1786.13
0.00	3.21	12.29	3.07E-05	2128.09	5.54E-08	1228.66
0.00	2.93	7.70	1.92E-05	2114.95	-1.17E-04	769.78

Appendix D: Properties of some dielectric liquids used for experiments

The properties of some dielectric liquids are presented in this section. Principally the physical properties of silicone oils and the Novec. Table D.1 is furnished by the specialized American company of silicone oil and lubricant products Clearco Products Inc. The table gives the properties of two types of silicone oils based on their viscosity: low viscosity liquids and standard viscosity liquids.

Table D.2 presents the properties of three types of Novec liquid. In both tables, the kinematic viscosity is given in terms of centistokes: 1 cSt $= 0.01$ St. $= 10^{-6}$ m^2 s^{-1}. The dielectric strength is also expressed in volt per mil (V/mil). This unit corresponds to the electric field obtained by applying a potential of 1V between two infinite parallel planes distanced by 1 mil. Therefore, $1\,V/mil = 39.37 \cdot 10^{-3}\,kV/mm = 1000\,V/inch$, with $1\,inch = 1000\,mil = 0.0254\,m$. The Novec fluids are manufactured by the 3M Novec Engineered Fluids. The values are determined at 25°C.

Table D.1: Properties of Polydimethylsiloxane Fluids (Clearco Products Inc.).

Product Code	Viscosity cSt	Viscosity Temp. Coefficient	Refractive Index	Specific heat@ 25°C Cal/g/°C	Coeff. of Thermal Expansion cc/cc/°C, 0-150°C	Thermal Conductivity @ 25°C g /cal/cm/sec °C	Dielectric Constant 50Hz	Dielectric Strength Volts/mil	Dielectric loss tangent 50Hz Dissipation factor
Low Viscosities									
PSF-0.65cSt	.65	0.31	1.3750	0.410	0.00134	0.00024	2.20	300	0.0001
PSF-1cSt	1.0	0.37	1.3825	0.410	0.00134	0.00024	2.30	350	0.0001
PSF-1.5cSt	1.5	0.46	1.3880	0.410	0.00134	0.00025	2.39	350	0.0001
PSF-2cSt	2.0	0.48	1.3900	0.410	0.00117	0.00026	2.45	350	0.0001
PSF-3cSt	3.0	0.51	1.3935	0.39	0.00114	0.00027	2.50	350	0.0001
PSF-5cSt	5.0	0.54	1.3970	0.39	0.00109	0.00028	2.60	375	0.0001
PSF-10cSt	10	0.56	1.3990	0.36	0.00108	0.00032	2.68	375	0.0001
PSF-20cSt	20	0.59	1.4000	0.36	0.00107	0.00034	2.72	375	0.0001
Standard Viscosities									
PSF-50cSt	50	0.59	1.402	0.36	0.00106	0.00036	2.75	400	0.0001
PSF-100cSt	100	0.60	1.4030	0.36	0.00096	0.00037	2.75	400	0.0001
PSF-200cSt	200	0.60	1.4031	0.36	0.00096	0.00037	2.75	400	0.0001
PSF-350cSt	350	0.60	1.4032	0.36	0.00096	0.00037	2.75	400	0.0001
PSF-500cSt	500	0.60	1.4033	0.36	0.00096	0.00038	2.75	400	0.0001
PSF-1,000cSt	1,000	0.61	1.4035	0.36	0.00096	0.00038	2.75	400	0.0001

Table D.2: Physical properties of Novec Fluids.

Dielectric Liquids	Novec 7100	Novec 7200	Novec 7500
Boiling Point (°C)	61	76	128
Pour Point (°C)	-135	-138	-110
Vapor Pressure (Pa)	$26.8 \cdot 10^3$	$15.7 \cdot 10^3$	$2.1 \cdot 10^3$
Density (kg/m3)	1510	1420	1610
Coefficient of Volume Expansion ($°C^{-1}$)	0.0018	0.0016	0.0013
Kinematic Viscosity (cSt.)	0.38	0.41	0.77
Specific Heat (J kg^{-1} $°C^{-1}$)	1180	1220	1130
Heat of Vaporization @ B.P. (J/g)	112	119	88.5
Dielectric Strength (kV, 0.1" gap)	~40	~40	~40
Dielectric Constant (1 KHz)	7.4	7.3	5.8
Volume Resistivity (Ω cm)	10^8	10^8	10^8

Appendix E: Pictures during the parabolic flight campaign

The following pictures show the experimental apparatus of the parabolic campaign of September 2018 downloaded inside the Aircraft at NOVESPACE in Bordeaux showing the two experimental boxes. The experiment control computer with the LabVIEW program opened. Figure E.2 presents the rectangular cavities, the cameras, and the illuminated dot patterns for the flow visualization.

Figure E.1: The experiment inside the aircraft. The picture on the right is the control computer with the LabVIEW main interface during a simulation run test inside the Aircraft on the ground.

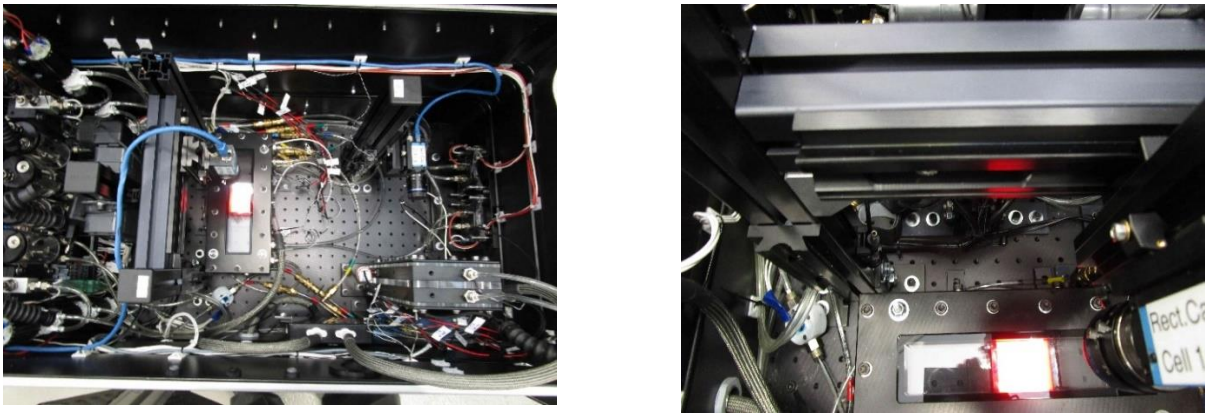

Figure E.2: Presentation of the interior of the experimental rack.

Figure E.3: The experiment inside the aircraft during a microgravity phase. Participants of the parabolic flight campaign of September 2018. From the left to the right of the up picture in the right: M. Meier, I. Mutabazi, E. B. Barry, M. Jongmanns, O. Crumeyrolle. In the same order for the picture below in front of the Zero-G aircraft: E. B. Barry, I. Mutabazi, A. Meyer.

Figure E.4: E. B. Barry and the French astronaut Thomas Pesquet during the 2018 PFC.

Figure E.5: E. B. Barry and the French journalist Jamy Gourmaud during the 2018 PFC.

List of Figures

List of Tables

Bibliography

[1] B. J. Kirby, *Micro- and Nanoscale Fluid Mechanics: Transport in Microfluidic Devices*, Cambridge university press (2010).

[2] A. Baïri, E. Zarco-Pernia, and J.-M. García de María, *A Review on Natural Convection in Enclosures for Engineering Applications. The Particular Case of the Parallelogrammic Diode Cavity*, Appl. Therm. Eng. **63**, 304 (2014).

[3] V. Kishor, S. Singh, and A. Srivastava, *Investigation of Convective Heat Transfer Phenomena in Differentially-Heated Vertical Closed Cavity: Whole Field Experiments and Numerical Simulations*, Exp. Therm. Fluid Sci. **99**, 71 (2018).

[4] M. H. Mousa, N. Miljkovic, and K. Nawaz, *Review of Heat Transfer Enhancement Techniques for Single Phase Flows*, Renew. Sustain. Energy Rev. **137**, 110566 (2021).

[5] B.-F. Wang, Q. Zhou, and C. Sun, *Vibration-Induced Boundary-Layer Destabilization Achieves Massive Heat-Transport Enhancement*, Sci. Adv. **6**, 8239 (2020).

[6] Y.-C. Xie and K.-Q. Xia, *Turbulent Thermal Convection over Rough Plates with Varying Roughness Geometries*, J. Fluid Mech. **825**, 573 (2017).

[7] B. Sitte and H. Rath, *Influence of the Dielectrophoretic Force on Thermal Convection*, Exp. Fluids **34**, 24 (2003).

[8] S. Laohalertdecha, P. Naphon, and S. Wongwises, *A Review of Electrohydrodynamic Enhancement of Heat Transfer*, Renew. Sustain. Energy Rev. **11**, 858 (2007).

[9] P. H. G. Allen and T. G. Karayiannis, *Electrohydrodynamic Enhancement of Heat Transfer and Fluid Flow*, Heat Recovery Syst. CHP **15**, 389 (1995).

[10] B. Chandra and D. E. Smylie, *A Laboratory Model of Thermal Convection under a Central Force Field*, Geophys. Fluid Dyn. **3**, 211 (1972).

[11] I. M. Yavorskaya, N. I. Fomina, and Yu. N. Belyaev, *A Simulation of Central-Symmetry Convection in Microgravity Conditions*, Acta Astronaut. **11**, 179 (1984).

[12] R. Hollerbach, *A Spectral Solution of the Magneto-Convection Equations in Spherical Geometry*, Int. J. Numer. Methods Fluids **32**, 773 (2000).

[13] V. V. Travnikov, H. J. Rath, and C. Egbers, *Stability of Natural Convection between Spherical Shells: Energy Theory*, Int. J. Heat Mass Transf. **45**, 4227 (2002).

[14] V. Travnikov, K. Eckert, and S. Odenbach, *Influence of an Axial Magnetic Field on the Stability of Convective Flows between Non-Isothermal Concentric Spheres*, Int. J. Heat Mass Transf. **55**, 7520 (2012).

[15] V. Travnikov, K. Eckert, and S. Odenbach, *Influence of the Prandtl Number on the Stability of Convective Flows between Non-Isothermal Concentric Spheres*, Int. J. Heat Mass Transf. **66**, 154 (2013).

[16] B. Futterer, A. Krebs, A. C. Plesa, F. Zaussinger, R. Hollerbach, D. Breuer, and C. Egbers, *Sheet-like and Plume-like Thermal Flow in a Spherical Convection Experiment Performed under Microgravity*, J. Fluid Mech. **735**, 647 (2013).

[17] M. Jongmanns, *Flow Control of Thermal Convection Using Thermo Electro Hydrodynamic Forces in a Cylindrical Annulus*, Mech. Eng., Thesis of Brandenburg University of Technology Cottbus (2019).

[18] I. Mutabazi, H. N. Yoshikawa, M. T. Fogaing, V. Travnikov, O. Crumeyrolle, B. Futterer, and C. Egbers, *Thermo-Electro-Hydrodynamic Convection under Microgravity: A Review*, Fluid Dyn. Res. **48**, 061413 (2016).

[19] V. Travnikov, O. Crumeyrolle, and I. Mutabazi, *Influence of the Thermo-Electric Coupling on the Heat Transfer in Cylindrical Annulus with a Dielectric Fluid under Microgravity*, Acta Astronaut. **129**, 88 (2016).

[20] A. Meyer, M. Jongmanns, M. Meier, C. Egbers, and I. Mutabazi, *Thermal Convection in a Cylindrical Annulus under a Combined Effect of the Radial and Vertical Gravity*, Comptes Rendus Mécanique **345**, 11 (2017).

[21] C. Kang and I. Mutabazi, *Dielectrophoretic Buoyancy and Heat Transfer in a Dielectric Liquid Contained in a Cylindrical Annular Cavity*, J. Appl. Phys. **125**, 184902 (2019).

[22] N. Dahley, B. Futterer, C. Egbers, O. Crumeyrolle, and I. Mutabazi, *Parabolic Flight Experiment "Convection in a Cylinder" – Convection Patterns in Varying Buoyancy Forces*, J. Phys. Conf. Ser. **318**, 082003 (2011).

[23] M. Meier, M. Jongmanns, A. Meyer, T. Seelig, C. Egbers, and I. Mutabazi, *Flow Pattern and Heat Transfer in a Cylindrical Annulus Under 1 g and Low-g Conditions: Experiments*, Microgravity Sci. Technol. **30**, 699 (2018).

[24] A. Meyer, M. Meier, M. Jongmanns, T. Seelig, C. Egbers, and I. Mutabazi, *Effect of the Initial Conditions on the Growth of Thermoelectric Instabilities During Parabolic Flights*, Microgravity Sci. Technol. **31**, 715 (2019).

[25] B. Futterer, M. Gellert, Th. von Larcher, and C. Egbers, *Thermal Convection in Rotating Spherical Shells: An Experimental and Numerical Approach within GeoFlow*, Acta Astronaut. **62**, 300 (2008).

[26] P. H. Roberts, *Electrohydrodynamic Convection*, Q. J. Mech. Appl. Math. **22**, 211 (1969).

[27] P. J. Stiles, *Electro-Thermal Convection in Dielectric Liquids*, Chem. Phys. Lett. **179**, 5 (1991).

[28] P. J. Stiles, F. Lin, and P. J. Blennerhassett, *Convective Heat Transfer through Polarized Dielectric Liquids*, Phys. Fluids A **5**, 3273 (1993).

[29] M. Tadie Fogaing, H. Yoshikawa, O. Crumeyrolle, and I. Mutabazi, *Heat Transfer in the Thermo-Electro-Hydrodynamic Convection under Microgravity Conditions*, Eur. Phys. J. E Soft Matter **37**, 9987 (2014).

[30] R. J. Turnbull, *Effect of Dielectrophoretic Forces on the Bénard Instability*, Phys. Fluids **12**, 1809 (1969).

[31] R. J. Turnbull and J. R. Melcher, *Electrohydrodynamic Rayleigh-Taylor Bulk Instability*, Phys. Fluids **12**, 1160 (1969).

[32] H. N. Yoshikawa, M. Tadie Fogaing, O. Crumeyrolle, and I. Mutabazi, *Dielectrophoretic Rayleigh-Bénard Convection under Microgravity Conditions*, Phys. Rev. E **87**, 043003 (2013).

[33] S. Chandrasekhar, *Hydrodynamic and Hydromagnetic Stability*, Dover Publications (1981).

[34] E. Bodenschatz, W. Pesch, and G. Ahlers, *Recent Developments in Rayleigh-Bénard Convection*, Annu. Rev. Fluid Mech. **32**, 709 (2000).

[35] F. H. Busse, *Non-Linear Properties of Thermal Convection*, Rep. Prog. Phys. **41**, 1929 (1978).

[36] A. Bahloul, I. Mutabazi, and A. Ambari, *Codimension 2 Points in the Flow inside a Cylindrical Annulus with a Radial Temperature Gradient*, Eur. Phys. J. Appl. Phys. **9**, 253 (2000).

[37] G. K. Batchelor, *Heat Transfer by Free Convection across a Closed Cavity between Vertical Boundaries at Different Temperatures*, Q. Appl. Math. **12**, 209 (1954).

[38] E. R. G. Eckertf and W. O. Carlson, *Natural Convection in an Air Layer Enclosed between Two Vertical Plates with Different Temperatures*, Int. J. Heat Mass Transf. **2**, 106 (1961).

[39] G. Z. Gershuni and E. M. Zhukhovitskii, *Convective Stability of Incompressible Fluids*, Keter Publishing House Jerusalem Ltd (1976).

[40] Y. Lee and S. A. Korpela, *Multicellular Natural Convection in a Vertical Slot*, J. Fluid Mech. **126**, 91 (1983).

[41] J. W. Elder, *Laminar Free Convection in a Vertical Slot*, J. Fluid Mech. **23**, 77 (1965).

[42] M. Tadie Fogaing, *Instabilités thermoconvectives dans un fluide diélectrique*, Physics, Thesis of Université du Havre (2013).

[43] J. W. Elder, *Turbulent Free Convection in a Vertical Slot*, J. Fluid Mech. **23**, 99 (1965).

[44] M. Tadie Fogaing, L. Nana, O. Crumeyrolle, and I. Mutabazi, *Wall Effects on the Stability of Convection in an Infinite Vertical Layer*, Int. J. Therm. Sci. **100**, 240 (2016).

[45] R. F. Bergholz, *Instability of Steady Natural Convection in a Vertical Fluid Layer*, J. Fluid Mech. **84**, 743 (1978).

[46] A. A. Ganguli, A. B. Pandit, and J. B. Joshi, *Numerical Predictions of Flow Patterns Due to Natural Convection in a Vertical Slot*, Chem. Eng. Sci. **62**, 4479 (2007).

[47] B. Roux, J. C. Grondin, P. Bontoux, and B. Gilly, *On a High-Order Accurate Method for the Numerical Study of Natural Convection in a Vertical Square Cavity*, Numer. Heat Transf. Part B Fundam. **1**, 331 (1978).

[48] T. Masaki, *The Stability of Natural Convection Due to Internal Heat Sources in a Vertical Fluid Layer*, Fluid Dyn. Res. **6**, 15 (1990).

[49] N. Marneni, *Transient Free Convection Flow Between Two Long Vertical Parallel Plates with Constant Temperature and Mass Diffusion*, World Congr. Eng. 2008 **Vol II**, 6 (2008).

[50] P. Le Quéré, *Transition to Unsteady Natural Convection in a Tall Water-filled Cavity*, Phys. Fluids A **2**, 503 (1990).

[51] J. L. Wright, H. Jin, K. G. T. Hollands, and D. Naylor, *Flow Visualization of Natural Convection in a Tall, Air-Filled Vertical Cavity*, Int. J. Heat Mass Transf. **49**, 889 (2006).

[52] B. L. Gelmont and I. V. Ioffe, *The Electric Field Influence on the Convection in the Liquid Dielectric*, Phys. Lett. A **26**, 253 (1968).

[53] M. J. Gross and J. E. Porter, *Electrically Induced Convection in Dielectric Liquids*, Nature **212**, 1343 (1966).

[54] B. L. Smorodin and M. G. Velarde, *On the Parametric Excitation of Electrothermal Instability in a Dielectric Liquid Layer Using an Alternating Electric Field*, J. Electrost. **50**, 205 (2001).

[55] V. A. Semenov, *Parametric Instability of a Nonuniformly Heated Horizontal Layer of Liquid Dielectric in a Variable Electric Field*, Fluid Dyn. **28**, 734 (1994).

[56] M. Takashima and A. K. Ghosh, *Electrohydrodynamic Instability in a Viscoelastic Liquid Layer*, J. Phys. Soc. Jpn. **47**, 1717 (1979).

[57] B. M. Shankar, J. Kumar, I. S. Shivakumara, and S. B. Naveen Kumar, *Effect of Horizontal AC Electric Field on the Stability of Natural Convection in a Vertical Dielectric Fluid Layer*, J. Appl. Fluid Mech. **9**, 3073 (2016).

[58] M. Takashima and H. Hamabata, *The Stability of Natural Convection in a Vertical Layer of Dielectric Fluid in the Presence of a Horizontal Ac Electric Field*, J. Phys. Soc. Jpn. **53**, 1728 (1984).

[59] A. Meyer, *Active Control of Heat Transfer by an Electric Field*, Physics, Thesis of Université Le Havre Normandie (2017).

[60] A. Meyer, O. Crumeyrolle, I. Mutabazi, M. Meier, M. Jongmanns, M.-C. Renoult, T. Seelig, and C. Egbers, *Flow Patterns and Heat Transfer in a Cylindrical Annulus under 1g and Low-g Conditions: Theory and Simulation*, Microgravity Sci. Technol. **30**, 653 (2018).

[61] T. Seelig, A. Meyer, P. Gerstner, M. Meier, M. Jongmanns, M. Baumann, V. Heuveline, and C. Egbers, *Dielectrophoretic Force-Driven Convection in Annular Geometry under Earth's Gravity*, Int. J. Heat Mass Transf. **139**, 386 (2019).

[62] J. R. Melcher, *Continuum Electromechanics*, MIT Press Cambridge Mass (1981).

[63] L. D. Landau and E. M. Lifshitz, *Course of Theoretical Physics*, Butterworth-Heinemann Ltd (1980).

[64] T. B. Jones, *Electrohydrodynamically Enhanced Heat Transfer in Liquids—A Review*, in *Advances in Heat Transfer*, edited by T. F. Irvine and J. P. Hartnett, Elsevier (1979).

[65] Yoshikawa, O. Crumeyrolle, and I. Mutabazi, *Dielectrophoretic Force-Driven Thermal Convection in Annular Geometry*, Phys. Fluids **25**, 024106 (2013).

[66] H. N. Yoshikawa, C. Kang, I. Mutabazi, F. Zaussinger, P. Haun, and C. Egbers, *Thermoelectrohydrodynamic Convection in Parallel Plate Capacitors under Dielectric Heating Conditions*, Phys. Rev. Fluids **5**, 113503 (2020).

[67] J. M. Wallace and P. V. Hobbs, *Atmospheric Science: An Introductory Survey*, Elsevier Academic Press (2006).

[68] J. E. Hart, G. A. Glatzmaier, and J. Toomre, *Space-Laboratory and Numerical Simulations of Thermal Convection in a Rotating Hemispherical Shell with Radial Gravity*, J. Fluid Mech. **173**, 519 (1986).

[69] D. D. Gray and A. Giorgini, *The Validity of the Boussinesq Approximation for Liquids and Gases*, Int. J. Heat Mass Transf. **19**, 545 (1976).

[70] R. B. Bird, W. E. Stewart, and E. N. Lightfoot, *Transport Phenomena*, John Wiley and Sons Inc. New York (2002).

[71] T. Hartlep, A. Tilgner, and F. H. Busse, *Transition to Turbulent Convection in a Fluid Layer Heated from below at Moderate Aspect Ratio*, J. Fluid Mech. **544**, 309 (2005).

[72] C. Kang, A. Meyer, I. Mutabazi, and H. N. Yoshikawa, *Radial Buoyancy Effects on Momentum and Heat Transfer in a Circular Couette Flow*, Phys. Rev. Fluids **2**, 053901 (2017).

[73] C. Kang, A. Meyer, H. N. Yoshikawa, and I. Mutabazi, *Thermoelectric Convection in a Dielectric Liquid inside a Cylindrical Annulus with a Solid-Body Rotation*, Phys. Rev. Fluids **4**, 093502 (2019).

[74] C. Kang and I. Mutabazi, *Columnar Vortices Induced by Dielectrophoretic Force in a Stationary Cylindrical Annulus Filled with a Dielectric Liquid*, J. Fluid Mech. **908**, A26 (2021).

[75] J. Jeong and F. Hussain, *On the Identification of a Vortex*, J. Fluid Mech. **285**, 69 (1995).

[76] P. G. Drazin and W. H. Reid, *Hydrodynamic Stability*, Cambridge University Press (2004).

[77] M. C. Cross, *Derivation of the Amplitude Equation at the Rayleigh–Bénard Instability*, Phys. Fluids **23**, 1727 (1980).

[78] E. D. Siggia and A. Zippelius, *Dynamics of Defects in Rayleigh-Bénard Convection*, Phys. Rev. A **24**, 1036 (1981).

[79] F. H. Busse and J. A. Whitehead, *Instabilities of Convection Rolls in a High Prandtl Number Fluid*, J. Fluid Mech. **47**, 305 (1971).

[80] R. M. Clever and F. H. Busse, *Steady and Oscillatory Bimodal Convection*, J. Fluid Mech. **271**, 103 (1994).

[81] S. Grossmann and D. Lohse, *Scaling in Thermal Convection: A Unifying Theory*, J. Fluid Mech. **407**, 27 (2000).

[82] A. Schlüter, D. Lortz, and F. Busse, *On the Stability of Steady Finite Amplitude Convection*, J. Fluid Mech. **23**, 129 (1965).

[83] Q. Wang, D. Lohse, and O. Shishkina, *Scaling in Internally Heated Convection: A Unifying Theory*, Geophys. Res. Lett. **48**, (2021).

[84] S. Zou and Y. Yang, *Realizing the Ultimate Scaling in Convection Turbulence by Spatially Decoupling the Thermal and Viscous Boundary Layers*, J. Fluid Mech. **919**, R3 (2021).

[85] P. G. Drazin, *Introduction to Hydrodynamic Stability*, Cambridge University Press (2002).

[86] E. B. Barry, H. N. Yoshikawa, M. Tadie Fogaing, C. Kang, and I. Mutabazi, *Critical Modes of Thermoelectric Convection Instabilities in a Vertical Slot*, Microgravity Sci. Technol. **33**, 16 (2021).

[87] L. Fung and Y. Hwang, *Linear Instability of Tilted Parallel Shear Flow in a Strongly Stratified and Viscous Medium*, JMST Adv. **2**, 37 (2020).

[88] V. Travnikov, O. Crumeyrolle, and I. Mutabazi, *Numerical Investigation of the Heat Transfer in Cylindrical Annulus with a Dielectric Fluid under Microgravity*, Phys. Fluids **27**, 054103 (2015).

[89] P. S. B. Szabo, M. Meier, A. Meyer, E. Barry, V. Motuz, I. Mutabazi, and C. Egbers, *PIV and Shadowgraph Measurements of Thermo-Electrohydrodynamic Convection in a Horizontal Aligned Differentially Heated Annulus at Different Gravity Conditions*, Exp. Therm. Fluid Sci. **129**, 110470 (2021).

[90] S. B. Dalziel, G. O. Hughes, and B. R. Sutherland, *Whole-Field Density Measurements by Synthetic Schlieren*, Exp. Fluids **28**, 322 (2000).

[91] K. Hayasaka, Y. Tagawa, T. Liu, and M. Kameda, *Optical-Flow-Based Background-Oriented Schlieren Technique for Measuring a Laser-Induced Underwater Shock Wave*, Exp. Fluids **57**, 179 (2016).

[92] G. Meier, *Computerized Background-Oriented Schlieren*, Exp. Fluids **33**, 181 (2002).

[93] L. Venkatakrishnan and G. E. A. Meier, *Density Measurements Using the Background Oriented Schlieren Technique*, Exp. Fluids **37**, 237 (2004).

[94] M. Raffel, *Background-Oriented Schlieren (BOS) Techniques*, Exp. Fluids **56**, 60 (2015).